Understanding Transient Red Blood Cell Shapes in Flow Using Numerical Methods

Von der Universität Bayreuth
zur Erlangung des Grades eines
Doktors der Naturwissenschaften (Dr. rer. nat.)
genehmigte Abhandlung

von

Katharina Gräßel

aus Bamberg

1. Gutachter: Prof. Dr. Stephan Gekle
2. Gutachter: Prof. Dr. Daniel de las Heras

Tag der Einreichung: 22.07.2024
Tag des Kolloquiums: 18.11.2024

Zusammenfassung

Blut ist die Flüssigkeit, die die Funktionsfähigkeit des menschlichen Körpers durch eine Vielzahl von Transportfunktionen im Herz-Kreislauf-System gewährleistet. Rote Blutkörperchen sind der wichtigste zelluläre Bestandteil und machen Blut zu einer hochkomplexen Flüssigkeit, deren Strömungsverhalten bei Weitem noch nicht vollständig erforscht ist. Diese Arbeit trägt zum Verständnis der Blutströmung bei, indem die Formen der roten Blutkörperchen in verschiedenen Strömungsgeometrien mit dreidimensionalen numerischen Simulationen untersucht werden.

In Mikrokanälen fließen rote Blutkörperchen in zwei charakteristischen Formen, die als *slipper* und *croissant* bezeichnet werden und die auch als transiente Zwischenformen auftreten können. In dieser Arbeit werden die Bedingungen und der Prozess des Übergangs zwischen diesen beiden Formen in einer zeitabhängigen Strömung untersucht. Außerdem wird die Dynamik des *slipper*-Zustands durch einen engen Vergleich der Simulationsergebnisse mit entsprechenden experimentellen Studien näher beleuchtet. Die beobachtete Unstimmigkeit in der Frequenz der *slipper*-Bewegung mit experimentellen Daten wird durch die zusätzliche Berücksichtigung der Membranviskosität der Zelle im Simulationsmodell aufgelöst. Der Einfluss der Erythrozytenparameter in verschiedenen Versuchsanordnungen wird untersucht, was insbesondere die Bedeutung der Viskosität der Membran der roten Blutzelle für die Dynamik des Deformationsprozesses aufzeigt, die sich von dem Einfluss der Viskosität der intrazellulären Flüssigkeit unterscheidet. Die untersuchten Systeme umfassen die Dynamik der Zellen in einer Scherströmung und in einem Kanal der Längenskala der Blutzellen sowie die Dehnung und anschließende Relaxation der Zelle in einem System (optischer) Mikropinzetten. Außerdem untersucht wird die Zellverformung in einer Expansionsgeometrie und in einem sich verengenden Kanal. Letzteres wird für den Vergleich einer großen Anzahl von Deformationsdaten einzelner Zellen mit experimentellen Daten aus einem Aufbau mit sehr hoher Durchsatzrate verwendet. Im letzten Teil der Arbeit wird neben der detaillierten Analyse der Einzelzelldynamik auch ein Ausblick auf das kollektive Zellverhalten in zeitabhängiger Strömung gegeben. Die Bereiche im Umfeld einer Verengung in einem Mikrokanal, in denen sich keine Zellen befinden, werden untersucht, wobei sich mithilfe der Simulationsergebnisse die Kopplung der Dynamik der zellfreien Regionen mit der Oszillation des Strömungsfeldes erklären lässt.

Die Untersuchung der beschriebenen Systeme basiert auf der *boundary integral*-Methode und der *lattice Boltzmann-immersed boundary*-Methode. Ein mathematischer Ausdruck für die zusätzlich wirkenden Kräfte durch die viskose Spannung aufgrund des bisher fehlenden Beitrags der Membranviskosität wird in einer Form hergeleitet, die mit dem *boundary integral*-Verfahren kompatibel ist. Dieser Beitrag wird erfolgreich implementiert und validiert. Im weiteren Verlauf der Arbeit wird ein neuartiger Ansatz für den Vergleich von experimentellen und numerischen Da-

ten entwickelt, um aus den statistischen Daten vieler Zellen auf die Verteilung der Zelleigenschaften zu schließen.

Abstract

Blood is the fluid that ensures the functionality of the human body through a variety of transport functions in the cardiovascular system. Red blood cells are the main cellular component and make blood a highly complex fluid, whose flow behaviour is far from fully understood. This thesis contributes to the understanding of blood flow, by investigating red blood cell shapes in various flow geometries with three-dimensional numerical simulations.

In microchannels red blood cells flow in two characteristic shapes, named *slipper* and *croissant*, which can also occur as transient intermediate shapes. This thesis elucidates the conditions for and the process of the transition between these two shapes in time-dependent flow and also sheds light on the dynamics of the slipper state, by closely comparing the simulation results to related experimental studies. The observed disagreement in the frequency of the slipper movement with the experimental data is resolved by the incorporation of a membrane viscosity contribution in the simulation model. The influence of the red blood cell parameters in different setups is investigated. This especially demonstrates the significance of the viscosity of the red blood cell membrane for the dynamics of the deformation process, which is distinct from the influence of viscosity of the intracellular fluid. The investigated systems include the study of the dynamics in shear flow and in the microchannel, the stretching and subsequent relaxation of the cell in a tweezer system and the cell deformation in an expansion geometry as well as a narrowing channel. The latter setup is used to compare the single cell deformation data for a large number of cells to an experimental high-throughput cell analysis method. In the last part of the thesis, in addition to the detailed analysis of single cell dynamics, an outlook on the collective cell behaviour in time-dependent flow is given. The cell-depleted regions around a constriction in a microchannel are studied, and the simulation results explain the coupling of the dynamics of cell-free regions to the flow field oscillation.

The investigation of the described systems is based on the boundary integral method and the lattice Boltzmann-immersed boundary method. A mathematical expression for the additional membrane forces from the viscous stress due to the previously missing membrane viscosity contribution is derived in a form compatible with the boundary integral approach. This contribution is implemented and validated successfully. In the last part of the thesis, a novel approach for the comparison of experimental and numerical data is developed, in order to infer the distribution of the cell properties from the statistical data for many cells.

Contents

List of Figures

List of Tables

1 Introduction

Some very general facts The study of blood flow is not only undertaken in the fields of biology and medicine, but also became a subject of interest for physicists. The goal is to gain systematic understanding of the physical mechanisms which determine the blood flow behaviour, especially that of the main blood component, the red blood cells (RBCs). About 40 % to 45 % of human blood consists of red blood cells (erythrocytes), the remaining volume is taken up by blood plasma and less than 1% by other solid components, such as white blood cells and platelets [1]. This makes blood a highly complex fluid that cannot be described on the length scale of individual cells, using the classic methods of hydrodynamics for simple fluids. The flow properties are primarily determined by the interaction of the erythrocytes with each other and with the surrounding plasma. RBCs are highly deformable and can pass through orifices much smaller than the RBC rest shape [2]. These aspects make it challenging to describe and understand the system using the methods of physics. The study of the microfluidic flow behaviour of RBCs advances our knowledge of in vivo blood flow. Changes in the mechanical properties of erythrocytes, such as the viscosity of the cytoplasm or the bending rigidity of the cell membrane, can change the red blood cell morphology and crucially impact flow behaviour in blood vessels [3–6].

Why it is interesting to study blood flow Moreover, understanding the dynamics of blood flow is interesting from the perspective of potential applications and can lead to insights into various diseases related to blood cell abnormalities and pathological changes in the circulatory system. If the morphology and behaviour of healthy red blood cells are known, pathological changes in the blood can be detected and investigated, such as those caused by diseases like malaria or sickle cell anemia [7]. Sorting cells based on their dynamic properties is also possible [8, 9]. Laboratory-on-a-chip applications for biomedical appliance can be developed based on theoretical and microfluidic investigation of microchannels and especially channel constrictions, which strongly impact the organisation of the red blood cells. Furthermore, the shape of RBCs is thought to influence oxygen transport in capillaries [10]. In recent studies, changes in the red blood cell behaviour have been linked to COVID-19 disease [11, 12].

From where this thesis starts The shape deformations of single RBCs in flow have been studied since at least the the nineteen-eighties [13]. Red blood cells flowing through microchannels exhibit different characteristic shapes. These are mainly *croissants*, observed centred in the parabolic flow and asymmetric *slippers*, which flow off-centred and show a characteristic tank-treading movement of the membrane around the cell interior [13–17]. Theoretical investigations began with simulation models for vesicles in two dimensions in unlimited and limited Poiseuille flow, where in addition to croissants and slippers, projectile-shaped cell forms (bullets) occur [18, 19]. Like RBCs vesicles have a double lipid layer but, unlike red blood cells, they do not possess shear elasticity. Since shear elasticity has no significance for a one-dimensional surface, the vesicle and erythrocyte models are equivalent in two dimensions. Further studies for two-dimensional vesicles find, that the interplay of channel width and viscosity difference between the cell interior and surrounding fluid determines the use of tank-treading for slippers [20]. In addition, the transition between *slipper* and *croissant* is determined not only by the channel geometry but also by the flow intensity, whereby the initial shape of the simulated vesicle can also be decisive in a region of coexistence [21]. Hariprasad et al. [22] find, that for certain channel widths, the initial position of the simulated cell determines, whether it converges to the center of the channel or moves away from the center line under tank-treading. Simulations of red blood cells in three dimensions lead to a phase diagram that predicts shape (slipper, croissant and discocyte) and dynamics (angle and distance to the channel axis, movement . . .) again as a function of channel width and flow rate [23]. Due to the cylindrical geometry, for strongly constricted channels this study finds no slippers, in contrast to the two-dimensional simulations mentioned above. Similar simulations, which take into account that for healthy individuals the viscosity of the cell interior has a larger value than the viscosity of the blood plasma, lead to a qualitatively similar phase diagram with croissants at high flow rates in narrow channels, which, however, only shows tumbling dynamics of the cells in the area of the discocyte shape [24]. The experimental phase diagram presented in this study [24] has no sharp transitions between the different cell shapes, instead, it is constructed from the probability distribution for the occurrence of certain shapes. These measured frequency distributions can be reproduced qualitatively by replacing the constant value of the shear elasticity of the RBCs with a continuous distribution in the simulation [24]. This approach is justified because RBCs are biological entities and their mechanical properties can vary in a physiologically reasonable range. Guckenberger et al. [17] discuss for different cell velocities the decisive influence that the starting position and initial shape of the blood cell have on the later shape in simulations, in three dimensions and for a viscosity contrast of 5 between the cell interior and the external fluid. The authors also compare their numerical results with corresponding experiments, which show a distribution of the various RBC shapes as a function of the flow velocity. Moreover, recent numerical studies find, that not only the viscosity of the cell interior but also the viscosity of the cell membrane influences the dynamic cell deformation [25–27]. The various experimental and simulation results on the flow behaviour of individual erythrocytes in microchannels show, that the extremely complex dynamics of red blood cells in flow are decisively influenced by e.g. the channel geometry and flow intensity, the cells' elastic and viscous properties as well as the initial position of the cell. The last two points in particular are parameters that are difficult to measure or even control in experiments. This fact and the large number of influencing factors makes it difficult to systematically compare different studies and leads to phase diagrams in the literature for the shape of RBCs, which are not always consistent. Moreover, Guckenberger et al. [17] point out that transient *slipper* and *croissant* states exist, which, however, cannot be clearly identified as non-stationary shapes. This observation suggests that a reliable comparison between experiment and simulation based on phase diagrams for stationary RBC shapes is difficult.

Aim and structure of this thesis The aim of this thesis is to help towards a better understanding of the transient red blood cell shapes in flow, using different numerical methods. *Transient shape* first of all refers to the two predominant shapes slipper and croissant but in the further development of the thesis also to other types of transient shapes, which form in different types of flow. Following on from previous observations [17] that croissant and slipper shapes can be transient states, chapter 3 investigates dynamic shape changes in time-dependent flow. In the first part of the chapter the flow velocity-induced transition between slipper and croissant shape is examined, together with the dynamics of slipper cells. The second part of the chapter investigates the robustness of the phase diagram in pulsatile flow. The slipper dynamics are for the first time compared to novel experimental results. The details of the dynamical comparison between experiment and simulation in this chapter reveal, that in the simulation model a contribution to the RBC mechanics is missing. This comparison also shows, that the study of the dynamical behaviour, such as frequency results or dynamic shape transitions, is preferable compared to the construction of static phase diagrams, which did not reveal this missing contribution. It can be hypothesised that the missing part is a contribution which describes the viscosity of the membrane of the cell. The next chapter 4 outlines how this contribution can be included in the simulation model and shortly describes the implementation. The influence of this additional viscous contribution on the RBC dynamics in the microchannel setup is discussed in chapter 5 and the agreement with the experimental data from previous chapters is analysed. In the literature the deformation of RBCs stretched with (optical) tweezers and RBCs under shear flow are frequently investigated to validate simulation models or infer RBC properties. Results for these systems with the implemented viscous RBC contribution, together with the results for these RBCs in a constriction geometry are presented and compared with experimental results in chapter 6. In addition to the investigation of single cell dynamics, in chapter 7 a many-cell statistical approach is pursued. It is interesting to study the accumulated deformation behaviour of many RBCs because RBCs, as biological objects, are subject to biological variability, which, in experiments, leads to a scattering of the measurement results and in simulations should be expressed as a variation of the RBC properties in a physiologically meaningful range. An approach to reconcile experimental and simulation data for such a setup and strategies to infer information about the physical properties of RBCs from that are presented in the chapter. Finally, in the last chapter 8, again a time-dependent flow is considered and its influence on the collective behaviour of many red blood cells in a constricted geometry is studied.

2 Numerical simulations of red blood cells

2.1 Overview

This chapter gives an overview of the simulation methods used in this thesis. First the structure of RBCs and their modelling in numerical simulations is described in section 2.2. There are different approaches to simulate RBCs in flow and to implement the coupling of the membrane to the surrounding fluid. Many simulations are based on implementations of the boundary integral method for systems with low Reynolds numbers [15, 17, 18, 21, 28], which is based on the solution of the Stokes' equation and thus neglects inertial effects. Section 2.3 explains the fundamentals of the boundary integral method (BIM) and its implementation by Guckenberger [29]. BIM simulations in this thesis and extensions of the code are based on this implementation. The second numerical method used for simulations in this thesis, the lattice Boltzmann method (LBM), is described in section 2.4, together with the immersed boundary method (IBM) for the interaction of RBC and fluid. The LBM-IBM method is not restricted to low Reynolds number systems and frequently used in blood flow simulations [20, 25].

2.2 Red blood cell model

RBCs consist of a thin membrane which encloses the inner fluid. The membrane is made up of a outer lipid bilayer and a inner membrane skeleton, mainly spectrin philaments which lie beneath the bilayer [30]. The membrane can be modelled as a two-dimensional (visco-)elastic sheet, because its thickness of around 100 nm is negligible compared the the large radius $R = 4\,\mu\text{m}$ of the cell [31]. In simulations the membrane is discretised with flat triangles with nodes at their edges as shown in figure 2.1(a). Properties of the membrane are resistance to bending and surface conservation due the lipid bilayer. In addition, the membrane skeleton is responsible for the cell's shear elasticity.

The latter two effects are described with phenomenological Skalak law [32, 33]

$$W_\mathrm{S} = \frac{\kappa_\mathrm{S}}{12}\left(I_1^2 + 2I_1 - 2I_2\right) + \frac{\kappa_\mathrm{A}}{8} I_2^2 \tag{2.1}$$

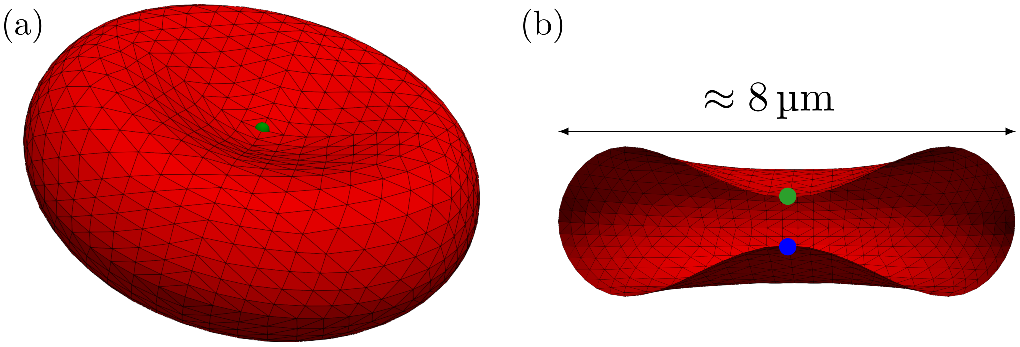

Figure 2.1: Modelling of RBCs in simulations. (a) The surface is discretised with flat triangles. (b) A cut through the cell shows the symmetry of the discocyte shape. The dimples of the cell are marked in green and blue.

where κ_S is the shear modulus, κ_A the area conservation modulus and I_1, I_2 are the deformation invariants of the surface displacement gradient [34]. Note that different conventions for the fractions of the prefactors in the Skalak law exist [32–36]. We use the principal of virtual work to compute the elastic force on a membrane point $\boldsymbol{x}_i$ [35]

$$\boldsymbol{F}(\boldsymbol{x}_i) = -\frac{\partial W_\mathrm{S}}{\partial \boldsymbol{x}_i}. \tag{2.2}$$

The Helfrich model describes the resistance to bending [37–40]

$$W_\mathrm{B} = \int_S 2\kappa_B (H - H_0)^2 \mathrm{d}S \tag{2.3}$$

where κ_B is the bending modulus and

$$H(\boldsymbol{x}) = \frac{1}{2}\sum_{i=1}^{3}(\Delta_\mathrm{S} x_i) n_i(\boldsymbol{x}) \quad \boldsymbol{x} \in S \tag{2.4}$$

is the local mean curvature [40, 41] with the reference curvature H_0. The reference curvature is commonly reported in dimensionless form as $c_0^* = 2H_0 a_0$ where $a_0 = 2.82\,\mathrm{\mu m}$ is the equivalent radius of a sphere whose surface area is identical to that of the RBC. The integral in equation (2.3) runs over the whole membrane surface S with normal vector $\boldsymbol{n}$ and points $\boldsymbol{x}$ on the surface. The resulting force on the membrane is computed as a bending force density on the membrane [40].

$$\Delta \boldsymbol{f}_\mathrm{B} = -2\kappa_\mathrm{B}\left[\Delta_\mathrm{S}(H - H_0) + 2(H - H_0)(H^2 - K + H_0 H)\right]\boldsymbol{n}, \tag{2.5}$$

with the Gaussian curvature $K(\boldsymbol{x}) = \kappa_1\kappa_2$ and the mean curvatures $\kappa_{1,2}$. The shear and bending energy contributions lead to membrane forces, which together with the volume conservation of the RBC lead to the characteristic rest shape of the cell, also called equilibrium shape. The RBC assumes its rest shape when located in a quiescent fluid without external flow [42]. The rest shape is a discocyte with a rim and two dimples, it has a long radius of $R = 3.91\,\mu\mathrm{m}$, abbreviated as radius of the RBC, the surface area is $A = 133.5\,\mu\mathrm{m}^2$ and the volume $V = 93.5\,\mu\mathrm{m}^3$ [1, 7, 43]. A mathematical expression for the discocyte shape is used to generate this shape in the simulation model [29, 43] shown in figure 2.1, in 2.1(b) the two dimples of the cell are highlighted in green and blue. The RBC exhibits a shape memory [42, 44], if external forces on the RBC are removed, it relaxes back to its discocyte rest shape with the dimples at the same position of the surface. Parameters in simulation models must be chosen such that this rest behaviour is ensured.

For the shear contribution an elastic reference shape of the RBC must be defined [45–49], other common names are stress-free shape or natural state. The elastic shear reference can be interpreted as the cytoskeleton shape in absence of external forces and is not necessarily identical to the rest shape of the RBCs. For the RBC mainly two different possibilities are used in the literature, the discocyte and a nearly spherical oblate spheroid. In recent years studies show a tendency towards an oblate spheroid replacing the discocyte as shear reference shape [50–54]. The spheroid is defined by its aspect ratio τ and its radius is chosen such, that the spheroid's and the RBC's surface area are identical.

Typical values of the shear and bending moduli of the red blood cells are $\kappa_\mathrm{S} = 5 \times 10^{-6}\,\mathrm{N\,m^{-1}}$ [31, 55, 56] and $\kappa_\mathrm{B} = 3 \times 10^{-19}\,\mathrm{N\,m}$ [17, 25, 31, 57, 58]. Depending on the reference shape, different reference curvatures c_0^* are appropriate [52], this is discussed in detail in section 5.3. The particular specification in the simulations is given in the setup description of the respective section.

The RBCs are suspended in a Newtonian fluid of dynamic viscosity μ_o and filled with another Newtonian fluid of viscosity μ_i. The ratio of these defines the viscosity contrast

$$\lambda = \frac{\mu_\mathrm{i}}{\mu_\mathrm{o}}. \tag{2.6}$$

The interior fluid of healthy RBCs is more viscous than blood plasma due to the haemoglobin inside the cell, therefore the implementation of a viscosity contrast is necessary for blood flow simulations [59].

Early experimental results proposed a value near $\lambda = 5$ for the viscosity contrast between blood plasma and the fluid inside the RBCs [60, 61], which was assumed for most simulation studies [17, 24]. We showed recently that larger values of the viscosity contrast might better capture experimental results [62]. In this thesis different values of λ are investigated, i.e. different values of the RBC internal viscosity. For the absolute value of the outer viscosity μ_o the value of the dynamic blood plasma viscosity $1.2\,\mathrm{mPa\,s}$ [63] is assumed if not stated otherwise.

2.3 Boundary integral method simulations

2.3.1 The boundary integral method

In systems where the viscous forces are significantly larger than the inertial forces the Navier-Stokes equation can be simplified to the Stokes equation

$$0 = -\nabla p + \mu \Delta \boldsymbol{v} + \boldsymbol{f}. \tag{2.7}$$

with pressure p, dynamic viscosity μ, velocity $\boldsymbol{v}$ and a force term $\boldsymbol{f}$. In general, the Stokes equation and the continuity equation $\nabla \cdot \boldsymbol{v} = 0$ together must be solved to compute the motion of the fluid.

A simple example is the velocity field [64]

$$v_i(\boldsymbol{x}) = \frac{1}{8\pi\mu} G_{ij}(\boldsymbol{x}, \boldsymbol{x}_0) F_j \tag{2.8}$$

which is the solution of (2.7) for a point force $\boldsymbol{f} = \boldsymbol{F}\delta(\boldsymbol{x} - \boldsymbol{x_0})$ at $\boldsymbol{x_0}$. Here $G_{ij}(\boldsymbol{x}, \boldsymbol{x}_0)$, $i, j = 1, 2, 3$ is the Green's function also called stokeslet. The associated stress tensor is

$$\sigma_{il}(\boldsymbol{x}) = \frac{1}{8\pi} T_{ijl}(\boldsymbol{x}, \boldsymbol{x}_0) F_j \tag{2.9}$$

with the stresslet $T_{ijl}(\boldsymbol{x}, \boldsymbol{x}_0)$. The concrete shape of the Green's function and stresslet depends on the simulated system, for example free space, or in many applications a three-dimensional periodic system [65, 66]. The expressions for G_{ij} and T_{ijl} in free space are given by [64]

$$G_{ij}^{\infty}(\boldsymbol{x}, \boldsymbol{x}_0) = \frac{\delta_{ij}}{r} + \frac{\hat{x}_i \hat{x}_j}{r^3} \qquad T_{ijl}^{\infty}(\boldsymbol{x}, \boldsymbol{x}_0) = -\frac{6\hat{\boldsymbol{x}}_i \hat{\boldsymbol{x}}_j \hat{\boldsymbol{x}}_l}{r^5} \qquad \text{with} \quad \hat{\boldsymbol{x}} = \boldsymbol{x} - \boldsymbol{x}_0, \; r = |\hat{\boldsymbol{x}}|. \tag{2.10}$$

The BIM is based on the idea to discretise the surface of all objects in the incident flow $\boldsymbol{v}^{\infty}$ and treat the elements of the surfaces as point forces in the Stokes equation. Then these point forces are sources of additional contributions to the background flow $\boldsymbol{v}^{\infty}$. Such objects can be RBCs, but channels are treated alike. Regarding the technical implementation, the Stokes equation is written as an integral equation over the discretised surface S [64, 67].

$$\begin{aligned} v_j(\boldsymbol{x}_0) = \frac{2}{1+\lambda_n} \Bigg[& v_j^{\infty}(\boldsymbol{x}_0) - \frac{1}{8\pi\mu_o} \sum_{m=1}^{N} \int_S \Delta f_i(\boldsymbol{x}) G_{ij}(\boldsymbol{x}, \boldsymbol{x}_0) \mathrm{d}S(\boldsymbol{x}) \\ & + \frac{1}{8\pi} \sum_{m=1}^{N} (1 - \lambda_m) \int_S v_i(\boldsymbol{x}) T_{ijl}(\boldsymbol{x}, \boldsymbol{x}_0) n_l(\boldsymbol{x}) \mathrm{d}S(\boldsymbol{x}) \Bigg]. \end{aligned} \tag{2.11}$$

Equation (2.11) is called Fredholm integral equation and gives the velocity at a surface point $\boldsymbol{x}_0$ for particle n out of $1, \ldots, N$ particles in the volume, and Δf_i is the traction jump across the particle surface [67]. The second term in (2.11) is called single-layer potential, the third term double-layer potential [64]. For RBCs the viscosity contrast is defined in (2.6) and for walls it is $\lambda = 1$ [29].

Systems which are adequately described by Stokes equation feature a low Reynolds number

$$Re = \frac{vL\rho}{\mu}, \tag{2.12}$$

which describes the ratio between the inertial and viscous forces of the system. Here L is a characteristic length scale of the system. In these cases the BIM can be used for numerical simulation. A prime example studied in this thesis are RBCs in the microcirculation, mimicked by RBCs in microfluidic channels. The diameter of the cell gives the characteristic length scale $L = 2R$ and in many cases studied in this thesis the viscosity is equal to the blood plasma viscosity, values are given in section 2.2. The density is given by the blood plasma density $\rho = 1\,\mathrm{g\,cm^{-3}}$ [68].

2.3.2 Implementation of the boundary integral method

The implementation of the BIM described here along general lines is the work of Guckenberger [29, 69]. The implementation was written in C++ and validated for several applications [17, 39, 65, 70, 71]. All objects in the flow, in this work RBCs and channels, are discretised with flat triangles. In order to prevent numerical problems, rectangular channels have slightly rounded corners. Channel nodes are fixed with springs of such high spring constant, that this implementation has negligible influence on the simulation outcome. This approach leads to non-vanishing velocity at the wall which is numerically favourable when solving the Fredholm integral equation [65, 72]. The membrane forces of the RBCs are included as traction jumps across the membrane $\Delta \boldsymbol{f}$ in the Fredholm integral equation (2.11). For the Skalak contribution the negative of the force (2.2) is divided by the area attributed to node $\boldsymbol{x}_i$, using 'Meyer's mixed area' [40, 73]. The traction jump for the bending contribution is directly given in (2.5). The numerical difficulty there is that because of the second Laplace-Beltrami operator Δ_S [74] in (2.4) a fourth derivative must be computed on the triangulated surface [39]. The method used for computation of the bending forces is Meyer's algorithm [73], further details are given in method C in [39]. For the integration of equation (2.11) a standard Gaussian quadrature [75] with 7 points per triangle is used and linear interpolation for each triangle [64]. Singularity removal procedures for single-layer [65, 76] and double-layer potentials [65, 67, 77] make numerical evaluation possible for surface points with diverging, but still integrable Green's function. In systems with periodic boundary conditions Ewald decomposition [78] in combination with a smooth particle mesh Ewald method [66, 79] increase the performance for the computation of the Green's functions. For the solution of the ensuing linear, dense, non-symmetric system GMRES [80] is used.

This procedure returns the surface velocity as solution of equation (2.11) and the surface nodes are moved accordingly using the kinematic boundary condition $\boldsymbol{v}(\boldsymbol{x}(t), t) = \mathrm{d}\boldsymbol{x}/\mathrm{d}t$ [67]. The time integration of the kinematic boundary condition is solved with a Bogacki-Shampine algorithm [81] with adaptive time step width, the absolute tolerance is around 10^{-5} times the RBC radius. The volume conservation of the cell is violated due to artificial changes related to the finite resolution of the surface triangulation. These are corrected with a no-flux velocity condition and a rescaling method for the volume [65, 82].

2.4 Lattice Boltzmann-immersed boundary method simulations

2.4.1 Lattice Boltzmann method

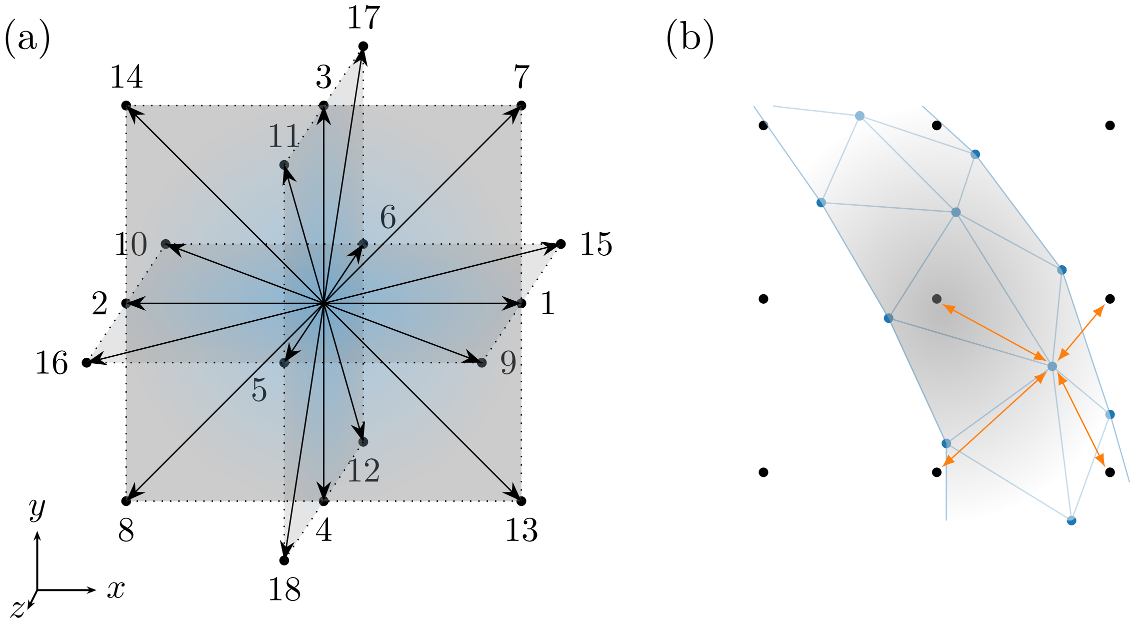

Figure 2.2: Discretisation for the lattice Boltzmann-immersed boundary method implementation. (a) The velocity set D3Q19 in three dimensions for discretisation of the velocity space in LBM. (b) In IBM the velocity on the LBM lattice points (black) is interpolated at the membrane vertices (blue points) as indicated with the orange arrows. For simplification only one layer of the three-dimensional LBM grid is shown.

The LBM can be used to simulate various fluid flows [83], including microfluidic flows with immersed soft particles or cells [84, 85]. It provides a numerical solution of the Boltzmann equation [86]

$$\frac{\mathrm{d}f}{\mathrm{d}t} = \frac{\partial f}{\partial t} + \xi_\beta \frac{\partial f}{\partial x_\beta} + \frac{F_\beta}{\rho}\frac{\partial f}{\partial \xi_\beta} = \Omega(f), \tag{2.13}$$

which describes the dynamics of the single particle distribution function $f(\boldsymbol{x}, \boldsymbol{\xi}, t)$ of the considered system, with space coordinates $\boldsymbol{x}$, velocity components $\boldsymbol{\xi}$ and time t. Here $\boldsymbol{F}$ summarise the external forces in the system and ρ is the density. The collision term $\Omega(f)$ describes the interaction with the other $N-1$ particles in the system.

For numerical implementation we discretise space on a regular grid with lattice distance Δx and time with increment Δt. In addition, the velocity space is discretised as shown in figure 2.2(a). The discrete velocities are summarised in the velocity set $\{\boldsymbol{c_i}\}$, here this set is D3Q19, i.e. $i = 0, \ldots, 18$. This leads to the discretised distribution function $f_i(x, t)$ where the index i refers to the position in velocity space. Its evolution is described by the discretised version of (2.13), the lattice Boltzmann equation

$$f_i\left(\boldsymbol{x} + \boldsymbol{c}_i \Delta t, t + \Delta t\right) = f_i\left(\boldsymbol{x}, t\right) + \Omega_i\left(\boldsymbol{x}, t\right) \tag{2.14}$$

The most simple possibility to choose the collision operator is the Bhatnagar-Gross-Krook (BGK) operator [86]

$$\Omega_i = -\frac{(f_i - f_i^{\mathrm{eq}})}{\tau}\Delta t \tag{2.15}$$

which describes relaxation of the system towards its local equilibrium f_i^{eq} with relaxation time τ. In the implementation used in this thesis a more accurate extension of the BGK, the multiple relaxation times (MRT) collision operator is used [84, 87]. External forces in (2.13) are represented as additional source term on the right hand side of the discretised lattice Boltzmann equation (2.14) [86]. For example a pressure gradient in a straight channel, but also forces from immersed membranes acting on the fluid can be included in the source term. One time step of the LBM basically consists of two steps. First the right hand side of equation (2.14) is calculated, this is called *collision*. Then the result is propagated to the lattice points in direct neighbourhood specified by $\{\boldsymbol{c}_i\}$ on the left hand side of equation (2.14), this is the *streaming* step. Physical quantities like the density or local velocity $\boldsymbol{v}(\boldsymbol{x}, t)$ can be obtained as moments of the distribution function [86]

$$\rho = \sum_i f_i \tag{2.16}$$

$$\rho \boldsymbol{v} = \sum_i \boldsymbol{c}_i f_i \tag{2.17}$$

If forces are included they lead to an additional force correction in equation (2.17) [86]. At the beginning of a simulation the density and velocity fields are initialised. Then the LBM algorithm is carried out for an arbitrary number of time steps: The local equilibrium distribution is calculated from the density and velocity fields and the collision-streaming scheme is carried out. This leads to an updated distribution function and with that an update of the physical fields as indicated in equations (2.16) and (2.17). No-slip boundary conditions at solid walls are implemented with a bounce-back scheme [86] and lead to the formation of a Poiseuille velocity profile in the absence of cells in a straight channel.

The LBM is a mesoscopic method as (in the context of fluid dynamics) it does not consider the direct particle interaction as a microscopic method would, but also does not directly solve the macroscopic Navier-Stokes equation. The approach via the particle distribution function lies in between with respect to length scales and level of abstraction. One major advantage of LBM is its straightforward parallelisability. The LBM implementation used in this thesis is from the software package ESPResSo [88–90].

2.4.2 Immersed boundary method

Cells immersed in the fluid move with the local fluid velocity at each membrane position and on the cell surface the velocity must obey the no-slip boundary condition. This coupling of the membrane to the fluid and vice versa is implemented with the IBM [86, 91–93]. The difficulty of the implementation is that there exist two different grids in the simulation, this is illustrated in figure 2.2(b). There are the LBM lattice points, shown as black points in figure 2.2(b) and the membrane vertices (blue points) of the triangulated cell membrane (shaded area in the figure). The IBM is a two-way coupling between the two grids. First the membrane forces, which are computed at the vertices, are allotted to the 8 LBM grid points in the neighbourhood of the respective vertex (orange arrows in figure 2.2(b), for simplification only one layer of LBM lattice points is drawn). These forces are included as a source term in the lattice Boltzmann equation. Then the local fluid velocity $\boldsymbol{v}$ is calculated with the LBM as described in 2.4.1. The second step of the coupling is the interpolation of the velocity field $\boldsymbol{v}$ at the membrane vertices, again shown by the orange arrows. This interpolated velocity is used to advect the respective vertex. The LBM lattice and cell triangulisation must have similar grid sizes. If the mean distance is much smaller than around half the LBM grid distance, the resolution of the flow field on the membrane surface is inadequate. If, on the other hand, the mean vertex distance is larger than about one time the LBM grid distance, the membrane forces are not distributed properly to all lattice points in vicinity of the membrane. In IBM there is flow on both sides of a closed surface [86], for cell membranes this is the interior fluid. The implementation of IBM used in this thesis is an extension of the ESPResSo software.

3 Dynamic shape changes of red blood cells in time-dependent flow

3.1 Overview

The aim of this chapter is to present the numerical investigation of RBC shape change in time-dependent flow with the boundary integral method. In small microfluidic channels whose diameter amounts to a few micrometers, RBCs are observed in mainly two characteristic shapes. These are the symmetric croissant shape, flowing in the centre of the channel, and the asymmetric slipper shape, which flows off-centred and is accompanied by a tank-treading movement of the membrane around the cell. Representative images of the two characteristic shapes are shownf in figure 3.1(a).

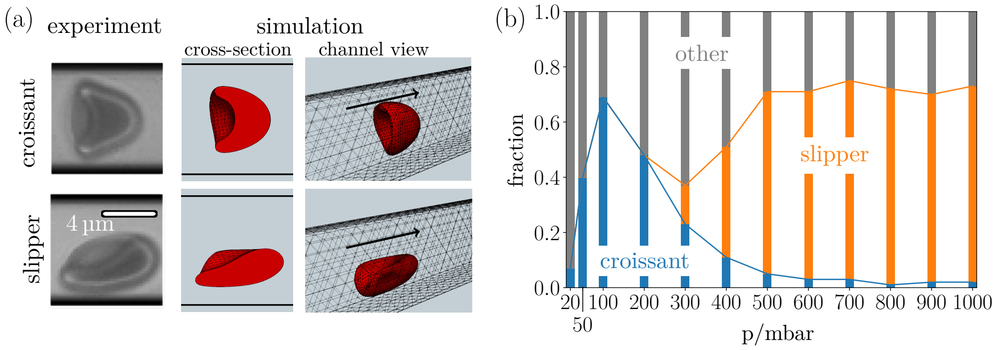

Figure 3.1: Red blood cell shapes in a microchannel of cross section 8 µm to 11.5 µm. (a) Experimental images of croissant and slipper shapes and corresponding simulation results in a discretised channel. (b) The experimental phase diagram shows bistability of slipper and croissant shapes in the experiment, depending on the pressure drop p in the channel, which can be converted to a flow velocity. Reproduced from [62] with permission from Cell Press.

The symmetric croissants are predominant at smaller pressure drops, i.e. smaller flow velocities and slippers at larger velocities, as the experimental phase diagram in figure 3.1(b) shows. Detailed comparison with simulation phase diagrams [17] at constant flow has shown the same bistability between croissant and slipper also in simulations.

A detailed investigation of the transition between these two bistable states in time-dependent flow is presented in the first section 3.3. Recent experimental developments make comparison of the slipper shape dynamics with experimental data possible. The results are discussed in section 3.4. Both sections 3.3 and 3.4 describe work which has been published in the paper [62], the experimental data was provided by S. M. Recktenwald, F. M. Maurer and T. John (members of the group of C. Wagner in Saarbrücken). Finally, the last section 3.5 discusses the stability of the phase diagram in time-dependent flow. The presentation of the results is preceded by a short section 3.2 on the details of the methods.

3.2 Method and parameters

The BIM is used to simulate single RBCs flowing through a rectangular microchannel of width W and height H in y-direction and z-direction, respectively. The length of the channel in x-direction is $L = 38.7\,\mu\text{m}$ and periodic boundary conditions are applied in this direction. In sections 3.3 and 3.4 $W = 11.5\,\mu\text{m}$ and $H = 8\,\mu\text{m}$ are used to make comparison with experiments in microchannels of the same size possible. In the last section the channel dimensions are identical to those of former numerical studies [17] with $W = 12\,\mu\text{m}$ and $H = 10\,\mu\text{m}$, which serve as constant flow reference. The Reynolds number (2.12) of the system is defined with the blood plasma viscosity and density and the radius of the RBC, compare section 2.3. For typical velocities of the system $v_\text{c} < 10\,\text{mm}\,\text{s}^{-1}$ the Reynolds number is well below one $Re < 0.1$ and the Stokes equation indeed adequately describes the flow. In sections 3.3 and 3.5 a time-dependent flow velocity is used.

The surface of the RBCs is discretised with 2048 flat triangles. The shear modulus is $\kappa_\text{S} = 5 \times 10^{-6}\,\text{N}\,\text{m}^{-1}$, the area dilation modulus $\kappa_\text{A} = 100\kappa_\text{S}$ and the discocyte is used as elastic reference shape. A bending modulus of $\kappa_\text{B} = 3 \times 10^{-19}\,\text{N}\,\text{m}$ and a flat bending reference shape are used. The RBC starts with its symmetry axis parallel to the channel axis and in the discocyte rest shape. In sections 3.3 and 3.4 it starts centred in the channel, in 3.5 the initial position varies, as specified there.

The outer fluid viscosity is chosen equal to the blood plasma viscosity. In some simulations larger values are employed to investigate the influence of more viscous surroundings on the cell dynamics, these are labelled accordingly. Different viscosity contrasts $\lambda = 5, 10, 20$ are used and discussed in section 3.4. In section 3.3 $\lambda = 10$ was used, in section 3.5 $\lambda = 5$ for better comparison with a former numerical study [17].

Corresponding experiments presented in section 3.3 and 3.4 used a high-precision pressure device for accurate modification of the pressure gradient in straight microchannels of cross section $W = (10.8 \pm 0.6)\,\mu\text{m}$ and $H = (7.9 \pm 0.3)\,\mu\text{m}$ and length $L = 40\,\text{mm}$. This device is combined with a feedback-mechanism of camera and movable stage to follow the cells during their transition through the channel and thus record their dynamic shape changes. Details are described in the joint publication [62].

3.3 Transition between red blood cell modes

3.3.1 Cell trajectories

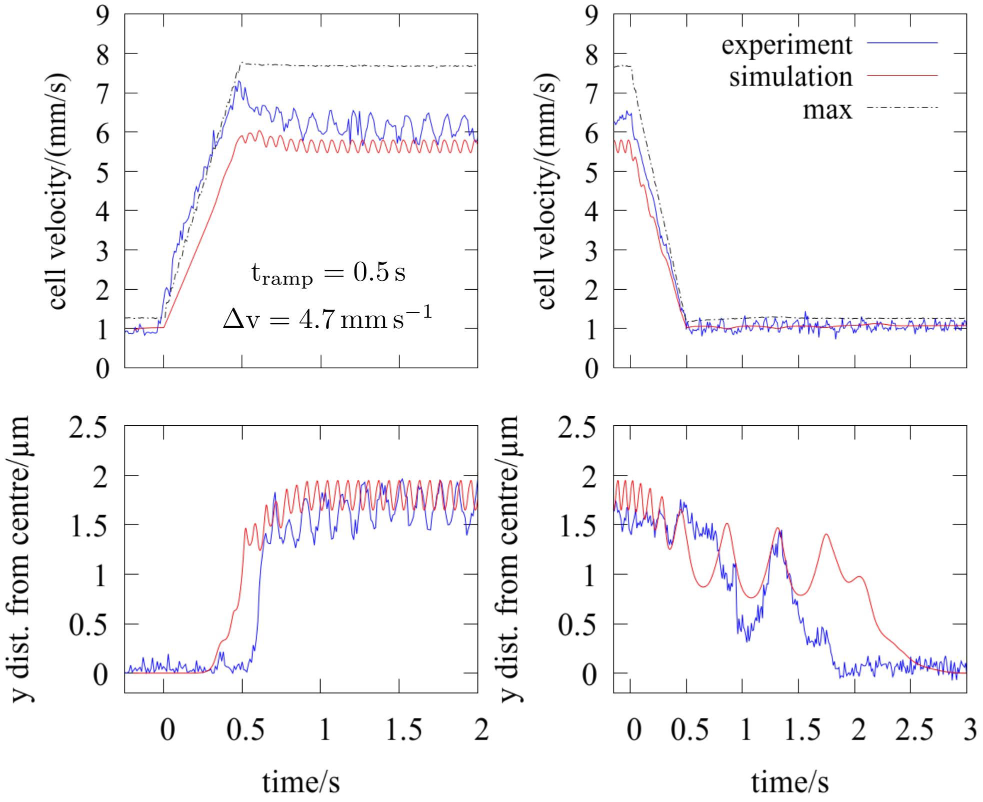

Figure 3.2: Red blood cell velocity and trajectory in time-dependent flow. Simulation curves are drawn in red, corresponding experiments in blue. The upper half of the figure shows the linear increase and decrease of the cell velocity over time. This is accompanied by a movement of the cell's centre of mass (lower half of the figure) away from the channel centre in y-direction for increasing velocity, and vice versa for decreasing velocity. Grey dashed lines show the maximum velocity. Reproduced from [62] with permission from Cell Press.

To study the dynamic transition between the two characteristic cell shapes croissant and slipper the flow velocity in the channel is increased linearly over time from a lower constant flow $v_{\mathrm{low}} = 1\,\mathrm{mm\,s^{-1}}$ to a variable upper mean velocity of v_{up} and vice versa for the opposite shape transition. An example of the velocity ramps and cell trajectory curves is shown in figure 3.2 in red for the simulations. The cell velocity is the centre of mass velocity extracted from the simulation data. For a short time of 0.2 s the RBC flows at constant velocity $v_{\mathrm{low}} = 1\,\mathrm{mm\,s^{-1}}$. Then the flow through the channel is increased during the ramping time $t_{\mathrm{ramp}} = 0.5\,\mathrm{s}$ until a mean velocity of $v_{\mathrm{up}} = 5.8\,\mathrm{mm\,s^{-1}}$ is reached. Due to the increase in the cell velocity the croissant-shaped RBC flowing at the channel centre transitions to a slipper and moves away from the centre. This transition is slightly delayed compared to the start of the velocity ramp as left column of figure 3.2 shows. The slipper exhibits a positional oscillation of the cells centre of mass and thus a fluctuation in the cell velocity. The opposite transition back to the centred croissant is induced by a subsequent decrease of the average flow through the channel after a velocity plateau of approximately 1.5 s in simulations. The downward transition is shown in the right panel of figure 3.2. The lower right graph shows that the shape change back to the symmetric croissant is considerably slower than the first transition and involves fluctuations of the centre of mass connected with cell rotations and strong membrane deformations.

The blue curves in figure 3.2 show corresponding experiments [62], which varied the pressure gradient in the channel to induce changes in the flow velocity. The gray dashed lines show the result of a calculation of the maximal velocity which could be reached in the channel for the applied pressure gradient [94]. During the velocity increase the experimental curve rises above that line. In addition, an overshoot of the cell velocity at the end of the upward transition can be observed. This is caused by a widening of the microfluidic channels fabricated from PDMS polymer with the (constant) increase of the pressure gradient [95], which in turn leads to a higher cell velocity due to the larger cross section.

3.3.2 Transition times

In section 3.3.1 the difference between the speed of the transition from croissant to slipper and vice versa was discussed. It can be characterised by the transition time for the shape changes. Start and end of the transition are determined manually based on the cell shape images [17]. In simulations and experiments two different velocity differences $\Delta v = v_{\mathrm{up}} - v_{\mathrm{low}}$ (or corresponding pressure gradient differences in experiments) of $4.7\,\mathrm{mm\,s^{-1}}$ and $6.2\,\mathrm{mm\,s^{-1}}$ were used, and four different ramping times $t_{\mathrm{ramp}} = 0.125\,\mathrm{s}, 0.25\,\mathrm{s}, 0.5\,\mathrm{s}, 1.0\,\mathrm{s}$ are investigated, similar to the example shown in figure 3.2. The resulting transition times for all trajectories are summarised in figure 3.3(a). Two major observations can be made. First, the mean transition time for the upward croissant-slipper transition is significantly lower than that for the slipper-croissant transition. This confirms that the transition time difference, discussed with figure 3.2 above, is a general feature of the system. The mean upward transition time for simulations is 0.37 s compared to 2.15 s for the downward trans-

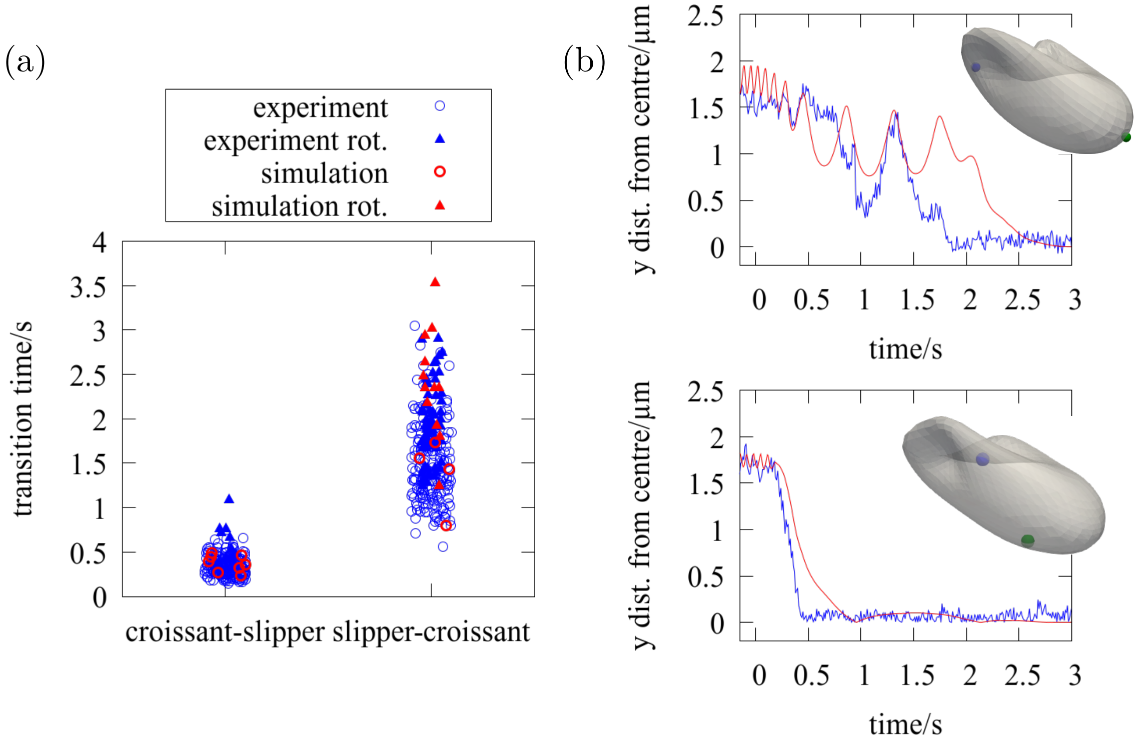

Figure 3.3: Transition times for cell shape changes. (a) Transition times for all simulations (red) and all experiments (blue) are summarised. Triangle symbols indicate whether the cell undergoes rotation during the shape change. (b) Two example trajectories of the cell centre of mass for the slipper to croissant transition illustrate the spread of the transition time distribution due to the cell orientation (insets) at the transition start. Reproduced from [62] with permission from Cell Press.

ition, experimental means are consistent with these. Second, the slipper-croissant transition times scatter more broadly than the croissant-slipper transitions.

There are two effects which explain these differences. The first is the difference in the rotation behaviour. RBCs that show a pronounced rotation during transition are marked with triangles in figure 3.3(a), this is in most cases connected with larger transition times. In simulations, rotation occurs only for the slipper-croissant transition. In experiments rotation is observed for 29 % of these, but only for 5 % of the croissant-slipper transition. The physical explanation behind this is the more symmetric shape of the croissant, were the membrane dimples are located at the side of the cell and thus the cell in general needs more time to adjust and assume the stable croissant shape. In addition, numerical simulations reveal that the transition dynamics crucially depend on the orientation of the RBC membrane at the start of the velocity change. In the slipper state the cell shows its characteristic tank-treading movement of the membrane were the dimples of the cell, visualised in figure 2.1(b) travel along the cell in the x-y-plane, consistent with previous studies [17]. The insets in figure 3.3(b) show the shape of the slipper cells and the location of its dimples at the beginning of the downward velocity ramp. All other simulation parameters equal, the difference in the slipper orientation leads to distinct transition trajectories drawn in red in the respective graphs in figure 3.3(b). In experiments similar curves can be observed, shown in blue in figure 3.3(b) but exact information of the slipper orientation is not available from experiments. Although a clear correlation between different dimple positions at the transition start and the resulting rotating behaviour could not be extracted, simulations show how sensitive the system is to the exact slipper orientation. All in all this effect leads to more variety in the slipper-croissant transition and can explain the broad scattering in figure 3.3(a) with in general larger transition times.

The second effect is the difference in the cell velocity during the largest part of the transition. As was shown exemplarily in figure 3.2 the croissant-slipper transition is delayed with respect to the velocity ramp, such that most of the transition happens at larger velocities. The delay in the opposite transition is less pronounced but also here most of the transition occurs at the target velocity, now v_{low}. Therefore, the upward transition is aided by a faster flow velocity which facilitates the slipper movement to its off-centre position. In contrast, the slipper-croissant transition is slowed down at v_{low}. In cases where cell rotation occurs, this effect further leads to acceleration or deceleration of the rotation.

Details of the transition time dependence on the velocity difference Δv or ramping time t_{ramp} are shown in figure 3.4(a) for the croissant-slipper and in (b) for the slipper-croissant transition for representative t_{ramp} and Δv [62]. If at an intermediate t_{ramp} the velocity difference Δv increases, a difference in the transition times for the upward transition is not observed. More surprising, the duration of the ramping process t_{ramp} also has no significant influence on the transition time, exemplified for $\Delta v = 4.7\,\mathrm{mm\,s^{-1}}$ in figure 3.4(a), with even less difference for other Δv [62]. Figure 3.4(b) shows that the same observation holds for the downward transition from slipper to croissant.

Furthermore the transition length Δx is studied, defined as the distance the RBC covers during the transition process. It is calculated from the transition time Δt as $\Delta x = \int_0^{\Delta t} v(t)\mathrm{d}t$. Here the transition start is set to $t = 0$ and the integral runs over the current velocity of the cell. The results for all parameter combinations are shown in figure 3.4(c). Aggregation of all results is justified as no dependence on the parameters t_{ramp} and Δv could be observed. In contrast to the transition time, the transition lengths in simulations for the two direction are similar, due to the differences in the integrated velocity, which is for the largest part of the integral smaller for the slipper-croissant transition. The experiments show a slightly larger mean transition length of 2.8 mm in croissant-slipper transition compared to 1.8 mm

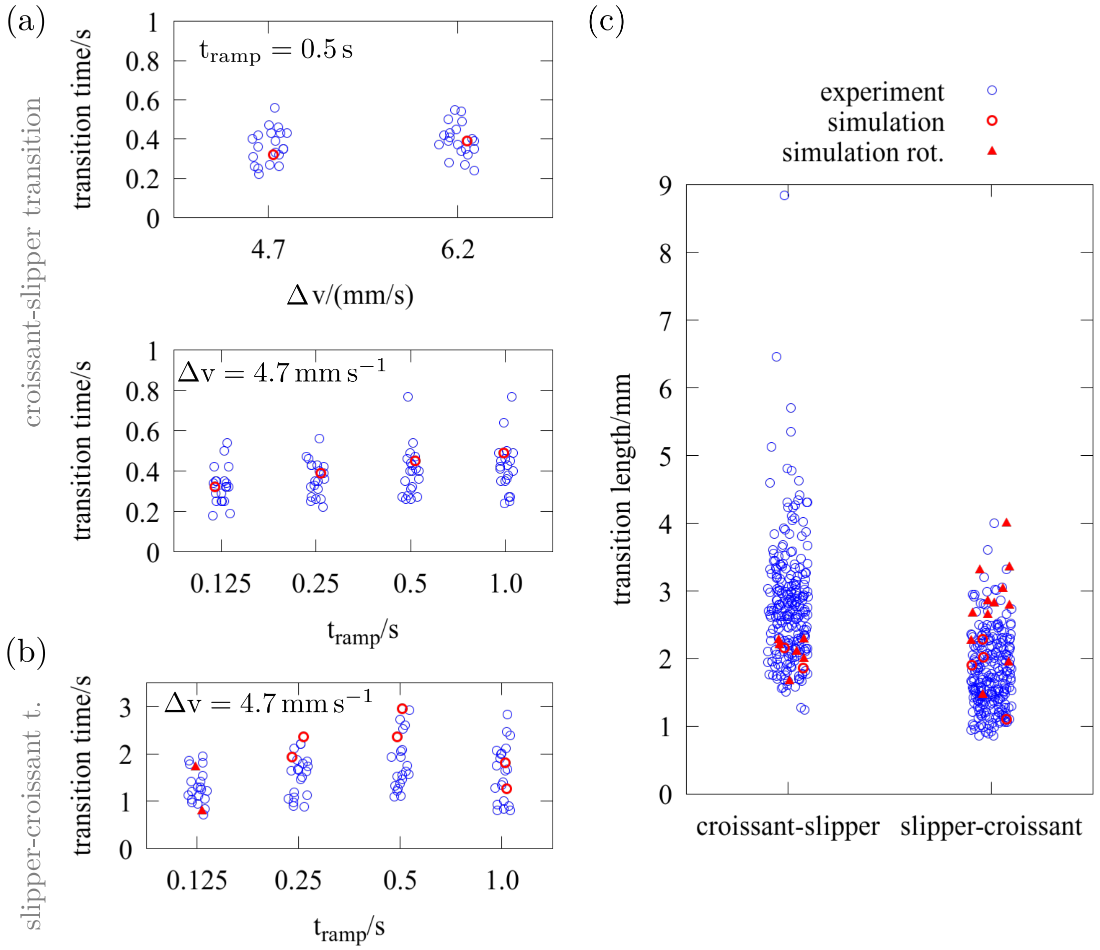

Figure 3.4: Details of the transition times and transition length. (a) Transition times for the croissant to slipper transition and (b) opposite slipper-croissant transition depending on the velocity difference Δv or ramping time t_{ramp} for selected t_{ramp} or Δv, respectively. (c) Transition lengths summarised for all results depending on the ramp direction. Triangles indicate that the cell undergoes rotation during the transition. Reproduced from [62] with permission from Cell Press.

in the opposite direction. This is again ascribed to the velocity overshooting due to the widening of the microfluidic channel during the pressure increase, discussed in section 3.3.1. The RBC travels a distance of around 250-375 times its rest diameter until the shape change is completed.

3.4 Dynamics of the slipper state

3.4.1 Influence of the viscosity contrast on the dynamics

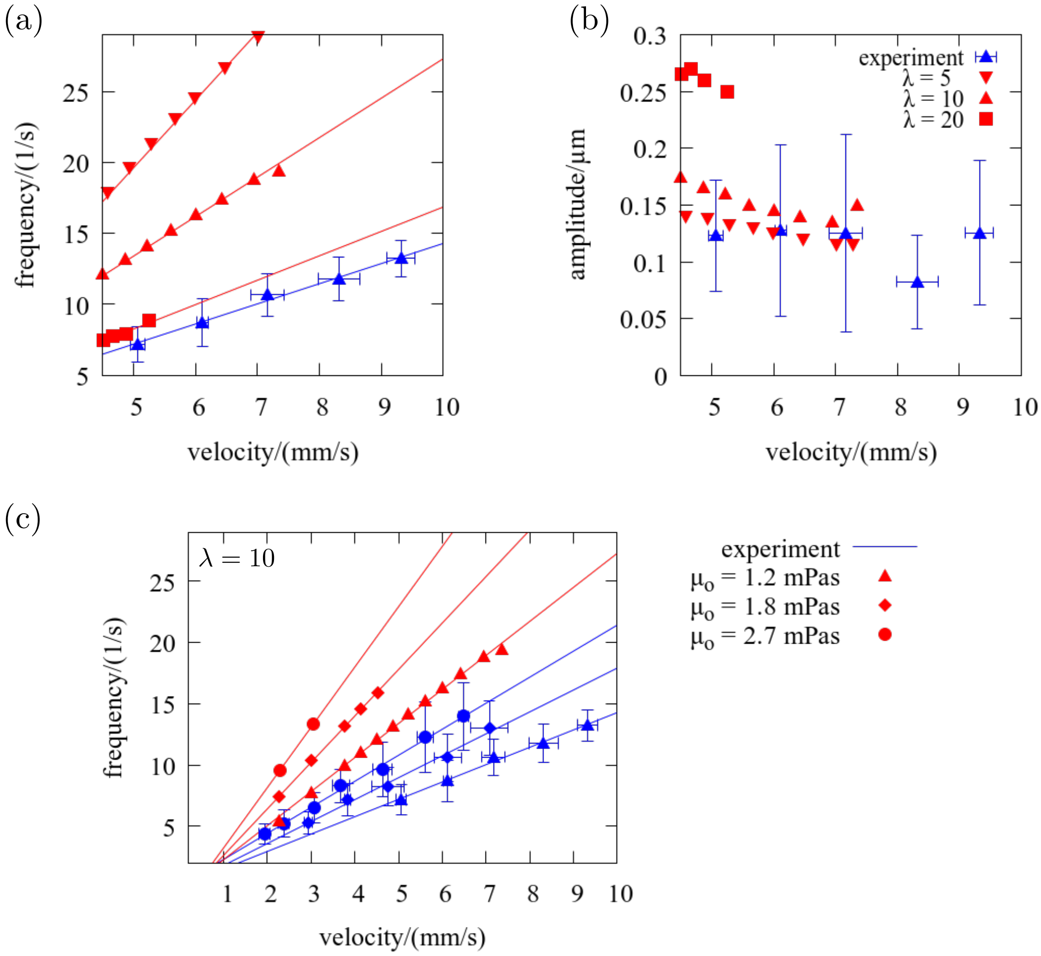

Figure 3.5: Dynamics of the slipper red blood cell shape. The (a) frequency and (b) amplitude of the slippers' centre of mass oscillation in y-direction are plotted against the cell velocity. In simulations (red symbols) the viscosity contrast λ is varied. Experimental results (in blue) are summarised with blue dots, marking the mean of all frequency/amplitude values, error bars are given as average of all measurements at the respective velocities. Linear fits (solid lines) serve as guide to the eye. (c) Oscillation frequency for increased outer viscosities μ_o, all with $\lambda = 10$. The results for $\mu_o = 1.2\,\mathrm{mPa\,s}$ from (a) are repeated. Reproduced from [62] with permission from Cell Press.

The cell trajectories in figure 3.2 show a pronounced oscillation of the cell's centre of mass at larger velocities when the cell is in the slipper state. These oscillations occur in all simulations and can be detected in approximately 50 % of the experimental slipper shapes. In order to compare the oscillation properties, the centre of mass trajectories are fitted with a sine function and frequency and amplitude are extracted. The results are shown in figure 3.5(a) and (b) for simulations (red) and experiments (blue). In addition to the simulations with viscosity contrast $\lambda = 10$ discussed in section 3.3 simulations of slipper cells were conducted for $\lambda = 5$ and $\lambda = 20$. Figure 3.5(a) shows that the frequency increases linearly with the RBC velocity for a given viscosity contrast. If the viscosity contrast increases, i.e. the interior fluid of the cell is more viscous, a decrease of the oscillation frequency for a given velocity is observed. The explanation for this effect is that the positional oscillation is connected to the tank-treading motion of the cell and an increase in viscosity slows down the dynamic movement. Moreover, it is consistent with older studies which identified an influence of the viscosity contrast on tank-treading in shear flow [96–99]. Only for the highest viscosity contrast of 20 the frequencies are in good agreement with the measurements. However, in simulations such RBCs show peculiar membrane rotation behaviour after only few oscillations and are unstable for larger velocities. The amplitude of the slipper as a function of the velocity in figure 3.5(b) in contrast shows no pattern. For $\lambda = 5, 10$ the simulation results lie within the large error bars of the experimental measurements, $\lambda = 20$ leads to a distinctly larger amplitude.

In the experiments the cytosol viscosity of the cells could not be measured or altered to obtain data for direct comparison with simulations. Hence, one must resort to changing the viscosity of the surrounding fluid μ_o, thus changing the ratio of the viscosities. Results for different μ_o in simulation and experiment are shown in figure 3.5(c). As can be expected from the results in (a), when increasing the outer viscosity, simulations and experiment show an increase in the slipper frequency. There is still a linear dependence between velocity and frequency and for all μ_o there is a constant factor of approximately 1.9 between simulation and experimental measurement.

Variation of some RBC simulation parameters in a physiologically meaningful range have been tested in simulations. The representative results for different bending reference shape and modulus κ_B and shear modulus κ_S are shown in figure 3.6. The influence on the oscillation frequency is negligible and the amplitude shows only slight changes depending on the parameter values.

To conclude, the RBC dynamics in channel flow crucially depend on the viscosity contrast, which is in agreement with results for vesicles in Poiseuille [15, 20, 100] and RBCs in shear flow [51, 52, 101]. For the velocity ramp simulations in section 3.3, $\lambda = 10$ was chosen as a good compromise between agreement in frequency and amplitude measurements. A possible explanation for the disagreement with the experimental results in figure 3.5 might be that the membrane viscosity of RBCs is not part of the simulation model. A higher inner viscosity could account for

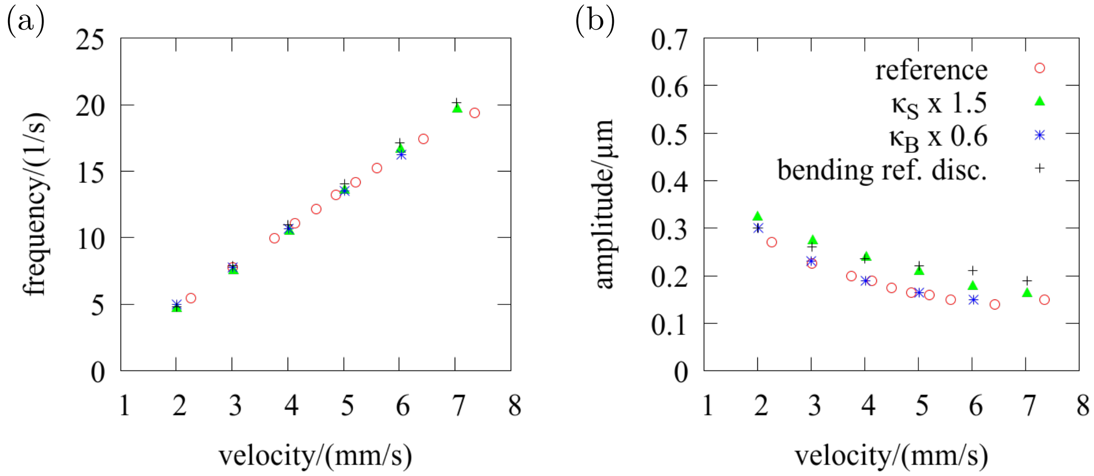

Figure 3.6: Influence of membrane parameters on the slipper dynamics. (a) Frequency and (b) amplitude of the centre of mass oscillations for different RBC membrane parameter combinations. Red symbols reproduce the results from figure 3.5 for $\lambda = 10$ as reference. Reproduced from [62] with permission from Cell Press.

some effects due to the viscosity of the membrane, but recent studies showed that their influence is 'similar but distinct' [102]. Investigations of RBCs in shear flow showed good agreement with experimental results if the membrane viscosity was incorporated [25, 26]. This hypothesis is investigated in detail in the next chapters.

Initially, the observation that only 50% of all slippers in experiments showed pronounced oscillation behaviour was attributed to a distribution of the RBCs' inner viscosity. Cells with larger cytosol viscosity in simulations after few slipper oscillation periods showed a rotation of the membrane. After this rotation the cell, although still a tank-treading slipper, exhibited a strong decrease in the oscillation amplitude. The oscillation and oscillation frequency of such rotated slippers would be undetectable in experiments due to the additional noise in the measured trajectories, which is on the same order of magnitude as the oscillation amplitude. However, this hypothesis was refuted after membrane viscosity was included and the shear reference state was adapted, because these changes did no longer allow a classification into the two categories *normal slipper* and *rotated slipper*. Details of these changes in the model and the discussion of the share of oscillating slippers observed in experiments are deferred to chapter 5.

3.4.2 Different frequencies of the system

The frequencies discussed in the previous sections of this chapter were always those of the RBCs' centre of mass oscillation with respect to the channel axis, which are ac-

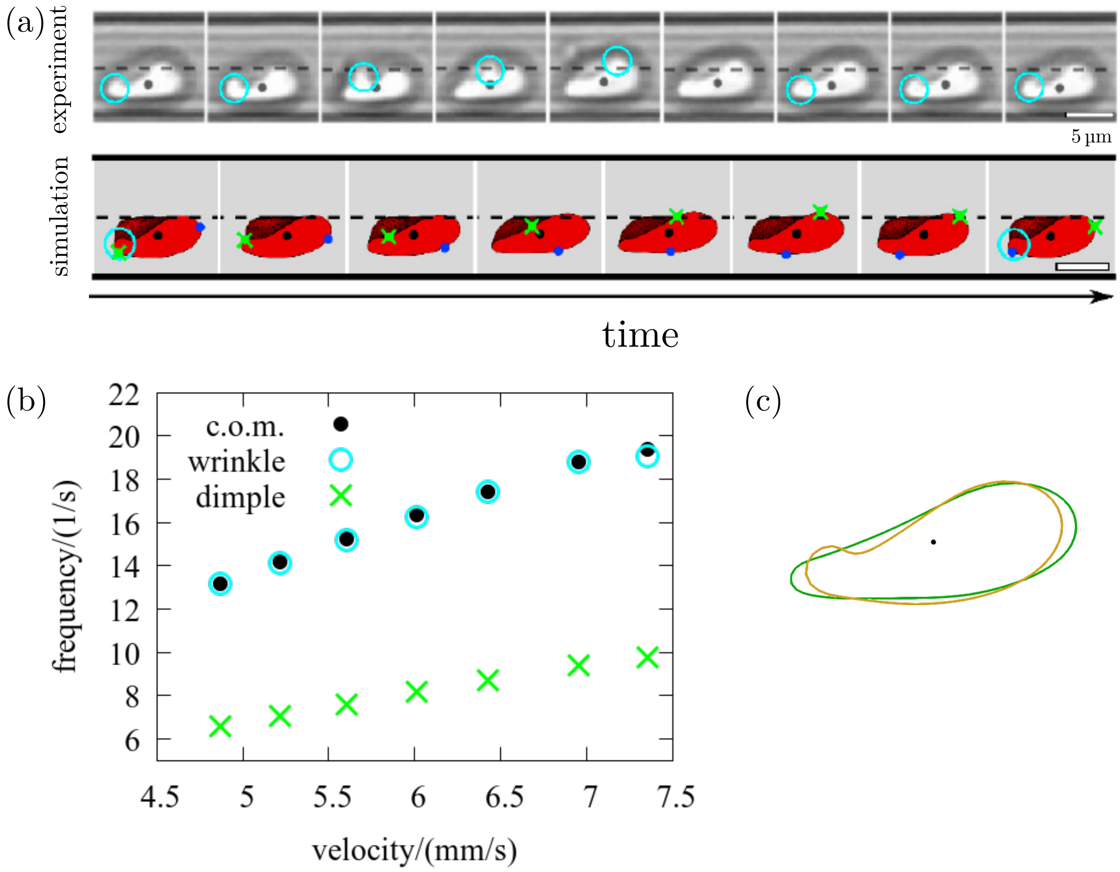

Figure 3.7: Frequencies of the slipper state. (a) Image sequence of the slipper motion in the channel during half a tank-treading period, as the blue and green markers on the simulated cell surface show. In experiments a wrinkle travels over the cell surface, marked with cyan circles. The cells' centre of mass (black dots) movement relative to the channel axis (dashed line) is difficult to discern. (b) Different frequencies of the slipper cell in simulations. (c) Slipper outlines for maximally stretched/compressed instances, overlaid such that the centre of mass positions coincide. Figures (a) and (b) are reproduced from [62] with permission from Cell Press.

cessible in experiments. The relation between positional oscillation and tank-treading movement of the cell membrane can be extracted from the simulation results. The image sequence in figure 3.7(a) shows the slipper cell during a full period of the positional oscillation. From the simulation images in the lower half of the figure one can observe that this corresponds to exactly one half of a tank-treading period. The blue and green markers on the cell surface visualise the dimples of the cell, which move with the membrane around the cell interior. The RBC is symmetric with respect to the dimples, compare the RBC shape in 2.1, which explains the factor of two between the two frequencies. Systematic extraction of the two frequencies for different cell velocities lead to the graph shown in figure 3.7(b). Cells with larger v show an increase in all frequencies. Green crosses show the tank-treading frequencies and black dots the previously discussed centre of mass oscillation. In addition, cyan circles show the frequency of a wrinkle travelling over the cell surface during one centre of mass oscillation, which can be observed in approximately 5 % of experimental slipper cells. In simulations the wrinkles increase in size if λ increases and thus possibly related to cell age [103]. Finally, figure 3.7(c) shows a crosssectional profile of the slipper at is maximal (green) and minimal (orange) elongation, which have a distance of one fourth of the tank-treading period.

3.5 Robustness of the phase diagram in pulsatile flow

3.5.1 Motivation

Previous numerical and experimental studies [17] investigated the RBC shape in Poiseuille flow in microchannels, depending on the constant flow velocity as well as starting position and starting shape of the cell. The results were summarised in phase diagrams with croissants predominantly at centred initial positions and with a pronounced croissant peak at intermediate velocities. The border between the croissant and slipper region from said study is reproduced in figure 3.8.

In this section the influence of an additional pulsatile component on the phase diagram is discussed. Results are presented for selected points in the phase diagram, marked in figure 3.8. The majority is located near the border between slipper and croissant region, because there the perturbation of the flow due to the additional pulsation is expected to lead to observable shape changes. The additional pulsatile component to the constant part v_c of the flow is a sine wave in time with frequency f_pulse and amplitude A

$$v_\mathrm{in} = v_\mathrm{c} + A \sin\left(2\pi f_\mathrm{pulse} t\right). \tag{3.1}$$

Amplitudes are given as relative amplitudes $A_\mathrm{r} = A/v_\mathrm{c}$. For all selected points simulations with three different amplitudes $A_\mathrm{r} = 0.2, 0.35, 0.5$ and three different pulsation frequencies $f_\mathrm{pulse} = 10\,\mathrm{Hz}, 20\,\mathrm{Hz}, 40\,\mathrm{Hz}$ are carried out, i.e. 9 simulations for each point. The location of the points in velocity direction in the phase diagram indicates the mean velocity of the pulsatile flow. The flow pulsation frequencies f_pulse are chosen such that they are of similar magnitude as the slipper frequency in the rectangular channel, compare figure 3.9.

3.5.2 Inside slipper region

First, simulations inside the slipper region were done for one point marked with a red circle labelled A in figure 3.8. At this point a reference simulation without

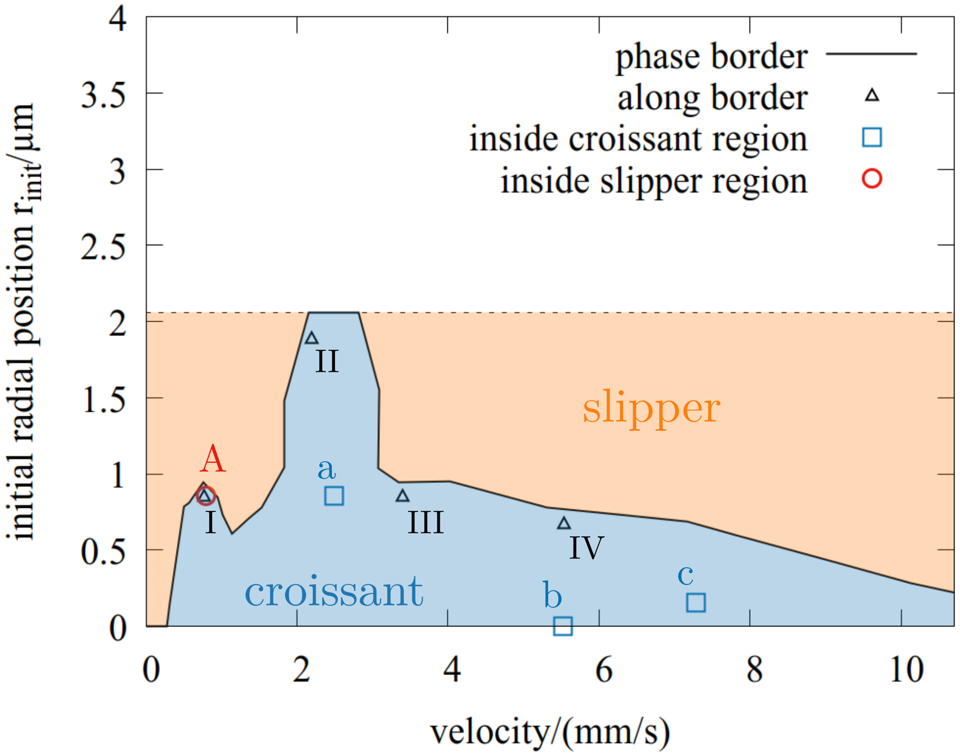

Figure 3.8: Positions of the pulsed flow simulations in the phase diagram. The border of the phase diagram which separates croissant and slipper regions for a discocyte as initial shape according to Guckenberger et al. [17]. The labelled symbols mark the positions of pulsatile flow simulations discussed in this section.

pulsation produced a slipper shaped cell. Note that the cell velocity at point A is nearly identical to the velocity of the neighbouring croissant-shape cell (point I, black triangle symbol). The reason for this is that slippers flow off-centred and are therefore not as fast as centred croissants, when comparing both for an identical mean flow through a channel.

All 9 simulations for different pulsatile frequencies and amplitudes at this point produce slippers, similar to the constant flow reference. Trajectories of two slippers are shown in figure 3.10(a,b) (red curves) in comparison with the constant flow reference (blue). Here only the radial position is shown which is nearly identical to the y-component in direction of the longer channel axis, as is typical for slippers. The cell trajectories hardly differ for all frequency and amplitude combinations. As can be seen from 3.10(a,b), the centre of mass frequencies are perfectly in line with the results shown in figure 3.9 (orange symbols). The corresponding cell velocities are shown in the second row of figure 3.10(c,d). The red velocity curves oscillate

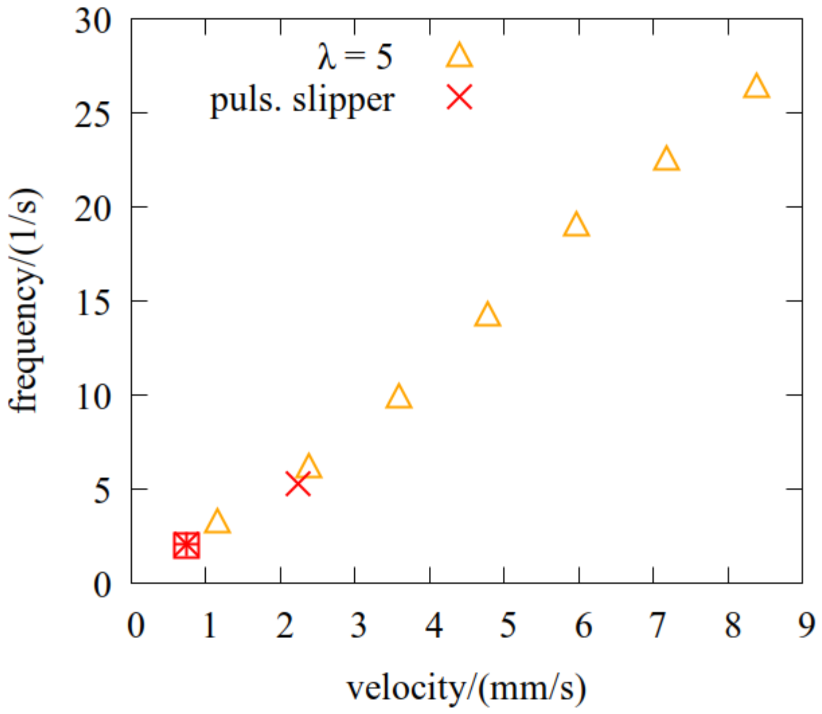

Figure 3.9: Slipper oscillations in a 10 µm to 12 µm channel. Frequency of the centre of mass oscillation of the slipper cells depending on the cell velocity in constant flow in the rectangular channel (orange symbols) for $\lambda = 5$. Frequency of slippers in pulsating flow are drawn with red symbols.

much more strongly, due to the additional pulsatile flow. This pulsation is superimposed by the velocity change due to the slippers positional oscillation which is also present in the blue cell velocity curve under constant flow. This means that under pulsatile flow the slipper is periodically accelerated and decelerated. This, however, does not significantly influence its inherent oscillation dynamics, as the positional oscillations in 3.10(a,b) show, and the slipper movement under pulsation is similar to that described in section 3.4

3.5.3 Inside croissant region

Second, three points in the croissant region of the phase diagram are selected, marked with blue squares (a to c) in figure 3.8. If at these points a pulsatile component is added to the flow, no shape change is expected because the resulting maximal and minimal velocities do not extend beyond the phase border. The results show that indeed all 27 simulations lead to croissant-shaped RBCs as depicted in figure 3.1(a).

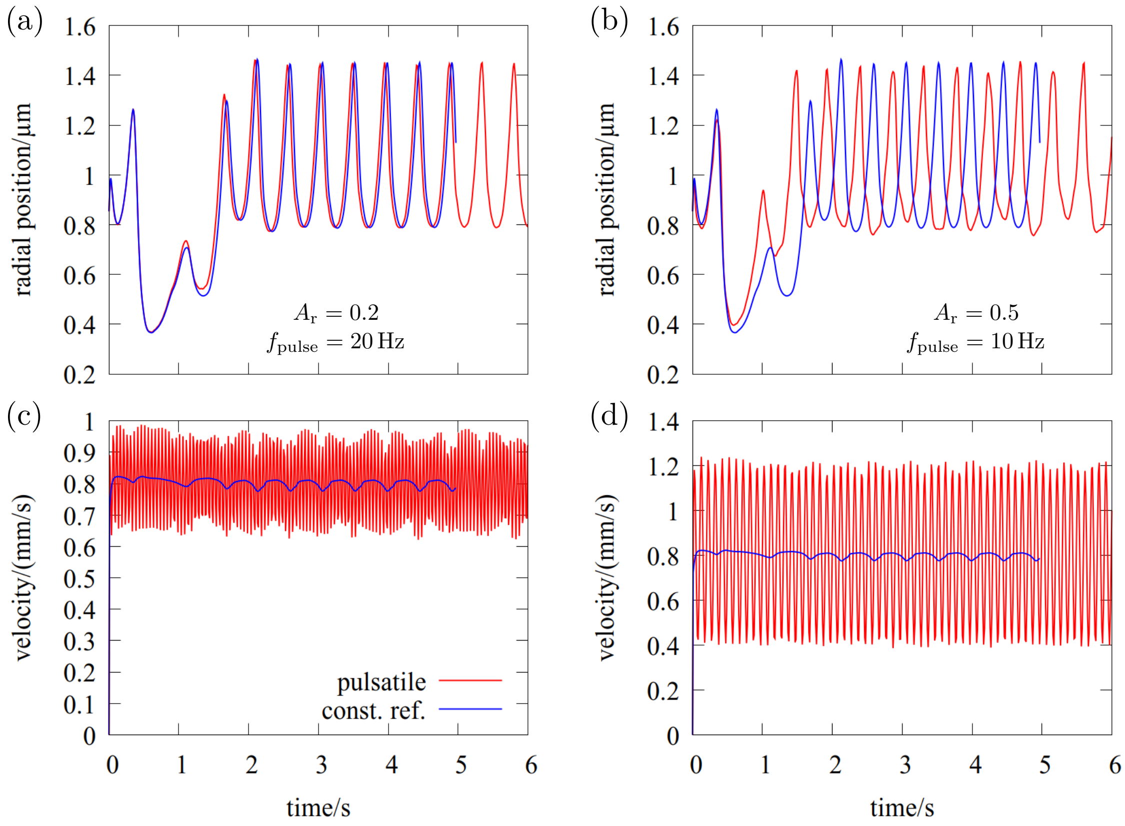

Figure 3.10: Positional and velocity oscillation of slippers under pulsation. Exemplary trajectories (a,b) and corresponding velocities (c,d) under pulsed flow (red curves). Simulations for (a,c) small and (b,d) large pulsation amplitude, both in the slipper region of the phase diagram at point A in figure 3.8. The blue lines show the reference simulation without pulsation.

However, these croissants show a different dynamic behaviour, discussed in the following.

In general, three croissant types can be distinguished, classification for all simulations is given in table 3.1. Their model trajectories as well as snapshots of their shapes are shown in figure 3.11. The coordinate system is centred in the channel. All cells start as discocytes and need time to deform to a steady state. The regular type in figure 3.11(a) after the initial deformation is almost perfectly centred and very symmetric, similar to previous observations [17]. The dimple positions marked on the surface are located at the side of the cell, in direction of the z channel axis. It should be noted that compared to previous sections and conventions [17, 62] the cell snapshots in figure 3.11 are shown with the smaller channel axis along z in vertical direction. The type in 3.11(b) is also quite symmetric and the dimples are located in

A_r	$f_\mathrm{pulse}/\mathrm{Hz}$	point a	point b	point c
0.2	10	reg.	reg.	reg.
	20	reg.	reg.	reg.
	40	reg.	reg.	reg.
0.35	10	reg.	reg.	reg.
	20	breathing	reg.	reg.
	40	breathing	reg.	reg.
0.5	10	reg.	rotated ($f_\mathrm{TT} \approx 1.3\,\mathrm{s}^{-1}$)	rotated ($f_\mathrm{TT} \approx 1.9\,\mathrm{s}^{-1}$)
	20	reg.	reg.	reg.
	40	breathing	rotated ($f_\mathrm{TT} \approx 1.1\,\mathrm{s}^{-1}$)	reg.

Table 3.1: Classification of the simulations in the croissant region with respect to croissant type. All nine simulations per point a to c in figure 3.8 are classified as regular (reg.), breathing or rotated shape, described in figure 3.11. For the rotated type an estimate of the tank-treading frequency f_TT is given.

the same direction with fixed position on the cell surface. However, the RBC flows slightly off-centred and oscillates with a small amplitude in z-direction. This oscillation is connected to a periodic contraction and elongation of the cell in flow direction as the superimposed cell outlines in figure 3.11(b) show. Due to this contraction-expansion movement this type is labelled *breathing*. The frequency of this oscillation is identical to the frequency of the pulsation, independent of the mean flow velocity. The third type in 3.11(c) is more asymmetric although still croissant-shaped. The dimples, however, move to the sides of the cell in y-direction, therefore this type is called *rotated*. The cell oscillates farther off-centred with the radial position nearly identical to the absolute value of the z-position. The frequency of the radial oscillation is not extracted because the minima and maxima cannot be determined unambiguously, even more so for other simulations of this croissant type. Most curious, this croissant type shows a tank-treading motion of its membrane, but such, that the dimples at the sides do not follow this tank-treading but retain an approximately constant position on the surface, in contrast to the slipper tank-treading described in the previous section. The frequency of this tank-treading motion is difficult to define because of the irregularity of the membrane movement, estimates are given in table 3.1. A relation to the pulsation frequency is not observed and the pulsation frequency for both mean velocities (compare location of the points in the phase diagram) is much smaller than a (tank-treading) slipper frequency at this velocity would be. Notably, the positional oscillation of the croissant types is in z-direction, in contrast to slipper oscillations which are always in direction of the longer channel axis in y-direction. The velocity curves show a oscillation around the mean due to the pulsation with the corresponding frequency.

To conclude, an additional pulsatile component with largest relative amplitude of

50 % leads in some cases to rotated croissants, which are remarkably different from the regular shape. For smaller amplitudes, in some cases a breathing motion with the same frequency as the pulsation is observed.

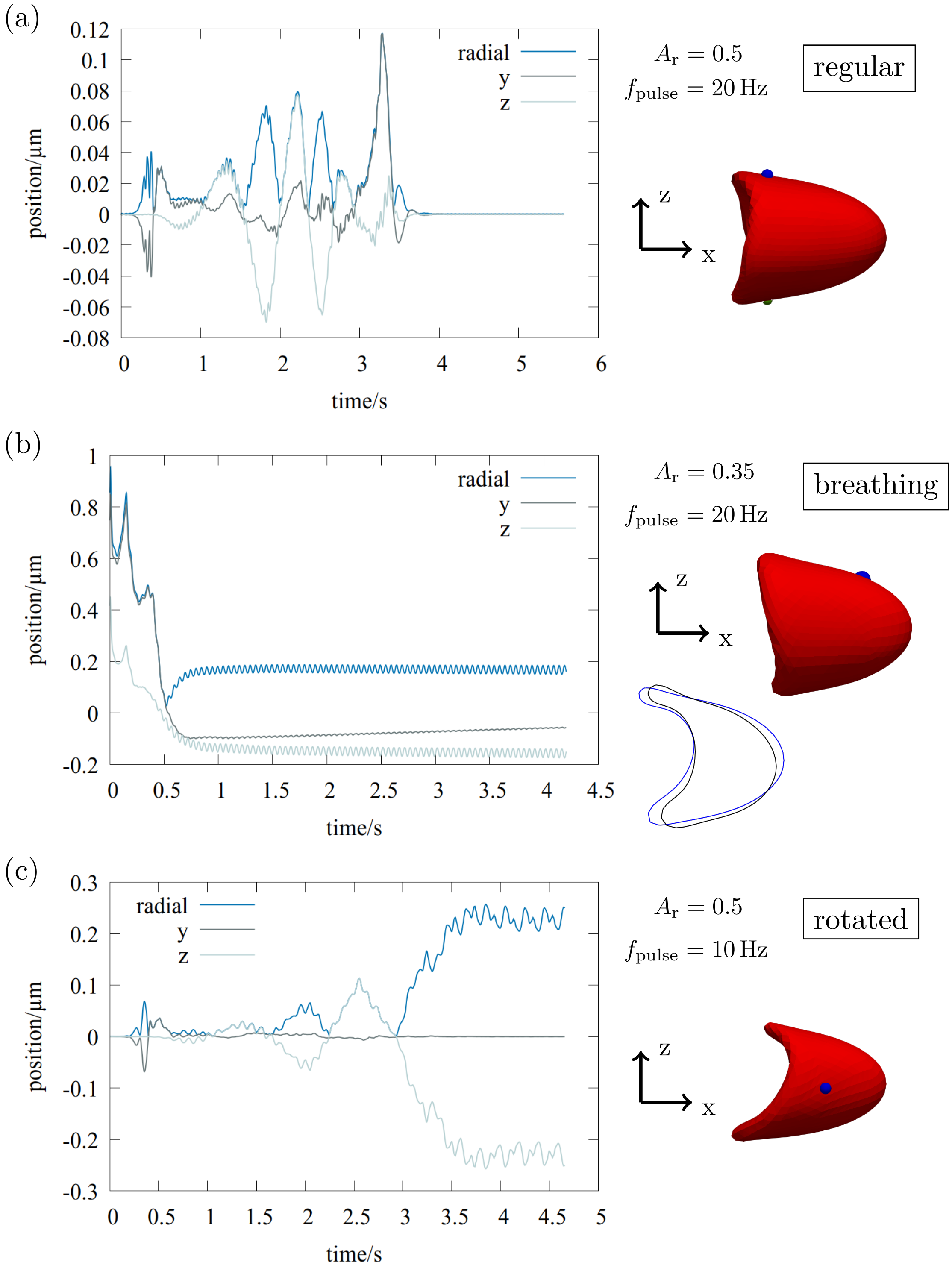

Figure 3.11: Different croissant types under pulsatile flow. Exemplary centre of mass trajectories (left column) and corresponding shapes (right column). RBCs in (a-c) are started at different initial positions and with different mean velocities. These correspond to (a,c) point b in figure 3.8 and (b) point a. The shapes are snapshots from the converged later part of the trajectories. In the right column in (b), in addition, the croissant outlines for maximum and minimum of the breathing motion are superimposed.

3.5.4 Transitions at the phase border

Finally, simulations are carried out for four points in the phase diagram near the border to the slipper phase, marked with black triangles in figure 3.8 (I to IV). Due to the additional sine component from the pulsation, at the maximum the velocity will be larger than its mean, marked in the phase diagram. Thus the border to the slipper region in the phase diagram might be crossed, which could induce the formation of slipper shapes. For each point one additional simulation without pulsation was conducted as reference. The results are summarised in table 3.2, slippers are highlighted in red, croissants are classified as in section 3.5.3. Again, the breathing frequency is identical to the pulsation frequency.

First, in the region of the croissant peak at point II in figure 3.8 a new croissant type is observed. The new type appears under pulsation as well as in the reference simulation and is characterised by a transition from the slipper to the croissant state, therefore called transient croissant. Transient cells have been observed in former studies [17]. Two exemplary trajectories are shown in figure 3.12. None of these croissants shows tank-treading. The duration of the transient slipper phase under pulsation is for some simulations longer than in the reference simulation, and for some shorter. Table 3.2 suggests that the croissant type depends on the mean flow velocity instead of the pulsation parameters.

The second observation is that due to the pulsatile flow component indeed slipper-shaped RBCs emerge, as listed in table 3.2. The dynamics of these slippers is similar to that described in section 3.5.2, regarding the dimple movement during tank-treading and the tank-treading frequency. Surprisingly, as for the results in 3.5.2 the centre of mass frequency depends only on the flow velocity and is independent of the pulsatile flow component. This is shown in figure 3.9, where the frequencies of the slippers from table 3.2 are plotted in red. Two slipper trajectories are shown in figure 3.13 in comparison with the respective constant flow reference cell, which forms a croissant. The trajectory for smaller mean velocity in (a) is similar to those in figure 3.10 at similar $\bar{v}$. The red curve in 3.13(b) shows an additional bead in the frequency curve and in contrast to (a) the centre of mass slipper frequency is much closer to the frequency of the pulsatile flow. In the synopsis in table 3.2 we notice that slippers appear for smaller pulsation frequencies and larger amplitudes. In addition, the points I and II at which slippers appear lie in croissant peaks near the border to the slipper region in the phase diagram. To conclude, only few slippers appear under pulsatile flow and only for slow pulsation.

A_r	f_{pulse}/Hz	point I	point II	point III	point IV
ref. sim.		reg.	transient	reg.	reg.
0.2	10	reg.	transient	breathing	reg.
	20	reg.	transient	breathing	reg.
	40	reg.	transient	breathing	reg.
0.35	10	slipper	transient	reg.	reg.
	20	reg.	transient	breathing	reg.
	40	reg.	transient	breathing	reg.
0.5	10	slipper	slipper	reg.	reg.
	20	reg.	transient	breathing	reg.
	40	reg.	transient	breathing	reg.

Table 3.2: Classification of the simulations along the border of the phase diagram. Slipper are marked in red, croissants, if applicable, are classified according to the types in figure 3.11. The transient croissant (blue) is the shape shown in figure 3.12. The first line in the table gives the classification of the reference simulation at constant flow velocity.

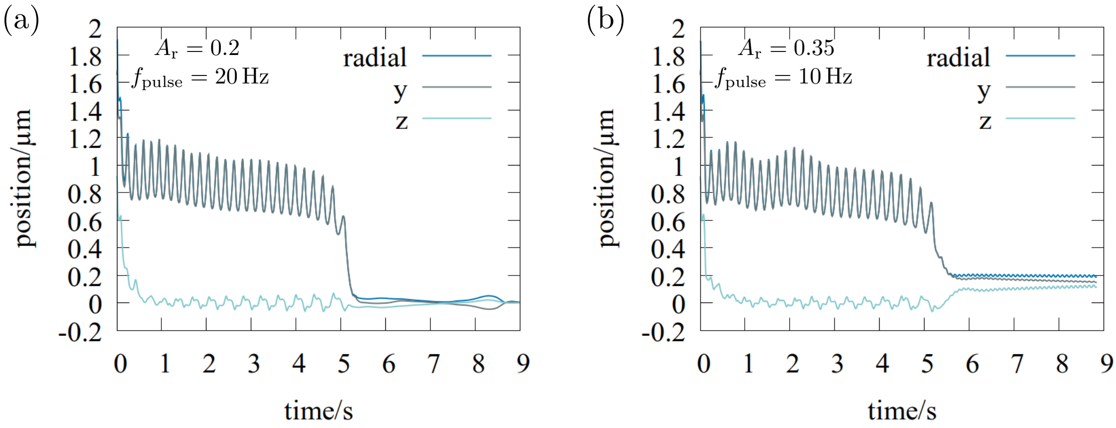

Figure 3.12: Trajectories of transient croissants. Radial, y and z development over time for two simulations at point II in figure 3.8 are shown.

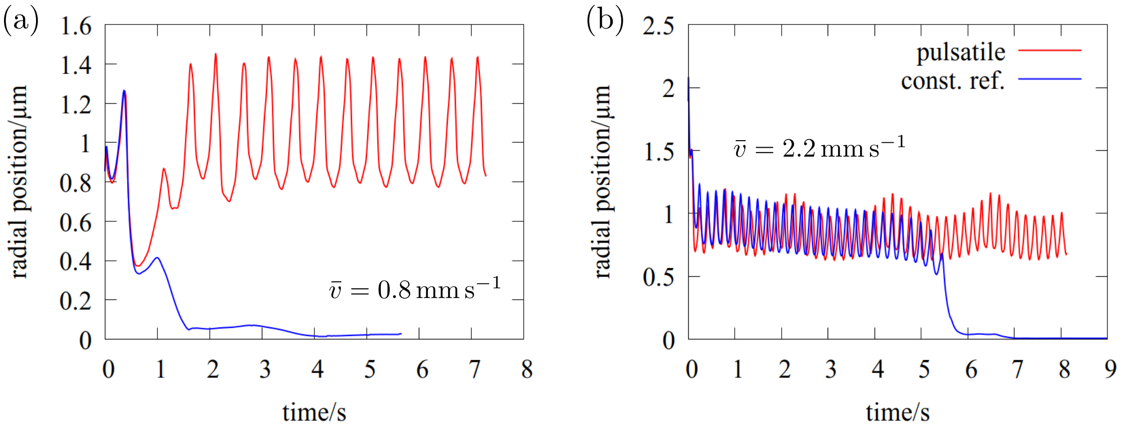

Figure 3.13: Trajectories of slippers under pulsating flow (red lines) in comparison with the respective reference simulation (blue lines) at (a) point I and (b) point II in figure 3.8. For both pulsatile simulations $f_{\mathrm{pulse}} = 10\,\mathrm{Hz}$ and $A_{\mathrm{r}} = 0.35\,\%$.

3.6 Conclusion

The study of time-dependent velocity changes in section 3.3 revealed an asymmetry in the transition between the two RBC states. The slipper-croissant transition happens significantly slower and transition times scatter more broadly. The numerical simulations show that the sensitivity of the system to the exact membrane orientation of the cell is the main explanation for the observed differences. In section 3.4 the dynamics of the slipper shaped RBCs are studied with a one-to-one comparison between experiment and simulation, made possible by recent advances in experimental measurement technique [62]. This reveals a difference in the observed tank-treading frequencies, which points to a viscosity contrast of RBCs larger than the usually assumed value of 5. It is hypothesised, that including membrane viscosity in the simulation model might resolve the observed discrepancy.

In section 3.5 the robustness of the RBC shape phase diagram under pulsatile flow was explored. Only in few cases for slow pulsation a change from croissant to slipper shape was observed and the slipper dynamics is robust against a pulsatile flow component. In addition it was shown that croissant shapes come in different types, which differ in details regarding their flow dynamics and orientation.

Both parts of this chapter used a time-dependent modulation of the flow through the microchannel but differ in time scale and magnitude of the modulation. The velocity ramps in the first part in 3.3 and 3.4 were one order of magnitude slower than the pulsation in the second part 3.5, but the magnitude of the velocity change was several orders larger. In the first part, the focus was on the dynamics of the controlled shape changes induced by the flow, while the second part concentrated on the robustness of the observed shapes under faster pulsation.

4 Including membrane viscosity in the simulation model

4.1 Overview

In recent years the viscosity of the membrane was recognised as important factor for the RBC behaviour and first models to include it in numerical simulations have been developed [104, 105]. Its effects are found to be similar and yet distinct from the interior fluid viscosity of the cell [102]. Recent numerical studies added membrane viscosity as part of their model and began to study its influence on the cells' dynamics, but detailed comparison with experiments remains scarce [25–27]. In this chapter the inclusion of the membrane viscosity as an additional viscous contribution to the membrane forces on the cell surface is described. The method is based on the finite-difference approach by Li et al. [36, 106] which as the authors show has some advantages compared to the simulation model by Yazdani et al. [105]. In section 4.2 the basic concept of this model for the membrane viscosity and its realisation as a numerical method is described.

Li et al. [36] propose an algorithm which calculates *viscous* stress elements $\boldsymbol{\tau}^{\mathrm{v,s}}$, $\boldsymbol{\tau}^{\mathrm{v,d}}$ (for shear and dilational) which are added to the elastic tensor $\boldsymbol{\tau}^{\mathrm{e}}$ (derived here for the Skalak law). From the total membrane stress $\boldsymbol{\tau}$, the forces on the nodes of the discretised cell surface must then be calculated. The force calculation method used by Li et al. [36] is different from the procedure proposed by Krüger [35] and described in chapter 2 of this thesis, where the forces are directly calculated from the elastic energy (Skalak law), without ever calculating the stresses. This approach cannot be used for the viscous contribution [36] as there is no formulation as an energy law. The calculation of the forces from the stress is not detailed by Li et al. [36] or Yazdani et al. [105], and only little information can be found in the work of Charrier et al. [107], which is given as reference. For the general non-axisymmetric problem formulas to obtain the forces from the stresses are presented by Shrivastava et al. [108], equation (49) (beware of confusing notation).

In section 4.4 these formulas to obtain the forces from the stress are first used to derive the forces for the Skalak elastic law, where the results are shown to be identical to the virtual force derivation in Krüger [35]. Having shown this, the additional viscous contribution to the forces is calculated in section 4.5 by following the same steps. The calculations are preceded by section 4.3 where definitions are introduced and necessary identities are derived. Section 4.6 introduces dimensionless parameters used in the simulations. In section 4.7 details of the implementation for BIM are described. The last section 4.8 provides an overview of experimental results for the strength of the membrane viscosity.

4.2 Short outline of the method

Li et al. [36] use a standard linear solid (SLS) model with a one-dimensional Maxwell element to describe the viscoelastic behaviour of the membrane. The derivation of membrane forces uses the idealised representation of the actual membrane surface as a sheet of plane triangular elements which can be seen as 'finite element idealisation' [107] of the surface. The membrane is considered to be infinitely thin and is modelled as a 2D sheet [36]. Using a finite difference (FD) scheme the authors derive a stress term $\sigma_{\mathrm{M}}(t)$ (equation (18) in [36]), which they then by analogy [106] translate to viscous stresses for the two-dimensional viscoelastic membrane in equations (21) to (24) in [36] which are repeated here

$$\tau_{xx}^{\mathrm{v,s}}(t_i) = A_{\mathrm{s}}^{\mathrm{FD}} \tau_{xx}^{\mathrm{v,s}}(t_i - \Delta t) + B_{\mathrm{s}}^{\mathrm{FD}} \left[E_{xx}^{\mathrm{s}}(t_i) - E_{xx}^{\mathrm{s}}(t_i - \Delta t)\right] \tag{4.1}$$

$$\tau_{xy}^{\mathrm{v,s}}(t_i) = A_{\mathrm{s}}^{\mathrm{FD}} \tau_{xy}^{\mathrm{v,s}}(t_i - \Delta t) + B_{\mathrm{s}}^{\mathrm{FD}} \left[E_{xy}^{\mathrm{s}}(t_i) - E_{xy}^{\mathrm{s}}(t_i - \Delta t)\right] \tag{4.2}$$

$$\tau_{xx}^{\mathrm{v,d}}(t_i) = A_{\mathrm{d}}^{\mathrm{FD}} \tau_{xx}^{\mathrm{v,d}}(t_i - \Delta t) + B_{\mathrm{d}}^{\mathrm{FD}} \left[E_{xx}^{\mathrm{d}}(t_i) - E_{xx}^{\mathrm{d}}(t_i - \Delta t)\right] \tag{4.3}$$

$$\tau_{yx}^{\mathrm{v,s}} = \tau_{xy}^{\mathrm{v,s}}, \qquad \tau_{yy}^{\mathrm{v,s}} = -\tau_{xx}^{\mathrm{v,s}}, \qquad \tau_{xy}^{\mathrm{v,d}} = \tau_{yx}^{\mathrm{v,d}} = 0, \qquad \tau_{yy}^{\mathrm{v,d}} = \tau_{xx}^{\mathrm{v,d}} \tag{4.4}$$

with the abbreviations

$$A_{\mathrm{s}}^{\mathrm{FD}} = \frac{4\mu_{\mathrm{s}} - k_{\mathrm{s}}^{'}\Delta t}{4\mu_{\mathrm{s}} + k_{\mathrm{s}}^{'}\Delta t}, \qquad B_{\mathrm{s}}^{\mathrm{FD}} = \frac{4\mu_{\mathrm{s}} k_{\mathrm{s}}^{'}}{4\mu_{\mathrm{s}} + k_{\mathrm{s}}^{'}\Delta t}, \tag{4.5}$$

$$A_{\mathrm{d}}^{\mathrm{FD}} = \frac{4\mu_{\mathrm{d}} - k_{\mathrm{d}}^{'}\Delta t}{4\mu_{\mathrm{d}} + k_{\mathrm{d}}^{'}\Delta t}, \qquad B_{\mathrm{d}}^{\mathrm{FD}} = \frac{4\mu_{\mathrm{d}} k_{\mathrm{d}}^{'}}{4\mu_{\mathrm{d}} + k_{\mathrm{d}}^{'}\Delta t}. \tag{4.6}$$

The shear and dilational strain tensor elements (equation (20) in [36]) are

$$E_{xx}^{\mathrm{s}} = \frac{E_{\mathrm{xx}} - E_{\mathrm{yy}}}{2}, \qquad E_{xy}^{\mathrm{s}} = E_{xy}, \qquad E_{xx}^{\mathrm{d}} = \frac{E_{\mathrm{xx}} + E_{\mathrm{yy}}}{2}. \tag{4.7}$$

Here μ_{s} and μ_{d} are the shear and dilational membrane viscosities and $k_{\mathrm{s}}^{'}$, $k_{\mathrm{d}}^{'}$ the respective artificial spring constants from the SLS model. Δt is the time interval for the recalculation of the viscous contribution. The strain tensor $\boldsymbol{E}$ is defined* as [34]

$$\boldsymbol{E} = \frac{1}{2}\left(\boldsymbol{F}^{\mathrm{T}}\boldsymbol{F} - \boldsymbol{I}\right) \tag{4.8}$$

---

*There is an unharmful mistake in equation (8) in [36] and equation (7) in [106] in the definition of $\boldsymbol{E}$ with the symmetric tensor $\boldsymbol{G}$, compare section 4.3 for the correct version.

with the deformation gradient tensor $\boldsymbol{F}$ and identity matrix $\boldsymbol{I}$. In the simulation implementation, $\boldsymbol{F}$ is calculated from the displacement vectors of vertices of the surface elements, for the BIM these are the nodes of the surface triangles.

Together the contributions (4.1) to (4.4) constitute the symmetric viscous stress tensor $\boldsymbol{\tau}^{\mathrm{v}}$ and we abbreviate

$$\boldsymbol{\tau}^{\mathrm{v}} = \boldsymbol{\tau}^{\mathrm{v,s}} + \boldsymbol{\tau}^{\mathrm{v,d}} = \begin{pmatrix} \tau_{xx}^{\mathrm{v,s}} + \tau_{xx}^{\mathrm{v,d}} & \tau_{xy}^{\mathrm{v,s}} \\ \tau_{yx}^{\mathrm{v,s}} & \tau_{yy}^{\mathrm{v,s}} + \tau_{yy}^{\mathrm{v,d}} \end{pmatrix} =: \begin{pmatrix} T_{xx} & T_{xy} \\ T_{xy} & T_{yy} \end{pmatrix} . \tag{4.9}$$

These viscous contributions are added to the elastic stress tensor $\boldsymbol{\tau}^{\mathrm{e}}$

$$\boldsymbol{\tau} = \boldsymbol{\tau}^{\mathrm{e}} + \boldsymbol{\tau}^{\mathrm{v,s}} + \boldsymbol{\tau}^{\mathrm{v,d}}. \tag{4.10}$$

Here the Skalak law is used to describe the elastic part and thus the elastic stress $\boldsymbol{\tau}^{\mathrm{e}}$ is calculated from the shear energy (2.1), details are given in section 4.4. From the stress tensor one can then derive the forces on the membrane. Li et al. [36] hint to older studies [105, 107] for the force calculation but give neither details of the derivation nor results.

4.3 Definitions and useful identities

4.3.1 Outline

In this section definitions for important quantities are given, together with the different terms used for them in the publications cited. Furthermore several identities necessary for the calculation of the membrane forces are derived.

4.3.2 Cauchy-Green deformation

The (surface) deformation gradient tensor (called $\boldsymbol{D}$ in [35] in equation (C.8) and used in its linearised form in equation (C.9)), also called surface displacement gradient [33]

$$\boldsymbol{F} = \begin{pmatrix} F_{xx} & F_{xy} \\ F_{yx} & F_{yy} \end{pmatrix} , \tag{4.11}$$

defines the squared displacement gradient $\boldsymbol{G}$ [35], called right Cauchy-Green deformation tensor [109]

$$\boldsymbol{G} = \boldsymbol{F}^T \boldsymbol{F} , \tag{4.12}$$

which is obviously symmetric, i.e. $\boldsymbol{G}^T = \boldsymbol{G}$. The left Cauchy-Green deformation tensor is [109]

$$\boldsymbol{C} = \boldsymbol{F}\ \boldsymbol{F}^T. \tag{4.13}$$

It is straightforward to show that trace and determinant of these matrices are identical

$$\begin{aligned}\mathrm{tr}(\boldsymbol{G}) &= G_{xx} + G_{yy} && (4.14)\\ &= \mathrm{tr}(\boldsymbol{C})\ , && (4.15)\\ \det(\boldsymbol{G}) &= G_{xx}G_{yy} - G_{xy}G_{yx} && (4.16)\\ &= \det(\boldsymbol{C}). && (4.17)\end{aligned}$$

4.3.3 Principal stretch ratios

The eigenvalues of $\boldsymbol{G}$ and equivalently of $\boldsymbol{C}$ are (equation (7) in [107]) are

$$\begin{aligned}\lambda_{1,2}^2 &= \frac{1}{2}\left(G_{xx} + G_{yy} \pm \sqrt{(G_{xx} - G_{yy})^2 + 4G_{xy}G_{yx}}\right) && (4.18)\\ &\overset{(4.14)(4.16)}{=} \frac{1}{2}\left(\mathrm{tr}(\boldsymbol{G}) \pm \sqrt{\mathrm{tr}(\boldsymbol{G})^2 - 4\det(\boldsymbol{G})}\right) && (4.19)\\ &\overset{(4.15)(4.17)}{=} \frac{1}{2}\left(\mathrm{tr}(\boldsymbol{C}) \pm \sqrt{\mathrm{tr}(\boldsymbol{C})^2 - 4\det(\boldsymbol{C})}\right) && (4.20)\end{aligned}$$

and can be identified as the squared principal stretch ratios. From this we can easily see that

$$\begin{aligned}\lambda_1^2 + \lambda_2^2 &= \mathrm{tr}(\boldsymbol{C}) = \mathrm{tr}(\boldsymbol{G}) && (4.21)\\ \lambda_1^2\lambda_2^2 = \frac{1}{4}\left(\mathrm{tr}(\boldsymbol{C})^2 - (\mathrm{tr}(\boldsymbol{C})^2 - 4\det(\boldsymbol{C}))\right) &= \det(\boldsymbol{C}) = \det(\boldsymbol{G}) && (4.22)\end{aligned}$$

and with (4.13)

$$(\lambda_1\lambda_2)^2 = \det(\boldsymbol{F}^T\boldsymbol{F}) = \det(\boldsymbol{F})^2. \tag{4.23}$$

The strain invariants in the energy functional for the Skalak law (2.1) are defined by the principal stretch ratios as in [33]

$$\begin{aligned}I_1 &= \lambda_1^2 + \lambda_2^2 - 2 && (4.24)\\ I_2 &= \lambda_1^2\lambda_2^2 - 1. && (4.25)\end{aligned}$$

4.4 Derivation of the forces from the stress tensor for the Skalak law

4.4.1 Stress tensor

The approach to calculate the elastic force for the Skalak law, defined in section 2.2, is the following. First the elastic stress (without the viscous contribution) is computed via equation (6) and (7) in [36]. Then equation (49) from [108] is used to obtain the nodal forces. This calculation method must lead to nodal forces identical to the results from appendix C.1 in [35].

The elastic stress tensor is [36]

$$\boldsymbol{\tau}^{\mathrm{e}} = \tau_1^{\mathrm{e}}\, \boldsymbol{e}_1 \otimes \boldsymbol{e}_1 + \tau_2^{\mathrm{e}}\, \boldsymbol{e}_2 \otimes \boldsymbol{e}_2 \tag{4.26}$$

with the principal directions $\boldsymbol{e}_1, \boldsymbol{e}_2$, which are eigenvectors of the left Cauchy-Green deformation tensor (4.13). The calculations to obtain these eigenvectors and the respective eigenvalues (4.18) are written out in appendix A.

The principal stresses are [36]

$$\tau_1^e = \frac{1}{\lambda_2}\frac{\partial W_{\mathrm{S}}}{\partial \lambda_1} \overset{\text{(B.6)}}{=} \frac{\kappa_{\mathrm{S}}}{3}\frac{\lambda_1}{\lambda_2}(\lambda_1^2 - 1) + \frac{\kappa_{\mathrm{A}}}{2}(\lambda_1^2\lambda_2^2 - 1)\lambda_1\lambda_2 \tag{4.27}$$

$$\tau_2^e = \frac{1}{\lambda_1}\frac{\partial W_{\mathrm{S}}}{\partial \lambda_2} \overset{\text{(B.7)}}{=} \frac{\kappa_{\mathrm{S}}}{3}\frac{\lambda_2}{\lambda_1}(\lambda_2^2 - 1) + \frac{\kappa_{\mathrm{A}}}{2}(\lambda_1^2\lambda_2^2 - 1)\lambda_1\lambda_2. \tag{4.28}$$

where identities from appendix B.1 have been used. This leads to the elastic stress tensor

$$\begin{aligned}
\boldsymbol{\tau}^{\mathrm{e}} &= \frac{\kappa_{\mathrm{S}}}{3\lambda_1\lambda_2}\left[\lambda_1^2(\lambda_1^2 - 1)(\boldsymbol{e}_1 \otimes \boldsymbol{e}_1) + \lambda_2^2(\lambda_2^2 - 1)(\boldsymbol{e}_2 \otimes \boldsymbol{e}_2)\right] \\
&+ \frac{\kappa_{\mathrm{A}}}{2}(\lambda_1^2\lambda_2^2 - 1)\lambda_1\lambda_2(\boldsymbol{e}_1 \otimes \boldsymbol{e}_1 + \boldsymbol{e}_2 \otimes \boldsymbol{e}_2) \qquad (4.29) \\
&\overset{\text{(A.19)}}{=} \frac{\kappa_{\mathrm{S}}}{3\lambda_1\lambda_2}\left[\lambda_1^2(\lambda_1^2 - 1)(\boldsymbol{e}_1 \otimes \boldsymbol{e}_1) + \lambda_2^2(\lambda_2^2 - 1)(\boldsymbol{e}_2 \otimes \boldsymbol{e}_2)\right] \\
&+ \frac{\kappa_{\mathrm{A}}}{2}\lambda_1\lambda_2(\lambda_1^2\lambda_2^2 - 1)\boldsymbol{I}. \qquad (4.30)
\end{aligned}$$

The first part in brackets can also be simplified

$$\begin{aligned}
&\lambda_1^2(\lambda_1^2 - 1)(\boldsymbol{e}_1 \otimes \boldsymbol{e}_1) + \lambda_2^2(\lambda_2^2 - 1)(\boldsymbol{e}_2 \otimes \boldsymbol{e}_2) && (4.31) \\
&\overset{\text{(4.21)}}{=} \lambda_1^2(\operatorname{tr}(\boldsymbol{C}) - \lambda_2^2 - 1)(\boldsymbol{e}_1 \otimes \boldsymbol{e}_1) + \lambda_2^2(\operatorname{tr}(\boldsymbol{C}) - \lambda_1^2 - 1)(\boldsymbol{e}_2 \otimes \boldsymbol{e}_2) && (4.32) \\
&\overset{\text{(A.19)}}{=} \lambda_1^2(\operatorname{tr}(\boldsymbol{C}) - 1)(\boldsymbol{e}_1 \otimes \boldsymbol{e}_1) + \lambda_2^2(\operatorname{tr}(\boldsymbol{C}) - 1)(\boldsymbol{e}_2 \otimes \boldsymbol{e}_2) - \lambda_1^2\lambda_2^2\boldsymbol{I} && (4.33) \\
&\overset{\text{(4.21)}}{=} (\lambda_1^2 + \lambda_2^2 - 1)(\lambda_1^2(\boldsymbol{e}_1 \otimes \boldsymbol{e}_1) + \lambda_2^2(\boldsymbol{e}_2 \otimes \boldsymbol{e}_2)) - \lambda_1^2\lambda_2^2\boldsymbol{I} && (4.34) \\
&\overset{\text{(A.26)}}{=} (\lambda_1^2 + \lambda_2^2 - 1)\boldsymbol{C} - \lambda_1^2\lambda_2^2\boldsymbol{I}. && (4.35)
\end{aligned}$$

In total the elastic stress tensor becomes

$$\boldsymbol{\tau}^{\mathrm{e}} = \frac{\kappa_{\mathrm{S}}}{3\lambda_1\lambda_2}\left[(\lambda_1^2 + \lambda_2^2 - 1)\boldsymbol{C} - \lambda_1^2\lambda_2^2\boldsymbol{I}\right] + \frac{\kappa_{\mathrm{A}}}{2}\lambda_1\lambda_2(\lambda_1^2\lambda_2^2 - 1)\boldsymbol{I}. \tag{4.36}$$

This intermediate result is identical to equation (2.8) in [33] which can be seen if we use the identities (B.1) and (B.2) from appendix B.1. We continue and use (4.13) to abbreviate

$$\boldsymbol{\tau}^{\mathrm{e}} = c_1 \boldsymbol{F}\boldsymbol{F}^T + c_2 \boldsymbol{I}. \tag{4.37}$$

with

$$c_1 = \frac{\kappa_{\mathrm{S}}}{3\lambda_1\lambda_2}(\lambda_1^2 + \lambda_2^2 - 1) \overset{(4.24)}{=} \frac{\kappa_{\mathrm{S}}}{3\lambda_1\lambda_2}(I_1 + 1) \tag{4.38}$$

$$c_2 = -\frac{\kappa_{\mathrm{S}}}{3}\lambda_1\lambda_2 + \frac{\kappa_{\mathrm{A}}}{2}\lambda_1\lambda_2(\lambda_1^2\lambda_2^2 - 1) \overset{(4.25)}{=} \lambda_1\lambda_2\left(-\frac{\kappa_{\mathrm{S}}}{3} + \frac{\kappa_{\mathrm{A}}}{2}I_2\right). \tag{4.39}$$

4.4.2 Force calculation

The membrane is modelled as a two-dimensional sheet and thus only in-plane stresses and forces are considered in the derivation [36]. The forces $\{\boldsymbol{P}\}$ on the nodes (described in detail and visualised in [35]) can be computed from the stresses with the help of equation (49) in [108].

$$\{\boldsymbol{\delta u}\}^T\{\boldsymbol{P}\} = \operatorname{tr}\left([\delta\boldsymbol{F}][\boldsymbol{F}]^{-1}[\boldsymbol{\tau}^{\mathrm{e}}]\right) A \tag{4.40}$$

where $\{\boldsymbol{P}\} = \{P_x^1, P_y^1, P_x^2, P_y^2, P_x^3, P_y^3\}^T$ and $\{\boldsymbol{\delta u}\}^T = \{\delta u_1, \delta v_1, \delta u_2, \delta v_2, \delta u_3, \delta v_3\}$. The number denotes the node number of the respective triangle (three nodes per triangle). u, v describe the velocity in the x-y-direction, respectively. A is the area of the deformed element. Compared to the original version [108], in equation (4.40) the stresses $\boldsymbol{\sigma}$, which are defined as force per area [108], are replaced with $\boldsymbol{\tau}^{\mathrm{e}}$, defined as force per unit length [34]. As a consequence the volume of the deformed element V must be replaced by the area A. Note however, that Shrivastava et al. [108] do consider thin membranes where the stress in the thickness direction is zero. $[\delta\boldsymbol{F}]$ is defined as (equation (50) in [108])

$$[\delta\boldsymbol{F}] = \begin{pmatrix} \sum_{i=1}^3 a_i\delta u_i & \sum_{i=1}^3 b_i\delta u_i \\ \sum_{i=1}^3 a_i\delta v_i & \sum_{i=1}^3 b_i\delta v_i \end{pmatrix}. \tag{4.41}$$

In contrast to [108] there is no prefactor $(2A^{(0)})^{-1}$, it is absorbed in the constants a_i, b_i which are defined as in equations (C.5) to (C.7) in [35]. Using equation (4.37) the right hand side of equation (4.40) can be simplified to

$$
\begin{aligned}
&c_1 \operatorname{tr}\left([\delta \boldsymbol{F}][\boldsymbol{F}]^T\right) A + c_2 \operatorname{tr}\left([\delta \boldsymbol{F}][\boldsymbol{F}]^{-1}\right) A && (4.42)\\
&= c_1 \operatorname{tr}\left(\begin{pmatrix} \sum_{i=1}^3 a_i \delta u_i & \sum_{i=1}^3 b_i \delta u_i \\ \sum_{i=1}^3 a_i \delta v_i & \sum_{i=1}^3 b_i \delta v_i \end{pmatrix} \begin{pmatrix} F_{xx} & F_{yx} \\ F_{xy} & F_{yy} \end{pmatrix}\right) A \\
&\quad + \frac{c_2}{\det(\boldsymbol{F})} \operatorname{tr}\left(\begin{pmatrix} \sum_{i=1}^3 a_i \delta u_i & \sum_{i=1}^3 b_i \delta u_i \\ \sum_{i=1}^3 a_i \delta v_i & \sum_{i=1}^3 b_i \delta v_i \end{pmatrix} \begin{pmatrix} F_{yy} & -F_{xy} \\ -F_{yx} & F_{xx} \end{pmatrix}\right) A && (4.43)\\
&= c_1 \left(F_{xx} \sum_{i=1}^3 a_i \delta u_i + F_{xy} \sum_{i=1}^3 b_i \delta u_i + F_{yx} \sum_{i=1}^3 a_i \delta v_i + F_{yy} \sum_{i=1}^3 b_i \delta v_i\right) A \\
&\quad + \frac{c_2}{\det(\boldsymbol{F})} \left(F_{yy} \sum_{i=1}^3 a_i \delta u_i - F_{yx} \sum_{i=1}^3 b_i \delta u_i - F_{xy} \sum_{i=1}^3 a_i \delta v_i + F_{xx} \sum_{i=1}^3 b_i \delta v_i\right) A && (4.44)
\end{aligned}
$$

Now the terms in front of all $\delta u_i, \delta v_i$ on the left and right hand side of equation (4.40) are compared and thus the forces P_x^i, P_y^i can be determined

$$
P_x^i = A \left[c_1 (F_{xx} a_i + F_{xy} b_i) + \frac{c_2}{\det(\boldsymbol{F})} (F_{yy} a_i - F_{yx} b_i)\right] \tag{4.45}
$$

$$
P_y^i = A \left[c_1 (F_{yx} a_i + F_{yy} b_i) + \frac{c_2}{\det(\boldsymbol{F})} (-F_{xy} a_i + F_{xx} b_i)\right] . \tag{4.46}
$$

With equations (4.38) and (4.39) and the ratio between deformed and undeformed surface area $\frac{A}{A^{(0)}} = \lambda_1 \lambda_2$ [34] this leads to

$$
\begin{aligned}
P_x^i = A^{(0)} &\left[\frac{\kappa_{\mathrm{S}}}{3} (I_1 + 1)(F_{xx} a_i + F_{xy} b_i)\right. \\
&\left. + \left(-\frac{\kappa_{\mathrm{S}}}{3} + \frac{\kappa_{\mathrm{A}}}{2} I_2\right) \det(\boldsymbol{F}) (F_{yy} a_i - F_{yx} b_i)\right] && (4.47)\\
P_y^i = A^{(0)} &\left[\frac{\kappa_{\mathrm{S}}}{3} (I_1 + 1)(F_{yx} a_i + F_{yy} b_i)\right. \\
&\left. + \left(-\frac{\kappa_{\mathrm{S}}}{3} + \frac{\kappa_{\mathrm{A}}}{2} I_2\right) \det(\boldsymbol{F}) (-F_{xy} a_i + F_{xx} b_i)\right] && (4.48)
\end{aligned}
$$

where in addition $\frac{\lambda_1^2 \lambda_2^2}{\det(\boldsymbol{F})} = \det(\boldsymbol{F})$, see (4.23), has been used.

The next step is the comparison of these forces on the single nodes with the expressions obtained with the method by Krüger [35]. Starting with equation (C.13) [35] and collecting all parts in the appendix C therein leads to

$$
\begin{aligned}
P_x^i &= -\sum_{j,k,l} A^{(0)} \frac{\partial W_\mathrm{S}}{\partial I_l} \frac{\partial I_l}{\partial G_{jk}} \frac{\partial G_{jk}}{\partial V_{ix}} && (4.49)\\
&= -A^{(0)} \left[\frac{\partial W_\mathrm{S}}{\partial I_1} \left(\frac{\partial I_1}{\partial G_{xx}} \frac{\partial G_{xx}}{\partial V_{ix}} + \frac{\partial I_1}{\partial G_{xy}} \frac{\partial G_{xy}}{\partial V_{ix}} + \frac{\partial I_1}{\partial G_{yx}} \frac{\partial G_{yx}}{\partial V_{ix}} + \frac{\partial I_1}{\partial G_{yy}} \frac{\partial G_{yy}}{\partial V_{ix}} \right) \right. \\
&\qquad \left. + \frac{\partial W_\mathrm{S}}{\partial I_2} \left(\frac{\partial I_2}{\partial G_{xx}} \frac{\partial G_{xx}}{\partial V_{ix}} + \frac{\partial I_2}{\partial G_{xy}} \frac{\partial G_{xy}}{\partial V_{ix}} + \frac{\partial I_2}{\partial G_{yx}} \frac{\partial G_{yx}}{\partial V_{ix}} + \frac{\partial I_2}{\partial G_{yy}} \frac{\partial G_{yy}}{\partial V_{ix}} \right) \right] && (4.50)\\
&= \dots && (4.51)\\
&= -A^{(0)} \left[\frac{\kappa_\mathrm{S}}{3} (I_1 + 1)(a_i F_{xx} + b_i F_{xy}) \right. \\
&\qquad \left. + \left(-\frac{\kappa_\mathrm{S}}{3} + \frac{\kappa_\mathrm{A}}{2} I_2 \right) \det(\boldsymbol{F})(a_i F_{yy} - b_i F_{yx}) \right] && (4.52)\\
P_y^i &= -\sum_{j,k,l} A^{(0)} \frac{\partial W_\mathrm{S}}{\partial I_l} \frac{\partial I_l}{\partial G_{jk}} \frac{\partial G_{jk}}{\partial V_{iy}} && (4.53)\\
&= \dots && (4.54)\\
&= -A^{(0)} \left[\frac{\kappa_\mathrm{S}}{3} (I_1 + 1)(a_i F_{yx} + b_i F_{yy}) \right. \\
&\qquad \left. + \left(-\frac{\kappa_\mathrm{S}}{3} + \frac{\kappa_\mathrm{A}}{2} I_2 \right) \det(\boldsymbol{F})(-a_i F_{xy} + b_i F_{xx}) \right] . && (4.55)
\end{aligned}
$$

The calculations omitted in (4.51) and (4.54) are listed in appendix B.2. Note that in the linearly approximated deformation gradient tensor $\boldsymbol{F}$, used for the BIM implementation in section 2.3, one off-diagonal element is zero, $F_{yx} = 0$ [35]. In this derivation, however, the contribution is carried along.

Comparing equations (4.47) and (4.48) with (4.52) and (4.55) shows that apart from the negative sign in the prefactor, the two approaches indeed lead to identical results. In [35] the forces are those acting on node i against the deformation (see equation (C.10) therein) while [108] uses the convention of [107], equation (26) therein, and thus does not have the negative sign.

4.5 Derivation of the forces from the stress tensor for the viscous contribution

Having derived the nodal forces from the elastic stress for the Skalak law, we can now add the viscous contribution to the stress tensor and derive the ensuing contribution to the nodal forces. The calculation is identical to that in section 4.4. The total stress tensor is (4.10) with viscous shear (s) and dilation (d) contributions and the viscous stress tensor (4.9) (note the symmetry). We replace $\boldsymbol{\tau}^\mathrm{e}$ in (4.40) by the total stress tensor and compute the additional forces on the nodes $\{\boldsymbol{P}^{\mathrm{v}}\}$. Because the full stress tensor is a sum of the individual components, the additional viscous forces are simply added to those computed from the Skalak law in (4.47), (4.47). The equation to solve is

$$\{\boldsymbol{\delta u}\}^T\{\boldsymbol{P}^{\mathrm{v}}\} = \operatorname{tr}([\delta\boldsymbol{F}][\boldsymbol{F}]^{-1}[\boldsymbol{\tau}^{\mathrm{v}}])A \tag{4.56}$$

The right hand side can be rewritten as

$$\frac{\lambda_1\lambda_2A^{(0)}}{\det\boldsymbol{F}}\operatorname{tr}\left(\begin{pmatrix}\sum_{i=1}^3 a_i\delta u_i & \sum_{i=1}^3 b_i\delta u_i\\ \sum_{i=1}^3 a_i\delta v_i & \sum_{i=1}^3 b_i\delta v_i\end{pmatrix}\begin{pmatrix}F_{yy} & -F_{xy}\\ -F_{yx} & F_{xx}\end{pmatrix}\begin{pmatrix}T_{xx} & T_{xy}\\ T_{xy} & T_{yy}\end{pmatrix}\right) \tag{4.57}$$

$$=A^{(0)}\operatorname{tr}\left(\begin{pmatrix}\sum_{i=1}^3 a_i\delta u_i & \sum_{i=1}^3 b_i\delta u_i\\ \sum_{i=1}^3 a_i\delta v_i & \sum_{i=1}^3 b_i\delta v_i\end{pmatrix}\begin{pmatrix}F_{yy}T_{xx}-F_{xy}T_{xy} & F_{yy}T_{xy}-F_{xy}T_{yy}\\ -F_{yx}T_{xx}+F_{xx}T_{xy} & -F_{yx}T_{xy}+F_{xx}T_{yy}\end{pmatrix}\right) \tag{4.58}$$

$$\begin{aligned}=A^{(0)}\Bigg(&\sum_{i=1}^3 a_i\delta u_i(F_{yy}T_{xx}-F_{xy}T_{xy})+\sum_{i=1}^3 b_i\delta u_i(-F_{yx}T_{xx}+F_{xx}T_{xy})\\ &+\sum_{i=1}^3 a_i\delta v_i(F_{yy}T_{xy}-F_{xy}T_{yy})+\sum_{i=1}^3 b_i\delta v_i(-F_{yx}T_{xy}+F_{xx}T_{yy})\Bigg)\end{aligned} \tag{4.59}$$

Now, analogously, we compare the coefficients of $\delta u_i, \delta v_i$ to obtain the forces

$$P_x^{\mathrm{v},i} = A^{(0)}\left(a_i(F_{yy}T_{xx}-F_{xy}T_{xy})+b_i(-F_{yx}T_{xx}+F_{xx}T_{xy})\right) \tag{4.60}$$

$$P_y^{\mathrm{v},i} = A^{(0)}\left(a_i(F_{yy}T_{xy}-F_{xy}T_{yy})+b_i(-F_{yx}T_{xy}+F_{xx}T_{yy})\right) \tag{4.61}$$

with T_{ij} from (4.9) and the components given in (4.1) to (4.4). In order to adhere to the convention in [35] and obtain the forces acting *on* node i, a negative sign must be added in the prefactor of equations (4.60) and (4.61).

4.6 Dimensionless parameters

We use the non-dimensional Boussinesq number to characterise the strength of the membrane viscosity contributions $\mu_{\mathrm{v,s}}, \mu_{\mathrm{v,d}}$ [36]

$$Bq_{\mathrm{s}} = \frac{\mu_{\mathrm{s}}}{\mu_{\mathrm{o}}R}\,, \qquad Bq_{\mathrm{d}} = \frac{\mu_{\mathrm{d}}}{\mu_{\mathrm{o}}R} \tag{4.62}$$

Both are defined with respect to the outer fluid viscosity in the system μ_{o}, similar to the definition of λ (2.6), except where otherwise specified. R is the characteristic length scale of the simulated system, e.g. for spherical capsules it is the radius of the sphere. For RBCs in blood flow simulations either the radius of a sphere with the same volume as the RBC or the large radius of the RBC in its rest shape is used. In blood flow simulations we always set

$$Bq \coloneqq Bq_{\mathrm{s}} = Bq_{\mathrm{d}} \tag{4.63}$$

with $Bq_\mathrm{s}, Bq_\mathrm{d}$ from equations (4.62). This is common practice [25], due to the fact that experimental results even for a 'general' membrane viscosity are scarce. Data from the literature will be discussed in detail in section 4.8. The artificial spring constants $k^{'}_\mathrm{s}, k^{'}_\mathrm{d}$ have the dimensionless representations

$$\kappa_\mathrm{s}/2 = \frac{k^{'}_\mathrm{s}}{\mu_\mathrm{s} t^{-1}} \ , \qquad \kappa_\mathrm{d}/2 = \frac{k^{'}_\mathrm{d}}{\mu_\mathrm{d} t^{-1}} \tag{4.64}$$

with a characteristic inverse time t^{-1}. This definition is identical to the definition of the non-dimensional stiffness parameter in section 4.3 in [106]. In shear flow t^{-1} is equal to the shear rate $\dot{\gamma}$ [106], and in channel blood flow $t^{-1} = \frac{U_\mathrm{avg}}{R}$, where R is the RBC radius and U_avg is the average flow strength in BIM which determines the flow velocity in the channel.

4.7 Implementation for the boundary integral method

4.7.1 Technical details

The derived forces for each triangles (4.60) and (4.61) are added in the BIM implementation described in section 2.3.2. Apart from the FD scheme [36] two integral schemes (Int1 and Int2) for the viscous stress computation [106] are implemented. Comparison of eq. (18) in [36] with eq. (20) and tables 1 and 2 in [106] shows that only the coefficients (4.5) and (4.6) in the computation of the viscous stresses (4.1) to (4.3) change, if other schemes are used, they become for the first integral scheme Int1

$$A_\mathrm{s}^\mathrm{Int1} = \exp\left(-\Delta t \frac{k^{'}_\mathrm{s}}{2\mu_\mathrm{s}}\right) \ , \qquad B_\mathrm{s}^\mathrm{Int1} = \frac{2\mu_\mathrm{s}}{\Delta t}\left[1 - \exp\left(-\Delta t \frac{k^{'}_\mathrm{s}}{2\mu_\mathrm{s}}\right)\right] \ , \tag{4.65}$$

$$A_\mathrm{d}^\mathrm{Int1} = \exp\left(-\Delta t \frac{k^{'}_\mathrm{d}}{2\mu_\mathrm{d}}\right) \ , \qquad B_\mathrm{d}^\mathrm{Int1} = \frac{2\mu_\mathrm{d}}{\Delta t}\left[1 - \exp\left(-\Delta t \frac{k^{'}_\mathrm{d}}{2\mu_\mathrm{d}}\right)\right] \tag{4.66}$$

and for Int2

$$A_\mathrm{s}^\mathrm{Int2} = \exp\left(-\Delta t \frac{k^{'}_\mathrm{s}}{2\mu_\mathrm{s}}\right) \ , \qquad B_\mathrm{s}^\mathrm{Int2} = \frac{k^{'}_\mathrm{s}}{2}\left[1 + \exp\left(-\Delta t \frac{k^{'}_\mathrm{s}}{2\mu_\mathrm{s}}\right)\right] \ , \tag{4.67}$$

$$A_\mathrm{d}^\mathrm{Int2} = \exp\left(-\Delta t \frac{k^{'}_\mathrm{d}}{2\mu_\mathrm{d}}\right) \ , \qquad B_\mathrm{d}^\mathrm{Int2} = \frac{k^{'}_\mathrm{d}}{2}\left[1 + \exp\left(-\Delta t \frac{k^{'}_\mathrm{d}}{2\mu_\mathrm{d}}\right)\right] . \tag{4.68}$$

In contrast to the lattice Boltzmann-immersed boundary method used in [36, 106] the time step Δt is not constant in BIM. The implementation described in 2.3.2 uses a time integration algorithm with an adaptive step width. Therefore, the viscous stresses τ_{ij}^{v} as well as the strain tensor elements E_{ij} of each successful time step must be saved for the computation of the new viscous stresses. In this context, the subsampling after $N\delta t$ from [36] is here implemented as a subsampling after every N-th successful time step. For best accuracy [106], $N = 1$ was chosen for the simulations discussed in this thesis.

4.7.2 Validation and comparison with the literature

Simulations of viscoelastic capsules in shear are used to validate the implementation. The radius of the spherical capsules is $R = 4\,\mathrm{\mu m}$ and they are immersed in a fluid of viscosity $\mu_{\mathrm{o}} = 1.2\,\mathrm{mPa\,s}$, the viscosity contrast is 1. Their membrane is endowed with shear elasticity with modulus $\kappa_{\mathrm{S}} = 5 \times 10^{-6}\,\mathrm{N\,m^{-1}}$ modelled with the Skalak law, with a sphere as reference shape. Capsules are volume conserving because the fluid inside the capsule cannot penetrate the membrane. The surface area, however, changes during the deformation and thus $\kappa_{\mathrm{A}} = \kappa_{\mathrm{S}}$. The membrane is discretised with $n_{\mathrm{t}} = 5120$ triangles, if not stated otherwise. The shear Boussinesq number Bq_{s} is varied between 0 and 40, the dilation part Bq_{d} is set to zero. We choose as shear rate $\dot{\gamma} = 208.3\,\mathrm{s^{-1}}$ for all simulation, which leads to a capillary number of

$$Ca = \frac{\dot{\gamma}\mu_{\mathrm{o}}R}{8/12\ \kappa_{\mathrm{S}}} = 0.3, \tag{4.69}$$

equal to the value chosen by Li et al. [106]. The constant factor 8/12 in the denominator is due to the different definition of the shear modulus in [106]. With a characteristic velocity of $v = \dot{\gamma}R$ the Reynolds number (2.12) of the simulated system is very small and the BIM can be used.

We compare the time-dependent Taylor deformation index D of the capsule with results from former studies [25, 26, 106] in figure 4.1(a). The four simulation implementations do not lead to exactly identical results, but the overall agreement is good. On the right in figure 4.1(b) the influence of the membrane viscosity strength on the deformation is shown. Increasing Bq_{s} leads to smaller deformation D in the shear flow, the rotating capsule is closer to the original spherical shape. This is due to the viscous membrane, which slows down the deformation and in combination with the tank-treading of the membrane in shear flow leads to smaller D.

In figure 4.2 the dependence of the deformation on the surface triangulation is presented. Surprisingly, the orientation of the initially spherical surface mesh in the shear flow has an equally strong influence on the results as the number of triangles n_t (inset in figure 4.2). The images of the capsule surface on the right in figure 4.2 show the wrinkles on the surface, whose development depends not only on the resolution but also on the orientation. Such wrinkles arise also for non-viscous capsules when resistance to bending of the surface is absent [110]. These findings might also explain

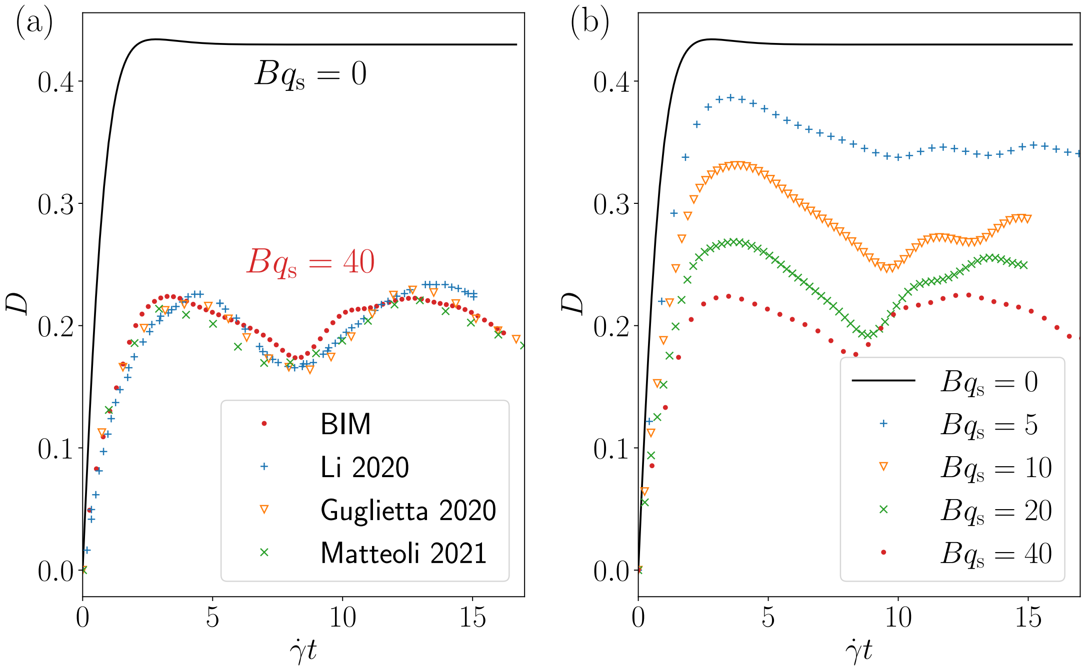

Figure 4.1: Deformation index D for various membrane viscosity values Bq_s. (a) Comparison with results from the literature by Guglietta et al. [25], Matteoli et al. [26] and Li et al. [106] shows good agreement. (b) Increasing the membrane viscosity leads to a decrease in the deformation index.

the difference between the curves shown in figure 4.1(a). Li et al. [106] for example use 5120 surface triangles, but the orientation is not discussed.

Finally, the different schemes for the viscous stress computation Fd, Int1 and Int2 and the influence of the (dimensionless) artificial spring constant (4.64) are tested. Figure 4.3(a) shows that the different computation schemes implemented here lead to identical results, as has been reported in [106]. The artificial spring constant $\kappa_s/2 = 5, 10, 20, 30$ has negligible influence for smaller membrane viscosity value $Bq_s = 5$,compare figure 4.3(b). At larger $Bq_s = 40$ a slight difference between $\kappa_s/2 = 10$ and 20 can be observed. Compared to the influence of the surface grid discussed in figure 4.2, however, the effect is very small.

Following the analysis of this section, in the applications of the following chapter the FD scheme with subsampling after a fixed number N of time steps is used, and $N = 1$. The dimensionless spring constants (4.64) are set to $\kappa_s/2 = \kappa_d/2 = 10$. The recursively defined viscous stresses (4.1) to (4.4) are initialised with zero at the beginning of the simulation.

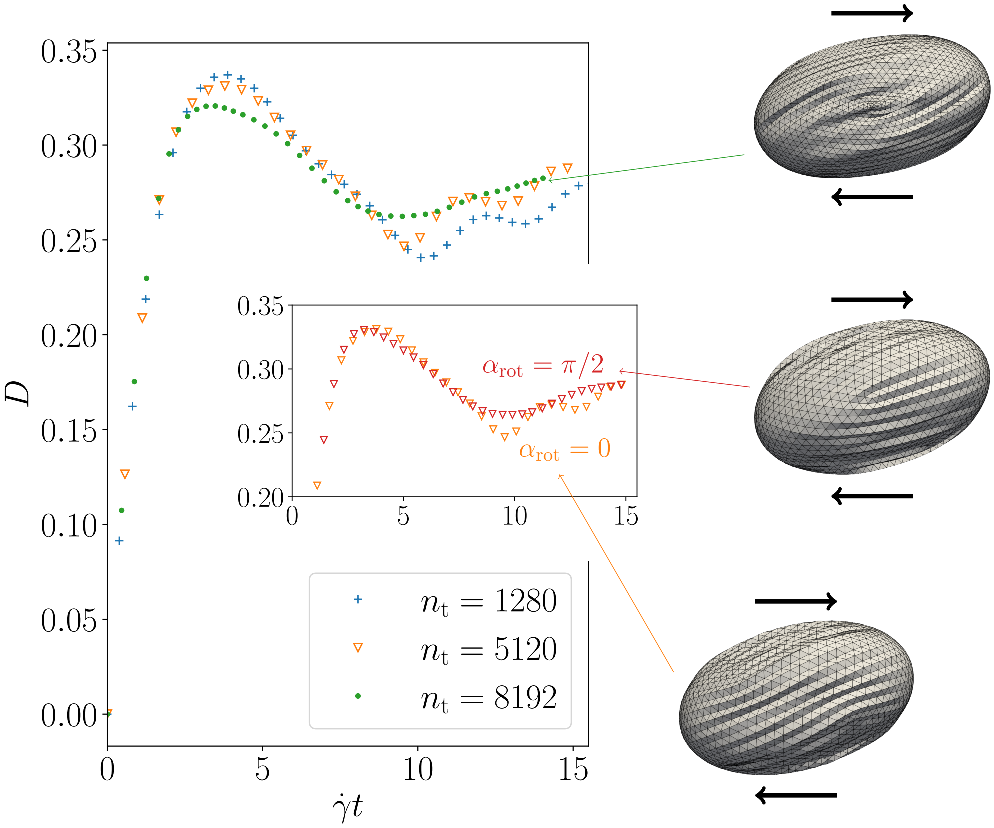

Figure 4.2: Deformation of the spherical capsule for different triangulation n_t of the capsule. The inset shows the deformation for a capsule with rotated spherical mesh (red curve) at $n_\mathrm{t} = 5120$. The images on the right illustrate the wrinkling of the capsule membrane for three different parameter combinations (see coloured arrows), black arrows indicate the shear direction. $Bq_\mathrm{s} = 10$ for all simulations.

4.8 Experimental results for the membrane viscosity

Experimental values for the membrane viscosity are rare and the results span a wide range, as summarised in table 4.1. For a better overview the table also includes the Boussinesq numbers used for the cell modelling in other simulation studies. The first part of the tables lists mainly experimental studies and one coarse-grained simulation approach, which used different techniques to determine the viscosity. The second part lists the upper boundary of the membrane viscosity for four recent simulation studies. The value of the membrane viscosity μ_m is taken from the respective study. The simulation studies mostly reported a dimensionless value which was converted into μ_m for better comparison. The last column gives the Boussinesq number calculated from μ_m via equation (4.63) with the RBC radius $R = 4\,\mu\mathrm{m}$ and the plasma viscosity

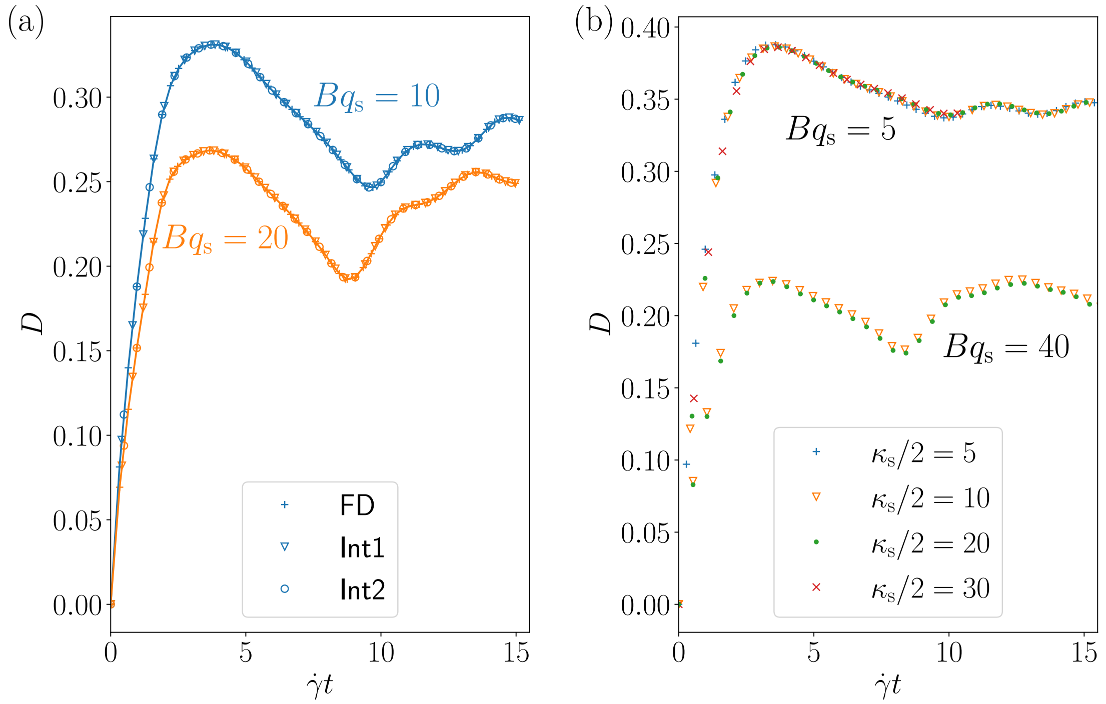

Figure 4.3: Influence of the technical parameters on the deformation. (a) Three different viscous stress computation schemes are tested for $Bq_s = 10, 20$. (b) Influence of the artificial spring constant $\kappa_s/2$ on the deformation for $Bq_s = 5, 40$.

$\mu_o = 1.2\,\mathrm{mPa\,s}$.

In addition to the inevitable scattering of experimental measurements Chien et al. [112] obtained different results for the membrane viscosity, depending on the strength and duration of the deformation of the cells. The authors hypothesise that this may be due to rearrangement of the surface molecules under strain [112]. After initial measurements at room temperature [113], Hochmuth et al. [114] found that the cell recovery from a stretched state is highly temperature dependent, which leads to different estimates of the Boussinesq number. Linderkamp et al. [115] measured the cell relaxation for centrifuged cells and found a difference in the relaxation time scale of around 50 % between the cells at the bottom, which are denser, and the cells at the top. The cell density increases with the cell age because the water loss of the cell over time leads to an increase of the relative haemoglobin concentration inside the cell. Hochmuth et al. [121] in addition discuss the membrane viscosity for various abnormal cell conditions.

With only few exceptions [117] membrane viscosity values are reported only for the *shear* contribution. This thesis therefore follows Guglietta et al. [25], setting $Bq_d = Bq_s$ as mentioned in section 4.6. The overview in table 4.1 shows that

	(exp.) technique	$\mu_{\mathrm{m}}/(10^{-7}\,\mathrm{Pa\,s\,m})$	Bq
Evans 1976 [111]	micropipette aspiration	10	213
Chien 1978 [112]	micropipette aspiration	0.06 - 206	1.3 - 4390
Hochmuth 1979 [113]	cell extensional recovery	6 - 8	128 - 171
Hochmuth 1980 [114]	cell extensional recovery	21 (at 6 °C) 14 (at 15 °C) 7.4 (at 25 °C) 3.6 (at 37 °C)	448 298 158 77
Linderkamp 1982 [115]	cell extensional recovery	9.5 ± 2.2 (bottom) 5.4 ± 1.5 (top)	202 ± 47 115 ± 32
Tran-Son-Tay 1984 [116]	tank-treading cells rheoscopy	0.57	12
Dimova 1996, 2006 [117, 118]†	falling ball viscosimetry	0.05	1.07
Mills 2004 [55]	optical tweezers (extens. recovery)	3-28	64-597
den Otter 2007 [119]	coarse-grained simulations	0.0001	0.002
Noguchi 2005 [120]	–	0.144	3.1
Yazdani 2013 [105]	–	10	213
Li 2019, 2020 [36, 106]	–	1.92	41
Guglietta 2020 [25], Matteoli 2021 [26]	–	3.18	68

† Study of lipid bilayer cells in general, not specifically RBCs.

Table 4.1: Literature overview for membrane viscosity values. Experimental studies in the first and simulation studies in the second part of the table. μ_{m} is taken from the literature, Bq is computed via equation (4.63) for RBCs in blood plasma. For simulation studies the upper boundary of the used viscosity values is given.

experimental measurements do not provide a precise value for the membrane viscosity of RBCs, the results can only give a rough estimate.

5 Influence of membrane viscosity on the red blood cell dynamics in microchannels

5.1 Overview

This chapter takes up the question of the RBC slipper dynamics from chapter 3.4. Here the influence of the membrane viscosity on the slipper dynamics is studied, using the implementation described in chapter 4. It will be shown that including membrane viscosity in the simulation model leads to slipper dynamics consistent with the experimental measurements. This extension of the simulation model requires discussion and adaptation of the RBC elastic reference shape which will also be part of this chapter. The outline of the chapter is as follows: Modifications of the simulation setup are described in the first section 5.2. The next section 5.3 focuses on the RBC shear reference state. In the first part 5.3.1 an overview of results from the literature on this problem is given, highlighting the fact that a definite solution for the appropriate reference state does not exist so far and different assumptions are made in simulation studies. Following this literature overview the influence of the reference state on the RBC rest shape is discussed. Section 5.3 finishes with a short discussion of the influence the reference shape has on the slipper dynamics in the microchannel. Section 5.4 finally shows the results for the slipper dynamics including viscosity of the membrane in comparison with the experiments and former results. In the subsequent section 5.5 the experimental evidence and reliability of the comparison is discussed in detail. This is based on a discussion and comparison of the data processing methods in experiment and simulation. Additional data for the slipper length oscillation is presented, as well as statistical information on the slipper observation. The experimental data discussed in this chapter was provided by S. M. Recktenwald (member of the group of C. Wagner in Saarbrücken). Some experimental data is repeated from section 3.4. The next section 5.6 presents the phase diagrams for RBCs in channel flow with membrane viscosity. In the conclusion in 5.7 the simulation settings and results from the previous sections are summed up and a short overview of how they fit in with the experimental evidence is given.

5.2 Simulation setup

Complementary to section 3.4 the dynamics of slippers in a rectangular channel of size 11.5 µm to 8 µm is studied with the BIM. Changes to these earlier simulations are variations of the elastic shear modulus κ_{S} and the stress-free shape, where in addition to the discocyte an oblate spheroid of aspect ratio $\tau = 0.9$ was used, compare section 2.2. Changes in the shear contribution of the RBC entail changes in the bending modulus κ_{B} and the (spatially constant) reference shape with reference curvature c_0^*, because bending and shear resistance together determine the rest shape in simulations, which must be the discocyte shape. Different parameter combinations are discussed in section 5.3.2. For the rest of the chapter the moduli were set to $\kappa_{\mathrm{S}} = 5 \times 10^{-6}\,\mathrm{N\,m^{-1}}$ and $\kappa_{\mathrm{B}} = 4 \times 10^{-19}\,\mathrm{N\,m}$ with reference curvature $c_0^* = 4$ for the oblate spheroid reference state. Simulations with a discocyte reference state for good comparison have the same simulation parameters as used in chapter 3. The Boussinesq number (4.63) is defined with respect to the RBC radius R. Different values for λ are use in this chapter. Very recent (still unpublished) experimental results by our collaborators from the group of C. Wagner in Saarbrücken lead to the conclusion that the internal fluid viscosity is indeed significantly larger than the formerly used value of $\lambda = 5$, the experimental mean lies between 10 and 20.

5.3 A short digression on the shear reference state

5.3.1 Literature overview

5.3.1.1 Discussion of the reference shape

Tsubota et al. [48] present simulations of stop-and-go shear flow and in that context discuss equilibrium shapes. The Skalak law is used to describe shear and dilation contributions and a spring model for the bending. Interpolations between a sphere and a discocyte are used as stress-free shapes. With this approach the authors rule out near-spherical shapes for the stress-free shape because in equilibrium for realistic moduli these lead to cup-shaped RBCs, similar to stomatocytes, a form of diseased RBC shape [48]. Tsubota et al. [48] argue for a near-oblate reference shape as this matches their shear flow results better. However, the bending model may have (crucial) influence on the equilibrium shape and the authors add that further investigations in this direction are necessary.

Lim H.W. et al. [122] use an ADE model [123] and show that depending on the area difference between the two monolayers of the lipid bilayer in the natural state, different equilibrium shapes like discocyte, stomatocyte and ‘spiky’ echinocyte result. The author discuss how different reference shapes lead to these equilibrium shapes, however, the analysis is expected to depend heavily on the ADE bilayer model. The area difference introduced in the study [122] is related to the concept of a (constant) reference curvature and the findings suggest that it is necessary to introduce a non-zero reference curvature. Interestingly, the authors included experimental images of the cup-shaped RBCs from Jay [124], which were obtained by adding albumin in the fluid surrounding the RBC. In this solution mechanical stirring led to reversible shape transition from discocyte to stomatocyte [124], which suggest that in this surrounding, it is a metastable state.

Cordasco et al. [52] present simulations in shear flow to compute, amongst others, phase diagrams and slipper frequencies. The Skalak and Helfrich laws are used with constant non-zero curvature and the authors check that the cells have the correct equilibrium shape. As reference shapes the discocyte and three oblate spheroids with different aspect ratios are used in the study. For the most spherical oblate spheroid with aspect ratio $\tau = 0.9$ the authors report that a bending modulus of $\kappa_\mathrm{B} = 6 \times 10^{-19}\,\mathrm{N\,m}$, a value larger than what is commonly used but still in the experimental range, and a spontaneous curvature of $c_0^* = 4$ is necessary to obtain the biconcave equilibrium shape [52]. The authors also consider negative spontaneous curvatures. The main finding of the study is that only for viscosity contrast values much smaller than the physiological range, significant changes due to different stress-free states are visible [52].

These parameter combinations, which lead to the correct rest shape of the RBC, are used for subsequent studies. Lanotte et al. [4] employ two different simulation methods to investigate RBCs in shear flow, a finite-volume method with the YALES2BIO software [125] and a smoothed dissipative particle dynamics (SDPD) method [126], and show that the variety of observed shapes agrees well experiments. A viscosity contrast of $\lambda = 5$ is used throughout the study and the authors state for one method that the RBC parameters are set as in the paper by Cordasco et al. [52].

In the theoretical study by Pozrikidis [127] constitutive equations are employed for the RBC bending moments and membrane tension. The author derives the rest shape for different oblate spheroid and discocyte reference shapes with different curvatures and compares the results with the experimental measurement results for RBCs. The results support Helfrich's notion that the Helfrich bending model with a negative natural state curvature, equal to approximately the curvature of the sphere with same surface area as the discocyte, leads to correct equilibrium shapes [127]. The author does not find cup-shaped RBCs and the difference between different rest shapes close to the experimental result are small.

Cordasco et al. [44] use shear flow go-and-stop simulations of RBCs and investigate the resulting equilibrium shapes. The stress-free shapes are similar to an earlier work [52] discussed above. The authors find a high dependence on the stress-free shape, e.g. in the time scales of the relaxation behaviour, but cannot compare the results to experiments and thus cannot give an answer as to which reference shape is the correct one. Other observations are, that larger viscosity contrast λ increases the relaxation time scales and, secondly, that the bending contribution is responsible for recovering the discocyte rest shape, while the shear contribution accounts for the shape position memory.

The study by Sinha et al. [51] presents RBC shear flow simulations with a discocyte as reference shape together with the Skalak and Helfrich law for RBC modelling and ascertain, that the correct equilibrium shape results. The authors investigate the bending reference curvature using a constant curvature, discocyte and oblate spheroid and find the best agreement with experimental results for an oblate spheroid [51]. Whether this finding also holds for other reference shapes was not investigated. Note that the authors also give an argument against the simplifying assumption of a spatially constant reference curvature, stating that ‘proteins have been shown to preferentially bind via curvature-sensing mechanism’ [51] (compare ref. 42 therein).

Peng et al. [53] develop simulations for a multiscale fluid-structure interaction model of the RBC and investigate the RBC’s rest shape and its behaviour in shear flows of small shear rate. Only spheroidal reference shapes are investigated and the authors find that more spherical spheroids need a larger spontaneous curvature to relax to the correct rest shapes. Moreover, for more spherical reference shapes the tank-treading is observed already at significantly smaller shear rates and these match experimental comparison best [53].

Dupire et al. [128] present an extended Keller and Skalak (KS) model, where the RBC is represented as an ellipsoid which now possesses shear elasticity. In this model the stress-free state has a large impact on the behaviour in shear flow. The authors obtain parameters by fitting their model to experimental results of tank-treading RBCs from the same group [98] and find that an oblate spheroid with aspect ratio $\tau = 0.993$ fits best. More experimental results and related observations from this group are presented in Viallat et al. [50] and Dupire et al. [129].

Levant et al. [54] study the in vitro dynamic states of a rabbit RBC in planar linear flow as a generalisation of simple shear flow to construct the phase diagram, describe the dynamic RBC states and study the transition between these. The authors report good agreement with experimental results for human RBCs in shear flow but state that their results are not in agreement with the experimental evidence by Dupire et al. [129] and the simulation results from the work of Tsubota et al. [48], Cordasco et al. [52] and Peng et al. [53]. More specifically, Levant et al. [54] argue that the interpretation of the experimental evidence [129] is no sufficient justification for the introduction of the modified simulation models with spheroid reference shape [48, 52, 53], which were based on this evidence. The second point the authors make is, that the theoretical models depend on many physical parameters which are specified (partly) from experimental measurement and crucially influence the RBC’s shape. Therefore, Levant et al. [54] state that so far the question of the correct stress-free shape has not yet been answered satisfactorily and the discocyte shape on these grounds should not be ruled out.

5.3.1.2 Further red blood cell simulation studies

In this subsection further RBC simulation studies are listed, which, however, do not specifically discuss the RBC rest shape, to give an impression of the different models and assumptions about the stress-free shape in the literature.

Yazdani et al. [130] use a discocyte reference shape with a negative reference curvature, as studied in [52], which implies that the rest shape conforms with the experimentally observed biconcave disc.

Fedosov et al. [96] model the RBC with connected elastic springs and perform an RBC recovery test, the simulation method is a dissipative particle dynamics (DPD) technique. Fedosov et al. [23] also use this spring model, together with a SDPD method, and note that for slow flows the shape is identical to the unperturbed RBC rest shape. Both studies use a stress-free membrane model and the bending contribution is included in the spring potential [23, 96]. In a subsequent study, the authors Mauer et al. [101] refer for the modelling of elasticity, bending energy, area and volume conservation to Fedosov et al. [96], but use an oblate spheroid stress-free shape. Reichel et al. [24] refer to earlier work [101] and also use an oblate spheroid stress-free shape, as it was shown to fit observations well. A recent study from the same working group [6] again uses the spheroid reference shape. In contrast to the Helfrich model (2.3), where the bending curvature is a direct input quantity in equation (2.4), this is not the case for the RBC spring model and thus direct comparison is not possible.

Mendez et al. [131] use a near-spherical oblate spheroid as stress-free shape but a zero reference curvature (compare supplementary material of the study [131]) and a low bending modulus of $\kappa_{\mathrm{B}} = 3 \times 10^{-19}\,\mathrm{N\,m}$. With these parameters, simulations with BIM conducted for this thesis did not lead to the correct biconcave rest shape, examples are given in the following sections. Comparison of this observation with results in the paper [131] is not possible, because results on the equilibration of the RBC in a quiescent fluid are not included there. A subsequent study by Matteoli et al. [26] also uses the oblate spheroid reference shape, details on the reference curvature or the RBC relaxation are not given.

Two recent studies, Guglietta et al. [25] and Guglietta et al. [132], do not mention the stress-free state and the bending reference but in relaxation simulations obtain the correct rest shape. The conclusion in the later work [132] suggests that a discocyte is used as reference shape.

5.3.1.3 Summary

In recent years, the oblate spheroid is increasingly being used as stress-free RBC shape in simulation studies, replacing the former choice of a discocyte. Choosing a spheroid as reference shape for the shear contribution effectively means that the RBC is pre-stressed in its natural rest shape, the biconcave disc. Most studies refer to earlier publications for motivation why they use certain stress-free states and (corresponding) bending reference curvatures, in particular these are the studies from Cordasco et al. [44, 52]. A necessary precondition for the choice of stress-free state and bending curvature is that it leads to the discocyte rest shape of the RBC. The justification for selecting a certain stress-free state and bending curvature is that experimental observations of RBC dynamics are better reproduced. As discussed above in 5.3.1.1, identification of the appropriate stress-free shape is difficult. The main difficulties are that many other parameters, e.g. the elastic and bending moduli, influence the RBC dynamics, and systematic testing of feasible parameter combinations for different flow systems amounts to a impractically large number of simulations. Moreover, RBCs are biological entities and thus experimental results scatter due to their biological heterogeneity, therefore, detailed comparison, e.g. of RBC rest shapes is problematic. Finally, as Levant et al. [54] point out, the spatial resolution of the RBC imaging crucially determines the shape characterisation, which hampers qualitative shape comparison in experiment and simulation.

5.3.2 Red blood cell rest shape in simulation models

All simulation models for RBCs must reproduce the discocyte as correct rest shape of the cell. In particular, simulation parameters such as bending and shear reference shapes and moduli must be chosen such that this outcome is ensured. An approach to check this for a particular parameter combination is discussed in the following. For any simulation parameter combination listed in table 5.1 two simulations with different start shapes are run, one with the discocyte shape specified in the RBC model and one with a deformed slipper-like shape. The cells are placed in an infinite quiescent fluid where they start to relax towards their rest shape. Example relaxation trajectories are shown in figures 5.1(a) and 5.2. Discocyte start shapes (solid lines) relax to discocytes with marginally different deformation parameter. This difference reflects the very slight difference in the cross section of the respective discocyte rest shape, shown in figure 5.1(b) in green and blue. The orange points in figure 5.1(b) show the inital discocyte shape at time 0 in (a), modelled according to experimental measurements [43]. It is marginally flatter in the middle, however, all the differences are within experimental measurement errors. The deformed cells (dashed lines in 5.1(a)) need more time for the relaxation towards the respective rest shape. Changes in the shear modulus can influence the exact form of the discocyte rest shape. This is exemplified for a larger κ_S in figure 5.2 (light blue lines). In addition, the relaxation towards the rest shape is marginally faster than for a smaller shear modulus. The viscosities of fluid and membrane do not influence the final rest shape but only the time scale on which a deformed cell relaxes towards the rest shape. An example trajectory for λ increased by a factor of two is shown in figure 5.2 (black dashed line). The relaxation time until the cell reaches the rest shape is significantly longer. This is in line with earlier results [44], discussed in section 5.3.1.1.

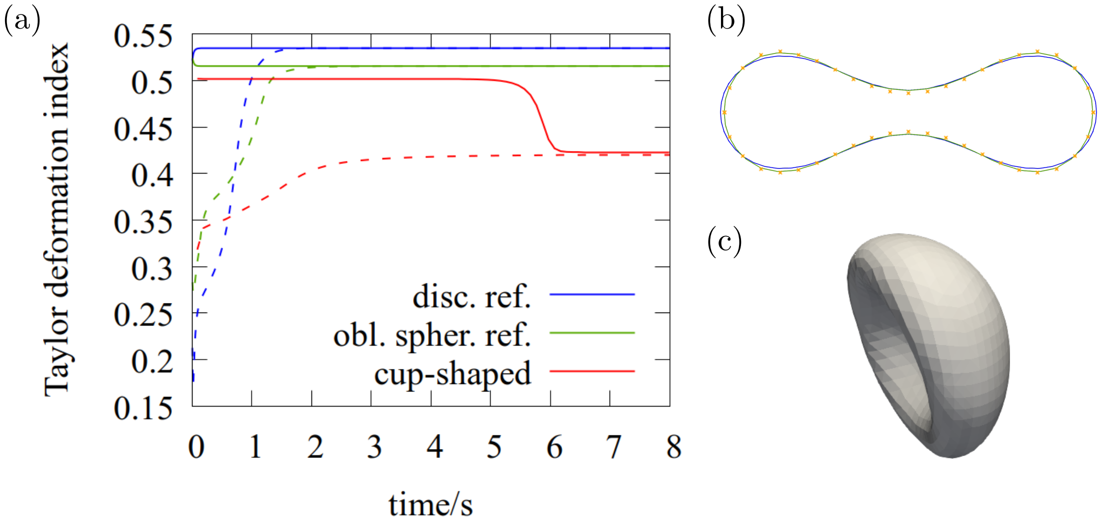

Figure 5.1: Red blood cell rest shapes in numerical simulation. (a) Relaxation of RBCs towards discocyte rest shapes for oblate spheroid (green) and discocyte (blue) reference shape, starting from a discocyte (solid lines) and a deformed slipper-like shape (dashed lines). The red curves show relaxation towards a cup-shape. Parameter combinations are given in table 5.1. (b) Slice through the two discocyte rest shapes (green and blue) in comparison with the initial discocyte shape (orange points). (c) Cup-shaped rest shape for different parameter combinations.

For some parameter combinations in table 5.1 (in red) the slipper-like deformed RBC does not relax towards a discocyte but instead towards a cup-like shape shown in figure 5.1(c). These parameter combinations should not be used in simulations. The deformation index for these is significantly lower as shown in figure 5.1(a) in red. Especially a flat reference curvature $c_0^* = 0$ which is used for the discocyte reference simulations in 3 does not work for the oblate spheroid reference shape.

For the discocyte reference the RBCs relax correctly in all cases, due to the influence of the shear reference. For the oblate spheroid reference, however, cup-like rest shapes occur if the bending reference curvature in combination with the bending modulus is not large enough to overcome the influence of the shear con-

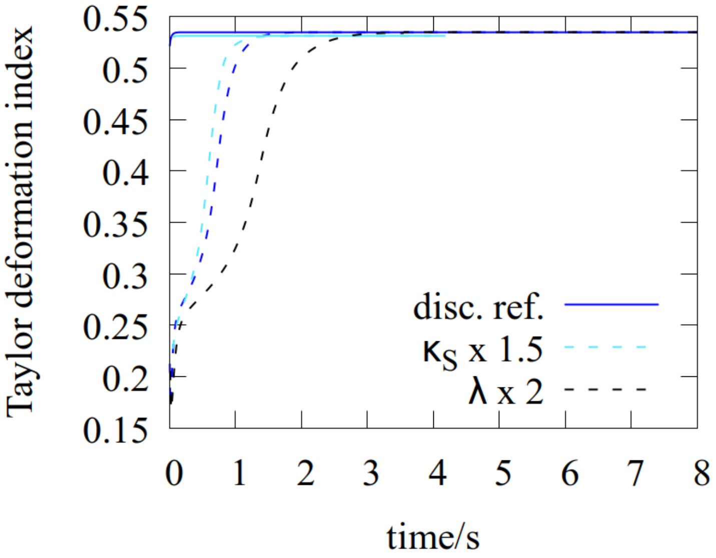

Figure 5.2: Influence of red blood cell parameters on the rest shapes. The relaxation of RBCs towards a discocyte rest shapes for a the discocyte reference shape is repeated from figure 5.1(a) (dark blue lines), again starting from a discocyte (solid lines) and a deformed slipper-like shape (dashed lines). The qualitative changes in the relaxation behaviour for increased shear modulus κ_S and increased viscosity contrast λ are added in light blue and black, respectively. Parameter combinations are given in table 5.1.

tribution, whose strength is given by κ_S. For an oblate reference shape with $\kappa_S = 5 \times 10^{-6}\,\mathrm{N\,m^{-1}}$ [31, 55, 56] at $c_0^* = 4$ [52], the correct rest shape is obtained if a moderately larger bending modulus $\kappa_B = 4 \times 10^{-19}\,\mathrm{N\,m}$, which is not significantly larger than the usually reported values [17, 25, 31, 57], is used. In the following, this combination is used for simulations with an oblate reference shape. Variations of the parameters have negligible influence on the dynamic RBC behaviour as has been shown before in section 3.6.

5.3.3 Slipper movement of red blood cells with oblate spheroid shear reference

In this section the influence of the oblate spheroid reference shape on the slipper movement is discussed. Figure 5.3(a) shows an example slipper trajectory at $\bar{v} \approx 5\,\mathrm{mm\,s^{-1}}$, in comparison with earlier results for the discocyte shear reference from chapter 3. The blue curve is representative for the slipper movement at these parameter combinations. It consists of an initial phase, where the slipper flows off-centred in y-direction but symmetric with respect to the x-y-plane, as the first inset

ref. shape	κ_S $/(10^{-6}\,\mathrm{N\,m^{-1}})$	c_0^*	κ_B $/(10^{-19}\,\mathrm{N\,m})$	remarks
disc.	5.0	-2.09	6.0	c_0^*, κ_B from [44, 52]
	5.0	0	3.0	fig. 5.1(a) for $\lambda = 5$, and fig. 5.2 for $\lambda = 5, 10$
	5.0	4.0	3.0	
	5.0	4.0	6.0	
	7.5	0	3.0	fig. 5.2 for $\lambda = 5$
obl. spher. ($\tau = 0.9$)	5.0	0	3.0	cup-shaped
	5.0	0	6.0	cup-shaped, fig. 5.1(a)
	5.0	2.8	6.0	
	5.0	4.0	3.0	cup-shaped
	5.0	4.0	6.0	
	5.0	4.0	4.0	fig. 5.1(a) for $\lambda = 5$
	7.5	4.0	4.0	cup-shaped
	7.5	4.0	6.0	$\kappa_\mathrm{S}, c_0^*, \kappa_\mathrm{B}$ from [44, 52]
	10.0	4.0	8.0	
	15.0	4.0	8.0	cup-shaped
	15.0	4.0	12.0	

Table 5.1: Simulation parameter combinations and resulting rest shapes. In the first four columns the cell parameters are specified, these are the reference shape, the shear modulus κ_S, the bending curvature c_0^* and the bending modulus κ_B. The last column contains remarks. Lines with parameter combinations which lead to the cup-shaped rest shape are marked in red, all other combinations lead to the correct discocyte rest shape.

of the three-dimensional RBC shape shows. It then transitions to a state with the slipper flowing slightly lopsided, connected to a smaller centre of mass offset and no longer centred in z-direction. This is connected to a decrease in frequency. For larger mean velocities the transition occurs at earlier times. However, in both states the slipper shows a regular tank-treading movement. From such trajectories, the frequency and amplitude of the *first* phase of the oscillation are extracted (if possible) and plotted in figures 5.3(b,c). For the two largest velocities, the first phase consist of very few oscillations such that extraction of e.g. the frequency is not possible. Hence, the oscillation parameters are extracted from the second phase. This explains the non-linear behaviour of the blue points in figure 5.3(b). Compared to the data for the discocyte the amplitudes shown in (c) are very small. In experiments, for such small amplitudes the oscillation is too small in comparison with experimental noise and in most cases impossible to extract from the data, as was already remarked in [62]. The graph inset in figure 5.3(a) shows the positional oscillation of an RBC with

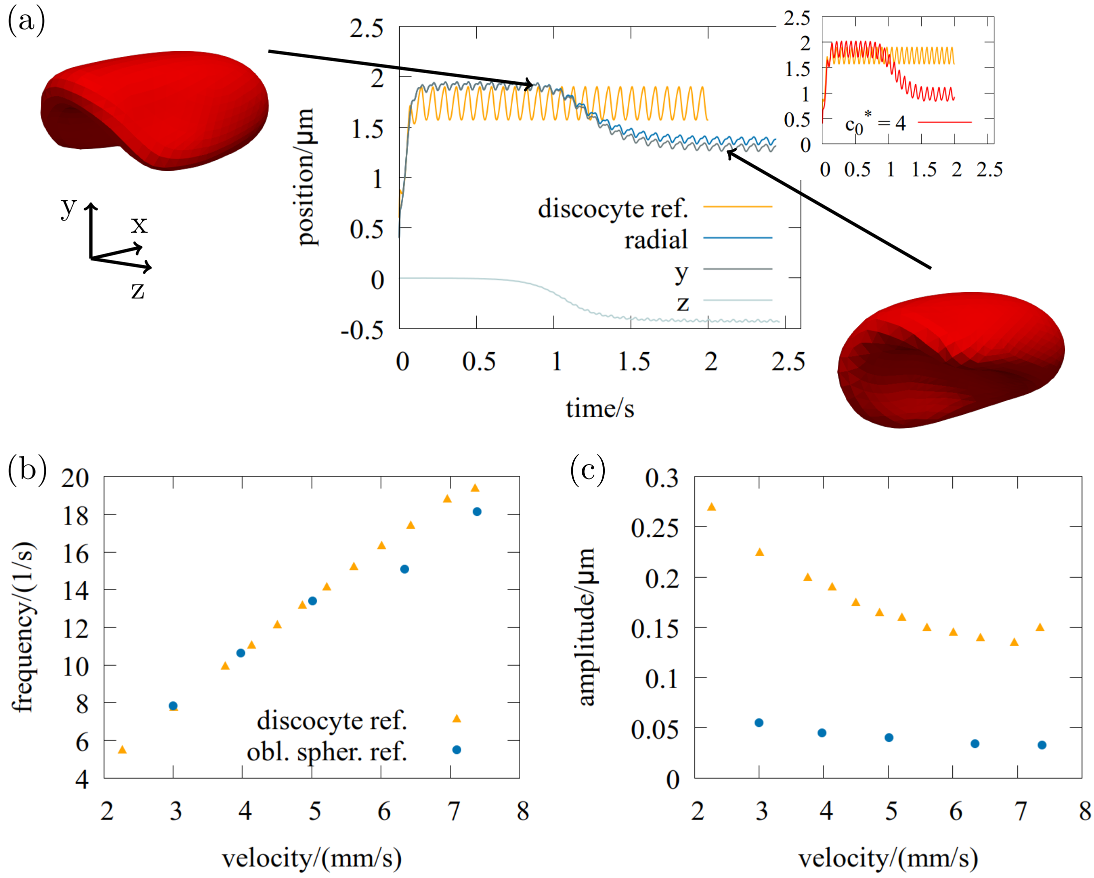

Figure 5.3: Slipper dynamics for oblate spheroid shear reference. (a) Comparison of the slipper oscillation for the spheroid reference (blue lines) with the earlier results for the discocyte reference shape (orange) at approximately identical mean velocity $\bar{v} \approx 5\,\mathrm{mm\,s^{-1}}$. The plot inset in addition shows a discocyte with positive bending reference curvature and $\kappa_\mathrm{B} = 6 \times 10^{-19}\,\mathrm{N\,m}$ (red curve). The (b) frequencies and (c) amplitudes at different velocities are compared to the results for discocytes shown earlier in figure 3.5(a,b). For all results the viscosity contrast is $\lambda = 10$.

discocyte shear reference and a positive bending reference curvature c_0^* (red curve). The amplitude is comparable to the orange curve but the transition to a lopsided slipper is identical to the behaviour for the oblate spheroid reference, the frequency decrease included. Note that for the discocyte with negative reference curvature or smaller bending modulus (compare table 5.1) no lopsided slippers appear.

This leads to the conclusion that the decrease in amplitude is due to the change from discocyte to spheroid *shear* reference, while the transition to the lopsided slipper must be attributed to the positive *bending* reference curvature in combination with large κ_B. The physical explanation for the decrease in amplitude is the sphericity of the oblate spheroid reference. During the tank-treading movement, the dimples of the

RBC follow the membrane rotation as shown in section 3.4 and the cell shows a length oscillation, described as breathing motion. If the shear reference is a discocyte, this leads to larger elastic restoring forces during this breathing motion when the dimples are at opposite sites of the elongated slipper, compared to the near-spherical oblate spheroid reference, and thus to more violent positional oscillations.

5.4 Influence of the membrane viscosity on the red blood cell slipper dynamics

5.4.1 Frequency, amplitude and offset of the slipper oscillation

In this section results for the slipper oscillation of RBCs with oblate spheroid reference shape and additional viscosity of the membrane are presented. These slippers show regular tank-treading oscillations similar to the discocyte reference RBCs in section 3.4. The rotations described in section 5.3.3 in the absence of membrane viscosity are no longer observed.

Similar to earlier analysis the frequency, amplitude and position of the slipper in the microchannel are analysed and summarised in figure 5.4. For comparison, the former results for the discocyte without membrane viscosity and the experimental measurements from chapter 3 are repeated in orange and black, respectively. Starting from former results for $\lambda = 5$ (orange squares), a membrane viscosity of $Bq = 5$ in the model (red squares) leads to a significant decrease in the frequency shown in figure 5.4(a). For larger values of $\lambda = 10, 20$ this effect of the increased membrane viscosity Bq is less pronounced (red circles and triangles). An explanation for this could be that membrane and interior viscosity have a similar influence on the dynamics and if λ is already comparatively large, the damping effect of additional membrane viscosity is smaller. If the membrane viscosity is increased to $Bq = 10$ (purple symbols) the frequency decreases only slightly compared to the former $Bq = 5$. Surprisingly, for even larger $Bq = 20$ (blue symbols) the frequency again increases by a small amount. The effect of λ and Bq on the amplitude in figure 5.4(b) is a clear increase with increasing viscosity of the inner fluid or the membrane. The difference in amplitude compared to the former discocyte results (orange symbols) is due to the spheroid reference shape, discussed in section 5.3. The mean RBC position in direction of the y channel axis is shown in figure 5.4(c). The increase in λ as well as Bq has an ambiguous influence on the position of the cell in the channel. The significance of the comparison to the experimental measurements will be detailed in section 5.5 below. In contrast to the earlier results without membrane viscosity it is now possible to reach higher velocities for $\lambda = 20$ in simulations. As a side effect the damping of the slipper dynamics due to the membrane viscosity leads to better numerical stability of the RBC moving through the channel.

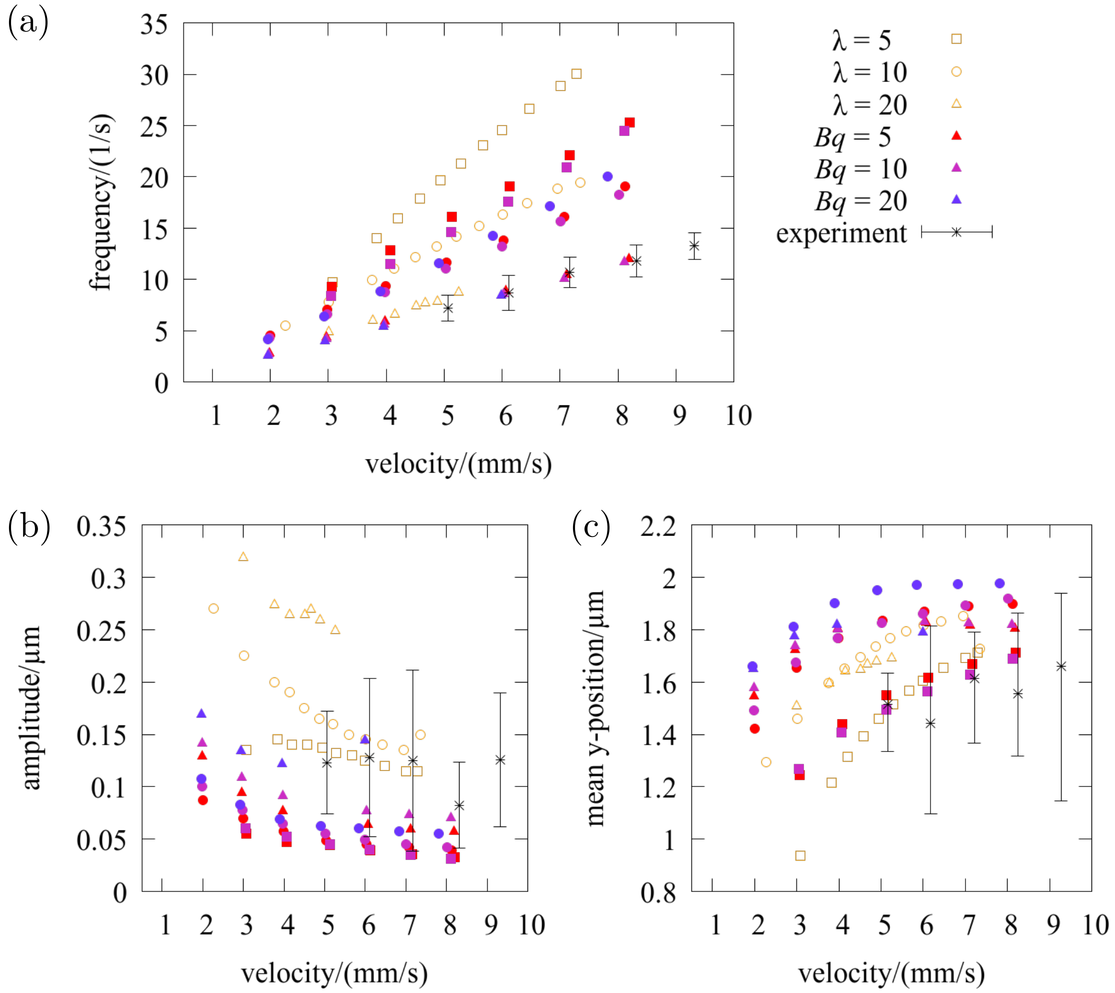

Figure 5.4: Dynamics of the slipper red blood cell state with membrane viscosity. The (a) frequency, (b) amplitude and (c) offset from the channel centre in y-direction of the slipper's centre of mass oscillations. Different symbols (squares, circles, triangles) are used for different viscosity contrasts λ. Simulation results for $Bq = 5, 10, 20$ are drawn in red, purple and blue, these have an oblate spheroid shear reference. Simulation data for $Bq = 0$ (orange symbols) and experimental data (black symbols) in (a,b) is reproduced from figure 3.5 for comparison, the respective data (orange, black symbols) in (c) is reproduced from the joint publication [62].

It must be noted that if the membrane viscosity is increased further to e.g. $Bq = 40, 60$ all slippers vanish and instead cell shapes classified as *others* [17, 62] emerge.

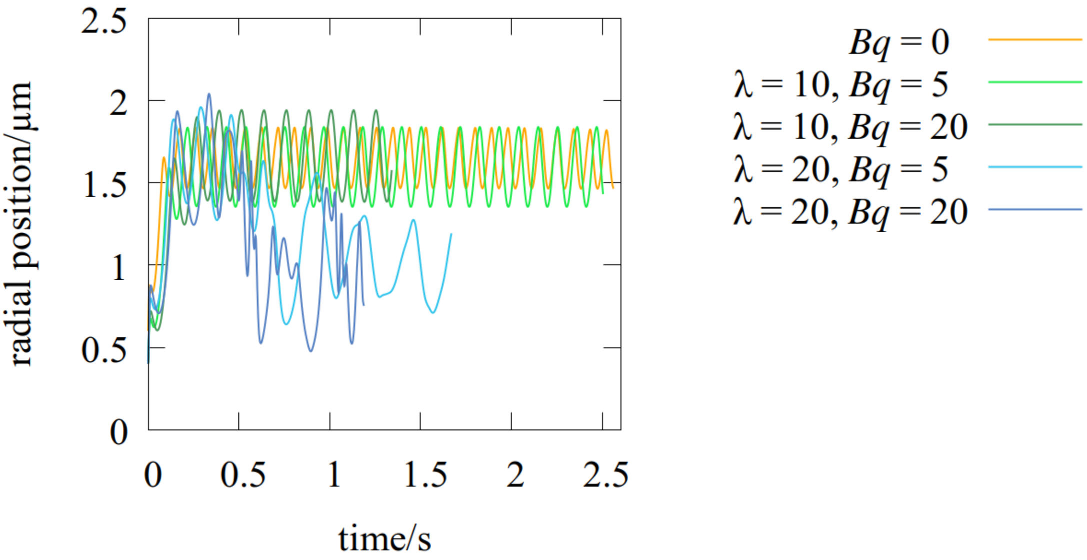

Figure 5.5: Trajectory of the red blood cells with membrane viscosity and discocyte reference shape. The reference curve for $\lambda = 10$ without membrane viscosity from figure 5.3(a) is repeated in orange. The green curves show the trajectories of the RBCs if membrane viscosity $Bq \neq 0$ is used. For larger $\lambda = 20$, the trajectories are drawn in blue.

5.4.2 Differences in case of discocyte shear reference shape

The previous section discussed the slipper dynamics of RBCs with oblate spheroid reference shape. If for the shear reference shape instead the discocyte is used, this leads to the trajectories shown in figure 5.5. For $\lambda = 10$ with membrane viscosity the oscillation frequency is nearly equal to the former result (orange curve) and the amplitude of the oscillation slightly larger. If, however, the viscosity contrast is increased to $\lambda = 20$ in the presence of membrane viscosity, the RBC starts to deform violently while moving through the channel (blue curves). Already for $Bq = 5$, the RBC is no longer clearly distinguishable as slipper shape and in experiments would be classified as type *other*. Similar trajectories were not observed in the analysed experimental data set. It should be noted that due to the uneven movement of the RBC membrane, including the formation of localised wrinkles on the surface for these large viscosity values (blue curves), the exact trajectory in simulations depends on the details of the cell's triangulation. This is similar to the effect observed in figure 4.2.

The source of the jerking movements at high viscosity in figure 5.5 is the combination of the large restoring forces due to the reference shape, analogously to the explanation at the end of section 5.3.3, and the viscous contributions which would slow down the movement.

5.5 Discussion of the experimental evidence

5.5.1 Methods to extract the dynamic cell characteristics

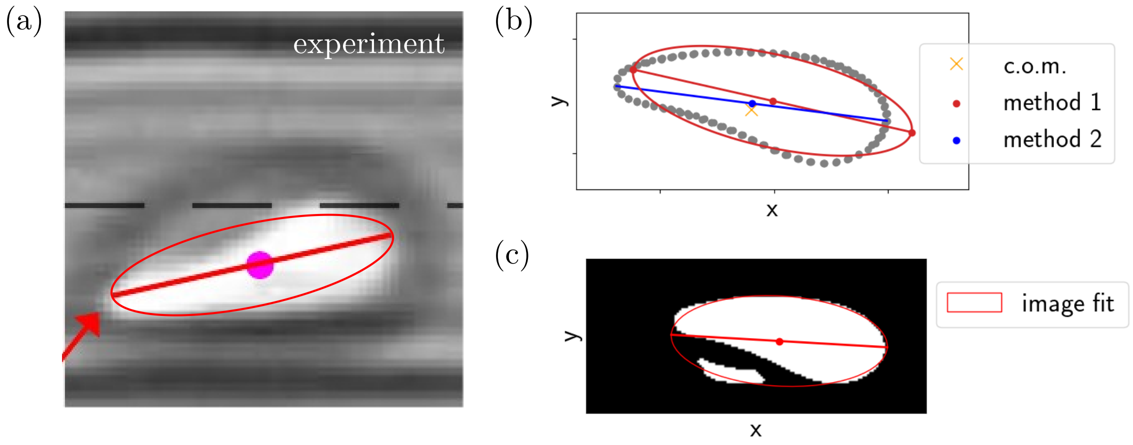

Figure 5.6: Fitting procedures to extract cell trajectories. (a) Ellipsoidal fit (red) to the experimental image. (b) Two fitting methods (in red and blue) to the cell contour (gray dots) from simulations. The coloured points mark the respective result for the centre of mass (c.o.m., exact position marked by orange cross). (c) Image fit for the centre of mass computation based on the visualisation of the simulation result. Note that the cell in the simulation flows in the upper half of the channel. Experimental image provided by S. M. Recktenwald (member of the group of C. Wagner in Saarbrücken).

The comparison between experiment and simulation results in figure 5.4(a) shows that if an oblate spheroid is used as shear reference, a large viscosity contrast $\lambda = 20$ leads to slipper frequencies which fit the experimental measurements. In addition, as figure 5.4(b) shows, in contrast to former studies [62] the amplitude of the oscillation also lies within the experimental measurement error. The mean channel position in simulations is slightly larger than expected from experimental results (figure 5.4(c)). In general, comparison of the frequencies is more reliable than that of amplitude and position. Measurement errors of the channel dimension on the micrometer scale and the fitting procedure for the centre of mass movement have no or only negligible influence on the frequency measurement. In the following, it will be discussed that the deviation in the amplitude and position comparison can be explained by the fitting procedure which is used to extract the experimental trajectories.

For evaluation of the experimental data an ellipse is fitted to the cell images as shown in figure 5.6(a) for every recorded time step. Then the position of its centre as well as the ellipse length (major axis) can be extracted and plotted over time. From the resulting trajectory, frequency, amplitude and position are extracted, together with the ellipse length. These results are compared in figure 5.4 to the simulation results, which are based on the exact centre of mass movement. Especially for the amplitude and position the exact centre of mass movement of the ellipse might differ from what is extracted from the image data. To investigate this and thus the reliability of the comparison, different fitting methods for the simulation data are discussed in the following. The frequency is expected to be identical to the conventional centre of mass calculation, while the amplitude and mean position of the cell oscillation are expected to differ from it, depending on the calculation method. It will be shown that this is indeed the case.

The first approach is based on the numerical information of the cell contour points plotted in figure 5.6(b). The cell is sliced in half along a plane perpendicular to the z-axis in the channel centre and the resulting contour (gray points) is extracted from the cell surface nodes in the vicinity of this plane. Method 1 (red curve) fits an ellipse to these points with the least squares method, the central point of the ellipse is taken as centre of mass. Method 2 (in blue) takes the leftmost and rightmost contour points and determines their mid-value. The orange cross in figure 5.6(b) for comparison shows the result from the exact centre of mass computation in simulations. For an exemplary simulation at approximately $8\,\mathrm{mm\,s^{-1}}$ the resulting trajectories for both methods are shown in figure 5.7.

Figure 5.7(a) shows the position in y-direction of the centre of mass according to method 1 on the left (red curve) and method 2 on the right (blue curve). Method 1 produces a regular curve while the trajectory from method 2 is very noisy. However it can be smoothed using an appropriate Savitzky–Golay filter which produces the black the curve overlaying the blue one, where the frequency is again clearly visible. Both fitting methods lead to similar mean y-position values which are larger than the conventional centre of mass results (orange curve) from simulations. For the length oscillations in 5.7(b) method 1 produces more noisy data, which can also be smoothed, and method 2 gives the smoother trajectory. In addition, method 2 here leads to a visibly smaller estimate for the mean cell length than method 1. For both position and length oscillation as a matter of course the noisy method leads to a larger amplitude estimate, indicated with horizontal gray lines in figure 5.7.

The second approach to extract the slipper oscillation is depicted in figure 5.6(c). It is based on a visualisation of the simulation results in Paraview, mimicking the experimental image data used for fitting. The cell form is converted to a greyscale image, binarised and then fitted with an ellipse. The y-position and length oscillations resulting from this procedure are shown in figure 5.8(a,b) together with an estimate for their respective amplitudes (horizontal dashed lines). Again the fitting method leads to a larger estimate for the offset than the conventional centre of mass data (orange curve) gives, but the difference is smaller than for the two other methods above. The mean length estimate is similar to that of method 2 in 5.7(b), but its amplitude is much less accurate. The second approach - image fitting - is concep-

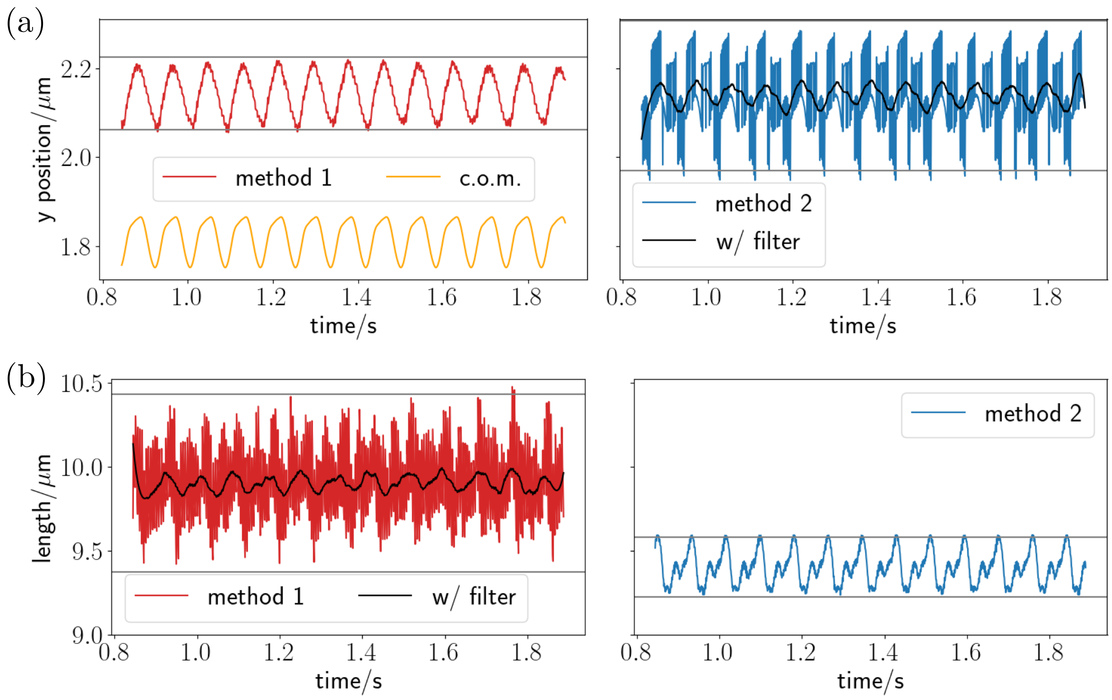

Figure 5.7: Oscillation detection from simulations with contour fitting methods. Oscillation of the (a) cell position and (b) cell length from method 1 (left column, red) and method 2 (right column, blue) from figure 5.6(b). The centre of mass (c.o.m.) curve is plotted in orange for comparison. Gray horizontal lines indicate the extracted amplitude. The simulation parameters are $\lambda = 20$, $Bq = 5$ and $\bar{v} = 8\,\mathrm{mm\,s^{-1}}$.

tionally closest to the experimental data analysis method and indeed compares good to the experimental oscillation characteristics, as shown in the following section.

5.5.2 Positional and length oscillation characteristics for different methods

Figure 5.9 shows the result of the fitting approaches presented in section 5.5.1, applied to the simulations at $\lambda = 20$ from section 5.4.1. For comparison, the former results from figure 5.4 in that section are repeated in figure 5.9 together with the experimental measurement results. The amplitudes extracted via the image fitting method and the two contour fitting methods scatter broadly in an irregular fashion and have on average larger values compared to the former results. Figures 5.7 and 5.8 show that the amplitude can only be roughly estimated with the fitting approaches. This can be an explanation for the observed experimental amplitude range, which is also based on image fitting. Regarding the mean cell position, fig-

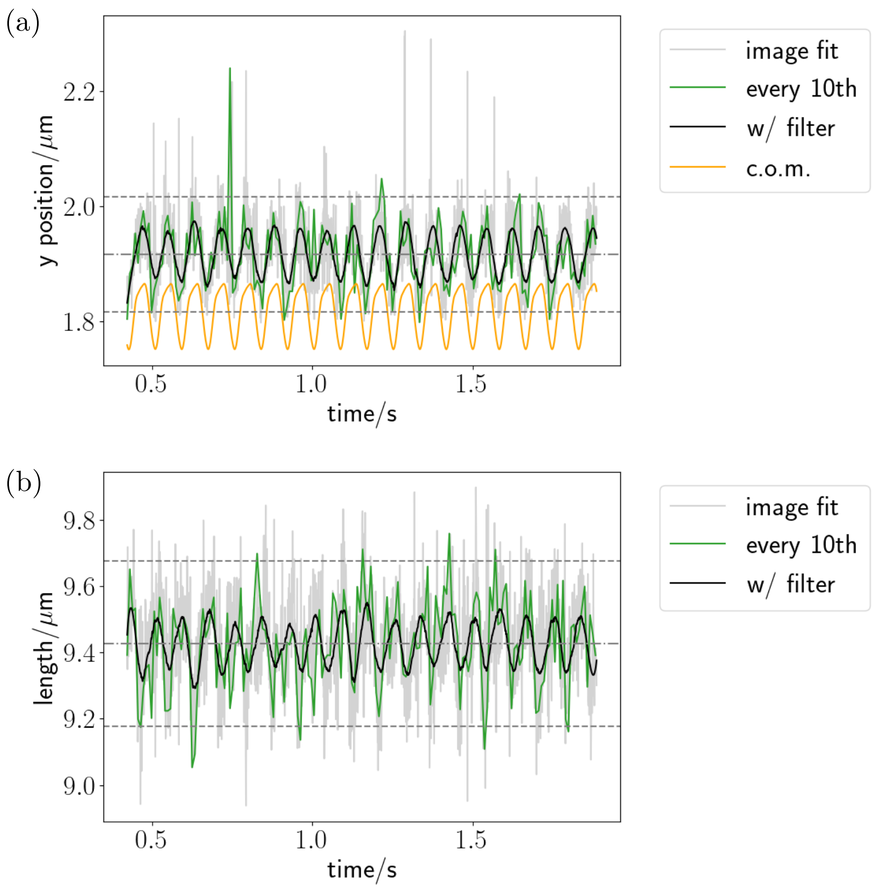

Figure 5.8: Oscillation detection from simulations with an image fitting method. Oscillation of the (a) cell position and (b) cell length from the image fit in figure 5.6(c). The centre of mass (c.o.m.) curve is again plotted in orange for comparison. Gray dashed lines indicate an estimate for the amplitude drawn by eye. The data is from the same simulation as in figure 5.7.

ure 5.9(b) shows that the image fitting overestimates the centre of mass position as was already observed in section 5.5.1 and is larger than the experimental y-position measurement. Here, two points must be made, which can explain the experimental mean cell position and its broad scattering. First, it is very difficult to determine the exact channel wall position in the experimental images, a variable, however, to which the position measurement is very sensitive. Second, in contrast to the simulation, the experimental microchannels are not constant in cross section along their length but are wider at the entrance due to the pressure drop applied along the channel. In addition, the measurements of the channel dimensions have a measurement error, leading to discrepancies between real channel size in experiment and numerical chan-

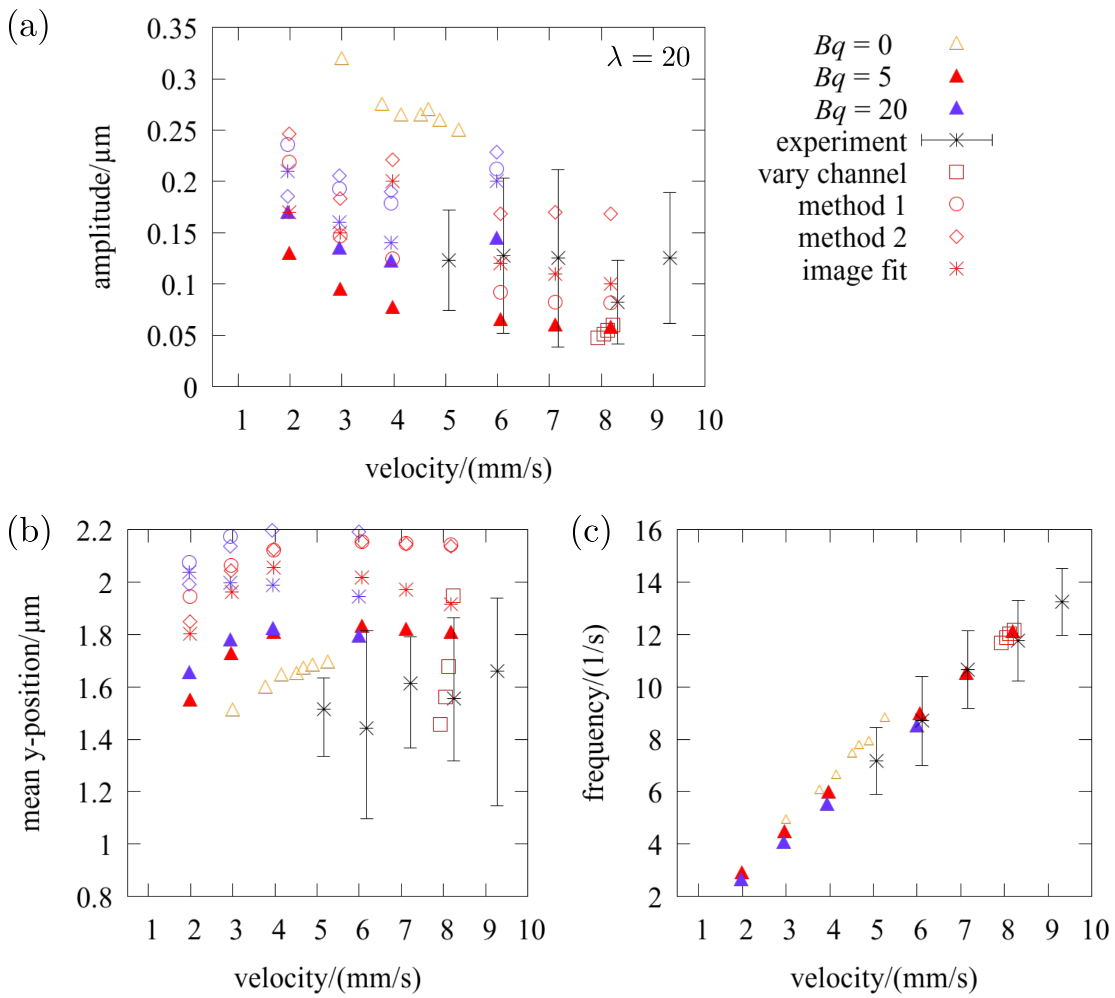

Figure 5.9: Dynamic cell characteristics from different fitting methods. (a) Amplitude, (b) mean y-position and (c) frequency of the slipper oscillation. The results for different Bq at $\lambda = 20$ are repeated for comparison from figure 5.4 (triangle symbols) together with the experimental results. Red square symbols show simulation results for exemplary variation of the channel dimensions. The results from the different fitting approaches are added. The respective Bq is indicated by the color of the symbol.

nel size in simulations and thus deviations in the slipper dynamics of these two. To support this second claim, simulations can show that the slipper mean positions are not robust against changes of the channel dimension in y-direction. In figure 5.9 red squares mark simulations with channel widths $W = 10\,\mu\text{m}$, $10.5\,\mu\text{m}$, $11\,\mu\text{m}$, $12\,\mu\text{m}$ compared to the standard $W = 11.5\,\mu\text{m}$. This is in line with the experimental spread of the channel widths, compare section 3.2. Here the simulation evaluation is again based on the centre of mass results, not on the image fitting. Figure 5.9(b) shows that indeed the channel width crucially influences the mean cell position. Changes in W, however, have negligible influence on amplitude and especially the frequency as figure 5.9(a,c) shows. Note that all fitting approaches presented in section 5.5.1 lead to the same frequency, as expected, and are therefore not included in the frequency plot.

To conclude, the contour and especially image fitting methods can explain the scattering of the amplitude results in the experiment. Deviations in the mean cell position in the simulation results can be explained by variations in the experimental channel size. The parameter values used here for λ and Bq therefore lead to results which agree with the experimental measurements of the slipper dynamics in the microchannel. The frequency measurement is best suited for detailed comparison as it is less prone to systematic errors due to channel variations or data analysis methods.

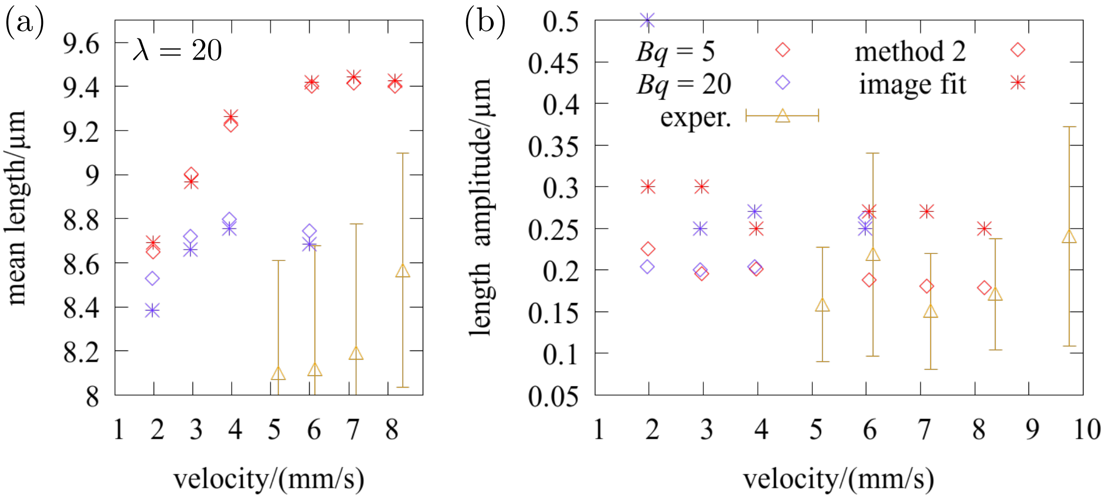

Figure 5.10: Dynamics of the slipper length oscillation. (a) Mean cell length and (b) amplitude of the length oscillation at different velocities for $\lambda = 20$ in comparison with experimental results (orange triangles). Two different fitting methods are used (diamond and asterisk shapes). Colours indicate the size of Bq. Experimental data provided by S. M. Recktenwald (member of the group of C. Wagner in Saarbrücken).

The results for the length oscillation analysis are summarised in figure 5.10. Method 2 and the image fitting lead to similar results for the mean length of the slipper but the image fit overestimates the length amplitude. In general, the experimental results for the slipper length in figure 5.10(a) lie clearly below the simulation estimates. Revisiting the length estimation methods shown in figure 5.6 above well explains this systematic deviation. The experimental image shows a fuzzy cell outline where the cell ends are not captured by the fitted ellipse, while the simulation fitting routines include the cell ends. Regarding the length amplitude, the results of method 2 agree well with the experimental results. Provided that the simulation model indeed captures the experimental setup correctly, this means that although conceptionally closest to the experimental analysis, the image fit in this case fluctuates more strongly around the cell shape than the experimental one does, compare figure 5.6. Looking at figure 5.8(b) it becomes clear that this amplitude is a approximate guess which might indeed overestimate the amplitude.

5.5.3 Statistics of the slipper oscillation occurrence

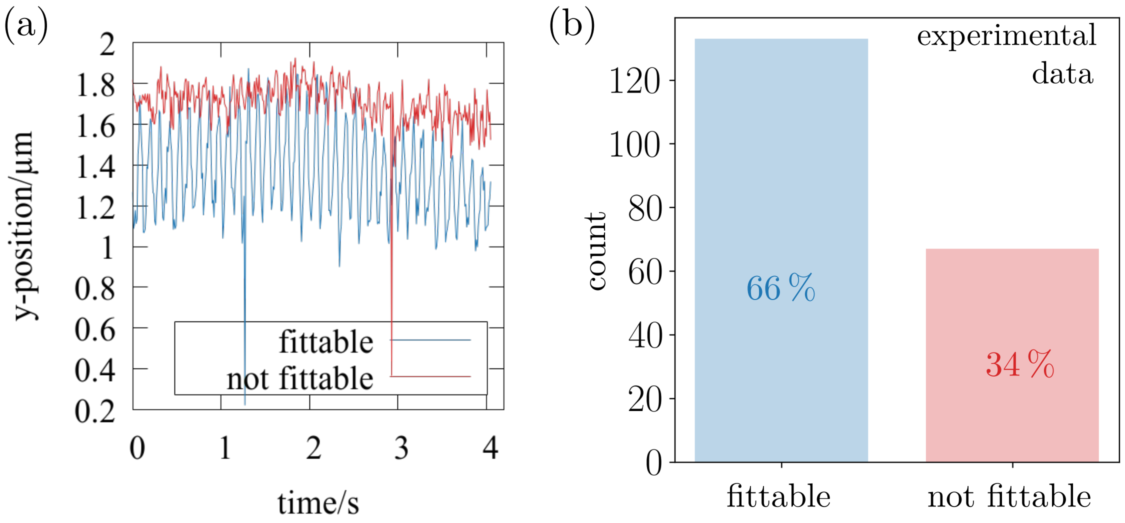

Figure 5.11: Slipper oscillation occurrence in experiments. (a) Examples of slipper cells whose trajectory allows or does not allow extraction of frequency and amplitude in blue and red, respectively. (b) Absolute number and percentage of these in the experimental measurements. The fittable data in the blue area contains all results presented in figure 3.5(a,b) and repeated in 5.4, 5.9. Experimental data provided by S. M. Recktenwald (member of the group of C. Wagner in Saarbrücken).

In experiments not all oscillating slippers allow the extraction of the frequency and amplitude. Two examples are shown in figure 5.11(a). If the positional oscillation has a small amplitude (red curve), due to experimental noise and the image processing error it might not be possible to fit a sinusoidal curve to the measurements. This is the case for about one third of all measurements, as figure 5.11(b) shows. Note that at least for this number of measurements, this ratio does not depend on the cell velocities and is similar if the measurements with larger outer viscosity from chapter 3 are analysed. Parameter combinations which in simulations were shown to lead to small amplitude oscillation, e.g. low Bq values in figures 5.4 and 5.9, might therefore not be reflected in experimental results due to this unavoidable limitation.

5.6 Phase diagrams

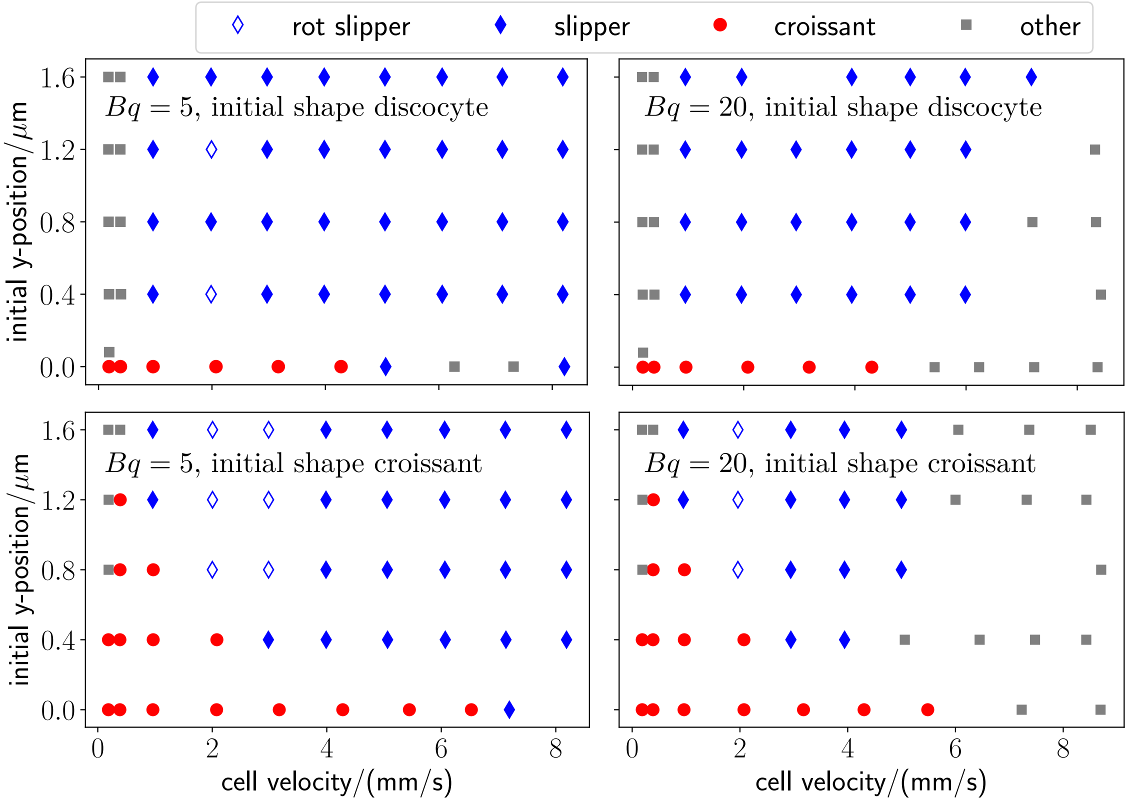

Figure 5.12: Phase diagrams of red blood cells in channels with membrane viscosity. The diagrams are obtained from simulations with $\lambda = 20$ for different initial shapes and different Bq.

In this section the simulation phase diagrams for different initial shapes and different Bq are presented in figure 5.12. All these simulations used the oblate spheroid reference and $\lambda = 20$. Slipper shapes are observed predominantly at higher velocities and for more off-centred initial cell positions in the channel. A croissant peak at smaller velocities near $1\,\mathrm{mm\,s^{-1}}$ is observed only for initial croissant shape. The phase diagrams show the same general features as earlier work without membrane viscosity for $\lambda = 5, 10$ [62] and in a slightly larger channel for $\lambda = 5$ [17]. One interesting difference, however, is the emergence of shapes classified as *others* at larger cell velocities for larger membrane viscosity $Bq = 20$. In section 5.4 it was remarked that if the membrane viscosity is increased further to $Bq = 40, 60$, only cells which are classified as ‘others’ are observed in simulations. As the experimental measurements of Bq collected in table 4.1 do not rule out such large values, cells, whose membrane is very viscous, contribute to the considerable fraction of *others* observed in experimental phase diagrams as shown in figure 3.1(b). Former numerical studies without membrane viscosity [17, 62] did not observe this substantial amount of RBCs classified as *others*.

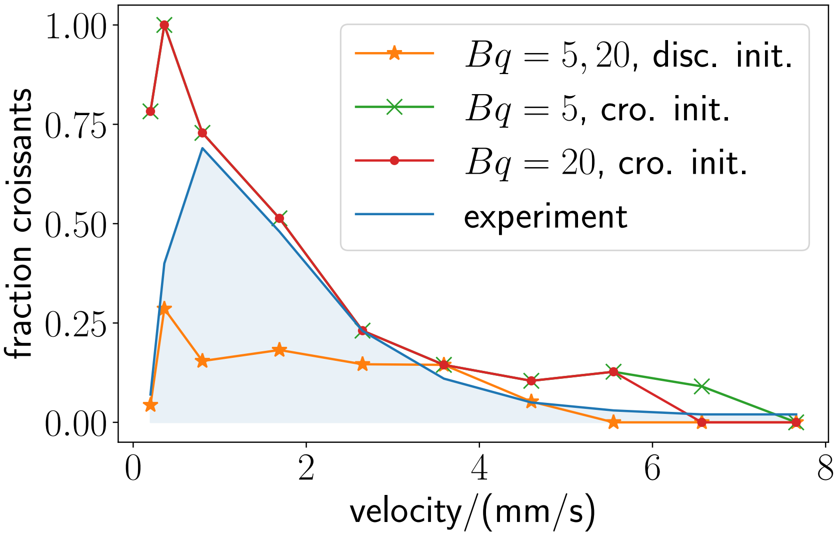

Figure 5.13: Fraction of croissants in experiment and simulation. The phase diagrams in figure 5.12 are combined with the experimental entrance distribution to obtain an estimate of the fraction in simulations. The curves for both Bq and discocyte initial shape (in orange) coincide, those for croissant initial shape differ for larger velocities (in green and red). The connecting lines serve as guide to the eye. Evaluation of the fraction is done at the experimental mean velocities for which the entrance distribution was measured. The experimental curve (in blue) is reproduced from figure 3.1(b), it is identical to the border of the croissant region.

Guckenberger et al. [17] used experimental results for the initial shape distribution in microchannels to convert the information from the phase diagram 5.12 into an estimate of the croissant fraction at different velocities in simulations. The results for the microchannel used in this chapter are presented in figure 5.13. The border of the croissant phase in figure 5.12 is identical for the two diagrams in the first line. The two diagrams for initial shape croissant (second line) differ only at larger velocities. Therefore, when the phase diagrams in 5.12 are folded with the experimental entrance distribution, the first two diagrams can be summarised in figure 5.13 in one line (orange) and the other two (green and red curves) coincide, except for at larger velocities. Below $3\,\mathrm{mm\,s^{-1}}$ with the discocyte initial shape, simulations predict less croissant shaped cells than observed while for the initial shape croissants only below $1\,\mathrm{mm\,s^{-1}}$ simulations predict a different fraction, in this case more croissants. For velocities from around $1\,\mathrm{mm\,s^{-1}}$ the results from simulation and experiment agree excellently. The initial shape cannot be observed in experiments and the overall agreement is satisfactory. The croissant peak in the experimental phase diagram lies at approximately $1\,\mathrm{mm\,s^{-1}}$, similar to experiments from an earlier study [17] in a slightly larger channel geometry. The authors of this earlier study, however, found that in the *simulation* phase diagrams the croissant peak was at cell velocities larger than $1\,\mathrm{mm\,s^{-1}}$. In order to elucidate the reason for the difference, simulation of RBCs with membrane viscosity are carried out in the larger channel from [17]. The results show a croissant peak shifted to the smaller velocity values of around $1\,\mathrm{mm\,s^{-1}}$, which suggests that the difference is indeed due to the additional membrane viscosity. The phase diagram in this larger channel is included in appendix C.

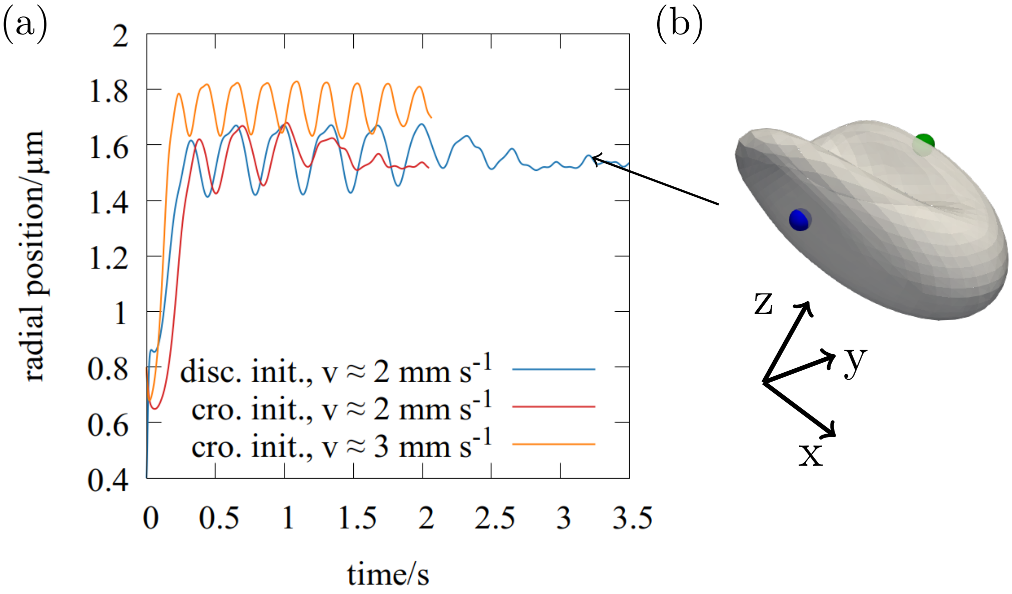

Figure 5.14: Rotated slippers in the microchannel. All simulations have $\lambda = 20$ and $Bq = 5$. (a) The rotation behaviour depends on the initial shape and the cell velocity. (b) Example shape of a rotated slippers whose dimples (in blue and green) are located at the outside of the cell.

Another type in the phase diagram is the rotated slipper, typical trajectories are shown in figure 5.14(a). After an initial phase of regular slipper oscillation, which allows the extraction of the amplitude, the oscillation ceases. The cell still shows the usual slipper shape but the dimples of the cell are then rotated to the outside, as shown in figure 5.14(b). For the regular slipper movement, the dimples follow the tank-treading of the slipper as illustrated before in figure 3.7(a) with the full shape shown in figure 3.3(b). The trajectories in (a) show that the croissant initial shape transitions quickly to the rotated slipper (red curve) but the transition begin is retarded if the cell flows faster (orange curve). The phase diagram in figure 5.12 shows that overall only few rotated slippers are observed and their number decreases if Bq is larger, possibly due to the dampening effect of the increased viscosity. If the initial shape is a croissant, there are a few more rotated slippers.

Note that for simulations without membrane viscosity and with discocyte reference shape rotated slippers occur in most simulations during the simulated time as was discussed in the joint publication [62]. In addition, there the dimples were almost perfectly centred at the two sides of the cells while the rotated slippers shown here sometimes have dimples which move irregularly along the sides of the cell during the tank-treading. A plausible explanation for this observation is that for the oblate spheroid shear reference the dimples are no longer distinguished by the stress-free shape but only by the bending reference shape and thus their exact position is less strongly coupled to the determinants of the cell deformation.

The rotated slippers show very small amplitudes and are potential candidates for the large fraction of not fittable cells in experiments from section 5.5.3. An argument against it, however, is that the these occur independent of the velocity while rotated slippers are observed at smaller velocities.

5.7 Conclusion

	$Bq = 0$	$Bq \neq 0$
discocyte shear ref.	• section 3.4 • f exceeds measurements ($f \gg f_{\text{exp.}}$)	• section 5.4.2 • irregular trajectories
obl. spher. shear ref.	• section 5.3.3 • small amplitude oscill. (smaller than exp. noise)	• section 5.4.1 • **matches exp. results**

Table 5.2: Overview of the investigated parameter combinations. The two different shear reference shapes discocyte and oblate spheroid in combination with simulations which exclude ($Bq = 0$) or include ($Bq \neq 0$) membrane viscosity are discussed in the section listed in the table. The second point in each case summarises the main result regarding the compatibility with experimental measurements.

The effect the membrane viscosity in the RBC model has on the slipper dynamics is closely linked to the respective shear reference shape of the cell. In table 5.2 the different investigated parameter combinations are listed. For all these combinations results regarding the slipper oscillation dynamics were presented in the sections listed in the table. For the first case, the frequently used combination of a discocyte reference shape without membrane viscosity, slipper frequencies were clearly above the experimental measurements. If membrane viscosity of a certain strength is included, this leads to irregular oscillations of the slipper cell. In the second line in table 5.2 the two cases for the oblate spheroid reference shape are listed. For negligible or zero membrane viscosity $Bq = 0$ the slipper shows very small oscillation amplitudes. The amplitude, however, increases with increasing Bq until amplitudes comparable to the experiments are reached. For these cells, frequency and amplitude of the slipper oscillation both agree with measurement results.

Note that the scattering of the frequencies and amplitudes in experiments is not only due to the unavoidable measurement error but is also caused by biological variability of the RBCs, for example variations in the interior viscosity or the viscosity of the membrane. The emergence of cells with small Bq, which leads to small amplitudes, is a possible explanation for the two different slippers categories observed experimentally. These are the regular and the non-fittable slippers discussed in section 5.5.3. This would mean that the experimental data does not consist of two clear-cut categories but instead a continuum of different amplitudes where some are too small for fitting a sinusoidal curve, due to the unavoidable measurement noise. The trajectory in section 5.5.3 shows an example which supports this hypothesis. There the amplitude of the non-fittable experimental curve is within or only slightly below the amplitude error bars in section 5.4.1, figure 5.4(b).

The phase diagrams for this most plausible parameter combination were presented in 5.6. They are consistent with the experimental phase diagrams, similar to earlier simulation studies. In addition, they can explain the large fraction of RBCs which are classified neither as slipper nor as croissant shapes in experiments at larger velocities. The comparison of the slipper dynamics and especially the frequencies is, however, the more promising approach.

6 Red blood cells with membrane viscosity in different applications

6.1 Cell stretching in optical tweezers

6.1.1 Introduction

In simulation studies, results for RBCs stretched in optical tweezers are frequently used for the purpose of model validation. In these cases the static deformation of the RBCs is compared with experimental measurements. The RBCs in experiment are stretched by attaching microscale beads to the cell which are then pulled apart with optical tweezers. More recently the time-dependent behaviour of the deformation has been investigated for RBC models which include membrane viscosity. In this section tweezer simulation results for RBCs are presented and discussed with regard to results from the literature. After a short literature overview in 6.1.2, details of the implementation are presented in 6.1.3. Finally in sections 6.1.4 and 6.1.5 the results are compared and discussed.

6.1.2 Literature overview

6.1.2.1 Experiments

The experimental data of RBCs stretched with optical tweezers comes from two papers, both around twenty years old. Mills et al. [55] fix the RBC between two beads, one held in place and the other one moved by the force F. A simulation model which mimics this setup is shown in figure 6.1. In simulations this is mimicked by applying F at the one and F at the other end of the cell and stretching it symmetrically. The experimental study by Mills et al. [55] includes example images of the resulting cell shapes. Experimental data for axial and transversal diameter of the stretched cell for different forces is presented in the study. In addition an exponential fit for the relaxation of the RBCs is provided, the calculated time constant is 190 ms. The authors in addition present simulations with the Abaqus software. The cells are fixed to the beads at a circular region of diameter 2 µm and then stretched. In this state they exhibit a peculiar bisection, dented in at the position of the cell dimples. Note that the paper is an extension and correction of older work from the same group [133], where a problem with the tweezer calibration occurred. The second main experimental paper for this problem by Suresh et al. [134] is a study of infected RBCs, where measurements of healthy RBCs are presented as control group. No detailed method description is given but references are made to the method by Mills et al. [55]. The results differ slightly from the first study as will be shown below, but lie within the limits of the error estimates. Complimentary FEM simulations agree very well with the authors results. Earlier tweezer experiments by Hénon et al. [135] disagree with the results discussed so far even for small forces, possibly due to disadvantages in the image acquisition. For the relaxation time, however, a similar result of $\tau = 206\,\text{ms}$ is obtained [135]. Regarding the RBC relaxation time, Bronkhorst et al. [136] present experiments where the RBCs are bended with three optical traps, not stretched. The measured time constants for the relaxation range from 100 ms for young to 300 ms for old cells.

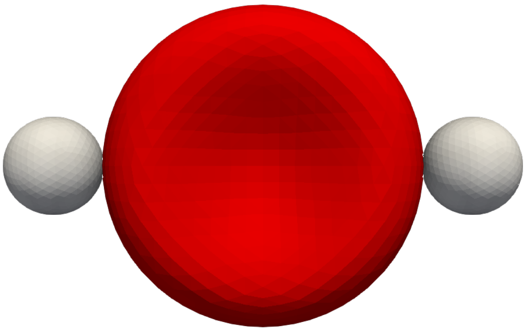

Figure 6.1: Illustration of the red blood cell stretch with (optical) tweezers. Example of a simulation model with two beads attached to the cell. The RBCs are stretched by applying a force on the two attached beads.

6.1.2.2 Simulations

Simulation studies use different approaches to model the tweezer experiment. Li et al. [137] perform FEM and MD simulations for a spectrin microstructure model. In their model the stretching forces act on the two opposite ends of the cell on all vertices above a fixed distance to the centre at the beginning of the simulations, in total on 10% of all vertices. The resulting cell shapes show protuberances at the cell ends, different to the experimental images. The long axial diameter, however, fits the experimental results [55] very well but the smaller transversal diameter is overestimated in the simulation. Pivkin et al. [138] use a coarse-grained model for the RBC and the same setup, i.e. 10% of all nodes are subject to the stretching force. The results very slightly underestimate the axial elongation from Mills et al. [55] and again overestimate the transversal one. As in Mills et al. [55] the simulations show a peculiar bisection. Walsh et al. [139] simulate RBC tweezers by applying a force on in total 4% of all vertices which mimics a contact region between cell and bead of radius 1 µm. The contact radius decreases during stretching which is consistent with experimental observations [55]. As before the axial deformations agree very well, the transversal is overestimated and the cells have pronounced protuberances at the ends. Fedosov et al. [140] apply a force on the two opposite ends of the RBC and on 2% of all nodes per side. In their model this is again equivalent to a contact region of radius of 1 µm. In the stretched state, contrary to the experimental results [55], the cell shows protuberances at the ends which contribute to the axial diameter calculation. Notwithstanding this additional contribution, the comparison with the experimental data [134] shows very good agreement in the axial diameter and good agreement in the transversal diameter up to 200 pN. Krüger et al. [141] present RBC stretching results up to a force of 90 pN. No information about the implementation is given, but the cell images suggest that a contact radius comparable to the experimental setup is ensured by cutting off or flattening the cell ends. The results are in excellent agreement with the experimental data [134]. This suggests that the details of the implementation have a crucial effect on the results, as the study by Fedosov et al. [96] also achieved very good agreement although the cell ends, which have decisive effect on the axial length estimate, have an entirely different shape. Guglietta et al. [25] fix two beads to the cell which leads to a contact radius of approximately 1 µm and apply a force on both beads. The cell deformation is plotted up to a force 90 pN, it is in very good agreement with the experimental data [134]. This paper [25] is the first tweezer simulation study which includes membrane viscosity of the RBC. In addition, time-dependent curves of deformation and relaxation for different membrane viscosity values are given. The authors compare their relaxation results for different membrane viscosities with relaxation times from the literature. Sigüenza et al. [142] finally argue that previous simulations often produced peculiarly deformed shapes because elasticity laws, which violated area conservation, were used. The author also present RBC stretching simulations for which they control the contact area. They show that the crucial parameter for the RBC deformation in these experiments and simulations is the contact radius, compare also appendix D. Moreover the authors argue that stress-free shape has little influence on the deformation behaviour.

6.1.3 Implementation

The implementation of the tweezer system is done within the framework of the BIM described in chapter 2.3. The surface of the RBC is discretised with 2048 triangles with the elastic moduli $\kappa_\mathrm{S} = 5 \times 10^{-6}\,\mathrm{N\,m^{-1}}$, $\kappa_\mathrm{B} = 4 \times 10^{-19}\,\mathrm{N\,m}$, reference curvature $c_0^* = 4$ and an oblate spheroid of aspect ratio $\tau = 0.9$ as stress-free shape. The Boussinesq number (4.63) is defined with respect to the RBC radius R. Different values for λ and Bq are used for the tweezer simulations in this section. The value of the membrane viscosity was restricted to $Bq \leq 20$ because larger values no longer lead to slipper-shaped RBCs in microchannels as discussed in the previous chapter.

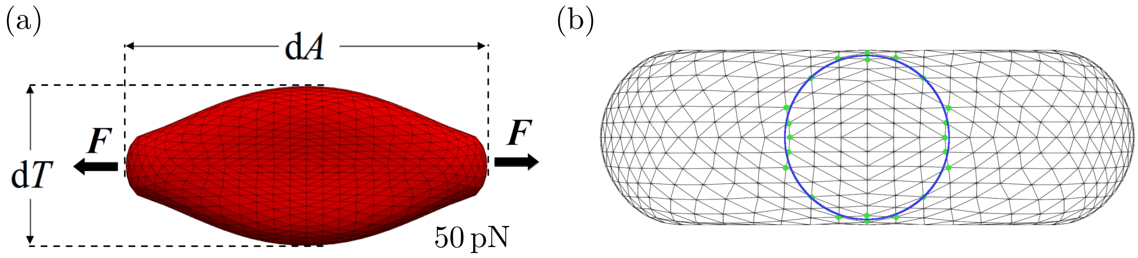

Figure 6.2: Details of the tweezer implementation. (a) Exemplary shape change for 50 pN. In simulations forces at the opposite ends are used to stretch the cell. (b) Sketch of the contact region, here with diameter 2.4 µm marked in blue. Stretching forces are applied on nodes near the contact radius (green points).

In simulations the beads attached to the RBC in experiments are not model explicitly but instead forces are applied directly on selected cell vertices. This approach is sketched in figure 6.2(a). A constant force $\boldsymbol{F}$ is symmetrically applied at two opposite sides of the RBC rim. Under the force the RBC stretches until a steady state is reached. The axial and transversal deformations dA and dT of the RBC are computed as shown in the figure. The forces replacing the beads are modelled such, that the cell shape in the stretched condition resembles the experimental images [55]. The force $\boldsymbol{F}$ at one end is distributed to the cell vertices marked in green in figure 6.2(b). They lie within an annulus on the RBC surface at (1.2 ± 0.1) µm, determined by the contact radius of 1.2 µm (blue line). Not distributing the forces to all vertices within the contact region prevents the cell ends to taper when stretched, which in experiments is prevented by the attached beads. Therefore, in this implementation the circular contact region at the cell end is replaced by a contact annulus.

Direct comparison of the shapes is not possible, as the images in Mills et al. [55] are contracted in axial direction due to the viewing angle of the microscope for which the authors have to correct for in the data analysis. However, the experimental images show that the final contact diameter significantly decreases with increasing stretching force, which the simulation setup implemented here also reproduces. The procedure to estimate the size of the experimental contact diameter is shown in figure 6.3. On the left in figure 6.3(a) a sketch visualises how the contact diameter is calculated from the image data. The margins of the cell-bead contact area are identified, marked with a red line, and then the distance is computed using the constant bead size. Estimates of the diameter for all applied forces in the experimental study [55] are listed in figure 6.3(b).

An earlier approach to implement the tweezers tested within this thesis is shown in figure 6.1. Two spherical beads modelled as stiff triangulated capsules (in the BIM

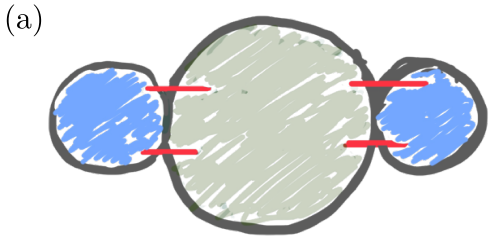

(b)

force/pN	contact diameter estimate/µm
0	2.43
67	1.51
130	1.44
193	1.03

Figure 6.3: Estimate of the size of the tweezer contact region from experiments. (a) A sketch illustrates how the contact diameter is estimated from the experimental images provided by Mills et al. [55]. Red marks are inserted at the margins of the contact region and their distance is calculated by making use of the constant bead size. (b) Size of the final tweezer contact diameter estimated from the experiments [55] for different forces.

code this runs faster than solid spheres) are attached to the cell and pulled apart with force $\boldsymbol{F}$. The cell nodes in the contact region are fixed to neighbouring bead nodes with stiff springs and the contact region is defined by specifying a maximal distance for the connection between bead nodes and cell nodes. There are two disadvantages of this method. First, it is computationally more than ten times slower than the implementation describe above. Second, the contact region is not clearly specified but depends on the combination of bead radius, maximal cell-bead distance and the results therefore indirectly depend on the node grid. Especially the second point is an important aspect in disfavour of this method, because the size of the contact region is crucial for the deformation of the cell.

6.1.4 Results

6.1.4.1 Steady state deformation

In the tweezer simulations forces in the range 5 pN to 200 pN are applied to stretch the cell. The results for the equilibrium axial and transversal deformation are shown in figure 6.4. The axial deformation is for all forces slightly larger than the mean experimental results but still within the experimental error estimation. For forces below 100 pN we find excellent agreement in the transversal deformation. For larger forces, the experimental values plateau while the simulation data continues to decrease. The steady state deformation is not influenced by changes in Bq, because increased membrane viscosity only slows down the dynamics of cell deformation. The same would apply to changes in the interior RBC viscosity, i.e. changes in λ.

The results from two other simulation studies [25, 141] are slightly closer to the experimental axial deformation [134], as shown in the appendix D in figure D.1. These studies, however, did limit the applied forces to below 100 pN.

The initial contact radius of $r_c = 1.2\,\mu\text{m}$ in figure 6.4 is motivated by the estimate

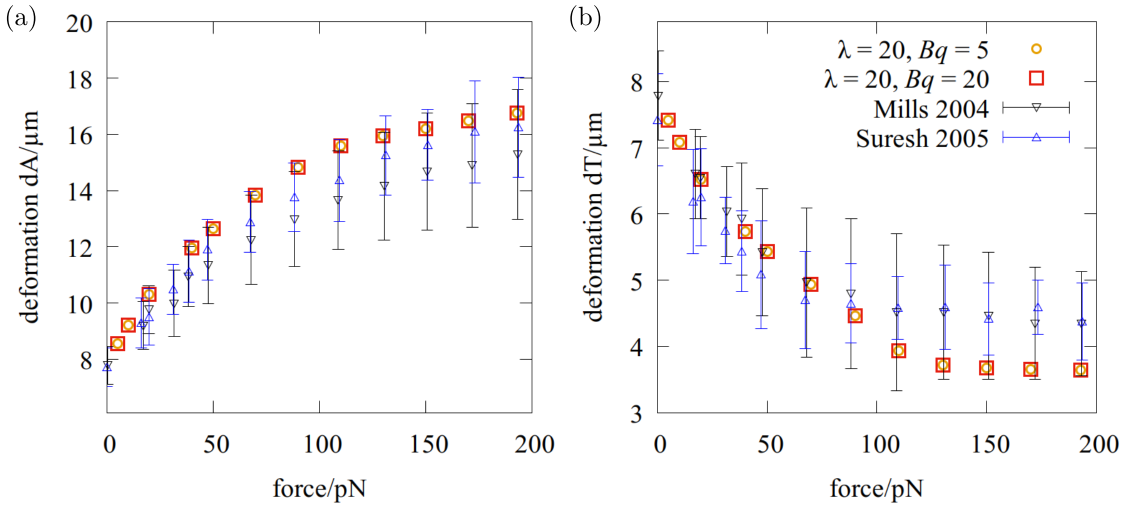

Figure 6.4: Deformation of the red blood cell in tweezer simulations in comparison with experiments. The (a) axial deformation dA increases and the (b) transversal deformation dT decreases with increasing stretching force. Simulation results are shown for viscosity contrast $\lambda = 20$ and membrane viscosities $Bq = 5$ (orange circles) and $Bq = 20$ (red squares) and compared with experimental data from Mills et al. [55] and Suresh et al. [134]. For all simulations the initial contact radius is $r_c = 1.2\,\mu\text{m}$.

in figure 6.3. The choice of the contact radius has distinct influence on the axial deformation dA but little on the transversal deformation dT as shown in appendix D in figure D.2. This is related to an earlier study [142], who for a slightly different simulation setup showed that the size of the beads in the tweezer model have precisely this effect, and also observe that dT is relatively robust to changes in the contact radius.

6.1.4.2 Time dependence of the deformation

While the interior and membrane viscosity do not influence the final deformation of the cell, they do determine the time dependence of the deformation until the steady state is reached. This is shown in figure 6.5 for both axial and transversal deformation. The time-dependent deformations $dA(t), dT(t)$ are normalised with the respective final deformations dA, dT from figure 6.4 and plotted over time. An increase of the internal viscosity or the membrane viscosity, measured by Bq, slows down the deformation process. The tweezer force in comparison has little influence on the deformation speed, as the comparison between the transversal deformation curves for 10 pN and the inset for 70 pN shows. For larger forces the absolute difference between undeformed state and final deformation is larger. For this reason, in the inset in figure 6.5(b) the slight overshooting of the transversal deformation, which is

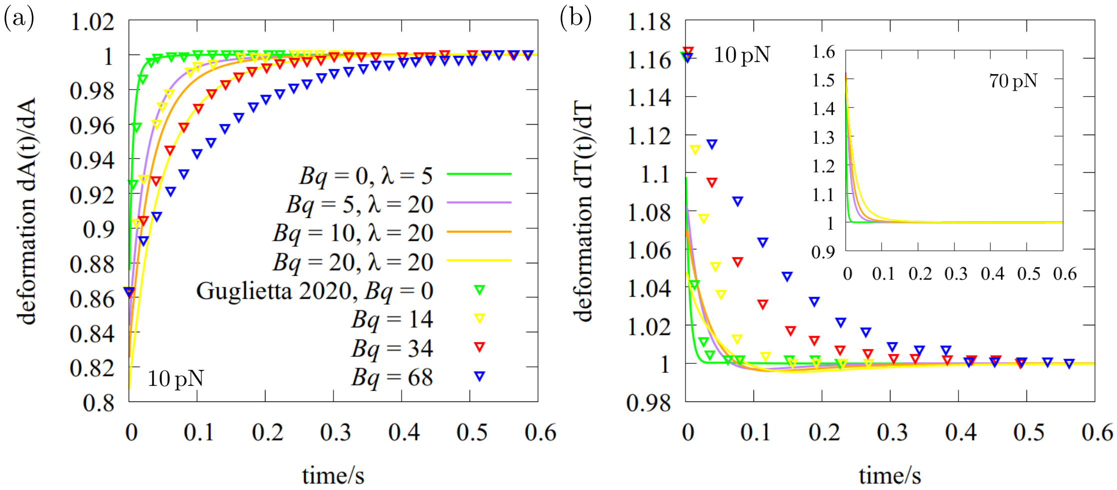

Figure 6.5: Time-dependent deformation in tweezer simulations. The time dependence of (a) axial and (b) transversal deformations relative to the respective final values are shown exemplarily for a tweezer force of 10 pN. Solid lines indicate the simulation results for different λ, Bq. The results from the simulation study by Guglietta et al. [25] are reproduce for comparison (coloured symbols, normalisation added). The inset plot shows the deformation over time for a tweezer force of 70 pN.

due to an additional relaxation of the cell after the tweezer force-induced deformation, is not visible.

For comparison the simulation results from the study by Guglietta et al. [25] are reproduced* in figure 6.5. The authors used $\lambda = 5$ throughout the study and the shear reference shape presumably is a discocyte, see the discussion in 5.3.1. The results without membrane viscosity for $\lambda = 5$ (green lines and symbols) are nearly identical to the axial deformation observed here, and the deformation dynamics is only slightly slower for the transversal deformation. For larger membrane viscosity values the literature values show a clearly slower deformation dynamics. One-to-one comparison was not aimed at and cannot be expected, due to the differences in the cell model and the implementation of the tweezer system.

6.1.4.3 Relaxation behaviour

Also of interest is the dynamics of the relaxation behaviour after the RBC is released from the stretching force and relaxes back to its rest shape. The relaxation behaviour

---

*Data is reproduced from fig. 7 in [25]. Comparison to the previous results therein leads to the conclusion that the results shown are indeed for a force of 10 pN, contrary to the figure caption.

is summarised with the elongation index defined as [55]

$$\Lambda(t) = \frac{[dA(t)/dT(t)]^2 - 1)([dA/dT]^2 + 1)}{[(dA(t)/dT(t)]^2 + 1)([dA/dT]^2 - 1)} \tag{6.1}$$

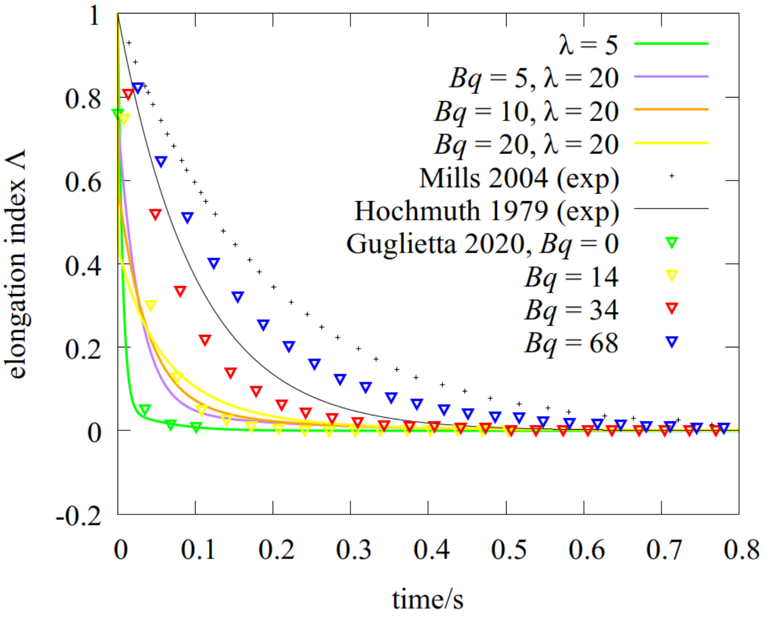

Figure 6.6: Relaxation behaviour of red blood cells released from the tweezer force. The elongation index is compared for RBCs with different interior and membrane viscosity after stretching with 70 pN. Relaxation data from simulation by Guglietta et al. [25] and from experiments by Mills et al. [55] and Hochmuth et al. [113] is reproduced for comparison.

The relaxation behaviour of the cell in simulations is shown in figure 6.6. The coloured solid lines are simulation results for different cell parameters which are compared to results from the literature. The experimental values from Mills et al. [55] are reproduced from a fitted exponential curve therein, single measurement relaxation curves are not provided. Hochmuth et al. [113] provided single measurement curves which, however, collapse nicely on one exponential fit with time constant $t_c = 0.1$, which is shown in figure 6.6 (black line). Note that the authors stretch the RBCs with mircopipettes, not tweezers. No direct experimental measurement data of the RBC relaxation behaviour with tweezers could be found in the literature. Mills et al. [55] and Hochmuth et al. [113] used their relaxation measurements of the elongated RBCs to estimate the size of the RBC membrane viscosity. The results are listed in table 4.1 in chapter 4.7. In both studies these are larger than the values used in the BIM simulations and the simulations by Guglietta et al. [25]. The results of the simulations even for large viscosity values show a faster relaxation than reported in the experiment. The simulation study [25] results reproduced in figure 6.6 for comparison also show much faster relaxation, although for very large $Bq = 68$ the curve approaches the measurement fit (in black). However, as discussed in the previous chapter, for the majority of RBCs Boussinesq numbers around and below 20 are expected.

Note that a shear reference shape discocyte and other parameter changes such as different shear moduli do not lead to different time scales of the relaxation.

6.1.5 Discussion

Different approaches from the literature have been described and are now reassessed, making use of the knowledge gained from the results of the tweezer simulations.

The analysis showed that the combination of contact region between cell and beads, in simulations the size of region where the forces act on the cell, together with the details of the tweezer implementation is decisive for the deformation result. A variety of implementations lead to good agreement with the experimental data, although, depending on the study, the forces act on $4\,\%$ to $10\,\%$ of all cell vertices [137–140]. Furthermore, some cell shapes have pronounced protuberances when stretched [137, 140] while other studies ensure flattened ends in the simulations [25, 141]. The approach used in this work is designed such that the cell shows a shape change during deformation which compares well to the experimental observations. This approach also leads to good agreement in the deformation curves.

In general, the transversal deformation dT can be determined more accurately from experiments than the axial deformation dA, because no beads are attached in that direction. Moreover, the deformation in the transversal direction is more robust to changes in the contact radius.

The relaxation of the cells after release from the tweezer force in simulations was found to be faster than the relaxation fit from one experimental study [55]. Note that in different setups the relaxation of RBCs towards their rest shape might exhibit different relaxation times as for example the relaxation of slipper-like cells in figure 5.1 showed. An overview of experimental relaxation times in different settings, e.g. micropipette aspiration, is given by Guglietta et al. [25].

To conclude, new experimental results for the time-dependent deformation as well as detailed experimental observations of the relaxation behaviour when releasing the stretched cell would be helpful for better comparison with the different simulation approaches. For the validation of an RBC simulation model the tweezer setup is suitable only to a limited extent, due to the scarce experimental data and the variety of implementation details, which lead to consistent results. For this reason tweezer simulation results do not provide a suitable basis for the inference of RBC parameter values like the Boussinesq number.

6.2 Red blood cells in shear flow

6.2.1 Introduction

RBCs in shear flow have been investigated both experimentally and with numerical simulations and ample results can be found in the literature. However, only one recent simulation study [26] quantifies the influence of the membrane viscosity of RBCs on the dynamics in shear flow.

RBCs in shear flow at small viscosity contrast λ and moderate shear rates follow a tank-treading motion, at small shear rates they transition to tumbling motion [4, 101, 130]. In this section we focus on the tank-treading motion and the deformation and frequency behaviour of the RBCs for this motion pattern and do not investigate in detail the transition to tumbling and other RBC modes, which has already been studied extensively [101, 130]. Some results of these transitions and the resulting phase diagram for RBCs with membrane viscosity, however, are shortly presented in appendix E. Apart from phase diagrams for the different shapes, former studies analysed the general dynamics of the RBC motion patters in shear [131, 143], in some cases this includes results on the tank-treading frequency of the cells [26, 48, 51, 52, 96, 99, 144–146]. In experiments, small λ is achieved by placing the cell in a fluid of high viscosity. Several experimental studies exist, which investigate the cells' tank-treading frequencies [97, 116, 147, 148]. Similar to the previous chapter 5 comparison of the frequency results is the most promising approach for the comparison of experimental results with different simulation outcomes.

In section 6.2.3 simulation results using the method from chapter 4 are presented for the tank-treading dynamics of the RBCs and compared with former simulation studies. The assessment of the results in comparison with experimental measurements is presented in section 6.2.4, followed by a discussion section 6.2.5.

6.2.2 Simulation setup and dimensionless quantities

The BIM is used for most simulations in this section. The RBC is placed in the centre of a shear flow of shear rate $\dot{\gamma}$ as visualised in figure 6.7(a). The strength of the shear flow $\dot{\gamma}$ and fluid viscosity are chosen in the range where the cell exhibits a tank-treading motion during its periodic deformation in the flow, compare the discussion in appendix E.

The RBC is discretised with 2048 flat triangles. It is endowed with resistance to shear with an oblate spheroid reference shape with $\tau = 0.9$. The shear modulus is $\kappa_\mathrm{S} = 5 \times 10^{-6}\,\mathrm{N\,m^{-1}}$. The area dilation modulus is $\kappa_\mathrm{A} = 100\kappa_\mathrm{S}$ and the bending modulus is $\kappa_\mathrm{B} = 4 \times 10^{-19}\,\mathrm{N\,m}$ with bending curvature $c_0^* = 4$. The inner viscosity is $\mu_\mathrm{i} = 24\,\mathrm{mPa\,s}$, which for RBCs in a fluid of the same viscosity as blood plasma, corresponds to a viscosity contrast of $\lambda = 20$. The small values of λ which are necessary for the tank-treading motion are achieved with an increased outer viscosity μ_o, similar to the experimental approach. Thus in simulations viscosity contrasts of $\lambda = 0.2, 0.5, 1$ are used. The Boussinesq number in this section is defined as

$$Bq = \frac{\mu_\mathrm{s}}{\mu_\mathrm{p} a_0}, \tag{6.2}$$

i.e. with respect to the blood plasma viscosity $\mu_\mathrm{p} = 1.2\,\mathrm{mPa\,s}$ instead of the outer fluid viscosity in (4.62). This facilitates the comparison with the previous chapters and prevents changes in the membrane viscosity when the outer viscosity is varied. The dimensionless length $a_0 = 2.82\,\mu\mathrm{m}$ is the radius of a sphere with its volume identical to the RBC volume.

The only exceptions to the above listed parameters occur in the literature comparison section 6.2.3.1. The main reference study [26] uses a definition of the Skalak law with prefactors different from Barthès-Biesel [34], which leads to a shear modulus defined as $G_\mathrm{S} = \kappa_\mathrm{S}/3$. For accurate comparison a value of $G_\mathrm{S} = 2.5\,\mathrm{N\,m^{-1}}$ in the literature therefore is equivalent to an increased value of $\kappa_\mathrm{S} = 7.5 \times 10^{-6}\,\mathrm{N\,m^{-1}}$. The inner RBC viscosity in this reference study is smaller $\mu_\mathrm{i} = 11\,\mathrm{mPa\,s}$ and λ is defined with respect to that. Finally, in section 6.2.3.1 the dimensionless membrane viscosity is defined with respect to the inner viscosity as

$$Bq^\mathrm{int} = \frac{\mu_\mathrm{s}}{\mu_\mathrm{i} a_0} \tag{6.3}$$

to facilitate the comparison.

As part of the literature comparison some simulations are performed using the LBM. For these no membrane viscosity is included and the RBC is discretised with 5120 triangles. The shear reference is again $\kappa_\mathrm{S} = 7.5 \times 10^{-6}\,\mathrm{N\,m^{-1}}$ for better comparison and the reference state is the discocyte shape with zero bending curvature. The inner RBC viscosity is $\mu_\mathrm{i} = 11\,\mathrm{mPa\,s}$ and simulations are performed for $\lambda = 1$.

The Reynolds number for the system is

$$Re = \frac{\dot{\gamma} R^2 \rho}{\mu_\mathrm{o}} \tag{6.4}$$

with the RBC radius R and the blood plasma viscosity ρ. For the shear rates used in the simulations the Reynolds number is well below 0.01 and the BIM can be used.

The RBC dynamics in the shear flow is analysed by calculation of the cell deformation and the tank-trading frequency, both depending on the shear rate. The deformation of the cell in the flow is defined as

$$D = \frac{L - W}{L + W} \tag{6.5}$$

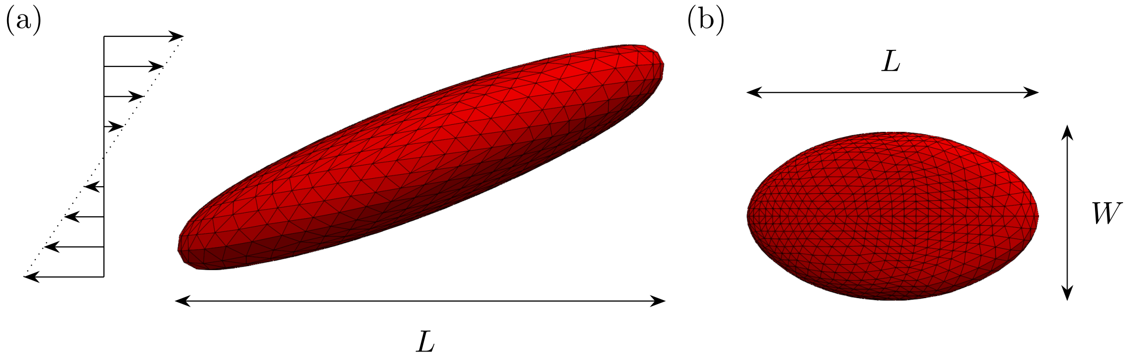

Figure 6.7: Red blood cells in shear flow. (a) Side view and (b) top view of a tank-treading RBC. The length L is measured direction of the shear flow and is not identical to the major cell axis. The cell width W is the second longest cell axis under shear. This definition of length scales is chosen with regard to the literature comparison [26].

where L is the cell elongation in direction of the shear flow and W is the second longest cell axis, compare the sketches in figure 6.7. During the tank-treading movement the deformation oscillates in time. The tank-treading frequency f is obtained by marking a point on the cell surface and calculating its movement with the membrane for several periods. Similar to the slipper movement in chapter 3 this frequency is half the deformation frequency of the cell. A dimensionless representation of the frequency is [26]

$$f^*_{\mathrm{TT}} = \frac{4\pi f}{\dot{\gamma}}. \tag{6.6}$$

For the dimensionless representation of the shear rate the capillary number is used, here defined as

$$\mathrm{Ca} = \frac{\mu_{\mathrm{o}}\dot{\gamma}a_0}{\kappa_{\mathrm{S}}/3}. \tag{6.7}$$

The factor 3 in the denominator is due to the different shear rate definitions as was explained above.

6.2.3 Tank-treading frequency and deformation

6.2.3.1 Detailed literature comparison for viscous red blood cells

As a first step simulations are presented which mimic the setup used for elastic and viscoelastic RBCs by Matteoli et al. [26], as described above. First, results without membrane viscosity but for different $\lambda = 0.2, 0.5, 1$ are compared in figure 6.8 (blue, green and purple symbols)[†]. For the smallest λ, membrane viscosity is added with

---

[†] Note that the Ca numbers in the original paper [26] in figure 5 are smaller by an erroneous factor 2, inconsistent with the Ca definition therein. The confusion was due to a reference to an

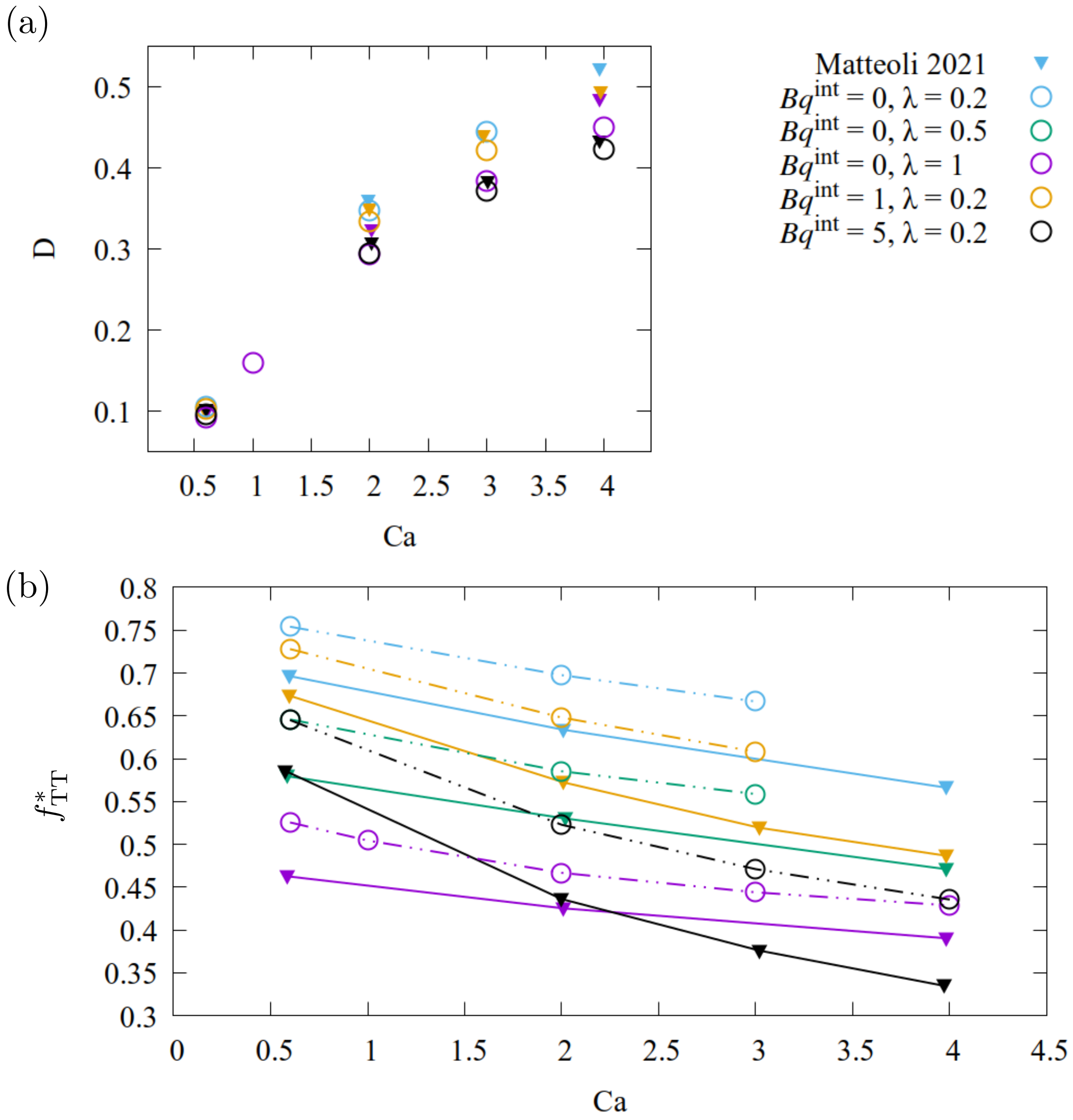

Figure 6.8: Comparison of the deformation and tank-treading frequencies of red blood cells in shear flow. (a) The mean deformation D and (b) the dimensionless frequency f^*_{TT} change with the capillary number Ca. The different colours indicate different membrane viscosities Bq^{int} and different outer viscosities, described by λ. Results from Matteoli et al. [26], figure 5 therein, are reproduced with triangle symbols, the simulations for different $Bq^{\mathrm{int}}, \lambda$ are equally colour coded. The lines serve as guide to the eye.

the Boussinesq numbers $Bq^{\mathrm{int}} = 1, 5$ (orange and black symbols). The results for the

---

older publication [130], which uses yet another definition of the shear modulus in the Skalak law, different by this additional factor 2.

mean deformation over time of the RBC in figure 6.8(a) scatter only for larger Ca and are in very good agreement with the literature results (triangle symbols, same colours for same parameter combination) with only a small negative deviation at larger Ca. The results for the tank-treading frequency, however, are significantly larger than the literature results. The displacement between them seems to be almost identical for the five different parameter sets. This in particular also holds for simulations without membrane viscosity. i.e. $Bq = 0$. From this it follows that the membrane viscosity implementation can be ruled out as the cause of the constant displacement. The results even confirm that the implementation presented here leads to qualitatively similar trends for f^*_{TT} as found in the literature.

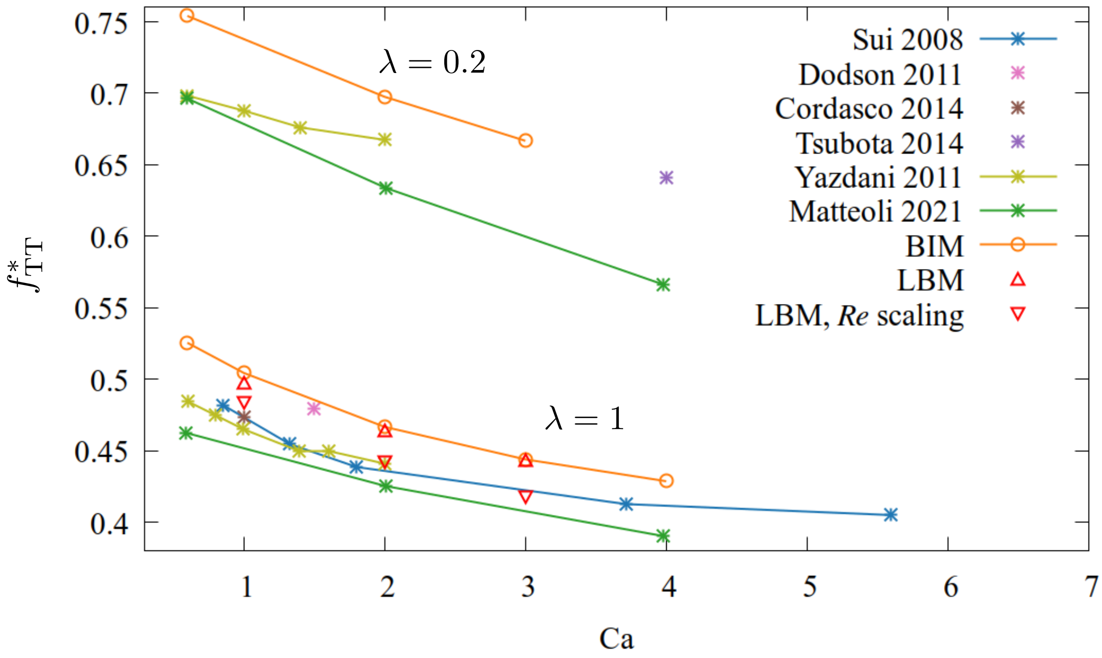

Figure 6.9: Shear tank-treading frequencies in comparison with other simulation studies. Results are shown for viscosity contrast $\lambda = 0.2$ (points with $f^*_{\mathrm{TT}} > 0.55$) and $\lambda = 1$, all with $Bq = 0$. The literature values plotted for comparison are taken from Matteoli et al. [26], Tsubota et al. [48], Cordasco et al. [52], Yazdani et al. [99], Sui et al. [144] and Dodson et al. [145]. Apart from these (differently coloured crosses) and the BIM simulation results (orange circles), LBM simulation results are shown (red triangles).

Therefore, the next step is to compare the results with $Bq = 0$ to older studies, which did not yet include membrane viscosity but also gave results for the tank-treading frequencies. This comparison is shown in figure 6.9 for two different λ. Results from the previous figure 6.8(b) are repeated in orange and in green for the literature comparison. The literature results [48, 52, 99, 144, 145] added in the figure are converted to a consistent Ca definition, see equation (6.7), and normalised frequencyf^*_{TT}, see equation (6.6). The results from different studies all show the decrease in the frequency with increasing capillary number, but the exact levels of the frequency results differ.

The scattering of the frequency results could originate from the different simulation methods. To further investigate this, results from LBM simulations at $\lambda = 1$ and $Ca = 1, 2, 3$ are added in figure 6.9 (upwards pointing red triangles). The frequency results are nearly identical to the BIM outcome, at maximum less than 2 % decrease in the frequency is observed. Similar to the BIM setup the Reynolds number was well below 0.1 in all simulations. To speed up LBM simulations for systems at small Re a Reynolds number scaling approach is frequently used. The Reynolds number is increased to some value < 1, which is still small enough, so that no artificial inertia effects are introduced. Matteoli et al. [26] used a Finite Volume solver method for the incompressible Navier-Stokes equation, coupled with IBM, and set $Re = 0.2$, following this scaling approach. To test the influence of a scaling to $Re \approx 0.2$ (for $Ca = 3$; other Ca proportionally smaller due to smaller $\dot{\gamma}$) in LBM simulations the shear rate was scaled up by a factor of 10 and the viscosity was scaled down by a factor of 10. While the Reynolds number (6.4) increases, this has no effect on the capillary number (6.7). The dimensionless frequency f^*_{TT} results from the ratio between the new tank-treading frequency and the increased shear rate and is again shown in figure 6.9 (downwards pointing red triangles). A significant decrease in the frequency towards the values from Matteoli et al. [26] is observed. Another indication that the simulation method in combination with the Reynolds number is indeed responsible, is the comparison with the other simulation studies. Dodson et al. [145] and Tsubota et al. [48] both use a boundary element method for Stokes flow and are very close to the BIM results. Cordasco et al. [52] and Yazdani et al. [99] use a front-tracking method developed by the group [149] and mention a Reynolds number of $Re \approx 0.01$. Sui et al. [144] use a LBM-IBM approach and state that $Re \approx 0.1$ in their simulations. The frequency results from these three studies are indeed closer to the results from Matteoli et al. [26]. Note that if the Reynolds number scaling relies on scale-down of the shear modulus κ_{S} instead of the scale-up of the shear rate it has no significant influence on the tank-treading frequency.

6.2.3.2 Discussion of the viscosity effects in the standard setup

Figure 6.10 shows the influence of viscosity contrast and membrane viscosity for the RBC parameter set used in channel flow and tweezer simulations in the previous chapters. Compared to the previous literature comparison, changes include an increase in the inner fluid viscosity of the RBC and a decrease in κ_{S}, confer section 6.2.2. The small dots in figure 6.10(b) are repeated from 6.9 and show that the changes in the setup have no influence on the dimensionless frequency. In order to achieve comparability with the previous chapters the membrane viscosity is here

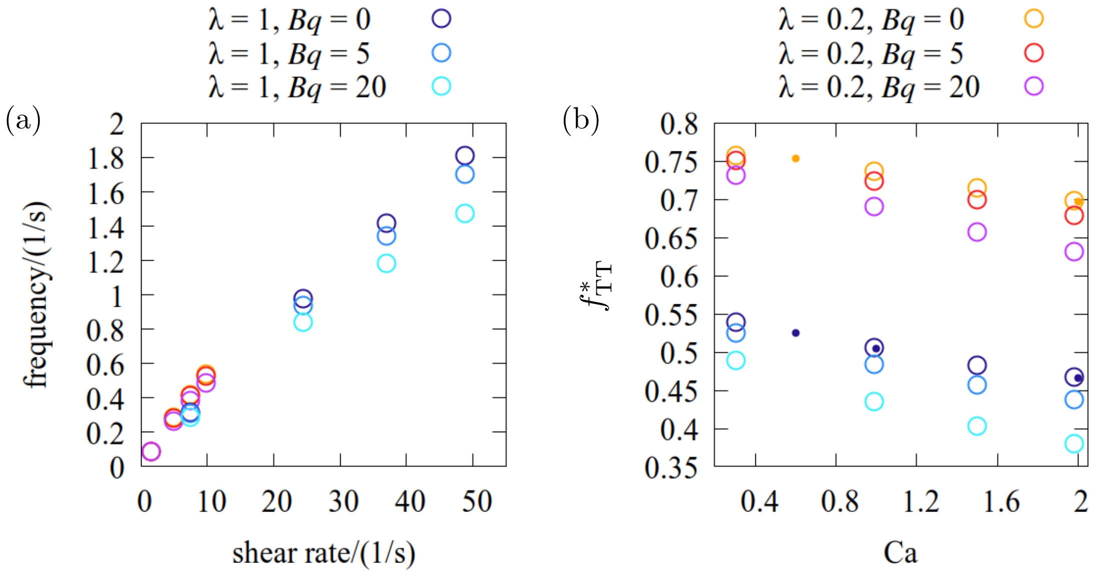

Figure 6.10: Tank-treading frequencies of red blood cells for different viscosities. Results are shown for viscosity contrasts $\lambda = 0.2, 1$ and $Bq = 0, 5, 20$ (a) directly and (b) in dimensionless form. Small dots in (b) are the BIM simulation results for $Bq = 0$ repeated from figure 6.9, which belong to another parameter combination used for the literature comparison.

computed with respect to the RBC plasma viscosity, see equation (6.2). Only results for zero membrane viscosity are repeated from the previous figure because previously the Boussinesq number was defined with respect to the inner viscosity and the real membrane viscosity is therefore larger by a factor of around 10.

An increase in the viscosity contrast or the membrane viscosity slows down the tank-treading movement, similar to the channel flow discussed in chapter 5. This is resolved better in the dimensionless figure 6.10(b), because f^*_{TT} decreases by only a small amount with Ca. Changes in the Boussinesq number have less influence on the tank-treading frequency than changes in the viscosity contrast λ have.

6.2.4 Comparison with experimental results

Several experimental studies exist for which the tank-treading frequency of RBCs in shear flows was measured. Figure 6.11 shows BIM simulation data in comparison with the experimentally measured tank-treading frequencies, in (a) for smaller shear rates and in (b) in a log-log plot for the whole measured range. The viscosity values for the surrounding fluid are reported in centipoise ($1\,\mathrm{cP} = 1\,\mathrm{mPa\,s}$) as in the original publications to facilitated to comparison.

The simulations have fixed inner viscosity $\mu_{\mathrm{i}} = 24\,\mathrm{mPa\,s}$ and viscosity ratios $\lambda =$

0.2 (circle), $\lambda = 0.5$ (square) and $\lambda = 1$ (diamond shape). The customary values for the membrane viscosities with $Bq = 0$ (green), $Bq = 5$ (blue) and $Bq = 20$ (red) are used. Some of the results have already been shown in figure 6.10. At larger shear rates, only the most viscous RBCs produce stable results in simulations, similar to the observation for Poiseuille flow in chapter 5. For example at $\dot{\gamma} \approx 200\,\mathrm{s}^{-1}$ and $\dot{\gamma} \approx 400\,\mathrm{s}^{-1}$ only simulations with artificially large $Bq = 100$ are stable, these are shown for comparison over the whole range.

In experiments, two different measurement approaches are used. Basu et al. [148] investigate optically trapped RBCs in direct shear flow while the other experimental studies [97, 116, 147] use a rheoscope. The frequencies measured by Basu et al. [148] are, for medium shear rates in figure 6.11(a), smaller than those from the other three studies. In contrast to the comparatively large outer viscosities in the other experimental studies, Basu et al. [148] report a small value of $\mu_\mathrm{o} = 0.92\,\mathrm{cP}$. The authors are aware of previous studies which did not obtain tank-treading cells at such parameter combination but still report tank-treading frequencies at all shear rates. Basu et al. explain that this discrepancy is the reason for the small frequencies observed up to medium shear rates around $30\,\mathrm{s}^{-1}$, while at high shear rates the difference is expected to vanish [148]. Assuming that the inner viscosity is around 24 mPa s the measurements by Fischer et al. [147] and Fischer [97] for different outer fluid viscosities fall in the range $\lambda = 0.4, \ldots, 2.2$, the measurements by Basu et al. [148] would correspond to $\lambda = 26$. The old and young cells from Tran-Son-Tay et al. [116] might differ considerably in their inner viscosity values. Older cells have lost some water over their lifetime which increases the relative haemoglobin concentration inside the cell. This leads to a higher density of the cytoplasma and possibly also to a higher viscosity of the inner fluid. Experiments with centrifuged blood have shown that denser (i.e. older) cells have a membrane viscosity twice as large as the less dense cells [115], values are listed in table 4.1. This is another possible explanation for the decreased frequency of the old cells in Tran-Son-Tay et al. [116].

Most experimental measurements discussed above were performed at room temperature around 23 °C to 25 °C [97, 116, 147]. In addition to the results reproduced in figure 6.11 the study by Basu et al. [148] presents results for temperatures between 20 °C and 40 °C. However, the outer fluid viscosity is again adjusted to 0.92 cP and at larger shear rates, where the frequency results at room temperature compare well to the other experimental studies, only few measurement points lie. For these, the authors show that a temperature increase can lead to a noticeably larger tank-treading frequency. As the membrane viscosity decreases with increasing temperature [114] this observation is in agreement with the influence of Bq on the frequency.

6.2.5 Discussion

Similar to the earlier observations for RBCs in Poiseuille flow, also in shear flow increased inner fluid viscosity and membrane viscosity lead to a decrease in the tank-treading frequency. Detailed comparison with a simulation study [26] in section 6.2.3.1 showed that changes in both λ and Bq have precisely the same influence on the frequency. The only difference is a constant shift between all curves, which can be explained by differences in the simulation method. It was shown that LBM simulations agree very well with the BIM results, but the scale-up of the Reynolds number in LBM simulations for computational efficiency can lead to an artificial drop in the frequency. Comparison with more simulation studies of purely elastic RBCs in shear flow [48, 52, 99, 144, 145] shows that the exact frequency levels in general scatter slightly.

The experimental data available for tank-treading RBCs in highly viscous fluid was compared to the BIM frequency results. All simulation results in a physiologically sensible parameter range are well compatible with the experimental measurements. To resolve the differences in the simulation results they are best converted to dimensionless numbers and plotted depending on the capillary number. In experiments, however, this is not feasible as the membrane shear properties are not known exactly. Moreover, especially the influence of the membrane viscosity is difficult to discern.

The very good qualitative agreement with the literature again confirms the implementation of the membrane viscosity simulation method in this work. Quantitative conclusions regarding the viscosity of RBC membrane and interior, however, cannot be drawn with this approach.

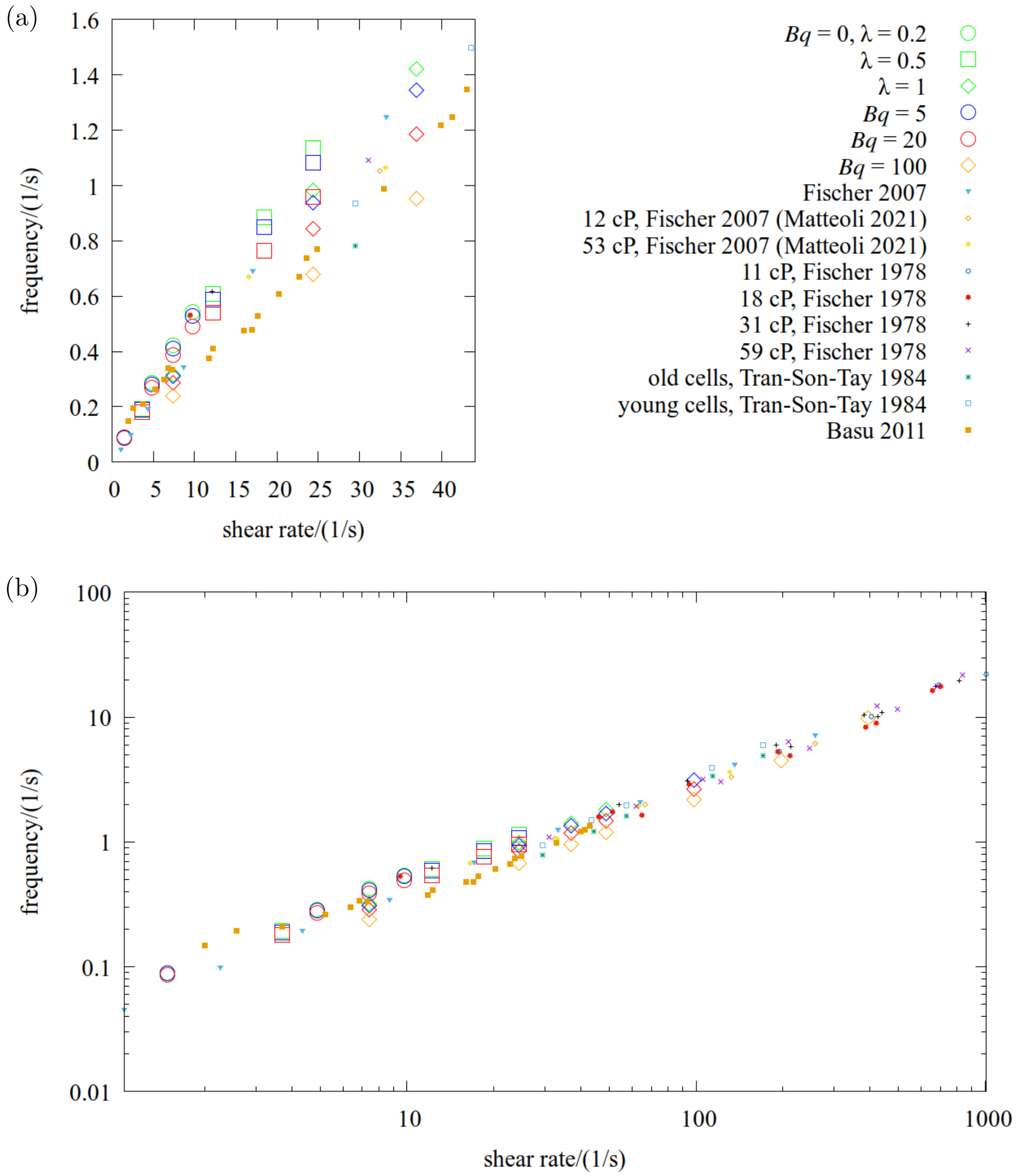

Figure 6.11: Shear tank-treading frequencies compared with experimental measurements. Frequencies are plotted (a) at small shear rates and (b) over the whole measurement range in a log-log graph. BIM simulation data is shown for different Bq (different colours) and different viscosity contrasts λ (circle, square and diamond shapes). The experimental data (coloured points) is reproduced from the literature from Fischer et al. (1978) [147], Fischer (2007) [97], Tran-Son-Tay et al. [116] and Basu et al. [148]. Some measurement data from Fischer (2007) [97] was taken from a secondary source (Matteoli et al. (2021) [26]). The viscosity values in centipoise for the experimental measurements refer to the viscosity of the outer fluid. The measurements by Tran-Son-Tay et al. [116] were done with an outer fluid viscosity of approximately 35 cP (value determined at 2 % RBC concentration). Basu et al. [148] have an outer viscosity of 0.92 cP, the data is reproduced from their fig. 4.

6.3 Expanding channel geometry

6.3.1 Introduction

A microscale expansion geometry offers another setup to study the RBC relaxation behaviour for viscoelastic RBCs in the comparison of experiment and simulation. The experiments include age-separated RBCs at different velocities in a microchannel with an expansion leading to a larger microchannel. A similar setup is modelled in simulations to compare the recorded deformation behaviour of the RBC. All experimental data was provided by M. Nouaman and S. M. Recktenwald (members of the group of C. Wagner in Saarbrücken).

In the first section 6.3.2 the setup and RBC parameters are introduced and the initial shapes and velocity curves are discussed. The results are presented in section 6.3.3, followed by a discussion in 6.3.4.

6.3.2 Setup and observation parameters

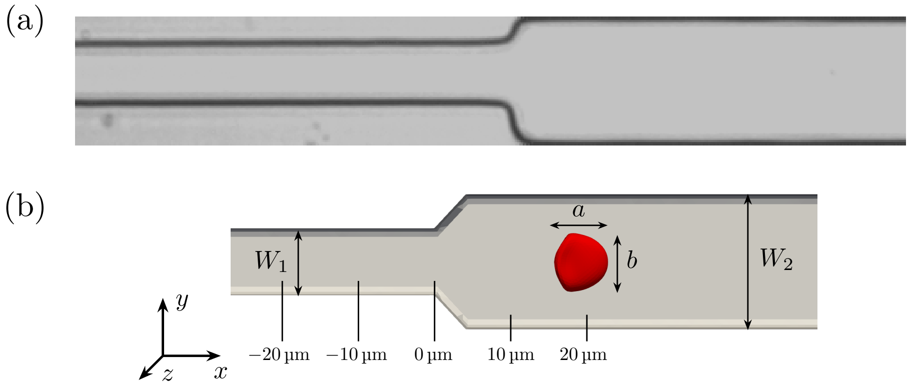

Figure 6.12: RBCs flowing in an expanding channel setup. (a) Region of interest of the experimental microchannel and (b) corresponding expansion geometry in BIM simulations in 2D projection. The starting point of the expansion is chosen as the origin in x-direction. The flow is in positive x-direction. Deformation of the red blood cell is measured with its extension a in x-direction and b in y-direction. Experimental image provided by M. Nouaman (member of the group of C. Wagner in Saarbrücken).

The expansion geometry studied in this section is shown in figure 6.12. The cells flow in from the left and travel through the smaller part of the channel up to the extension, where they enter the broader part of the channel. The width in y-direction before the expansion is $W_1 = 8.4\,\mu m$ and behind the expansion $W_2 = 17\,\mu m$. The height of the microchannel in z-direction is $H = 5\,\mu m$. The experimental microchannel in figure 6.12(a) is fabricated with standard soft lithography. The channel geometry in BIM shown in figure 6.12(b) is constructed with the program Gmsh [150] to mimic the experimental channel. The channel has a triangulated surface, it is not periodic and is treated as object in the flow. The simulated channel is much shorter than the experimental setup, this allows comparison of the cell trajectories and deformation at the region of interest, around the expansion, at reasonable computation times.

The RBCs are discretised with 2048 flat triangles, shear and bending contributions are modelled with the Skalak law with $\kappa_\mathrm{S} = 5 \times 10^{-6}\,\mathrm{N\,m^{-1}}$, $\kappa_\mathrm{A} = 100\kappa_\mathrm{S}$ and the Helfrich model with $\kappa_\mathrm{B} = 4 \times 10^{-19}\,\mathrm{N\,m}$ and a constant bending reference curvature $c_0^* = 4$. The shear reference shape is the oblate spheroid with $\tau = 0.9$. The inner viscosity of the RBC is varied in the simulations which leads to changes in the viscosity contrast λ, defined via equation (2.6) with respect to the constant outer viscosity $\mu_\mathrm{o} = 1.2\,\mathrm{mPa\,s}$. The Boussinesq number (4.63) is defined with with respect to the length scale R, the radius of the RBC in rest. The characteristic inverse time for the definition of the spring constants in (4.64) is the average flow divided by R. The cell dimensions in x- and y-direction, a and b, are marked in figure 6.12(b), these are recorded during the simulation. From the two lengths a and b the non-dimensional deformation of the cell is calculated as

$$D = \frac{a-b}{a+b}\,. \tag{6.8}$$

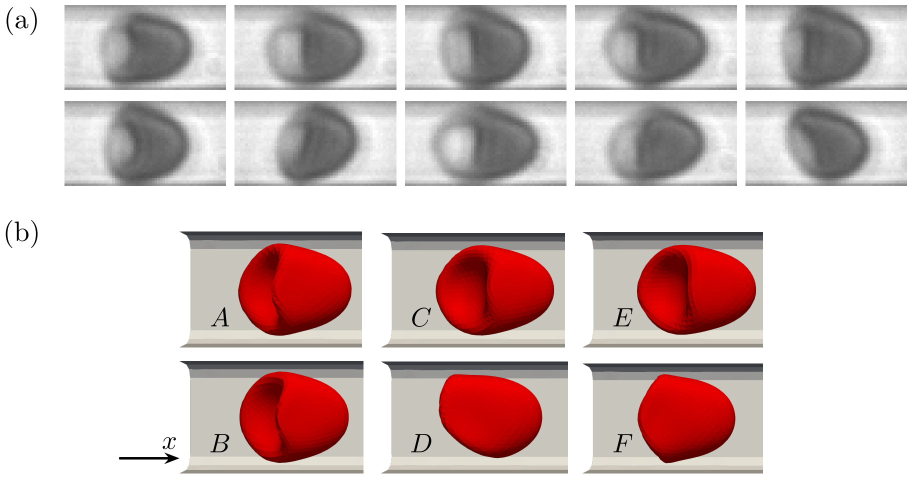

Figure 6.13: Inflowing red blood cell shapes at the expansion geometry. (a) Experimental snapshots in the smaller channel part and (b) initial RBC shapes in the simulations. The flow direction is from the left to the right. The capital letters in (b) label the different initial shapes whose dynamics is discussed in the following sections. Experimental images provided by M. Nouaman and S. M. Recktenwald (member of the group of C. Wagner in Saarbrücken).

In the experiments, the cells enter the smaller channel part in figure 6.12(a) on the left from a larger reservoir and are thus pre-deformed. Examples for these are shown in figure 6.13(a). In order to mimic this deformation prior to the channel section shown in figure 6.12, in the simulations deformed RBCs from a periodic channel simulation are used. These shapes are shown in figure 6.13(b). The shape differences result from different cell parameters, λ and Bq, or different starting conditions in the preliminary periodic channel. In total six different initial RBC shapes at the channel entrance are investigated in the simulations.

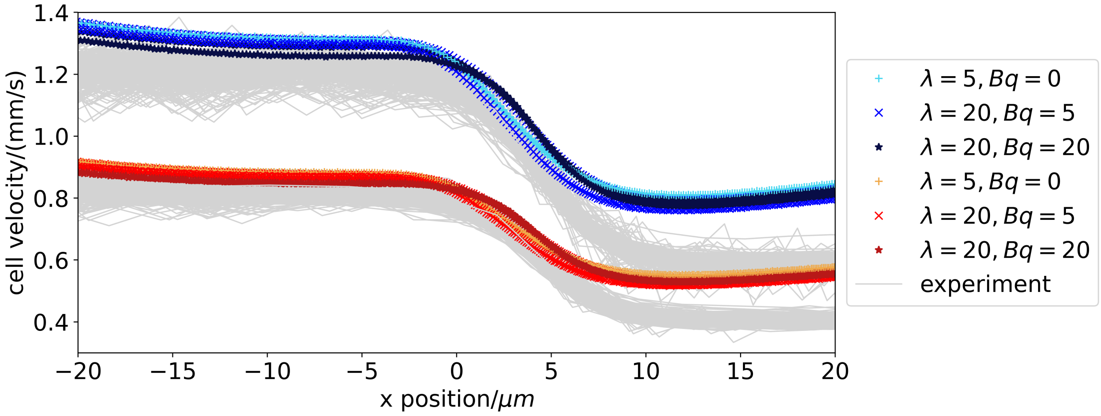

Figure 6.14: Velocity of the red blood cells in the expanding channel. The bluish curves show the simulation results for larger cell velocities, corresponding to an experimental pressure drop of 100 mbar, with different RBC parameters λ and Bq. The curves in red and orange represent simulations results corresponding to a pressure drop of 70 mbar. Experimental measurement curves of single cells for the two pressure drops are added in light grey. The origin of the x-axis lies at the expansion, compare figure 6.12(b).

The constant flow strength in BIM is adapted such that different cell velocities result, these are shown in figure 6.14, the RBCs move with around $0.9\,\mathrm{mm\,s^{-1}}$ and $1.3\,\mathrm{mm\,s^{-1}}$ in the smaller channel part. These velocities lead to a Reynolds number (2.12) well below 0.1. In experiments different cell velocities are obtained by adapting the pressure drop in the channel, the pressure drops corresponding to the simulation cell velocities are 70 mbar and 100 mbar. The velocity curves of the cells in experiments show a wide spread, compare figure 6.14 (light grey curves). In both experiment and simulation the cell velocity decreases at and behind the expansion due to the increase of the channel cross section. A qualitative agreement between the velocity development is observed for the region of interest around the constriction. In experiments, however, farther behind the constriction the velocity decreases to a smaller value compared to the simulations. A possible reason for this observation is that the channel widens behind the constriction when a pressure drop is applied, thus leading to a larger cross section and smaller velocity. The significance of this observation for the result of the comparison is discussed below. The results in the following sections concentrate on the region of interest directly around the constriction.

The experimental channel in figure 6.12(a) is slightly asymmetric with respect to the expansion in its middle. Test cases in BIM simulations with corresponding channel asymmetry showed that this has negligible influence on the cell behaviour.

6.3.3 Results

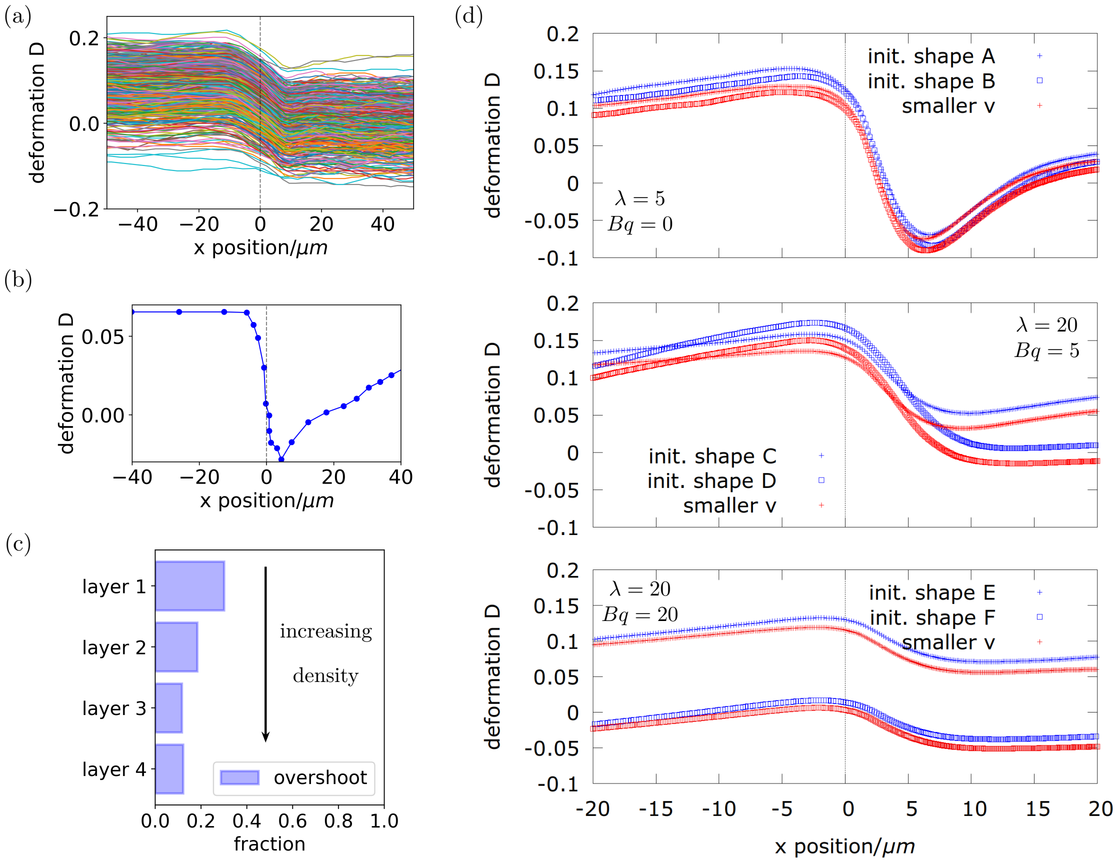

Figure 6.15: Deformation behaviour of the red blood cells at the expansion. (a-c) Experimental and (d) simulation results are shown in comparison. (a) Deformation curves around the constriction for 650 cell measurements at the lowest pressure drop of 70 mbar. (b) Single cell measurement exemplarily shows the overshooting of the deformation at the constriction. (c) The fraction of cells which show overshooting of the deformation D changes with the cell density in the different layers in experiments, all data shown is for a pressure drop of 70 mbar. (d) Deformation curves in the simulations for different λ, Bq with different initial shapes at the channel entrance and different velocities, compare figure 6.14.

Example trajectories for experiment and simulation are shown in figure 6.15. The experimental measurements in (a) show the broad scattering of the deformation D. A large number of cells has a flat deformation transition at the expansion. Some deformation curves, however, show an overshooting at the expansion, which means that the RBC first expands quickly in y-direction, i.e. the length b increases compared to a, and then relaxes back. An exemplary single cell measurement is shown in figure 6.15(b). In experiments, the RBCs are separated by centrifugation and thus form several layers of increasing density. Separate measurement for these layers shows that the fraction of cells, whose deformation curve overshoots, depends on the density of the cell, compare figure 6.15(c). The simulation results shown in figure 6.15(d) shed light on the origin of the experimental observations. First, the simulations show that slight variations in the start shapes, see especially for the shapes E and F and, though less pronounced, for C and D, can have a distinct influence on the level of the deformation curves. This observation can explain the wide scattering of deformation levels in the experiment in 6.15(a). All deformations observed in the simulations agree with the experimental range. Second, the cell velocity has no significant influence on the deformation behaviour as the two velocities investigated in simulations show (red vs. blue curves), which suggests that the difference in the velocity development in figure 6.14 is not harmful for the comparison. Finally, the three plots in figure 6.15(d) show that in simulations the overshoot in the deformation occurs only at smaller values of λ and Bq, larger inner and membrane viscosity suppress this effect.

The experimental data from the group of C. Wagner includes results of the deformation behaviour of RBCs treated with different concentrations of diamide. Data evaluation analogously to the bar chart in figure 6.15(c) shows that for cells treated with the largest concentration of $2\,\mathrm{mmol\,l^{-1}}$ diamide, the fraction of overshoots increases by the factor 2.5 compared to untreated whole blood RBCs. As discussed in section 7.3.2 diamide links the cytoskeletons' proteins and thus increases the cells stiffness. In simulations this could be reflected by a larger shear modulus κ_S, however, the exact relation between diamide concentration and shear modulus remains unclear, compare again section 7.3.2. Mainly for this reason but also because the simulations in the expansion geometry are time-intensive, additional simulations with larger κ_S have not been run here. The overshooting is a dynamic process and thus reference to the relaxation behaviour of RBCs in quiescent flow in section 5.3.2 is of interest. In figure 5.2, for one example it was shown that larger shear modulus leads to a slightly faster relaxation back to the rest shape of the RBC, but the effect of the change in κ_S is marginal. One can hypothesise that the overshooting is more frequent for stiffer cells because the relaxation dynamics is faster, for a definitive conclusion, however, more simulation data is necessary.

6.3.4 Discussion

The experiments show that cells with larger density, which is attributed to older cell age, have a smaller fraction of overshooting deformation behaviour. In simulations, the same decrease in overshooting is observed for larger interior and membrane viscosity of the cells. In the literature, a connection between haemoglobin concentration inside the cell, due to variations in the cell density, and the viscosity of the cell is discussed. The review article by Hochmuth et al. [121] summarises results from earlier studies. It was shown that the concentration of haemoglobin in the cytoplasm of the cell has a strong influence on the cell's membrane viscosity, possibly because the haemoglobin proteins can bind to the cell membrane [121, 151, 152]. The shear modulus κ_S of normal cells, however, was found to be independent of the haemoglobin concentration [58, 115, 121, 153–155]. This supports the simulation approach, where the influence of κ_S was not further investigated. Moreover, the authors showed in relaxation experiments that from a collection of cells, the 5 % of highest density needed 1.5 times longer for the relaxation compared to the 5 % of lowest density [115, 121, 153], compare the shear simulations section 6.2.4.

If the connection is made between the denser/older cells in the experiments and the more viscous cells in simulations, the comparison of experiment and simulation provides an explanation for the observed overshooting cell behaviour. The more viscous cells, i.e. those which have larger inner fluid viscosity and larger membrane viscosity, react on a slower time scale and thus 'miss' the deformation overshoot. Cells which are less dense and have smaller viscosity values, however, react on a faster time scale and show a deformation overshoot. This argument is also in line with the observations of the RBC relaxation behaviour in section 5.3.2, where the doubling of the inner viscosity ($\lambda \times 2$) was shown to lead to a twice slower relaxation back to the RBC rest shape. A detailed quantitative comparison of simulation and experimental results remains challenging in this setup, due to the sensitivity to the start shape and the resulting scattering of the deformation curves. Inference of specific viscosity values of RBCs from this setup is therefore not possible.

The recent study by Nouaman et al. [103] investigated the influence of the age-separated cell layers discussed here on the phase diagrams of RBCs flowing through microchannels. It was found that with increasing cell density the fraction of croissants at small velocities increased and the fraction of slipper cells at larger velocities decreased, where other cell shapes become predominant [103]. In section 5.6 of this work the influence of membrane viscosity on the simulation phase diagrams is presented for cells with viscosity contrast $\lambda = 20$. The results show that an increase in Bq leads to a pronounced increase in the occurrence of RBCs classified as *others*, which is in agreement with the increase of *other* cell shapes in experiment. Resolving changes in the fraction of croissants, however, is not possible for the presented data, because their occurrence heavily depends on the choice of the initial shape and initial cell position as the simulation phase diagrams in figures 5.12 and 5.13 confirm. In order to make a clear statement of that from simulations, more information about the initial cell state would be necessary. This fact makes the comparison of phase diagrams in this setup challenging.

7 Analysis of red blood cell properties based on many-cell statistical behaviour

7.1 Overview

The validation of simulation results against experimental measurements of the RBC dynamics so far was based on the comparison of single RBC observations, with the aim of inferring the physical properties of RBCs. RBCs are, however, biological objects and their properties are thus subject to biological variability. In experiments, this is reflected in the fact that the scattering of measurement results is not only due to measurement error but also due to this natural variation. For simulations, this implies that physical properties of RBCs cannot be expressed in single quantities for certain parameters but should rather be expressed on a range. The new approach in this chapter is to explore this many-cell statistical behaviour of RBCs by comparing statistical measurement results from experiments with numerical simulations of RBCs whose cell properties are varied on a physiologically appropriate range. The experimental data comes from real-time deformability cytometry (RT-DC), a technique developed by the group of J. Guck at the MPL in Erlangen. With this technique it is possible to analyse thousands of blood cells in a few minutes and process the images of the deformed cells in real time [156]. The recorded cell characteristics, for example the deformation and size of the cells, can be used to distinguish RBCs from other blood constituents and for the investigation of the mechanical properties of RBCs in health and disease [156]. This method has been applied to study changes in the RBC deformability linked to COVID-19 [11] and depressive disorders [157].

The key question, namely whether it is possible to deduce the mechanical properties of RBCs from these many-cell measurements, will be addressed in this chapter. In section 7.2 first the flow setup modelled with the BIM, based on the experimental RT-DC geometry, is introduced in 7.2.1, followed by the discussion of the cell shape data analysis in 7.2.2. The next section 7.3 consists of a presentation and comparison of the RBC deformation result, with respect to the shape data in 7.3.1 and based on the statistical data in 7.3.2. This qualitative comparison shows good agreement between the simulation results and the experimental data, which scatter due to biological cell variability and initial conditions, as well as measurement error in experiments. The purpose of the next section 7.4 is to examine whether and how information about the distribution of RBC properties from the statistical data is possible. Two different methods are considered in 7.4.1 and 7.4.2, followed by a short discussion and outlook in section 7.4.3. Finally, a concluding discussion is given in section 7.5.

All experimental data presented in this chapter was provided by F. Reichel (member of the group of J. Guck at MPL in Erlangen).

7.2 Setup and methods

7.2.1 Boundary integral method simulations based on the experimental setup

The BIM is used in this work to investigate the RT-DC measurement setup in numerical simulations. The experimental flow setup in RT-DC is shown in figure 7.1(a) [156]. The cells enter the channel on the left, are focused in the stream and enter the measurement section marked with the solid red box in the experimental image. An example measurement of one RBC is shown in figure 7.1(b). The RBCs are stretched in a peculiar drop-like shape in the measurement channel. When the experimental data is processed, cells whose detected area is below or above a certain threshold and whose contour has an aspect ratio which is not between 2 and 20, are filtered out, leaving in total 8299 single cell observations for the analysis. The filtering is done with the software Shape-Out [158], developed to process the RT-DC measurements. This prevents that cell aggregates and other invalid events, like recorded debris in the channel, are included in the analysis, but is also intended to exclude other blood cell types [156, 159].

In BIM, the section highlighted with a dashed red line in figure 7.1(a) is rebuild, the resulting three-dimensional channel model is shown in figure 7.2(a). As in the experiments, the smaller measurement channel has a quadratic cross section with side length $W = H = 20\,\mu\mathrm{m}$. The channel is discretised with flat triangles and has slightly rounded corners for numerical stability. At the beginning of the simulation the cells start at negative x-values in figure 7.2(b) at different y-positions. Due to the symmetry of the channel only positive y-values are chosen.

Note that in initial test simulations only the smaller measurement channel section from experiments with quadratic cross section was simulated. The results did not agree with the experimental cell shapes, which is ascribed to the fact that most of the cell deformation in experiments takes place before the cell enters the channel. Therefore, it is necessary to include the funnel-shaped entrance region in simulations. In BIM, including an even larger entrance region to model the full deformation history

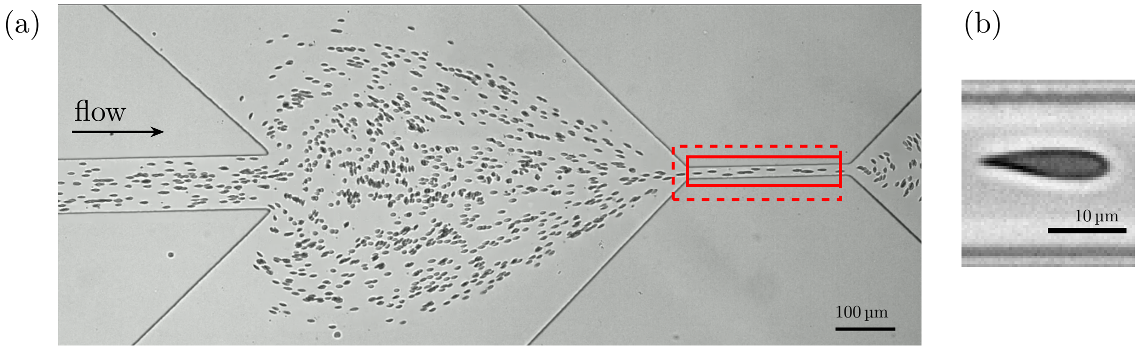

Figure 7.1: Experimental flow setup for the RT-DC measurements. (a) Measurement channel with flowing RBCs, the image is reproduced from the work of Toepfner et al. [156] published in eLife, here flow direction, scale bar and regions of interest (in red) were added [160]. The solid red line surrounds the experimental observation region, the dashed line the region which is rebuild in simulations. (b) Shape of a single RBC in the RT-DC measurement. Image data provided by F. Reichel (member of the group of J. Guck at MPL in Erlangen), the scale bar was added here.

of the cell would further increase the computation time. Thus, the model shown in figure 7.2 is a compromise between accurate emulation of the experimental setup and reasonable computing times.

In the experimental measurements the cells are suspended in a buffer solution containing methyl cellulose (0.6 %). This solution is shear thinning [161] with a viscosity at rest of $\mu_\mathrm{o} = 15\,\mathrm{mPa\,s}$, measured in a falling-sphere viscometer. At the experimental flow rate of $0.06\,\mathrm{\mu l\,s^{-1}}$ in the small measurement channel and at room temperature of 25 °C, this leads to an effective viscosity [162] of around $\mu_\mathrm{o}^\mathrm{eff} = 5.2\,\mathrm{mPa\,s}$.

In the BIM implementation the inflow is adapted such, that the flow velocity in the smaller channel part matches the experimental flow rate if an Poiseuille velocity profile is assumed. The fluid in the measurement channel thus has a mean velocity around $v = 15\,\mathrm{cm\,s^{-1}}$. The outer fluid viscosity in simulations is $\mu_\mathrm{o} = 5 \times 10^{-3}\,\mathrm{mPa\,s}$, larger by a factor of 4.17 compared to the blood plasma viscosity. This leads to an estimate for the Reynolds number (2.12) in the channel of $Re = \frac{vL\rho}{\mu_\mathrm{o}} \approx 0.6$, where as characteristic length scale L the channel height H is used and for ρ the density of the blood plasma is taken. As detailed in section 2.3.1 the BIM is developed for systems with low Reynolds number, where inertia effects are small compared to the viscous effects. Therefore, this system is near the limit where the BIM can still be used.

The RBCs are discretised with 1280 triangles, preliminary tests with 2048 triangles did not show significant differences in the cell shape. The shear reference is an oblate spheroid with moduli $\kappa_\mathrm{S} = 5 \times 10^{-6}\,\mathrm{N\,m^{-1}}$ and $\kappa_\mathrm{A} = 1000\kappa_\mathrm{S}$. The phenomenological area dilation modulus κ_A is chosen by a factor of 10 larger compared to the previously

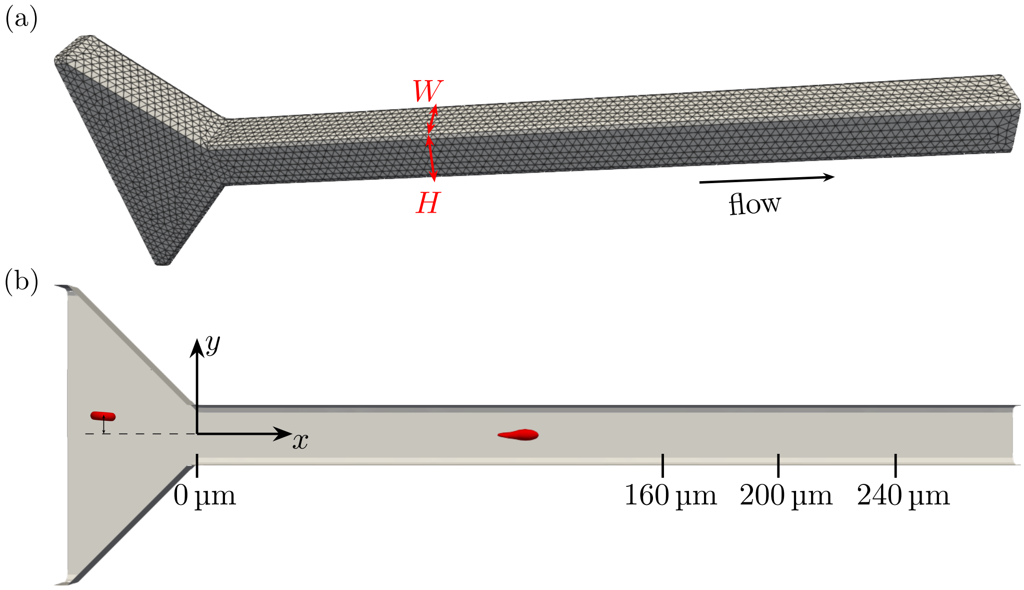

Figure 7.2: Channel model in boundary integral method simulations. (a) The three-dimensional discretised channel has equal width W and height H of 20 µm. (b) The cut through the whole channel section shows the inlet on the left and different observation points at the channel end in the right part of the channel. Two exemplary RBC shapes at an initial position and in the middle of the channel are included (red shapes).

used values, in order to guarantee that the surface area deviation of the RBC remains small, albeit strong deformations occur due to the large flow velocity. The bending reference curvature is $c_0^* = 4$ and the bending modulus $\kappa_\mathrm{B} = 4 \times 10^{-19}\,\mathrm{N\,m}$. The cells are started slightly off-centred in z-direction, shifted by one tenth of the cell radius $z_\mathrm{init} = 0.4\,\mathrm{\mu m}$. This is done in order to prevent a perfectly symmetric entry in simulations which does not occur in experiments. The initial position in y-direction y_init is varied in the simulations such that $y_\mathrm{init} = 0.4\,\mathrm{\mu m}, 2\,\mathrm{\mu m}, 4\,\mathrm{\mu m}, 6\,\mathrm{\mu m}, 8\,\mathrm{\mu m}, 10\,\mathrm{\mu m}$ or $12\,\mathrm{\mu m}$. For illustration, one RBC with $y_\mathrm{init} = 6\,\mathrm{\mu m}$ is shown in figure 7.2(b) at its initial position at the left channel entrance. In different simulations the viscosity ratio λ and the Boussinesq number Bq are also altered. Here Bq is defined as in equations (4.63) and (4.62), but with respect to the blood plasma viscosity $\mu_\mathrm{p} = 1.2\,\mathrm{mPa\,s}$ instead of the outer viscosity μ_o, to facilitate comparison with the results in the previous chapters. For the length scale in the Bq definition the long radius R of the RBC is used. In simulations the Boussinesq number was varied between $Bq = 1$ and $Bq = 25$ in steps of 1. The viscosity ratio λ was varied between $\lambda = 1$ and $\lambda = 5$. Because the viscosity of the fluid in the channel is 4,17 times larger than the blood plasma viscosity, the values of λ must be rescaled with 4,17 for comparison with the previous chapters of this thesis. The start shape of the cell is either the discocyte rest shape or a slipper shape. The characteristic inverse time in the definition of the artificial spring constants in equation (4.64) is the flow velocity divided by the RBC radius.

Taking into account the different starting shapes and positions, and the variations in Bq and λ, in total 1750 simulations have been carried out. One can observe that for small membrane viscosities the cell shapes are in many cases unstable, especially for the deformed slipper starting shape. Therefore, the analysis of the following sections is limited to simulations with $Bq = 5, 6, \ldots, 22$ for discocyte initial shape and $Bq = 5, 6, \ldots, 17$ for the slipper.

In the simulations the details of the rheology of the outer fluid, e.g. its shear thinning property, have been neglected. This is a reasonable good approximation, because the cells flow very close to the channel centre and it is assumed that the viscosity does not vary significantly on the length scale of the deformed cell. Accurate LBM simulations of strongly shear thinning fluid are difficult to achieve and a field of ongoing research [163].

7.2.2 Analysis of the red blood cell shape data

The numerical simulations output the full three-dimensional shape of the RBC at different positions along the channel length. Following the experimental results, the key cell features extracted in the analysis are the two-dimensional cell area or cell size A and the deformation D of the cell. The cell size A is defined as the two-dimensional area of the convex hull of the cell contour, the length of the hull contour is l. From these two the non-dimensional deformation D of the RBC is calculated as

$$D = 1 - \frac{2\sqrt{\pi A}}{l}. \tag{7.1}$$

This measure is zero for a circular shape and approaches one for a degenerate ellipse whose eccentricity approaches one, i.e. a line. Computation of the convex hull was done using SciPy's *ConvexHull* class, based on the Qhull library [164].

Another measure to characterise the deformed cell shape is its aspect ratio, here approximated as the ratio between the longer and shorter side of the cell contour's bounding box, in analogy to the procedure used in Shape-Out [158]. This is a reasonably good approximation because the cells are stretched primarily in flow direction as shown in figure 7.1.

In order to compute the convex hull, first the cell contour must be determined from the simulation output. The contour can be obtained from the three-dimensional shape in two different ways, illustrated in figure 7.3. The straightforward approach is to project all the surface points of the RBC onto the x-y-plane and compute the contour of these, as shown in the left images in figure 7.3(a,b). The second approach is to consider only a small slice of the RBC of ±1 µm around the channel centre in z-direction, and project the surface points of this slice onto the x-y-plane. This is

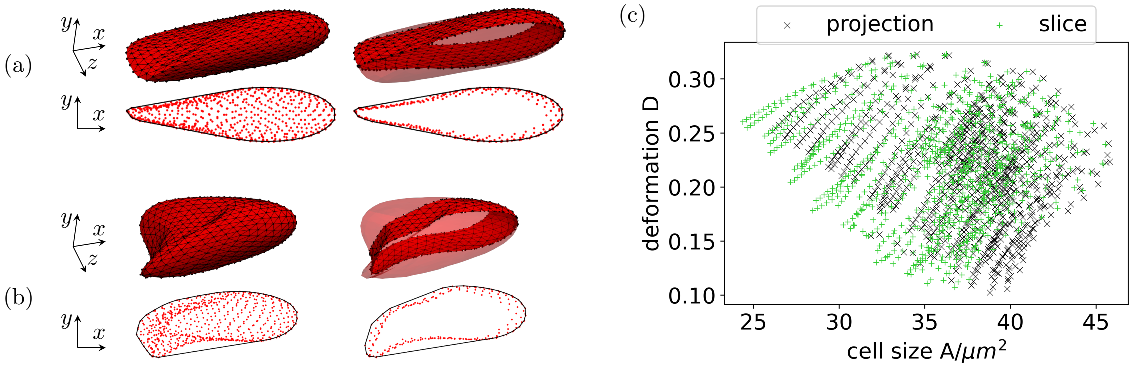

Figure 7.3: Extraction of the cell features from the simulation. (a,b) Two examples of deformed RBCs illustrate how from the three-dimensional shape (first row, respectively) the cell contour (black line in the second row images, respectively) is extracted. The red points illustrate the projection of the selected surface points onto the x-y-plane. The left images show the projection method, the right images the slice method. (c) The different methods lead to differences in the results for the cell features size and deformation. Here the data from all valid simulations is included.

illustrated in the right images in figure 7.3(a,b). The second approach is motivated by the experimental imaging technique, where the focus lies in the channel centre and only a slice of thickness 2 µm around it is recorded. For elongated RBCs as the one shown in figure 7.3(a), the difference between projection and slice method is small. If, however, the RBC shows a complex deformed shape, exemplified in figure 7.3(b), the contours calculated from the two methods differ visibly. An overview over all valid simulation results is given in figure 7.3(c), excluded are only those cells which have an aspect ratio smaller than 2, in accordance with the experimental analysis. The deformation is plotted against the cell size for the projection method (grey) and the slice method (green). In general, the projection method leads to larger cell sizes because more surface points are included. The range of the observed deformations is hardly affected. The two methods lead to different results especially for RBCs which show a small deformation, i.e. are closer to a circular shape, in combination with a small cell size. This is consistent with the observations made for figures 7.3(a,b). The results shown in figure 7.3(c) belong to RBCs flowing near the channel end around $x = 240$ µm, compare figure 7.2(b). For the analysis in the following sections the slice method is used because it is conceptionally closer to the experimental analysis.

The automatised output of the experimental analysis with Shape-Out described in section 7.2.1 is the two-dimensional image of the cell as shown in figure 7.4(a), cropped to a length in x-direction of around 80 µm, together with the detected cell contour (drawn in blue). The Shape-Out analysis algorithm directly cuts channel images to small parts in x-direction, which include the single cells. Therefore it is not possible to directly observe changes in the aggregated cell features along the

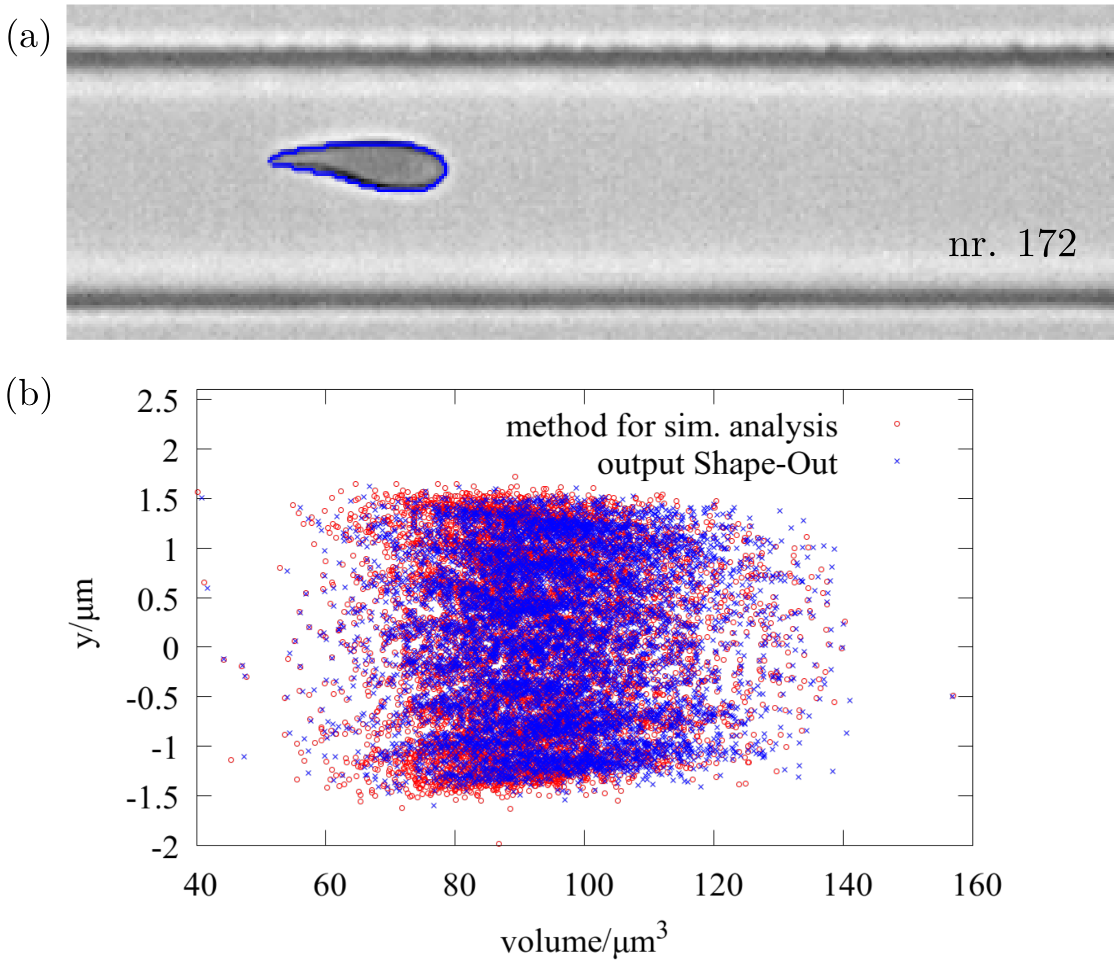

Figure 7.4: Results of the analysis of the experimental cell shapes for different methods. (a) Cell image and contour in the Shape-Out output. (b) Comparison of the y-position and volume results for the experimental data. The blue points show the results for the RBC features in the Shape-Out output, the red points are computed with the method used for the simulation analysis, which is applied on the experimental data. Experimental data provided by F. Reichel (member of the group of J. Guck at MPL in Erlangen).

whole channel length and compare them to simulation results, where slight changes along the channel are observed. In addition, Shape-Out directly provides a list of computed cell features, such as the cell size, deformation, volume and y-position of the cell in the channel. For the volume computation, rotational symmetry of the RBC is assumed. Applying the simulation analysis method described above on the experimental data leads to perfect agreement of the cell size and deformation results with the cell feature data from Shape-Out, which uses the same computation routine.

Apart from the deformation and size, an analysis routine for the y-position in the channel and the volume of the cell has been developed. The y-position is computed as the mean of the cell surface points. For the volume computation first the principle axis of the cell contour is calculated. Then the cell contour is divided into a lower and upper half by the principal axis. Assuming rotational symmetry of the cell around the principal axis separately for these two halves of the cell allows the calculation of the RBC volume. Finally these two volume results are averaged to obtain an estimate for the RBC volume. The position and volume calculation methods are also applied to the experimental cell contour and compared to the direct feature output by Shape-Out in figure 7.4(b). Here slight differences between the two methods are observed although the overall agreement is satisfactory. The figure shows, that for all offset position in the channel the volume scatters broadly. Note that the stripes in the data in the y-direction are due to the image resolution in the experiments. Due to the volume conservation of RBCs in simulations the volume is identical for all cells. If the volume is computed based on the two-dimensional cell contour, however, the results also scatter broadly. The rotational symmetry for the cells is an inaccurate assumption, as will be shown below. Moreover, in experiments the volume is directly obtained from the cell size measurement which is already used for comparison. Therefore, the volume computation was not pursued further for this study.

7.3 Deformation of the red blood cells in the channel

7.3.1 Comparison of the shape data

The deformed cell shapes in the numerical simulations very well match the experimental observations. Different examples are shown in figure 7.5. In the first row the experimental images are overlaid with the cell contour from simulations (in red). A visualisation of the full three-dimensional shape of the cells is shown in the second row in figure 7.5 from the same observation perspective as in the experiments. In the third row the same cell shapes are shown rotated by 90° around their long axis. Note that the simulation with small membrane viscosity $Bq = 5$ shown in (b) shows a tendency towards becoming unstable. Due to the asymmetric channel inlet and the orientation of the cell before the channel entrance, the cell has formed a flattened cell rear. The simulation results shows that the rotational symmetry assumption for the deformed RBCs is not applicable. If this assumption is used to calculate the volume of the cell, however, the error is expected to be small, because the rear of the cell contributes much less to the volume than the larger front part.

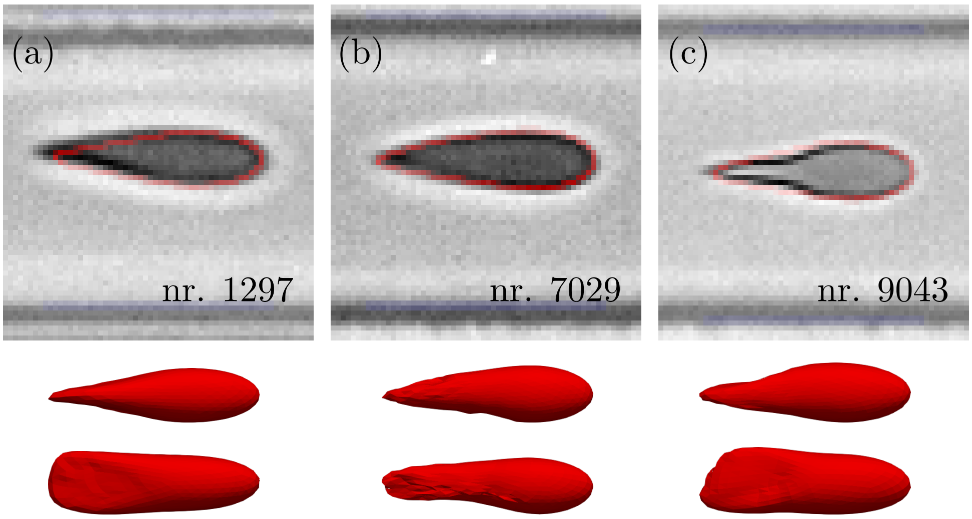

Figure 7.5: Comparison of deformed red blood cell shapes in experiment and simulation. The cell images from different RBCs (numbers are added in the images) in the experimental measurement series are overlaid with fitting cell contours from the simulations in red (first row). The second row shows the full 3D shape from the simulation from the same point of view. The third row shows the respective cells from the top view, i.e. rotated by 90° around the x-axis. The respective simulations differ in the initial shape, the viscosity contrast λ, the membrane viscosity Bq and the initial y-position. The properties in the simulations are (a) discocyte initial shape with $\lambda = 2$, $Bq = 6$, $y_{\text{init}} = 0.1$ (b) slipper initial shape with $\lambda = 2$, $Bq = 5$, $y_{\text{init}} = 0.1$ (c) slipper initial shape with $\lambda = 3$, $Bq = 9$ and $y_{\text{init}} = 0.5$. Experimental image data provided by F. Reichel (member of the group of J. Guck at MPL in Erlangen).

7.3.2 Comparison of the statistical data

Apart from the direct shape comparison for single cells, the cell feature data for all measurements and simulations can be compared. Figure 7.6(a) shows the cell deformation plotted against the cell size. Each blue cross is one experimental cell measurement, the simulation results (green points) are superimposed on these. The simulations cover most of the experimentally observed range, except for observations with very large cell sizes. The second observation is that the simulation results at small deformations of 0.1 to 0.15 are not observed in experiments. The RBCs at small deformations are more spherical and have a smaller aspect ratio, as is shown in figure 7.6(b). The aspect ratio and the deformation both measure the sphericity of the cell and the plots therefore show a high correlation between these two. The colour encoding of the simulation results shows, that higher membrane viscosity is associated with smaller deformation, i.e. less cell elongation and smaller cell size. The second effect must be due to a different allocation of the cell mass perpendicular to the observation plane for different Bq.

A visualisation of the deformation D and the cell size A depending on the y-

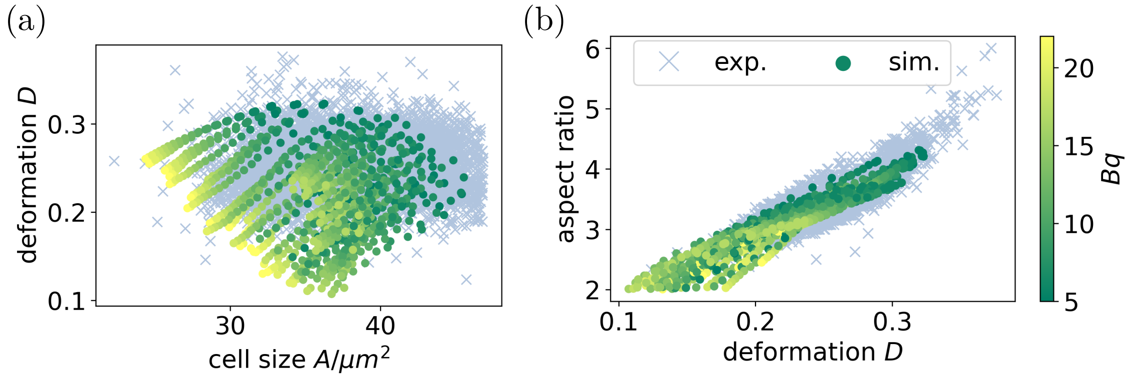

Figure 7.6: Comparison of the statistical data for the cells' size and deformation measures. (a) The deformation D is plotted against the cell size A. (b) The aspect ratio of the shape is plotted against the deformation D. The blue crosses represent the measurement points for single cells from the experiment. The greenish yellow points represent all simulation results, including both initial shapes slipper and discocyte. The colour encoding shows the Boussinesq numbers used in the simulations.

position of the RBC is given in figure 7.7, again showing the experimental data in blue and superimposed the simulation results in greenish yellow. In both plots, clusters around different y-positions are clearly distinguishable. These stem from the seven different initial positions y_{init} listed in section 7.2.1. This leads to the conclusion that inside the channel, there is very little cross-streamline migration of the RBCs. Figure 7.7(a) shows that RBCs which start far off-centre show a smaller deformation D. These are more spherical and rarely observed in experiments. The plot also shows that the simulations do not capture the highly deformed cells at larger y-position recorded in the experiment. The focusing of the cells in the flow before the channel entrance in experiments is complicated and not in detail replicated in the simulations, compare section 7.2, which also influences the cell shape at the entrance. For the off-centred initial position, these differences are expected to be more relevant and could thus explain the mismatch between experimental and simulation results at larger y-position. Figure 7.7(b) shows that the cell size variation in experiments is covered by the simulations. The experimentally observed sizes, however, are independent of the y-position, while in simulations a tendency towards larger sizes for larger offsets is observed. For larger y-offset the deformation decreases as discussed for 7.7(a), i.e the hull of the cell contour is more spherical. This is illustrated in the RBC example in figure 7.3(b). The two-dimensional cell size is approximated as the area of the convex hull, therefore, a more spherical deformation as in the example is associated with an increase in the cell size, which can explain the correlation observed in figure 7.7(b) for the simulations.

Another experimental study by Reichel et al. [165] uses the RT-DC setup to in-

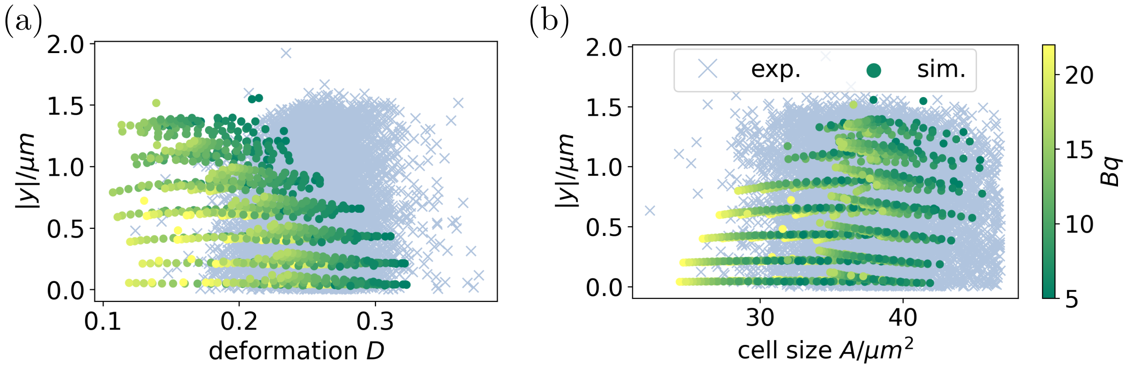

Figure 7.7: Comparison of the statistical data for the cells' size and deformation depending on the cross-stream position. Experimental (blue crosses) and simulation data (greenish yellow points) for the y-position relative to the channel center plotted against (a) the deformation D and (b) the cell size A. The colour bar shows the Boussinesq number belonging to the respective simulation.

vestigate changes in blood cell deformability in a neurodegenerative disorder and the influence of drug treatment. In addition, the study presents results for RBCs treated with diamide, which crosslinks the proteins of the cell's spectrin network. The authors find that both the cell size and the deformation of the cells decrease for large diamide concentrations. For smaller concentrations the opposite effect, albeit small, on the deformation was observed. An overview of the results is shown in figure S3 in the supplementary material of the publication [165]. The cell size decreases by up to 7 %, the deformation by up to 15 % for the largest diamide concentration, with the values for intermediate concentrations in between. The linking of the proteins of the cytoskeleton adds additional stiffness, in simulations represented by a larger shear modulus κ_S of the RBC, compare section 2.2. The magnitude of the change in κ_S induced by different concentrations of diamide remains unexplored, as measurement results of the shear modulus even for healthy, unmodified RBCs are difficult to obtain. One additional series of simulations with larger shear modulus $\kappa_S \times 3$ has been run, the results are shown in appendix F.1 in figure F.1. The stiffer RBCs show the same trend as the experiments with smaller cell sizes and smaller deformations for all simulation pairs. The areas decrease by around 3 % to 5 % and the deformations between 2.5 % and 4 % for the different initial positions.

7.4 Inference of the cell properties from the statistical data

7.4.1 Method 1: Weighting of the simulation points with the frequency of the attributed experimental observations

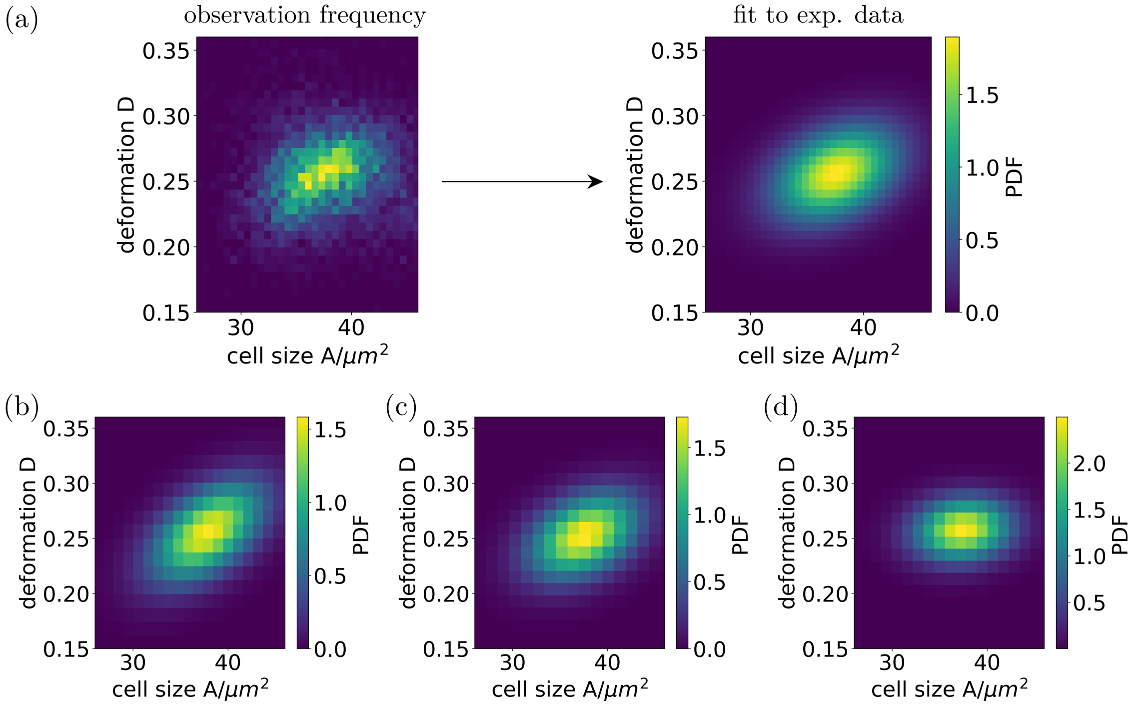

Figure 7.8: Fits of the distribution of the observables in experiments. (a) The observation frequencies of different deformation and cell size combinations (left plot) is used to fit a two-dimensional Gaussian distribution to the full experimental data (right plot), on a grid of 40 × 40. (b-d) The fit is limited to data points of cells with a distance to the channel centre (b) smaller than 0.5 µm (c) between 0.5 µm and 1 µm and (d) beyond and including 1 µm. Here a grid of 20 × 20 is used to fit to the fewer experimental observations.

In the previous section 7.3 the qualitative comparison of the shape and statistical deformation data showed good agreement between simulation and experiment. The scattering of the simulation data arises from the cell property variation, which is due to the biological variability of the RBCs, and from different initial conditions. These two factors in experiments also lead to a scattering of the results, together with the measurement error. From the simulations, however, the relation between RBC property and resulting observable, e.g. deformation or cell size, can be obtained.

The purpose of this section is to infer information about the distribution of the cell properties from the statistical data by using the informations provided by the simulations. The procedure is as follows. First, the experimental observation frequency in the two-dimensional space of cell deformation versus cell size shown in figure 7.8(a), is fitted with a two-dimensional Gaussian distribution. In the second step this distribution is used to assign to the simulation results a likelihood of their occurrence. This is then transferred to a likelihood for the respective parameter combination.

fig. 7.8(a) all data	fig. 7.8(b) $\lvert y\rvert < 0.5\,\mu\mathrm{m}$	fig. 7.8(c) $0.5\,\mu\mathrm{m} \leq \lvert y\rvert < 1.0\,\mu\mathrm{m}$	fig. 7.8(d) $1.0\,\mu\mathrm{m} \leq \lvert y\rvert$
$\bar{A} = 37.6\,\mu\mathrm{m}^2$ $\sigma_\mathrm{A} = 3.7\,\mu\mathrm{m}^2$	$\bar{A} = 37.9\,\mu\mathrm{m}^2$ $\sigma_\mathrm{A} = 3.9\,\mu\mathrm{m}^2$	$\bar{A} = 37.5\,\mu\mathrm{m}^2$ $\sigma_\mathrm{A} = 3.8\,\mu\mathrm{m}^2$	$\bar{A} = 37.4\,\mu\mathrm{m}^2$ $\sigma_\mathrm{A} = 3.4\,\mu\mathrm{m}^2$
$\overline{D} = 0.256$ $\sigma_\mathrm{D} = 0.024$	$\overline{D} = 0.256$ $\sigma_\mathrm{D} = 0.030$	$\overline{D} = 0.253$ $\sigma_\mathrm{D} = 0.026$	$\overline{D} = 0.258$ $\sigma_\mathrm{D} = 0.019$
$r_\mathrm{A,D} = 0.34 \pm 0.01$	$r_\mathrm{A,D} = 0.51 \pm 0.02$	$r_\mathrm{A,D} = 0.37 \pm 0.02$	$r_\mathrm{A,D} = 0.10 \pm 0.02$

Table 7.1: Overview of the results of the multivariate Gaussian distribution fitted to the experimental data. The mean cell size $\bar{A}$ and deformation $\overline{D}$ are listed together with the respective standard deviations σ_A, σ_D for the different data sets from figure 7.8. In the last line the correlation coefficient from the fit is given, together with its standard deviation from the fitting procedure.

The first step is illustrated in figure 7.8(a). The observation frequency of the observables (left) is fitted with a Gaussian distribution (plot shown on the right) using the SciPy method `curve_fit` [166]. The fit again shows the positive correlation between deformation and cell size. As discussed in the previous section, the simulations show that the y-coordinate of the RBCs in the channel is crucial for the observed deformation and size, compare figure 7.7. Therefore, the fitting procedure is repeated for different parts of the experimental data, separated by their y-coordinate in the channel. The results are shown in figure 7.8(b-d), where the grid for the fit is coarser than in (a), due to the decrease in the number of included experimental observation points. Table 7.1 summarises the fitting results, i.e. the results for the multivariate Gaussian distribution. The mean value of cell area and deformation $\bar{A}$ and $\overline{D}$ do not vary significantly if the cells are separated by their y-coordinate, the same is true for the related spreads measured with the standard deviations of the distributions σ_A and σ_D. This is in line with the observations in figure 7.7 although it does not directly follow from it. The computed correlation $r_\mathrm{A,D}$, however, decreases strongly for the cells which flow off-centred. This difference is reflected in the plots in figure 7.8. The standard deviation of the correlation from the fitting procedure - not to be confused with the standard deviation of the Gaussian distribution - is added in the table, which is related to the uncertainty of the fit. For the mean values and standard deviations this measure for the fit uncertainty is only around or below 1 % of the respective result in table 7.1 and therefore not listed. The correlation for the most off-centred positions has the largest uncertainty.

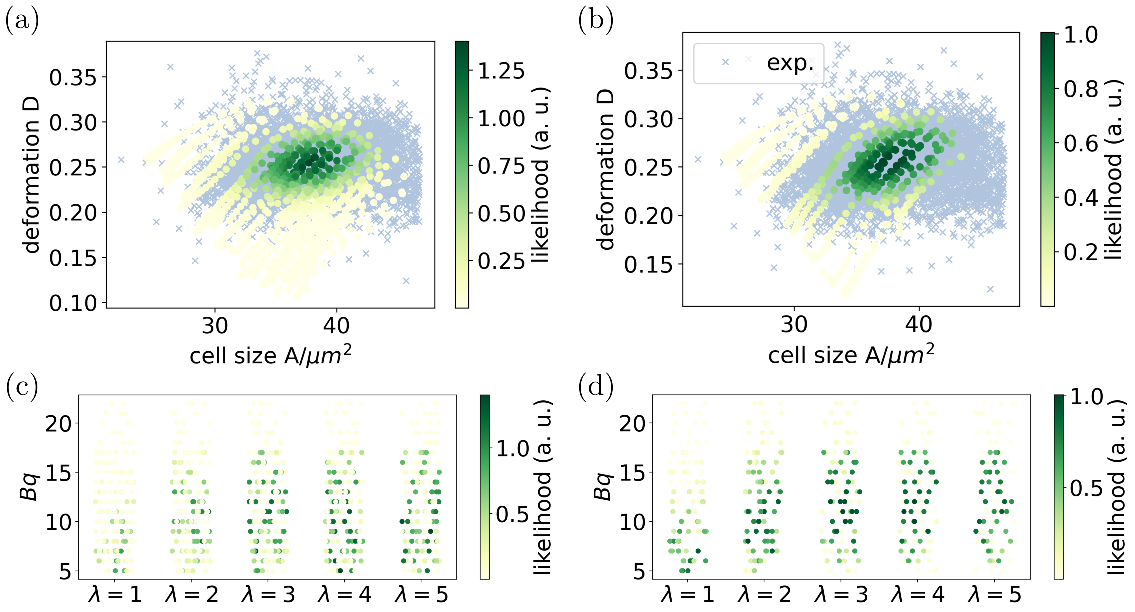

Figure 7.9: Weighting of the simulation points with their likelihood based on the experimental results. Likelihood of the respective simulations (a,b) in the space of the observables and (c,d) in λ-Bq space. The left column (a,c) shows the results including all simulations and weighted with the experimental distribution from figure 7.8(a). The right column includes only those simulations started at the three smallest y_{init}-positions, corresponding to y-positions with $y \leq 0.5\,\mu\text{m}$, and accordingly weighted with the results from figure 7.8(b).

The results of the second step are shown in figure 7.9. All single simulation points are weighted with their likelihood according to the respective fitted experimental distribution. The first plot 7.9(a) shows the same data as figure 7.6(a) but weighted with the fit result from figure 7.8(a), the resulting likelihood of the simulation points is colour coded. In the second plot 7.9(b) the simulation results are restricted to those y-positions closest to the channel centre and thus the fit from figure 7.8(b) is used for the weighting. The discussion in section 7.3.2 showed that this subset at small y-positions of the results is best suited for comparison and further analysis. The second line of plots shows the weighted simulation results for the respective first plot in parameter space, λ plotted versus Bq. The spread around the different values of λ on the x-axis is chosen randomly for illustrative purposes only, to prevent complete overlapping of the simulation points at same λ and Bq.

Figure 7.9 shows that the full set of results on the left and the subset at centred cell positions on the right lead to a similar pattern in the parameter space. Intermediate values of Bq for $\lambda \geq 2$ tend to have larger likelihood values. For the subset of RBCs in figure 7.9(d), as expected, a clearer picture emerges, because experimental and simulation results are better matched. The maximal likelihood values predominantly appear between $Bq = 10$ and $Bq = 15$ around $\lambda = 3$, however, unambiguous assignment is not possible and results related to small likelihood values also appear at these positions. The interpretation of these observations is the following: Those λ-Bq combinations with (more) darker green points are *more likely* because for some initial condition they lead to observation values D and A which are frequently observed in experiments. However, these λ-Bq combinations can also lead to observation values which are less frequent (light green beige points). In general, it would be incorrect to average over the likelihood of the simulation results in the λ-Bq space, because the location and density of these points is arbitrarily chosen and the result of this averaging depends on this choice of simulation points.

7.4.2 Method 2: Estimation of the parameter distribution

The second method aims at a more quantitative and precise characterisation of the cell parameter distribution. After some assumptions are made, this method estimates the parameter distribution from the simulation and experimental results.

Parameters can be cell properties such as λ and Bq but also initial conditions such as the cell position y_{init} and the initial shape of the cell can be included. An experimental measurement of one cell in this framework is perceived as a random draw of a parameter combination from a random distribution, and experimental noise is neglected, i.e. experimental scatter is assumed to be caused by heterogeneity in the initial conditions and the properties of the cells. First, assumptions about the shape of these distributions have to be made. Here for the initial cell shape, a discrete parameter, equal probabilities for both discocyte and slipper are assumed and for the continuous y_{init} a uniform distribution is assumed. The continuous quantities λ and Bq are modelled with a multivariate Gaussian distribution, which is biologically motivated by the assumption, that biological cell properties scatter around a mean value. This distribution is determined by the means $\overline{\lambda}$, $\overline{Bq}$, the respective standard deviations σ_λ, σ_{Bq} and the correlation coefficient $r_{\lambda,Bq}$. Apart from λ and Bq, independence of the parameters is assumed. The initial cell shape, for example, is assumed not to correlate with the initial position.

Observables in this setup are the cell area A and the cell deformation D, which are both continuous and summarised as $\boldsymbol{f} = (A, D)$. From experiments, we determine the first two moments of the joint observable distribution by fitting a two-dimensional

Gaussian distribution in figure 7.8, the extracted values are given in table 7.1 and are in the following abbreviated with the vector of means $\overline{\boldsymbol{f}}_{\mathrm{exp}}$ and the corresponding covariance matrix $\boldsymbol{M}_{\mathrm{exp}}$ of the cell deformation and cell area. In simulations, the cell parameters are chosen beforehand, on a regular grid as discussed in 7.2.1. The observables depend on these parameters, we abbreviate $A \coloneqq A(\lambda, Bq, y_{\mathrm{init}}, \dots)$, $D \coloneqq D(\lambda, Bq, y_{\mathrm{init}}, \dots)$.

Now, to compute the vector of means $\overline{\boldsymbol{f}} = (\overline{A}, \overline{D})$ and corresponding covariance matrix $\boldsymbol{M}$ of the observables from all simulations, the integrals

$$\overline{\boldsymbol{f}} = \int \mathrm{d}\lambda \; \mathrm{d}Bq \dots \; \boldsymbol{f} \; \Pi\left(\lambda, Bq, \dots\right) \tag{7.2}$$

$$\boldsymbol{M} = \int \mathrm{d}\lambda \; \mathrm{d}Bq \dots \; \left(\boldsymbol{f} - \overline{\boldsymbol{f}}\right) \left(\boldsymbol{f} - \overline{\boldsymbol{f}}\right) \; \Pi\left(\lambda, Bq, \dots\right) \tag{7.3}$$

must be computed. Here the probability density function $\Pi\left(\lambda, Bq, \dots\right)$ depends on all varied simulation parameters, i.e. λ, Bq, y_{init} and the initial shape, over which the integrals (for discrete parameters substituted by a sum) run. As discussed above, Π contains a multivariate Gaussian distribution for Bq and λ and a uniform distribution (discrete or continuous) for the remaining parameters. The integration in λ-Bq space is computed over the simulation grid, on which the parameter values and results for the observables are known. For the numerical integration the trapezoidal rule is used, details are given in appendix F.2.

Finally, an iterated fitting routine is used to find the best fit for the unknown parameters $\overline{\lambda}$, $\overline{Bq}$ and their standard deviations and correlation σ_λ, σ_{Bq}, $r_{\lambda,Bq}$ in the probability distribution Π, by matching simulation and experimental results. This is done with a standard non-linear optimisation method which minimises the discrepancies between $\overline{\boldsymbol{f}}$, $\boldsymbol{M}$ and the respective experimental values $\overline{\boldsymbol{f}}_{\mathrm{exp}}$, $\boldsymbol{M}_{\mathrm{exp}}$. Note that while for the distribution of the *parameters* it is necessary to assume a shape of the probability distribution Π, for the *observables* only the first two moments, means and (co)variances are used and computed. In particular, this means that the full distribution is not computed and representation of the results as a two-dimensional Gaussian distribution in A-D space is an additional assumption, which is useful for visualisation of the results. Note that for the integration in the iterated fitting routine, start values for the unknown quantities $\overline{\lambda}$, $\overline{Bq}$, σ_λ, σ_{Bq}, $r_{\lambda,Bq}$ in the probability distribution Π must be set.

The database used for this second method here is the subset shown in figures 7.8(b) and 7.9(b,d), these are the cells with a centre of mass distance smaller than 0.5 µm in experiments, in simulations the respective cells start at the three smallest y_{init}-positions. In figure 7.8 it was shown that there is a noticeable difference between the cell subsets and therefore it is appropriate to separate the data according to the cell position and match the respective subsets from experiment and simulation.

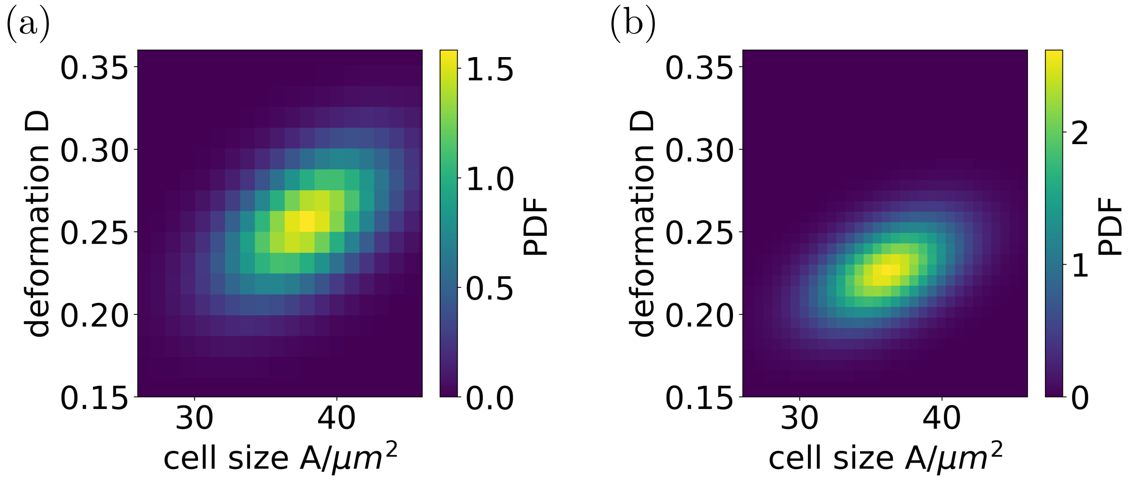

Figure 7.10: Observables distribution from the parameter distribution estimation. (a) The fit to the experimental data in figure 7.8(b) is repeated here for comparison. (b) Estimation of the distribution of area and deformation from the fitting of the simulation data. The predicted values are $\bar{A} = 36.2\,\mu\mathrm{m}^2$, $\sigma_\mathrm{A} = 3.26\,\mu\mathrm{m}^2$, $\overline{D} = 0.226$, $\sigma_\mathrm{D} = 0.021$, $r_\mathrm{A,D} = 0.46$, they are visualised as parameters of a two-dimensional Gaussian distribution.

A result of the fitting procedure is visualised in figure 7.10. A discussed above, the results of the fitting are estimates of the means and (co)variances of the observables A and D. These are visualised in figure 7.10(b) by plotting a Gaussian distribution with these parameter values, which can easily be compared to the experimental result in (a), repeated from the previous section. The mean deformation and area estimates are slightly smaller than the experimental result, as well as their standard deviations. The correlation coefficient is also smaller, which is clearly visible comparing the two plots in figure 7.10. This fitting method returns estimates for the RBC parameters, unobservable in experiments, which are $\overline{\lambda} = 2.0$, $\overline{Bq} = 14.4$, $\sigma_\lambda = 1.0$, $\sigma_{Bq} = 6.0$ and $r_{\lambda,Bq} = 0.92$. Comparing these results with the previous section shows that the mean and standard deviation values are well compatible with the findings of the previous section 7.4.1. However, for the correlation between λ and Bq a comparably large value near 1, the completely linear correlation, is observed. The interpretation of this observation is that for cells with a large λ, a large value for Bq is also to be expected. This is a plausible statement, considering that both variables describe viscosity contributions, which might increase with increasing cell age.

Evidently, method 2 returns plausible results for both observable and parameter values. Closer examination of the fitted values, however, reveals that the mean and standard deviation results for λ are identical to the lower bound for each parameter, which is necessarily set during the optimisation routine, and the standard deviation of Bq is at its upper bound. Therefore, variation of the bound for the variables can crucially influence the fitting outcome, which, in addition, is also true for the start values for the probability distribution. Moreover, it is found that technicalities of the fitting process also influence the outcome of the fitting routine. These include changes in the definition of the minimised quantities, for example whether the discrepancy of standard deviations and correlation coefficient, as opposed to the discrepancy of variances and covariance, is minimised. The normalisation of the computed discrepancies with the constant experimental values is another influencing factor. Therefore, while this second method presented in this section is technically interesting, further investigation is necessary to reliably estimate the observables and parameter distribution.

7.4.3 Outlook

One possible extension of the method is the combined fitting of the different data subsets, which are delimited by different values of the cells' position in the channel, compare figure 7.8. If this approach is pursued, the assumption of a uniform initial position distribution must be adapted.

Regarding the analysed cell parameters, this set could be extended to include additional parameters or broaden the range on which the existing parameters vary, e.g. including other initial shapes. Moreover, additional correlations could be included, for example the initial shape might correlate with the initial position or the viscous properties of the cell, which determine the speed of shape changes.

An observable, which was left out in the analysis, is the cell's position in the channel, because it is very strongly correlated with the initial position in simulations. Very useful for the analysis would be to have an observable, which is sensitive to only one of the parameters λ and Bq and could thus allow isolation of the respective parameter distribution. Another approach could be to include not only the first two moments of the observable distribution from experiments, but also higher moments.

An altogether different approach regarding the simulations could be to use a Monte Carlo method for the cell parameter distribution. The disadvantage of this approach would be that existing simulations cannot be reused and a large number of new simulation runs is necessary.

7.5 Discussion and conclusion

One major challenge of the experimental-numerical comparison are the variations in the experimental setup. The channel geometry and general measurement architecture remain the same, however, the flow conditions such as flow rate, properties of the buffer solution and selection of RBCs (donors health, artificially stiffened cells etc.) can be varied easily in experiments. In simulations, however, such changes would require re-running of all simulations with adapted parameters. A further experimental study is from Kubánková et al. [11], who investigate RBCs from healthy but also from COVID-19 patients, using the same flow rate of $0.06\,\mu\mathrm{l\,s}^{-1}$ as used for the data presented above. The medium, however, has a higher percentage of methyl cellulose (0.84% MC) and thus a viscosity in rest of $\mu_\mathrm{o} = 60\,\mathrm{mPa\,s}$. Following the approach discussed in section 7.2, this leads to an effective outer viscosity of $\mu_\mathrm{o}^\mathrm{eff} = 6.75\,\mathrm{mPa\,s}$. As a result, Kubánková et al. [11] report higher RBC deformations. Moreover, the raw data [11] shows a concentration of the cells in one half of the symmetric channel, in contrast to the data analysed above, possibly due to changes in the measurement analysis or calibration during data evaluation. The study by Toepfner et al. [156] has the same viscosity of the medium as describe in section 7.2.1 but the total channel flow rate is higher with $0.12\,\mu\mathrm{l\,s}^{-1}$. Walther et al. [157] investigate the connection between depressive disorders and the morphological features of blood cells under flow with the RT-DC setup. In this study the flow properties are the same as summarised in section 7.2.1, the cell deformations results are shown in boxplots.

In general, the analysis of the data is very sensitive to inaccuracies in the length scaling, which influences the cell size axis and could shift the fitted experimental distribution relative to the simulation results, visible e.g. in figure 7.9, where precise comparison is necessary.

The first method in section 7.4 allows to determine the range of the RBC parameter values, while the second method aims at a quantitative estimate of the parameter distribution from dynamic measurements and simulation results of deformed RBCs. Possible future modifications and improvements are outlined in section 7.4.3.

Another direction of future studies could be the implementation of membrane viscosity also for the LBM, which allows simulation of larger Reynolds number systems. Moreover, the combination of the viscoelastic RBCs with a shear thinning fluid could be treated with this method.

8 Cell-free layer of red blood cells in a constricted microchannel under time-dependent flow

8.1 Overview

The last chapter of this work picks up on chapter 3, where the dynamics of single RBCs in time-dependent flow has been discussed. The focus here lies on the collective behaviour of RBCs instead of the single cell dynamics.

In the small vessels of the microcirculation, RBCs form a core flow, leaving a small cell-free layer (CFL) at the walls [167, 168]. The CFL has been studied in both experiments [169–172] and numerical simulations [173–182], showing that flow rate, haematocrit, channel size and RBC parameters influence the formation and size of the CFL. The CFL in turn is an important factor influencing the blood separation at vessel branches, the particle and leukocyte transport in the blood, or the oxygen exchange with the surrounding tissue [72, 169, 173, 174, 183]. Constricted channel geometries are of special interest because they serve as a model for blood vessels with a stenosis which hinders the blood circulation. Studies which investigate the CFL in constricted channels [171, 175, 179, 182, 184] focus on steady flow or technical applications for the extraction of blood plasma [185–187]. The aim of the work presented here is to extend the investigation to time-dependent flow in constricted channels.

Here the CFL around a constriction in a rectangular microchannel is investigated. Section 8.2 gives an overview of the method used. First, benchmark simulations for steady flow in the constricted microchannel are carried out, these are presented in section 8.3. In the next section 8.4 the results for time-dependent flow through the constriction are discussed. The results described in this chapter have been published in the joint paper [188], all experimental results were provided by S. M. Recktenwald (member of the group of C. Wagner in Saarbrücken).

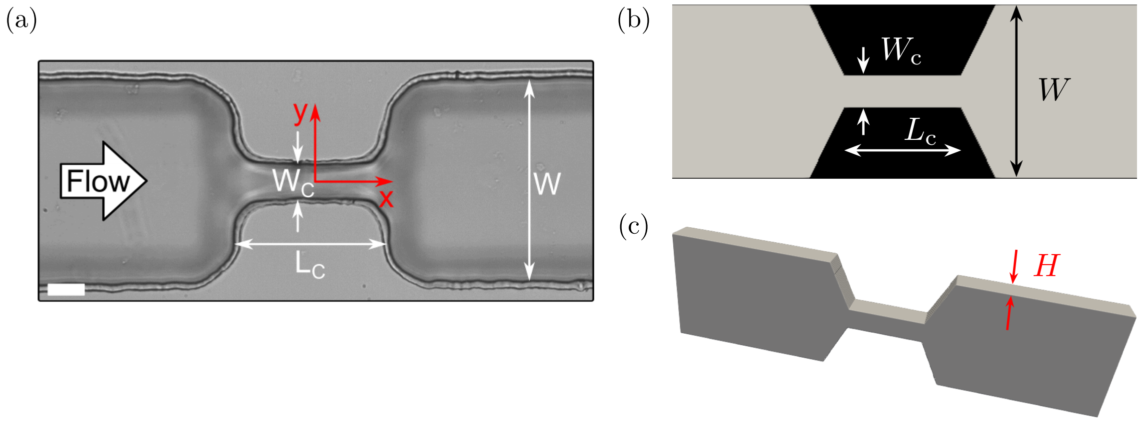

Figure 8.1: Constriction geometry in experiment and simulation. (a) Experimental channel section around the constriction. Reprinted from [188] with permission from APS. (b) Discretised simulation channel in plane view, reproduced from [188] with permission from APS. (c) Three-dimensional image of the simulated channel.

8.2 Methods and setup

8.2.1 Numerical simulations

The simulated channel was modelled after the microfluidic constriction used in experiments, which is shown in figure 8.1(a). In figure 8.1 the channel geometry is shown in (b) in plane view around the constriction and in (c) three-dimensionally over the whole simulated length. The width of the channel pre- and postconstriction is $W = 211\,\mu\mathrm{m}$, it has a constant height of $H = 50\,\mu\mathrm{m}$ and the total length is $L = 832\,\mu\mathrm{m}$. The constriction has a length of $L_\mathrm{c} = 142\,\mu\mathrm{m}$ and is $W_\mathrm{c} = 38\,\mu\mathrm{m}$ wide. The slope of the inclined wall is 2. The cells are inserted at the channel entrance at randomised positions to mimic the inflow from a fluid reservoir. The feed-in haematocrit at the entrance is $Ht = 1\,\%$. When the cells have reached the end of the simulated channel they are removed from the simulation.

The fluid inside the channel is Newtonian with the dynamic viscosity of $\mu = 1.2\,\mathrm{mPa\,s}$ and a density of $\rho = 1\,\mathrm{g\,cm^{-3}}$ of blood plasma. The flow velocities at the channel centre under steady flow are $v_\mathrm{c} = 80\,\mathrm{mm\,s^{-1}}$, $120\,\mathrm{mm\,s^{-1}}$, and $160\,\mathrm{mm\,s^{-1}}$, larger flow velocity quickly lead to numerical instabilities at the constriction. This leads to Reynolds numbers (2.12) of $Re \approx 5.3, 8$ and 11, respectively. The characteristic length used for the calculation of Re is the hydraulic diameter of the channel $L = 2WH/(W + H)$, the density and viscosity are in good approximation the values of the plasma due to the small haematocrit of $1\,\%$. The time-dependent flow is modelled as a sinusoidal oscillation between the flow velocities $v_\mathrm{c} = 80\,\mathrm{mm\,s^{-1}}$ and $v_\mathrm{c} = 160\,\mathrm{mm\,s^{-1}}$ at the channel centre, i.e. with a relative amplitude of 0.33. This amplitude is a compromise between a significant velocity variation on the one hand

and on the other hand a sufficiently large lower velocity in relation to the channel size and oscillation timescale. The constant frequency of the oscillating flow is $f = 20\,\text{Hz}$. The dimensionless Womersley number Wo relates inertial effects from the pulsation to viscous effects and is defined as $Wo = L/2\sqrt{\omega\rho/\mu}$ [189], $\omega = 2\pi f$ is the frequency in radians. If the Womersley number is large $Wo > 1$, the viscous effects are dominated by inertia effects, which can lead to significant deviation from the steady Poiseuille flow profile. In simulations $Wo \approx 0.4$ and in experiments $Wo \approx 0.05 \ll 1$, as discussed in section 8.2.2 below. The numerical and experimental flow profiles under steady flow are in good agreement as shown in figure 8.2. Under pulsatile flow in simulations the flow profile oscillates in a regular fashion between the purple and orange curve in figure 8.2, therefore, one can conclude that the viscous forces dominate.

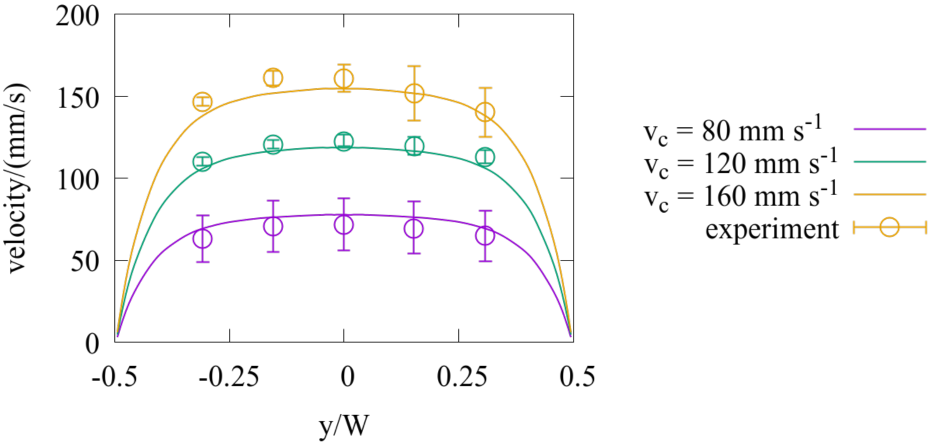

Figure 8.2: Flow profiles before the constriction in steady flow. Simulation (solid lines) and experiment (symbols) are in good agreement for different flow velocities v_c at the channel centre. The haematocrit is 1 %. Reproduced from [188] with permission from APS.

The simulation method is the three-dimensional LBM together with the IBM, implemented in the software package ESPResSo. Details of this method are described in section 2.4. The LBM-IBM is well suited for systems with larger Reynolds number $Re > 1$ and simulations run reasonably fast for larger channel geometries with many cells.

The RBCs are modelled as described in section 2.2. Their surface is discretised with 162 flat triangles per RBC. The shear modulus is $\kappa_\text{S} = 25 \times 10^{-6}\,\text{N}\,\text{m}^{-1}$, which is 3 to 5 times larger than the values usually used for RBCs, compare section 2.2. It is reasonable to expect that this modification has negligible influence on the collective behaviour of the RBCs. The stability of the cell under high shear stresses at the constriction entrance, however, is increased, such that the target velocities and Reynolds number Re can be achieved. The empirical area dilation modulus κ_A is set to $40\kappa_\text{S}$, the bending modulus is $\kappa_\mathrm{B} = 2 \times 10^{-19}\,\mathrm{N\,m}$ and the bending reference shape is flat. The viscosity contrast between cell interior and surrounding fluid is $\lambda = 1$. Because here the focus lies on the collective behaviour of a suspension of many cells and not on the detailed dynamics of a single cell the viscosity contrast is neglected. In the LBM implementation no viscous contribution of the RBC membrane is included.

8.2.2 Comparison to microfluidic experiments

An image of the channel geometry for the corresponding microfluidic experiments by from the group of C. Wagner is shown in figure 8.1(a) above. In front and behind the constriction section shown there, the channel continues for a length of 10 mm in both directions until it opens out into a reservoir. In the straight channel the RBC flow equilibrates and forms its CFL before reaching the constriction or the outlet reservoir. Due to the limitation of the total runtime, this cannot be mimicked in simulations. Moreover, the channel geometry in experiments is proportionally smaller by a factor of two, e.g. the constant channel height is 25 µm. The difference is due to the stability limitations in simulations, where very small constriction size leads to high shear rates at the constriction and thus instabilities of the triangulated cell membranes. As a consequence, the Reynolds numbers of experimental and numerical velocity profiles in figure 8.2 for each matching curve disagree by a factor of around two. Again for performance reasons, simulations were restricted to $Ht = 1\,\%$, i.e. to fewer cells in the system, and the oscillation frequency of the flow is larger by a factor 20 than the experimental 1 Hz. Compared to the velocity time scale, the $f = 20\,\mathrm{Hz}$ oscillation in simulations is slow enough, such that its effects can be observed separately, but it does not require a large increase in computation time.

8.2.3 Computation of the cell-free layer

For quantitative comparison it is necessary to develop a routine to compute the size of the CFL along the channel axis. An exemplary visualisation of the simulation result is shown in figure 8.3.

In experiments the CFL in steady flow is usually determined by stacking a multitude of images and thus detecting the region of the RBC core flow. Analogously, in simulations the analysis of data can be carried out on the basis of the graphical representation of the simulation results as shown in figure 8.3, using this experimental image stacking routine. The second possibility for simulation analysis is to use the numerical information of the cell node positions and construct the RBC core flow from these, which is called cell contour method in the following. The advantage of the first method is that direct comparison with the experimental results is possible, the disadvantage is that under pulsating flow it requires a large number of simulated periods. The results from both methods for the example from figure 8.3 are shown

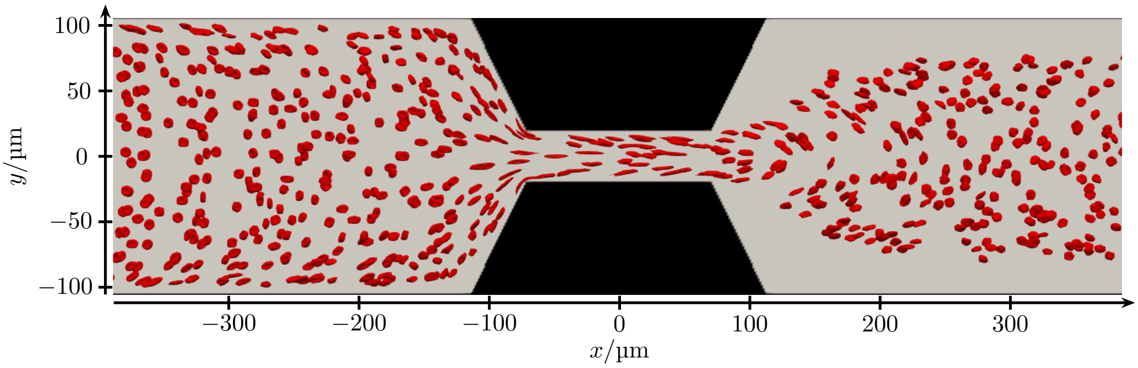

Figure 8.3: Snapshot of the red blood cell flow through the constriction in the simulation. The flow is constant and from left to right with centre flow velocity $v_c = 80\,\mathrm{mm\,s^{-1}}$. The haematocrit in the simulations is 1 %.

in figure 8.4(a) and compared to experimental results in (b). For the cell contour method the channel is divided in x-direction into bins approximately 10 µm wide. For the steady flow simulations inside each bin the cell surface position (considering all cells inside the respective bin) is determined, which is nearest to the upper/lower channel border, and then the minimal distance is taken. This is repeated for all time frames of the simulation and the minimum distance per bin over all frames gives the CFL(x). Because every cell membrane part of every RBC is considered over the whole simulation time, this method gives a CFL smaller than the image stacking method. In the image stacking routine a single RBC flowing closer to the wall might not contribute to the RBC core flow, because this detection mechanism is not sensitive enough to register singular events. For the sinusoidal flow simulations, in addition to the positional bins in the channel, one time period is divided into 50 time bins, in order to compute the CFL separately for different phases of the oscillating flow. The simulations run over more than one period, and all simulation frames are assigned to one of the 50 bins, which matches the phase of the frame. Then the steady flow cell contour method is used separately for each time bin, which gives a CFL(x) for each time bin.

Analysis of the experiments for oscillating flow follows the same principle, the technical details are complicated, these are presented in the joint work Recktenwald et al. [188].

Directly before and after the constriction not only the CFL but also large cell-free areas (CFA) can form, as can be seen in the channel snapshot in figure 8.3. The CFA pre- and postconstriction in the steady case and the CFA per time bin is obtained by numerical integration of the respective CFL result along the channel length. This is illustrated in the graphs in figure 8.4 with the shaded regions. Start point (preconstriction) and end point (postconstriction) of the integration are determined by the channel position, up to which the CFL is approximately constant, the respective second integration boundary is the constriction start/end. It should be noted that for consistent simulation data evaluation the fit boundary is chosen constant over the oscillation period. Comparison of the experimental and simulation CFL post-constriction in figure 8.4 shows that in experiments the CFL is smaller by a factor of around two, due to the smaller channel dimensions in all directions. Detailed comparison of the CFL development is not possible, because the channel length in simulations is significantly smaller than in experiments, such that the RBCs do not equilibrate before they reach the channel end.

The results from the oscillation simulations are based on 7 periods of sinusoidal flow, with around 1060 frames output per period for the CFL determination.

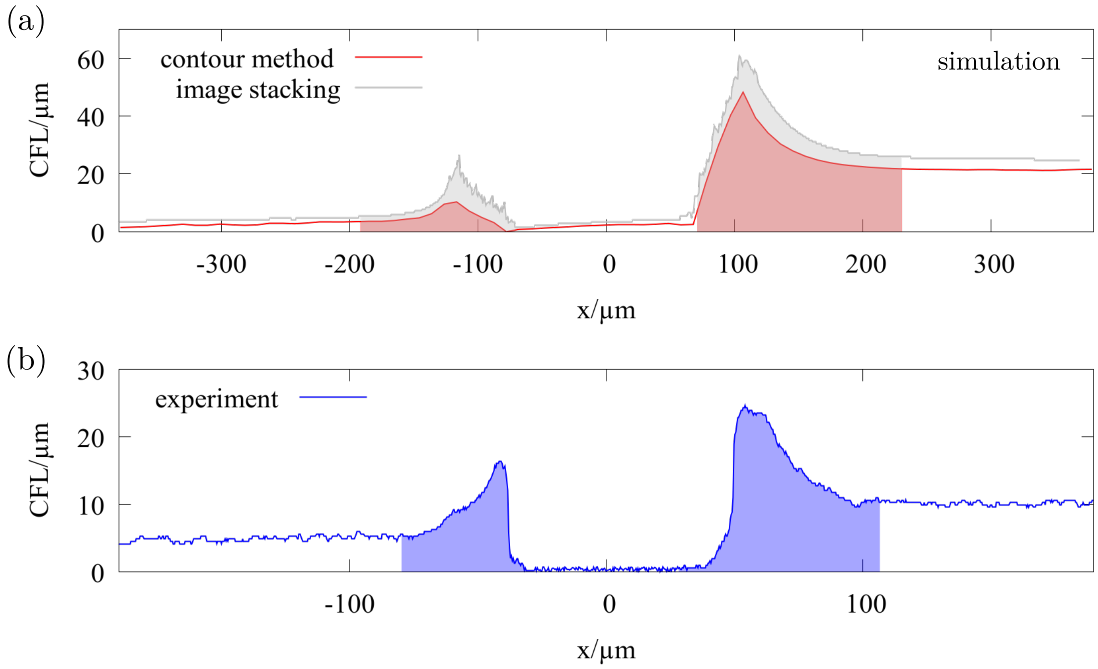

Figure 8.4: Exemplary cell-free layer (CFL) along the flow direction y at the constriction under steady flow. Contour method (red) and image stacking (grey) are used for the simulation analysis in (a). The corresponding experimental measurements (blue) are shown for comparison in (b). Flow velocity and pressure drop are $v_c = 80\,\mathrm{mm\,s^{-1}}$ and 250 mbar. The shaded regions correspond to the cell-free area post- and preconstriction. Reproduced from [188] with permission from APS.

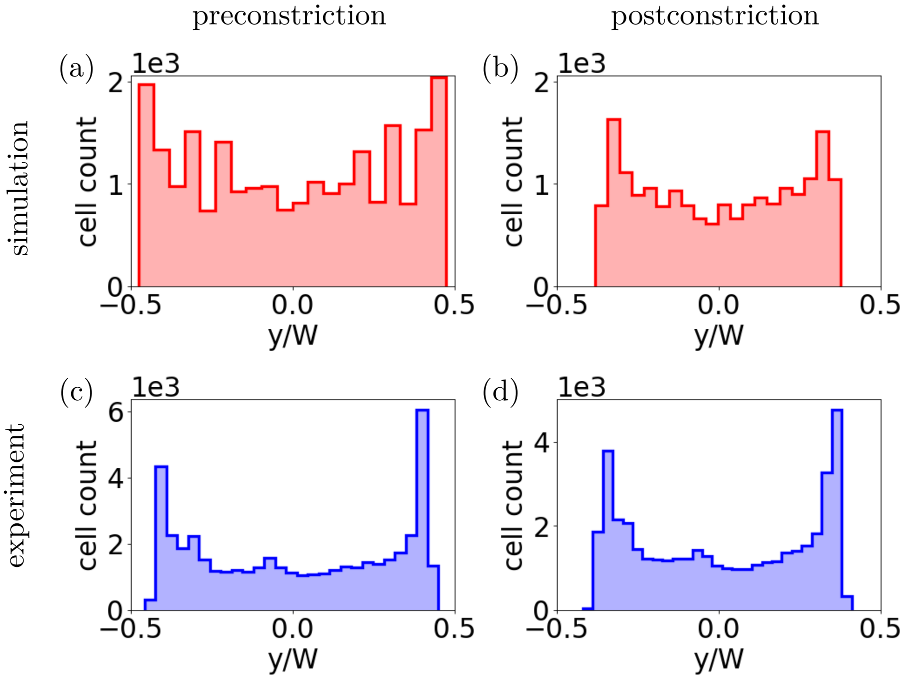

Figure 8.5: Red blood cell distribution pre- and postconstriction. In simulations the distribution is calculated around (a) $x = -300\,\mu\mathrm{m}$ (preconstriction) and (b) $x = 300\,\mu\mathrm{m}$ (postconstriction), all cells within one cell radius around these positions are included. The experimental distribution is shown for the region of interest directly (c) before and (d) behind the constriction. The flow velocity and pressure drop are $v_\mathrm{c} = 80\,\mathrm{mm\,s^{-1}}$ and 250 mbar, respectively. Adapted from [188] with permission from APS. Slight differences in the exact height of the histogram bars compared to figure 3 in [188] are due to minor differences in the bin division.

8.3 Cell-free layer under steady flow

8.3.1 Cell distribution over the channel cross section

First the spatial cell distribution in front of and behind the constriction is investigated. Figure 8.5 exemplarily shows these RBC distributions for a velocity of $80\,\mathrm{mm\,s^{-1}}$. The cell count is based on the cells' centre of mass position and is shown over the cross section of the channel along the longer channel wall in (a) and (b), in comparison with experimental results in (c) and (d). At all channel positions the distribution shows two pronounced peaks near the channel walls while fewer RBCs flow in the channel centre. The CFL appears in the distribution as the small section next to the channel walls at $y = \pm 0.5W$ which is devoid of RBCs. In simulations, the peaks of the distribution become more centred postconstriction, which is connected to a larger CFL postconstriction, as the comparison of figure 8.5(a) and (b) shows.

Comparison to the experimental results in figures 8.5(c) to (d) shows the same trend. The distribution preconstriction in (c) is recorded 10 mm behind the inlet reservoir in experiments, in the region directly preceding the constriction. Such long channels are not feasible in the simulations, where the cells are fed in around 410 µm before the constriction, and thus travel a much shorter distance before they reach the constriction. This difference could explain the quantitative differences between the experimental and simulation distribution, especially the smaller CFL before the constriction in simulations. Postconstriction, the CFLs in experiment and simulation are of similar size, as figures 8.5(b) and (d) show. Similar two-peaked cell distribution profiles for RBC suspensions of low concentration are reported by Zhou et al. [170], using experiments as well as LBM-IBM simulations. The authors studied a rectangular channel of similar size in experiment and simulation, but used a flow rate around one to two orders of magnitude smaller, i.e. at negligible inertia $Re \ll 1$. They find the peaks of the distribution at $|y/W| \approx 0.35 - 0.4$ and, moreover, showed, that the inflow configuration has an influence of the RBC ordering in the channel [170].

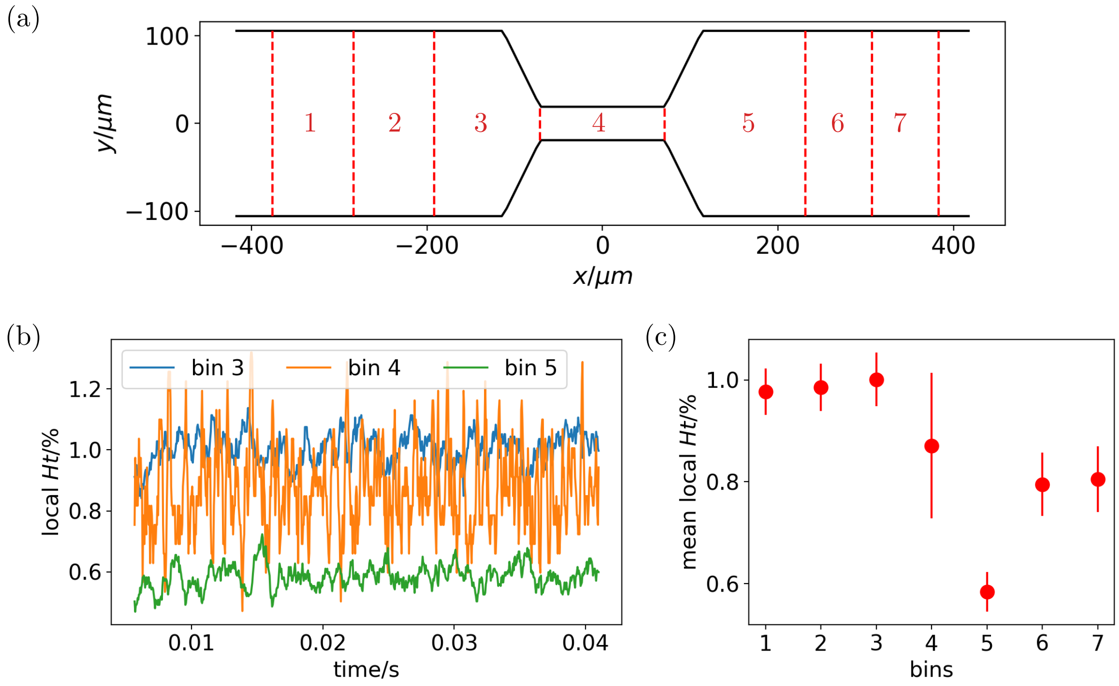

Figure 8.6: Local haematocrit in the constricted simulation channel. (a) The simulation channel is divided into 7 bins of different size. (b) Local haemtocrits Ht fluctuate over time. (c) Mean of the local haematocrits for the different bins with standard deviation as error bars. Results are shown exemplarily for the simulation at $v_c = 80\,\mathrm{mm\,s^{-1}}$.

A local haematocrit Ht can be calculated for different channel sections. The simulated channel is divided into several bins of different size, shown in figure 8.6(a). The haematocrit is calculated for the representative example at flow velocity $v_\mathrm{c} = 80\,\mathrm{mm\,s^{-1}}$. Figure 8.6(b) shows the haematocrit over time exemplarily for the three bins before, inside and directly after the constriction. In bin 3 (blue curve) the local haematocrit varies around the feed-in value $Ht = 1\,\%$. Inside the constriction (orange curve) it is smaller and fluctuates strongly, because fewer cells move faster through the constriction. Directly behind the constriction Ht fluctuates on an even lower level because of the large cell-free region which occur there. Bin 5 is chosen such, that the areas with the increase CFL in figure 8.3 are included. These findings are summed up in figure 8.6(c), where the mean local haematocrit is shown for all bins. In addition, one can observe a slight increase in Ht in bin 3 preconstriction, the cells accumulate before entering the narrow section. Postconstriction, in bins 6 and 7 the haematocrit has returned to a slightly lower level of $0.8\,\%$. This shows that at least for the simulated channel lengths, postconstriction the influence of the constriction is still noticeable. In the haematocrit calculation the start-up flow with the first cells entering the channel from the left has been excluded.

8.3.2 Development of the cell-free layer along the channel

The development of the CFL along the channel is shown exemplarily for a flow strength of $v_\mathrm{c} = 80\,\mathrm{mm\,s^{-1}}$ in figure 8.4(a). Before the constriction in the region $x < -180\,\mathrm{\mu m}$, the CFL is overall small, but shows a slight increase in x-direction after the feed-in region, when the RBCs move away from the channel walls. After a subsequent increase directly preconstriction, the CFL approaches zero where the cells enter the constriction. Inside the constriction, again a very thin CFL starts to form. Postconstriction, after a sudden increase of the CFL, where the cells leave the constricted region, it decreases to a stable value on the length scale of around $50\,\mathrm{\mu m}$.

The experimental results exhibit a quantitative similar behaviour as figure 8.4(b) shows. The different shape of the CFL curve around the constriction in experiment and simulation is due to the differences in the shape of the channel edges, compare figure 8.1. All details of the experimental findings are presented in the joint publication [188].

Numerical simulations of RBCs flowing through a cylindrical microchannel with a stenosis showed that for very small channel diameters (e.g. $11\,\mathrm{\mu m}$) and reasonably large pressure drops the effect can be reversed, the CFL preconstriction exceeds the CFL postconstriction [179]. However, for increasing channel diameter Vahidkhah et al. [179] also report a larger CFL postconstriction.

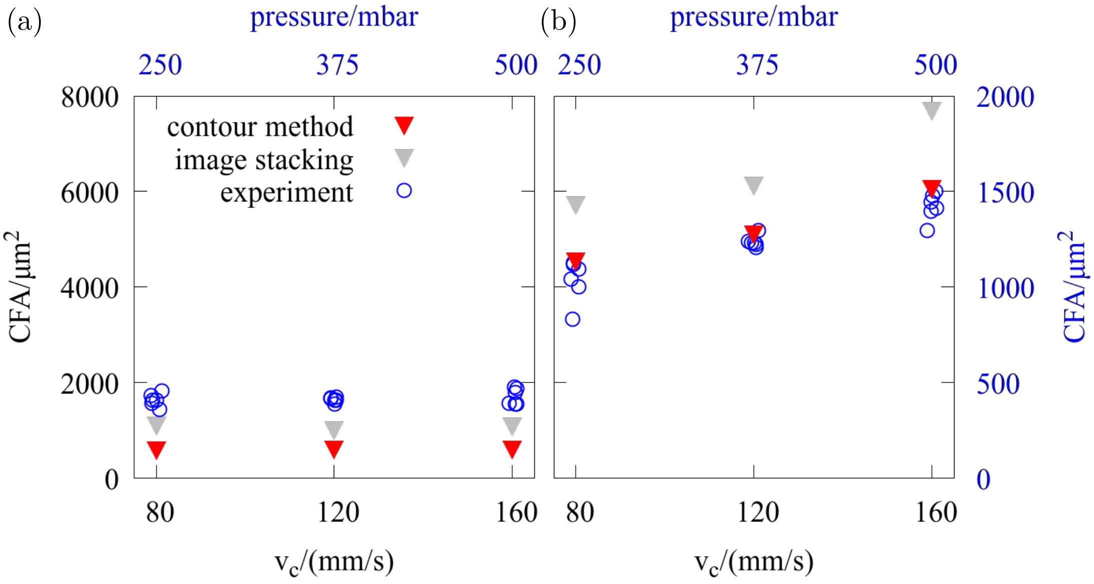

Figure 8.7: Cell-free areas (CFAs) at different flow velocities v_c. Results of the simulation evaluation (red and grey symbols and black axes) are shown for the areas (a) pre- and (b) postconstriction and compared with experimental measurements (blue circles and blue axes at the top and right). Every blue circle represents a single measurement run. The contour method and image stacking results for the simulation evaluation are shown in red and grey, respectively. Reproduced from [188] with permission from APS.

8.3.3 Cell-free areas at the constriction

The exemplary CFL curves in figure 8.4 show that the CFAs (shaded regions) before the constriction are significantly smaller than postconstriction. The results under steady flow for different velocities are summarised in figure 8.7. The CFA preconstriction in (a) does not significantly change with the flow velocity while the CFA postconstriction increases with increasing flow strength. The image stacking method yields larger results for the CFA than the contour method, due to its larger CFL estimate, discussed in section 8.2.3. This effect is more pronounced postconstriction, which leads to the conclusion that postconstriction more singular events occur, i.e. more RBCs enter the typically cell-depleted region. These are taken into account for the CFL calculation with the contour method, but not the image stacking.

Comparison with the experimental results in figure 8.7 (blue circles and axes) shows that the experimentally measured CFAs in good approximation amount to one fourth of the simulation results. This observation is consistent with the channel scaling in the experiment, where all channel dimensions are smaller by a factor of two. In addition the shape of the constricted section in figure 8.1 shows minor differences in experiment and simulation which also influences the CFA results. Experiments show that the increase in CFA size with increasing pressure drop is larger for smaller haematocrits [188].

The experimental studies by Rodríguez-Villarreal et al. [171] and Abay et al. [184] report a similar increase of the CFA after a constriction with increasing pressure drops for steady flow. However, no quantitative estimate of the size of the cell-depleted areas is given in that study.

8.4 Cell-free layer under time-dependent flow

8.4.1 Cell-free area dynamics at the constriction

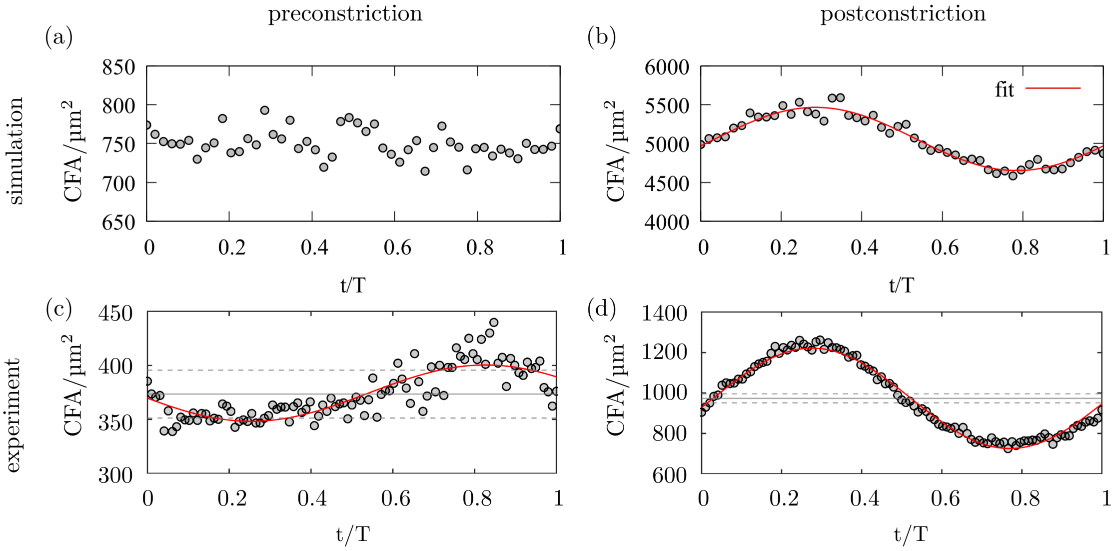

Figure 8.8: Time-dependent development of the cell-free areas (CFAs) around the constriction. (a,b) Simulation results for one oscillation period T with mean centre velocity $v_0 = 120\,\mathrm{mm\,s^{-1}}$ and amplitude $v_\mathrm{A} = 40\,\mathrm{mm\,s^{-1}}$, reproduced from [188] with permission from APS. (c,d) Experimental measurements at $p_0 = 250\,\mathrm{mbar}$ and $p_\mathrm{A} = 200\,\mathrm{mbar}$, reprinted from [188] with permission from APS. The solid lines show the sinusoidal fit to the data. The CFA dynamics is shown preconstriction in (a,c) and postconstriction in (b,d).

In this section the results for a time-dependent flow through the channel are collected. In addition to the constant mean centre velocity $v_0 = 120\,\mathrm{mm\,s^{-1}}$, the flow has an oscillating part such that $v(t) = v_0 + v_\mathrm{A} \sin(2\pi t f)$, with amplitude $v_\mathrm{A} = 40\,\mathrm{mm\,s^{-1}}$ and frequency $f = 20\,\mathrm{Hz}$. In experiments, analogously, an sinusoidal pressure modulation $p(t) = p_0 + p_\mathrm{A} \sin(2\pi t f)$ is applied. The time-dependent dynamics of the CFA around the constriction is studied by determining CFL and CFA as for the steady flow, but separately for different phases of the sinusoidal oscillation. This means that for every phase a CFL curve as shown in figure 8.4 is recorded and the CFA is extracted. The result is shown in figure 8.8 over one oscillation period $T = f^{-1}$ of the flow velocity. Each point gives the CFA for one of the phases. The CFA values preconstriction in simulations in figure 8.8(a) scatter over time, its dynamics does not reflect the sinusoidal flow. In contrast, in the CFA oscillation postconstriction in (b) the flow oscillation is clearly mirrored.

An exemplary measurement result is shown in figure 8.8(c-d). The time-dependent behaviour preconstriction here also shows a sinusoidal dependency, although clearly out of phase. The grey dashed lines in 8.8(c,d) indicate the estimate of the experimental error, details of its computation are given in [188]. Behind the constriction the CFA result is clearly above the error limit, while preconstriction the measurement is of the same order of magnitude as the experimental error. These curves are recorded at an RBC concentration of $Ht = 1\,\%$ and a pressure modulation with $p_0 = 250\,\mathrm{mbar}$ (this corresponds to a flow velocity of $v_\mathrm{c} \approx 80\,\mathrm{mm\,s^{-1}}$) and $p_\mathrm{A} = 200\,\mathrm{mbar}$. The small experimental frequency of $f = 1\,\mathrm{Hz}$ allows this flow modulation with a minimal pressure drop of 50 mbar in the channel. In experiments other combinations of mean pressure, pressure amplitude and haematocrit were investigated. Most noticeable is the strong increase in the amplitude of the CFA with an increase of the pressure amplitude, while the mean value of the CFA is not significantly influenced [188]. This means, conversely, that a pressure amplitude smaller than in figure 8.8(c) could lead to a CFA oscillation below the detection limit. This can explain why the preconstriction CFA does not mirror the sinusoidal flow behaviour in simulations, where the relative velocity amplitude is only $v_\mathrm{A}/v_0 \approx 33\,\%$, which is small compared to the experimental $p_\mathrm{A}/p_0 = 80\,\%$. In simulations the flow velocity at the minimum is restricted by a detection time scale, due to the faster oscillation frequency $f = 20\,\mathrm{Hz}$, and the maximal flow velocity is limited by numerical stability. Therefore, such large relative amplitudes cannot be achieved in the simulations.

8.4.2 Phase shift

In addition to the data points in figure 8.8, a sinusoidal fit to the data over the whole period is shown. From this fit, the phase shift φ is extracted from the CFA data as $\mathrm{CFA}(t) \propto \sin\left(2\pi(t-\varphi)f\right)$. The results are summarised in figure 8.9. The experimental data shows a peculiar phase shift preconstriction, the values of φ scatter around $T/2$. This was observed exemplarily in figure 8.8(c). As discussed in section 8.4.1 this effect cannot be resolved in the CFA trajectory from simulations. Postconstriction, φ is above but close to zero. This means that the CFA dynamics is slightly slower than the oscillation of the flow but in principle in-phase with the flow velocity, as both simulation and experiment show.

The velocity field of the flow extracted from the 3D simulations can help to un-

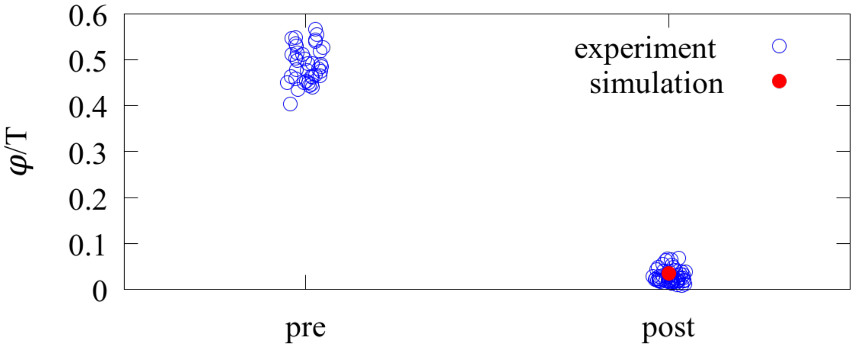

Figure 8.9: Phase shift of the cell-free area. The phase shift φ over the oscillation period T is shown for the CFA dynamics pre- and postconstriction for simulation (red) and experiments (blue). Only experiments at 1 % haematocrit with $p_0 = 500\,\text{mbar}$ and $p_\text{A} = 400\,\text{mbar}$, where detection of the CFA oscillation preconstriction is possible, are included here. Reproduced from [188] with permission from APS.

derstand this phase shift. In general, in front of the constriction there must be a net flow towards the channel centreline at $y = 0, z = 0$ and postconstiction, there is an expanding flow towards the channel walls. In figure 8.10 the normalised velocity component in y-direction v_y is shown at $z = H/2$ over the channel length and width. The top image (a) shows the velocity at the maximum of the sinusoidal modulation, the bottom image (b) at the minimum of the modulation. The absolute value of the component v_y is symmetric with respect to the channel centre. Preconstriction no difference of the lateral flow fields at v_max and v_min can be observed, but postconstriction they differ visibly. During the increase of the velocity to v_max the region of heightened v_y is extended further in x-direction. At the minimal velocity v_min, in contrast, directly behind the constriction it is shifted towards the channel walls. Moreover, the maximal value of $|v_y/v_c|$ postconstriction is larger at v_min.

Figure 8.11 shows the corresponding streamlines along a horizontal channel slice at $z = H/2$ for the maximum and minimum velocity during the oscillation. Each pair of streamlines starts at the same y-value at the channel entrance and due to the symmetry around $y = 0$ only the bottom half of the channel is shown. The observed difference of the flow field postconstriction is reflected clearly in the course of the streamlines. Behind the constriction the streamlines at the minimal velocity (blue lines) run much closer to the wall than those at maximal velocity (red lines). Moreover, in the streamline plot a very slight difference between the flowfield v_max and v_min preconstriction can be resolved. Preconstriction, the course of the streamlines is reversed, the red lines are bent minimally closer to the walls than the blue lines.

For higher velocity amplitudes, which could not be reached in the simulations described above, the magnitude of the observed differences is expected to increase.

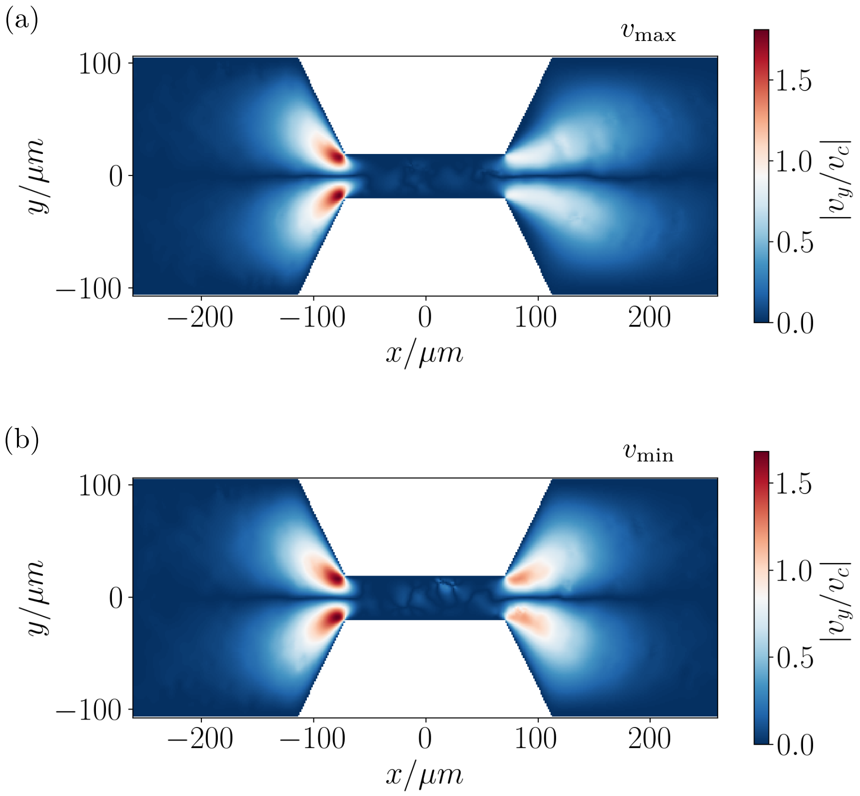

Figure 8.10: Flow field towards the channel centre at the constriction during time-dependent flow. Absolute values of the y-component of the flow v_y at (a) the maximum and (b) the minimum flow velocity during the modulation, normalised with the respective centre flow velocity v_c. The flow field is taken in the centre of the channel in z-direction. Adapted from [188] with permission from APS. Here both channel halves are shown for the minimal and maximal velocity.

Thus, phase shifts similar to the experimental observation at high pressure drop differences are expected. The flow field visualisation in figure 8.11 can explain the occurrence of these phase shifts. At higher velocities the cells follow the red streamlines which are pressed closer to the wall preconstriction, flow through the constriction and are then swept away quickly along the red line behind the constriction. Therefore, at the maximal velocity the CFA preconstriction decreases and increases postconstriction. At the minimal flow velocities, in contrast, the RBCs flow further away from the walls before entering the constriction but can flow closer to the walls postconstriction. Hence, the effect of the velocity modulation on the CFA is reversed postconstriction, it is approximately in phase with the flow oscillation. Due

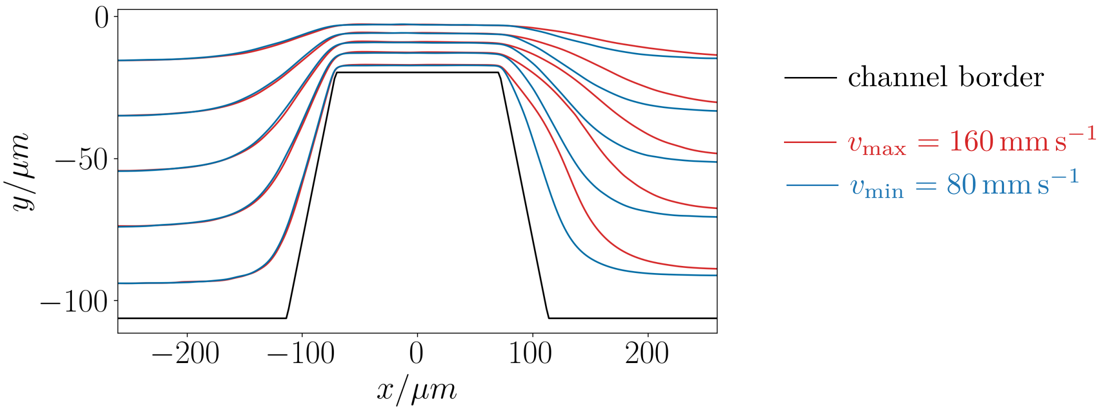

Figure 8.11: Streamlines of the flow around the constriction during time-dependent flow. The streamlines are shown for the bottom half of the constriction at the maximal $v_{\max}$ (red) and the minimal $v_{\min}$ (blue) flow velocity. All streamline pairs have the same y-position at the beginning of the channel. The flow field is taken in the centre of the channel in z-direction. Reproduced from [188] with permission from APS.

to these effects a phase shift of $T/2$ for the CFA dynmics preconstriction, but not postconstriction, is observed in the microfluidic experiments. The slight delay of the phase shift postconstriction is due to the propagation delay of the velocity oscillation along the channel length. To further support this interpretation of the velocity field dynamics, numerical simulations at higher velocity amplitudes, which could not be reached in the simulation setup presented here, should be performed.

8.5 Conclusion

Simulations and corresponding experiments of the blood flow through a microchannel with a narrow constriction show the emergence of smaller cell-depleted zones before and larger ones behind the constriction. Extending the investigation to time-dependent flow through the constriction shows the dynamic evolution of the CFAs at the constriction. The CFA postconstriction follows the sinusoidal oscillation of the velocity modulation. In corresponding experiments from the group of C. Wagner, where higher relative amplitudes of the flow modulation are feasible, in addition an out-of-phase oscillation of the CFA preconstriction could be detected. The CFA dynamics in front of the constriction shows a phase shift of half the oscillation period compared to the velocity modulation. Detailed study of the time-dependent velocity field in the numerical simulations can explain the coupling of the CFA dynamics to the flow field oscillation.

For future work, increasing the feasible range of the flow velocity in simulations would be interesting. This would allow larger velocity amplitudes such that resolution of the CFA dynamics preconstriction could be improved and the influence of the velocity field could be confirmed. Constrictions can appear in blood vessels in the human body in the form of stenoses, where the dynamics of the blood flow before and behind this blockage is of great interest. Moreover, the LBM used for the numerical simulations could be adapted to investigate the dynamics of the cell-depleted regions in time-dependent blood flow through other, more complex, geometries. The method presented here could be adapted to study arbitrary time-dependent flows, for example the influence of the blood pressure waveform on the CFAs around a constriction could be investigated. Another interesting research direction might be the investigation of complex fluids of non-Newtonian flow behaviour for RBC suspensions. Due to their different rheological properties, these fluids can have a decisive influence on the RBC suspension dynamics in constricted channels and thus the emergence and time-dependent behaviour of the CFAs.

9 Conclusion

This thesis investigated transient red blood cell shapes in various flow geometries, using different numerical methods. Starting point of the thesis was the investigation of the transition between the two prevailing red blood cell shapes in microchannel flow, the slipper and the croissant, in order to be able to identify a potential stationary shape and conditions for its formation. This research question was motivated by the observation, also found in earlier studies, that shape changes, e.g. from croissant to slipper, could still be observed after simulated times of several minutes, which makes the construction of a phase diagram for the cell shape problematic. The transition between the two predominant shapes was studied in time-dependent flow. First, the stability of the phase diagram with the addition of a pulsatile flow component was investigated. The phase diagram was found to be robust under the pulsation. However, the analysed croissant shapes showed significant differences in their dynamic behaviour and orientation in the channel, raising doubt whether the assumption of two clear-cut categories, slipper and croissant, was correct. Secondly, when examining the transition between the croissant and slipper shape by means of a gradual flow velocity increase in the channel, a new experimental setup made the investigation of the slipper dynamics possible. Here it became apparent, that the dynamical behaviour of the slipper cells observed experimentally, was not sufficiently matched in simulations. This was attributed to a missing viscous contribution of the cell in the simulation model. These two points led to the implementation of a membrane viscosity contribution in the boundary integral method simulation code, which was subsequently validated successfully. When the membrane viscosity effect was integrated in the model, simulations of RBCs in channel flow quickly showed, that its effect on the dynamics of the slipper cell is closely linked to the shear reference state of the red blood cell. Combinations which are compatible with the experimental results regarding the slipper oscillations in the microchannel were identified for further use in the simulation setup. The analysis of these results in addition well explains the relatively large fraction of red blood cells in experimental studies which cannot be identified as slipper or croissant shape. This full simulation model was tested for various applications. It was demonstrated that the results for red blood cell stretching with (optical) tweezers and red blood cells in shear flow agree well with the experimental data, as well as with former simulation studies available for these. However, it was shown that neither of the two approaches is suitable for drawing conclusions about the correct red blood cell parameter values, for example the membrane viscosity strength, because for variation in a physiologically sensible range the results for the output quantities are not sufficiently distinct. In case of the tweezer model, moreover, variation of the implementation details was found to have a crucial effect on the stretching behaviour, which makes it questionable to draw conclusions from this comparison. Another flow setup, for which novel experimental data was available, was compared to the respective simulations in this context. Here the qualitative comparison of cells with smaller and larger membrane viscosity values could indeed explain observed differences in the deformation behaviour. Again, detailed quantitative comparison of simulation and experimental results and inference of red blood cell parameter values remained challenging, due to the sensitivity to the start shape, which is not controlled in experiments, and leads to scattering of the deformation results.

The first part of the work described so far was based on the comparison of single cell dynamics in different flow setups, e.g. the cell deformation under different shear rates. In contrast to this, the novel approach in the second part of the work was to analyse the statistical behaviour of many cells under constant flow conditions. The motivation for this approach is twofold. First, it must be assumed that the scattering of experimental results, for biological entities like red blood cells, is not only caused by the unavoidable measurement error, but also by the inherent biological variability of the cells. From this consideration it follows, that in simulations the cell parameters should vary on a certain range and the resulting multiple simulation outcomes should be appropriately compared to the experimental values. Second, the red blood cell dynamics is influenced by the *combination* of different parameters, e.g. the membrane viscosity and interior cell viscosity. Separate variation of these parameters might not correctly reflect the biological reality. Moreover, the variation of all parameters together leads to a multitude of simulation results, which differ only slightly, such that determination of the correct parameter combination based on single-cell dynamical comparison is not feasible. The first method developed for this many-cell statistical comparison allowed to determine a range, on which the parameters, describing the red blood cell properties, vary. The second method aspired to give a quantitative estimate of the red blood cell parameter distribution from the comparison of many-cell simulation and experimental results.

Finally, the last chapter of the thesis provided an outlook on the collective behaviour of red blood cells, flowing through a microchannel with a narrow constriction, again under time-dependent flow, as investigated in the first part of the thesis. The study of the cell-depleted zones before and behind the constriction showed, that the cell-free area postconstriction follows the sinusoidal oscillation of the flow velocity modulation. The out-of-phase oscillation of the cell-free area preconstriction observed in experiments, could not be resolved in simulations, however, the simulations were able to explain the coupling of the cell-free area dynamics to the flow field oscillation.

Based on the results of this thesis, different interesting future research questions arise. If more detailed, time-resolved experimental results for the tweezer cell stretching and relaxation setup were available, comparison with the time-resolved simulation data could verify and possibly improve the cell model and thus our understanding of the cells' dynamics.

Regarding the many-cell statistical approach, two lines of future research are proposed. First, the fitting method could be improved in different ways. The presented approach could be extended to yield fitting results for all data subsets, which are then combined for the final parameter estimation, or more, possibly correlated parameters could be included in the estimated set, instead of assigning them a fixed distribution. This improvement of the fitting method is closely related to the second proposal, the extension of the data base, both in simulations and regarding the analysed experimental data sets. In simulations this could include an extension of already considered variations, for example additional initial cell shapes, but also the variation of other cell parameters, which were previously kept constant, for example the shear reference shape of the cell. Such variations lead to a very rapid increase in the parameter space, such that additional methods are required in the simulation procedure and for the analysis of the results, in order to keep the computational effort within feasible limits.

For systems with larger Reynolds number, where the BIM cannot be used, in this thesis a LBM was employed. Implementation of the membrane viscosity method also for the LBM would permit the investigation of RBC flow in systems, where the inertial force contribution cannot be neglected. In addition, with the LBM, the simulation of fluids with shear thinning and possibly viscoelastic properties, as are used for example in RT-DC measurements, is feasible. These fluids have different rheological properties and could crucially influence the flow behaviour and thus a combination with the viscoelastic RBC model in simulations is highly desirable. Moreover, in the framework of LBM, construction of various flow geometries is straightforward. This allows the investigation of more complex geometries, e.g. the constriction geometry discussed in the last part of the thesis. Such geometries are found in the blood circulation system and thus the blood flow dynamics around them is of great interest.

Appendices

A Eigenvalues and eigenvectors of the Cauchy-Green tensor

This section shows the calculation of the eigenvalues and corresponding eigenvectors of the left Cauchy-Green deformation tensor (4.13). These results are not new, but are collected and recapitulated here to aid the reader's understanding. The eigenvalues are called λ_i^2. First the respective eigenvectors $\boldsymbol{e}_i$ are calculated

$$\begin{pmatrix} C_{xx} & C_{xy} \\ C_{yx} & C_{yy} \end{pmatrix} \begin{pmatrix} e_i^x \\ e_i^y \end{pmatrix} = \lambda_i^2 \begin{pmatrix} e_i^x \\ e_i^y \end{pmatrix} \tag{A.1}$$

$$C_{xx} e_i^x + C_{xy} e_i^y = \lambda_i^2 e_i^x \tag{A.2}$$

$$C_{yx} e_i^x + C_{yy} e_i^y = \lambda_i^2 e_i^y . \tag{A.3}$$

The condition for normalised eigenvectors is

$$(e_i^x)^2 + (e_i^y)^2 = 1. \tag{A.4}$$

Now the squared equation (A.2) is combined with (A.4) and e_i^x is eliminated

$$(C_{xx} - \lambda_i^2)^2 (1 - (e_i^y)^2) = C_{xy}^2 (e_i^y)^2 \tag{A.5}$$

and solving for the second vector component leads to

$$e_i^y = \pm \frac{C_{xx} - \lambda_i^2}{\sqrt{(C_{xx} - \lambda_i^2)^2 + C_{xy}^2}}. \tag{A.6}$$

The first entry follows as

$$e_i^x \overset{(A.4)\_(A.6)}{=} \mp \left(1 - \frac{(C_{xx} - \lambda_i^2)^2}{(C_{xx} - \lambda_i^2)^2 + C_{xy}^2} \right)^{1/2} = \mp \frac{C_{xy}}{\sqrt{(C_{xx} - \lambda_i^2)^2 + C_{xy}^2}}. \tag{A.7}$$

The sighs of e_i^x follow from the first condition (A.2). We choose the positive sign in (A.6) and thus the negative in (A.7). Note that this choice is irrelevant for the second condition (A.4). Now writing out the first vector explicitly leads to

$$\boldsymbol{e}_1 = \frac{1}{\sqrt{(C_{xx} - \lambda_1^2)^2 + C_{xy}^2}} \begin{pmatrix} -C_{xy} \\ C_{xx} - \lambda_1^2 \end{pmatrix}. \tag{A.8}$$

The second vector $\boldsymbol{e_2}$ could be obtained analogously, exchanging λ_1 for λ_2. Using equation (4.20) we can show that these eigenvectors $\boldsymbol{e}_1, \boldsymbol{e}_2$ and respective eigenvalues also fulfil the condition (A.3)

$$C_{yx} e_i^x + (C_{yy} - \lambda_i^2) e_i^y = 0 \Leftrightarrow \tag{A.9}$$

$$C_{yx}(-C_{xy}) + (C_{yy} - \lambda_i^2)(C_{xx} - \lambda_i^2) = 0 \Leftrightarrow \tag{A.10}$$

$$-C_{xy}C_{yx} + \lambda_i^4 + C_{xx}C_{yy} - \lambda_i^2(C_{xx} + C_{yy}) = 0 \Leftrightarrow \tag{A.11}$$

$$\det(\boldsymbol{C}) + \lambda_i^2(\lambda_i^2 - \operatorname{tr}(\boldsymbol{C})) = 0 \overset{(4.20)}{\Leftrightarrow} \tag{A.12}$$

$$\begin{aligned} \det(\boldsymbol{C}) + \left[\frac{1}{2}\left(\operatorname{tr}(\boldsymbol{C}) \pm \sqrt{\operatorname{tr}(\boldsymbol{C})^2 - 4\det(\boldsymbol{C})}\right)\right] \\ \left[\frac{1}{2}\left(-\operatorname{tr}(\boldsymbol{C}) \pm \sqrt{\operatorname{tr}(\boldsymbol{C})^2 - 4\det(\boldsymbol{C})}\right)\right] = 0 \Leftrightarrow \end{aligned} \tag{A.13}$$

$$\det \boldsymbol{C} + \frac{1}{4}\left[-\operatorname{tr}(\boldsymbol{C})^2 + \operatorname{tr}(\boldsymbol{C})^2 - 4\det(\boldsymbol{C})\right] = 0. \quad \square \tag{A.14}$$

In order to avoid the second parameter λ_2 in the eigenvector $\boldsymbol{e_2}$ one can make use of the orthogonality of the two vectors $\boldsymbol{e}_i$

$$\boldsymbol{e}_1 \cdot \boldsymbol{e}_2 = 0 \Leftrightarrow e_1^x e_2^x + e_1^y e_2^y = 0. \tag{A.15}$$

Together with (A.4) for the second vector this finally leads to

$$\boldsymbol{e}_2 = \pm \frac{1}{\sqrt{(C_{xx} - \lambda_1^2)^2 + C_{xy}^2}} \begin{pmatrix} C_{xx} - \lambda_1^2 \\ C_{xy} \end{pmatrix} \tag{A.16}$$

where instead of the parameter λ_2 the parameter λ_1 appears.

Now it can easily be shown that

$$\boldsymbol{e}_1 \otimes \boldsymbol{e}_1 = \frac{1}{(C_{xx} - \lambda_1^2)^2 + C_{xy}^2} \begin{pmatrix} C_{xy}^2 & -C_{xy}(C_{xx} - \lambda_1^2) \\ -C_{xy}(C_{xx} - \lambda_1^2) & (C_{xx} - \lambda_1^2)^2 \end{pmatrix} \tag{A.17}$$

$$\boldsymbol{e}_2 \otimes \boldsymbol{e}_2 = \frac{1}{(C_{xx} - \lambda_1^2)^2 + C_{xy}^2} \begin{pmatrix} (C_{xx} - \lambda_1^2)^2 & C_{xy}(C_{xx} - \lambda_1^2) \\ C_{xy}(C_{xx} - \lambda_1^2) & C_{xy}^2 \end{pmatrix} \tag{A.18}$$

and thus

$$\boldsymbol{e}_1 \otimes \boldsymbol{e}_1 + \boldsymbol{e}_2 \otimes \boldsymbol{e}_2 = \boldsymbol{I}. \tag{A.19}$$

For the difference we find

$$\boldsymbol{e}_1 \otimes \boldsymbol{e}_1 - \boldsymbol{e}_2 \otimes \boldsymbol{e}_2 = \tag{A.20}$$

$$= \frac{1}{(C_{xx}-\lambda_1^2)^2 + C_{xy}^2} \begin{pmatrix} C_{xy}^2 - (C_{xx}-\lambda_1^2)^2 & -2C_{xy}(C_{xx}-\lambda_1^2) \\ -2C_{xy}(C_{xx}-\lambda_1^2) & (C_{xx}-\lambda_1^2)^2 - C_{xy}^2 \end{pmatrix} \tag{A.21}$$

$$\overset{(B.8)}{=} \frac{1}{(C_{xx}-\lambda_1^2) + (C_{yy}-\lambda_1^2)} \begin{pmatrix} (C_{yy}-\lambda_1^2) - (C_{xx}-\lambda_1^2) & -2C_{xy} \\ -2C_{xy} & (C_{xx}-\lambda_1^2) - (C_{yy}-\lambda_1^2) \end{pmatrix} \tag{A.22}$$

$$= \frac{1}{\mathrm{tr}\boldsymbol{C} - 2\lambda_1^2} \begin{pmatrix} C_{yy} - C_{xx} & -2C_{xy} \\ -2C_{xy} & C_{xx} - C_{yy} \end{pmatrix} \tag{A.23}$$

$$\overset{(4.21)}{=} \frac{1}{\lambda_2^2 - \lambda_1^2} \begin{pmatrix} C_{yy} - C_{xx} & -2C_{xy} \\ -2C_{xy} & C_{xx} - C_{yy} \end{pmatrix} \tag{A.24}$$

$$\overset{(4.20)}{=} \frac{-1}{\sqrt{\mathrm{tr}(\boldsymbol{C})^2 - 4\det(\boldsymbol{C})}} \begin{pmatrix} C_{yy} - C_{xx} & -2C_{xy} \\ -2C_{xy} & C_{xx} - C_{yy} \end{pmatrix}. \tag{A.25}$$

Another useful identity is

$$\lambda_1^2(\boldsymbol{e}_1 \otimes \boldsymbol{e}_1) + \lambda_2^2(\boldsymbol{e}_2 \otimes \boldsymbol{e}_2) = \boldsymbol{C}. \tag{A.26}$$

We can show this

$$\lambda_1^2(\boldsymbol{e}_1 \otimes \boldsymbol{e}_1) + \lambda_2^2(\boldsymbol{e}_2 \otimes \boldsymbol{e}_2) = \tag{A.27}$$

$$\begin{aligned} \overset{(4.20)}{=} &\frac{1}{2}\left(\mathrm{tr}(\boldsymbol{C}) + \sqrt{\mathrm{tr}(\boldsymbol{C})^2 - 4\det(\boldsymbol{C})}\right)(\boldsymbol{e}_1 \otimes \boldsymbol{e}_1) + \\ &+ \frac{1}{2}\left(\mathrm{tr}(\boldsymbol{C}) - \sqrt{\mathrm{tr}(\boldsymbol{C})^2 - 4\det(\boldsymbol{C})}\right)(\boldsymbol{e}_2 \otimes \boldsymbol{e}_2) \end{aligned} \tag{A.28}$$

$$= \frac{1}{2}\mathrm{tr}(\boldsymbol{C})(\boldsymbol{e}_1 \otimes \boldsymbol{e}_1 + \boldsymbol{e}_2 \otimes \boldsymbol{e}_2) + \frac{1}{2}\sqrt{\mathrm{tr}(\boldsymbol{C})^2 - 4\det(\boldsymbol{C})}(\boldsymbol{e}_1 \otimes \boldsymbol{e}_1 - \boldsymbol{e}_2 \otimes \boldsymbol{e}_2) \tag{A.29}$$

$$\overset{(A.19)}{=} \frac{1}{2}\mathrm{tr}(\boldsymbol{C})\boldsymbol{I} + \frac{1}{2}\sqrt{\mathrm{tr}(\boldsymbol{C})^2 - 4\det(\boldsymbol{C})}(\boldsymbol{e}_1 \otimes \boldsymbol{e}_1 - \boldsymbol{e}_2 \otimes \boldsymbol{e}_2) \tag{A.30}$$

$$\overset{(A.25)}{=} \frac{1}{2}\mathrm{tr}(\boldsymbol{C})\boldsymbol{I} - \frac{1}{2}\begin{pmatrix} C_{yy} - C_{xx} & -2C_{xy} \\ -2C_{xy} & C_{xx} - C_{yy} \end{pmatrix} \tag{A.31}$$

$$= \frac{1}{2}\begin{pmatrix} 2C_{xx} & 2C_{xy} \\ 2C_{xy} & 2C_{yy} \end{pmatrix} \tag{A.32}$$

$$= \boldsymbol{C}. \quad \square \tag{A.33}$$

B Derivation of the membrane forces

B.1 Useful derivatives and identities

The derivatives of the Skalak law (2.1) are

$$\frac{\partial W_\mathrm{S}}{\partial I_1} \overset{(2.1)}{=} \frac{\kappa_\mathrm{S}}{6}(I_1+1) \overset{(4.24)}{=} \frac{\kappa_\mathrm{S}}{6}(\lambda_1^2+\lambda_2^2-1) \tag{B.1}$$

$$\frac{\partial W_\mathrm{S}}{\partial I_2} \overset{(2.1)}{=} -\frac{\kappa_\mathrm{S}}{6}+\frac{\kappa_\mathrm{A}}{4}I_2 \overset{(4.25)}{=} -\frac{\kappa_\mathrm{S}}{6}+\frac{\kappa_\mathrm{A}}{4}(\lambda_1^2\lambda_2^2-1) \tag{B.2}$$

$$\frac{\partial I_1}{\partial \lambda_1} = 2\lambda_1 \qquad \frac{\partial I_2}{\partial \lambda_1} = 2\lambda_1\lambda_2^2 \tag{B.3}$$

$$\frac{\partial I_1}{\partial \lambda_2} = 2\lambda_2 \qquad \frac{\partial I_2}{\partial \lambda_2} = 2\lambda_1^2\lambda_2. \tag{B.4}$$

These derivatives can now be combined

$$\frac{\partial W_\mathrm{S}}{\partial \lambda_1} = \frac{\partial W_\mathrm{S}}{\partial I_1}\frac{\partial I_1}{\partial \lambda_1} + \frac{\partial W_\mathrm{S}}{\partial I_2}\frac{\partial I_2}{\partial \lambda_1} \tag{B.5}$$

$$= \frac{\kappa_\mathrm{S}}{3}(\lambda_1^3-\lambda_1)+\frac{\kappa_\mathrm{A}}{2}(\lambda_1^2\lambda_2^2-1)\lambda_1\lambda_2^2 \tag{B.6}$$

$$\frac{\partial W_\mathrm{S}}{\partial \lambda_2} = \frac{\kappa_\mathrm{S}}{3}(\lambda_2^3-\lambda_2)+\frac{\kappa_\mathrm{A}}{2}(\lambda_1^2\lambda_2^2-1)\lambda_1^2\lambda_2. \tag{B.7}$$

Another useful identity is

$$(C_{xx}-\lambda_1^2)(C_{yy}-\lambda_1^2) = C_{xy}^2. \tag{B.8}$$

The proof is simple

$$(C_{xx}-\lambda_1^2)(C_{yy}-\lambda_1^2) = C_{xx}C_{yy}+\lambda_1^4-\lambda_1^2(C_{xx}+C_{yy}) = \tag{B.9}$$

$$= C_{xx}C_{yy}+\lambda_1^2(\lambda_1^2-\operatorname{tr}\boldsymbol{C}) = \tag{B.10}$$

$$\overset{(4.21)}{=} C_{xx}C_{yy}+\lambda_1^2(\lambda_1^2-\lambda_1^2-\lambda_2^2) = \tag{B.11}$$

$$\overset{(4.22)}{=} C_{xx}C_{yy}-\det\boldsymbol{C} = \tag{B.12}$$

$$= C_{xy}C_{yx} \tag{B.13}$$

$$\overset{\text{symm.}}{=} C_{xy}^2. \tag{B.14}$$

B.2 Details of the force calculation

In the following, the individual terms of the calculation omitted in (4.51) and (4.54) in section 4.4.2 are collected. These results are listed similarly in appendix C in Krüger [35] but without intermediate steps and with slightly different notation. In addition, due to the linear approximation of $\boldsymbol{F}$ the author directly sets $F_{yx} = 0$ in all expressions [35], while for the general derivation in section 4.4.2 this term is carried along. Furthermore, Krüger [35] omits all terms including G_{yx}, using the symmetry (4.12) of $\boldsymbol{G}$, hence $G_{yx} = G_{xy}$, and instead includes an additional factor 2 in all appropriate equations. The BIM implementation described in 2.3 does not use this symmetry but instead carries along G_{yx}. For all these reasons, the calculations are repeated here for better overview with the conventions used for the derivation and the BIM implementation.

The derivatives of W_S are already written down in (B.1) and (B.2), in each case the first identity is needed here. Next, the derivatives of I_1, I_2 are calculated.

$$\frac{\partial I_1}{\partial G_{xx}} = \sum_{i=1,2} \frac{\partial I_1}{\partial \lambda_i^2} \frac{\partial \lambda_i^2}{\partial G_{xx}} \overset{(4.24)}{=} \frac{\partial\left(\lambda_1^2 + \lambda_2^2\right)}{\partial G_{xx}} \overset{(4.18)}{=} 1 \tag{B.15}$$

$$\frac{\partial I_1}{\partial G_{yy}} = \frac{\partial\left(\lambda_1^2 + \lambda_2^2\right)}{\partial G_{yy}} \overset{(4.18)}{=} 1 \tag{B.16}$$

$$\frac{\partial I_1}{\partial G_{xy}} = \frac{\partial\left(\lambda_1^2 + \lambda_2^2\right)}{\partial G_{xy}} \overset{(4.18)}{=} 0\ , \quad \frac{\partial I_1}{\partial G_{yx}} \overset{\text{symm.}}{=} \frac{\partial I_1}{\partial G_{xy}} = 0 \tag{B.17}$$

$$\frac{\partial I_2}{\partial G_{xx}} = \sum_{i=1,2} \frac{\partial I_2}{\partial \lambda_i^2} \frac{\partial \lambda_i^2}{\partial G_{xx}} \overset{(4.25)}{=} \lambda_2^2 \frac{\partial \lambda_1^2}{\partial G_{xx}} + \lambda_1^2 \frac{\partial \lambda_2^2}{\partial G_{xx}} \tag{B.18}$$

$$\overset{(4.18)}{=} \frac{1}{2}\left(\lambda_2^2 + \lambda_1^2\right) + \frac{1}{2}\left(\lambda_2^2 - \lambda_1^2\right) \frac{(G_{xx} - G_{yy})}{\sqrt{(G_{xx} - G_{yy})^2 + 4G_{xy}G_{yx}}} \tag{B.19}$$

$$\overset{(4.18)}{=} \frac{1}{2}(G_{xx} + G_{yy}) - \frac{1}{2}(G_{xx} - G_{yy}) = G_{yy} \tag{B.20}$$

$$\frac{\partial I_2}{\partial G_{yy}} = \lambda_2^2 \frac{\partial \lambda_1^2}{\partial G_{yy}} + \lambda_1^2 \frac{\partial \lambda_2^2}{\partial G_{yy}} \overset{(4.18)}{=} G_{xx} \tag{B.21}$$

$$\frac{\partial I_2}{\partial G_{xy}} = \lambda_2^2 \frac{\partial \lambda_1^2}{\partial G_{xy}} + \lambda_1^2 \frac{\partial \lambda_2^2}{\partial G_{xy}} \overset{(4.18)}{=} -G_{yx} = -G_{xy}\ , \quad \frac{\partial I_2}{\partial G_{yx}} = -G_{xy}. \tag{B.22}$$

Finally, the derivatives of G_{ij} must be calculated. The components of the deformation tensor $\boldsymbol{G}$ written out are

$$\begin{pmatrix} G_{xx} & G_{xy} \\ G_{yx} & G_{yy} \end{pmatrix} \overset{(4.12)}{=} \begin{pmatrix} F_{xx}^2 + F_{yx}^2 & F_{xx}F_{xy} + F_{yx}F_{yy} \\ F_{xx}F_{xy} + F_{yx}F_{yy} & F_{xy}^2 + F_{yy}^2 \end{pmatrix}. \tag{B.23}$$

The relation of the deformation gradients F_{ij}, in turn, to the constants a_i, b_i (compare section 4.4.2) is give by equation (C.9) in [35] as

$$F_{xx} = 1 + \sum_{i=1}^{3} a_i V_{ix} \tag{B.24}$$

$$F_{xy} = \sum_{i=1}^{3} b_i V_{ix} \tag{B.25}$$

$$F_{yx} = \sum_{i=1}^{3} a_i V_{iy} \tag{B.26}$$

$$F_{yy} = 1 + \sum_{i=1}^{3} b_i V_{iy}. \tag{B.27}$$

Starting with G_{xx} yields

$$\frac{\partial G_{xx}}{\partial V_{ix}} \overset{\text{(B.23)}}{=} 2F_{xx}\frac{\partial F_{xx}}{\partial V_{ix}} + 2F_{yx}\frac{\partial F_{yx}}{\partial V_{ix}} \overset{\substack{\text{(B.24)}\\ \text{(B.26)}}}{=} 2a_i F_{xx}\ , \quad \frac{\partial G_{xx}}{\partial V_{iy}} = 2a_i F_{yx} \tag{B.28}$$

where all calculations follow the same scheme. The remaining derivatives are for G_{xy}

$$\frac{\partial G_{xy}}{\partial V_{ix}} = a_i F_{xy} + b_i F_{xx}\ , \quad \frac{\partial G_{xy}}{\partial V_{iy}} = a_i F_{yy} + b_i F_{yx} \tag{B.29}$$

and for G_{yy}

$$\frac{\partial G_{yy}}{\partial V_{ix}} = 2b_i F_{xy}\ , \quad \frac{\partial G_{yy}}{\partial V_{iy}} = 2b_i F_{yy} \tag{B.30}$$

Due to symmetry the respective derivatives of G_{yx} are identical to those of G_{xy}. Obtaining the solution in (4.52) is now straightforward, all terms in (4.50) are collected using the calculated derivatives, (4.55) is analogous.

C Phase diagrams for viscous red blood cells in a larger channel geometry

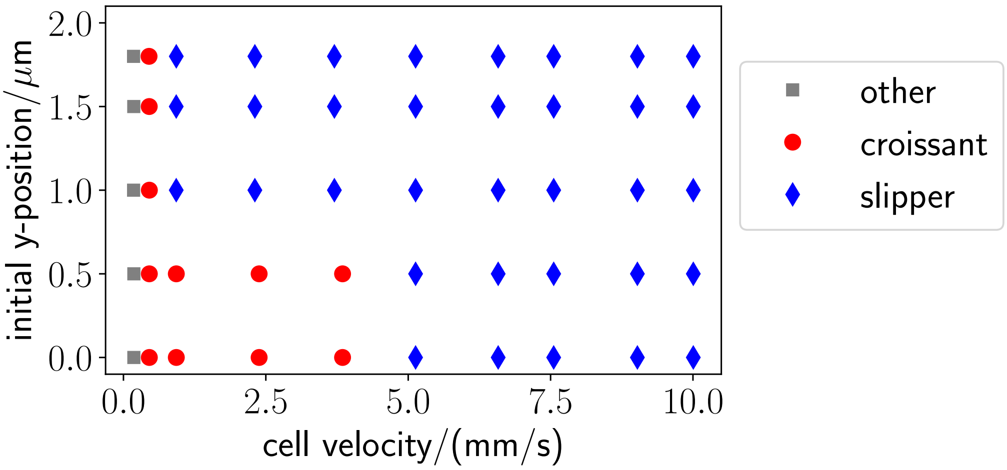

Figure C.1: Phase diagram of RBCs in a rectangular channel of cross section 12 µm to 10 µm. The RBCs have a viscosity contrast of $\lambda = 10$ and membrane viscosity $Bq = 5$ and the initial shape in the channel is a discocyte. Compared to [17] the croissant peak of the phase diagram is shifted.

D Further comparison of tweezer simulation results with the literature

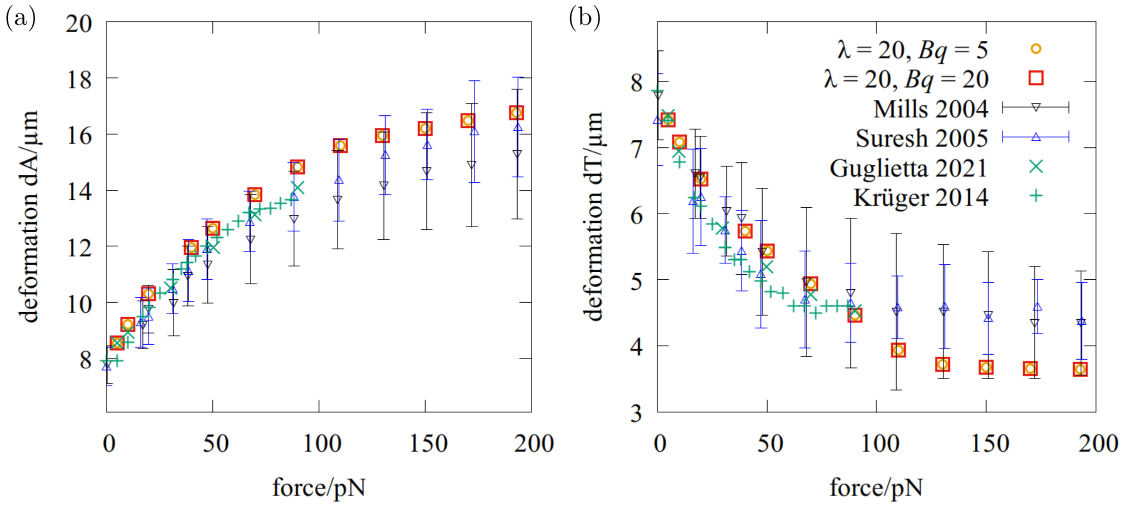

Figure D.1: Deformation of the red blood cells in tweezer simulations in comparison with other simulation studies. Simulation results from Guglietta et al. [25] and Krüger et al. [141] for (a) axial dA and (b) transversal dT deformation are added to figure 6.4, where experimental results from Mills et al. [55] and Suresh et al. [134] were discussed. No results for forces beyond 100 pN are presented in the simulations studies [25, 141]. The green symbols are for dA closer to the mean experimental results by Suresh et al. [134] than the results of the simulations presented herein. Note that in both studies the contact region is held constant during stretching, contrary to experimental observations.

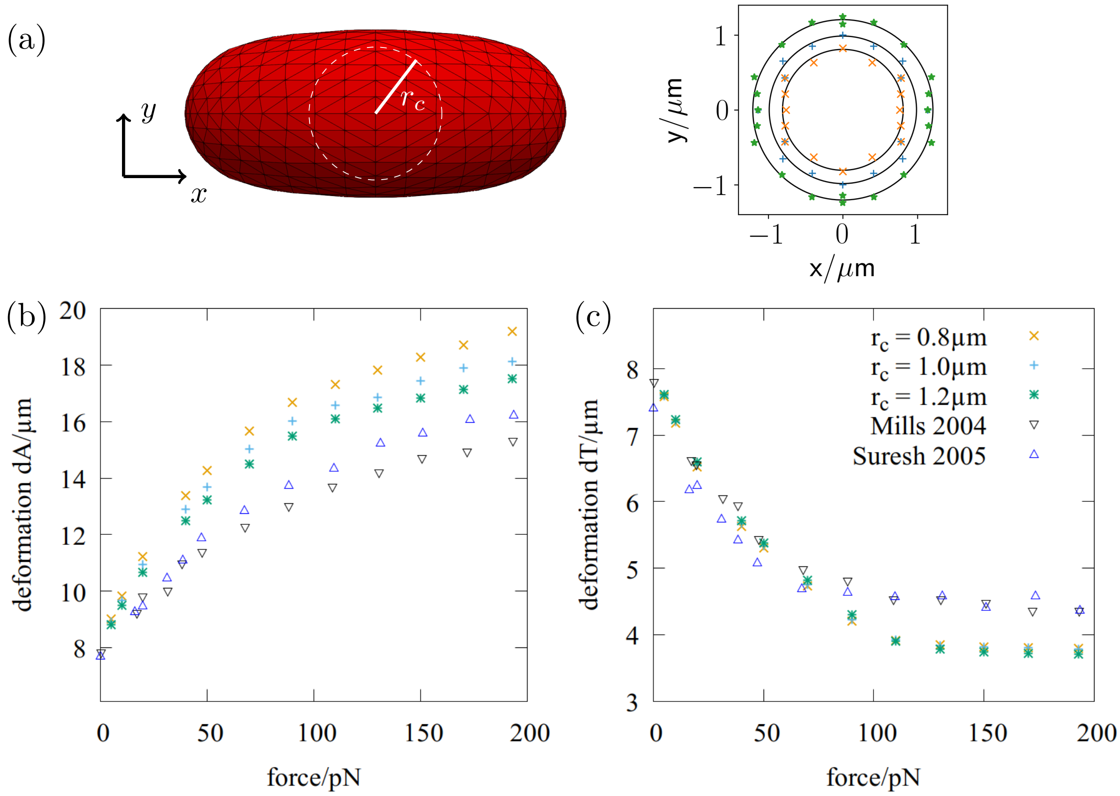

Figure D.2: Importance of the contact radius in tweezer simulations. (a) Illustration of the contact region on the triangulated RBC surface (side view) and different contact radii r_c. Coloured points mark the x-y-position of contact nodes on the cell surface. The black circles visualise the respective contact radius, which is computed as the mean of the radial distance of the contact nodes. (b,c) Deformation for different forces in axial and transversal direction. The results for different radii (blue, orange and green symbols) are compared to the mean experiment results from Mills et al. [55] and Suresh et al. [134], for the sake of clarity here without the errorbars. All simulations used for this figure have a discocyte reference shape with $c_0^* = 0$ and $\lambda = 5, Bq = 0$.

E Phase diagram of a single red blood cell with membrane viscosity in shear flow

Yazdani et al. [130] investigated in detail the phase diagram for RBCs in shear flow without membrane viscosity. In figure 6 therein, the authors present the RBC's dynamical modes depending on the flow strength, measured by Ca, and on the viscosity contrast λ. For $Ca > 0.3$ the authors mainly observe tank-treading and tumbling modes, depending on the value of λ. The border between these modes in the phase diagram lies around $\lambda = 2$.

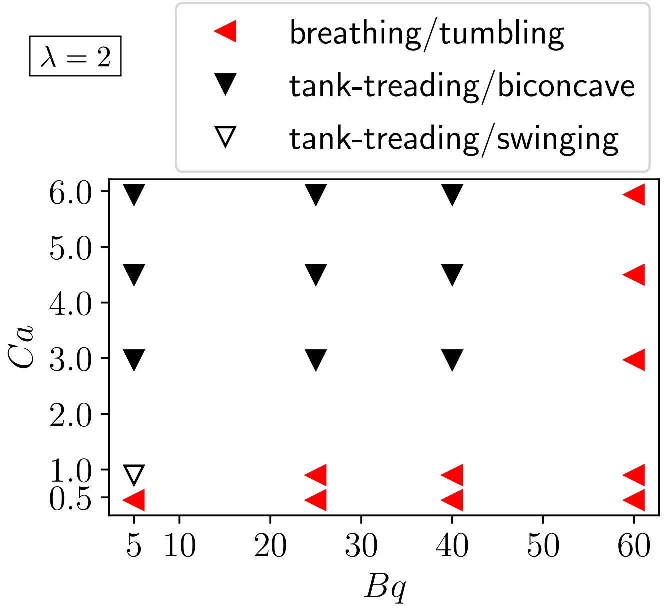

Figure E.1: Phase diagram of the RBC dynamics in shear with membrane viscosity at $\lambda = 2$. Capillary number Ca and dimensionless membrane viscosity Bq determine the transition between the tank-treading (black) and tumbling (red) modes.

In order to investigate the influence of Bq on the phase diagram, simulations with membrane viscosity are conducted at $\lambda = 2$, where the additional influence of the membrane viscosity is expected to determine the RBC dynamical mode. The parameters of the simulation are chosen as described in section 6.2.2, Bq is defined in (6.2). The results are presented in figure E.1 analogously to figure 6 in [130]. On the x-axis, however, Bq instead of λ is plotted. An increase in the membrane viscosity induces the transition from the tank-treading (black symbols) to the tumbling mode (red symbols), analogously to the transition observed for increased λ in [130]. This observation again highlights the fact that the membrane viscosity of the RBC can have a similar effect on the RBC dynamics as the interior viscosity of the cell. Details of the RBC's dynamical behaviour in the different modes are presented and analysed in [130] and therefore not repeated here. Note that the discrimination between tank-treading in biconcave shape (black filled symbols) and in combination with swinging (black empty symbol) is difficult, to emphasise this fact the single simulation point with tank-treading/swinging is also coloured black. The tumbling cells at large capillary number are extreme cases, where due to the high flow velocity the cell rotation in the dented state (compare figure 4 in [130]) is so fast, that the cell no longer relaxes back to its elongate shape in between dented states.

F Analysis of the many cell statistical behaviour

F.1 Influence of the cell shear modulus on the deformation behaviour in the RT-DC setup

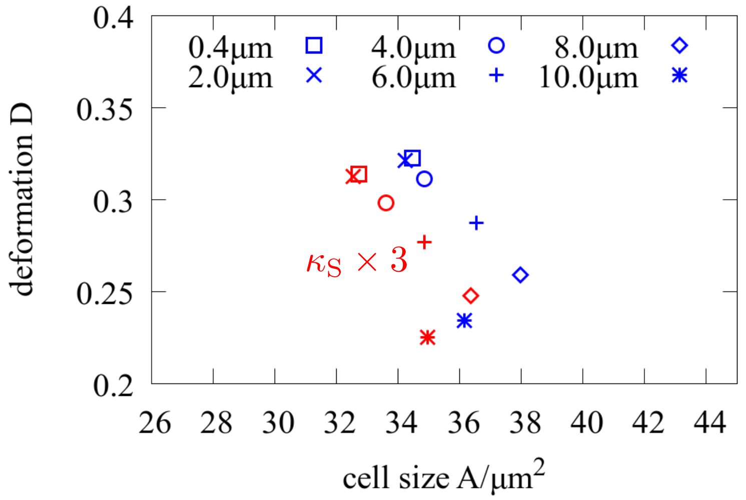

Figure F.1: Influence of the red blood cell shear elasticity on the deformation features of the cell in simulations. The deformation D and two-dimensional cell size A for RBCs with $\lambda = 4$, $Bq = 5$ and discocyte initial shape for the setup described in section 7.2.1 are shown in blue. The different symbols show the different initial positions y_{init}. The red symbols give the position of the simulation results for increased shear modulus κ_S.

F.2 Details of the integration routine

Here, some details of the evaluation of the integrals (7.2) and (7.3) are given. The integration over the different initial positions y_{init} and inital shapes is omitted, because it was assumed that these are represented by a uniform distribution, which greatly simplifies the resulting sums. The integration over λ and Bq is approximated with the trapezoidal rule on the simulation grid as sketched in figure F.2.

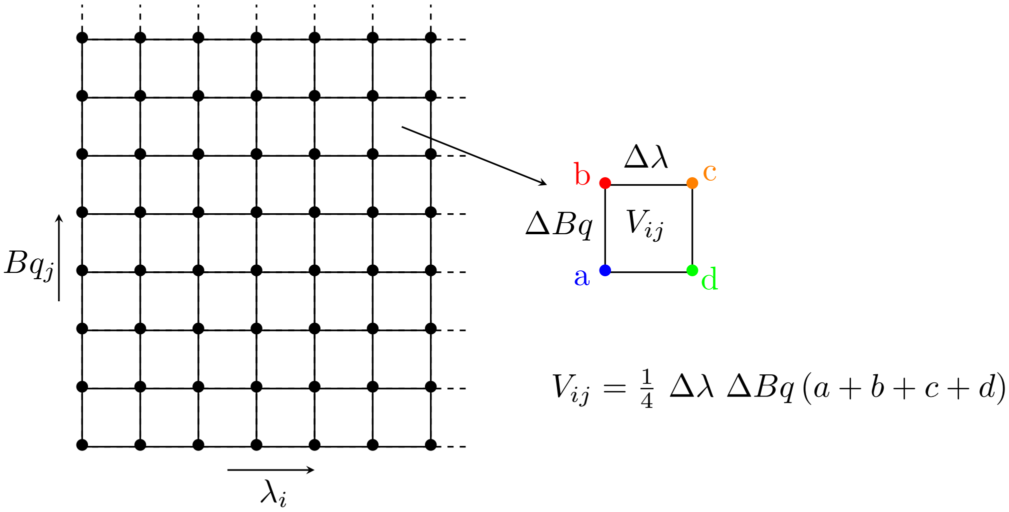

Figure F.2: Integration scheme for the trapezoidal rule. The simulations are run for a regular grid of the parameters λ and Bq. The other two parameters, the initial shape and initial position y_{init} are omitted in the sketch. For each grid cell, its contribution V_{ij} is approximated by calculating the mean of the values at the grid points belonging to the respective cell and taking into account the size of the grid cell.

The integrals are thus approximated by two sums along the two directions of the grid

$$\overline{\boldsymbol{f}} = \frac{1}{V}\sum_{i=1}^{n-1}\sum_{j=1}^{m-1}\frac{1}{4}\,\Delta\lambda\,\Delta Bq\left[\boldsymbol{f}_{i,j}\Pi\left(\lambda_i, Bq_j\right) + \boldsymbol{f}_{i,j+1}\Pi\left(\lambda_i, Bq_{j+1}\right) + \right.$$
$$\left. \boldsymbol{f}_{i+1,j}\Pi\left(\lambda_{i+1}, Bq_j\right) + \boldsymbol{f}_{i+1,j+1}\Pi\left(\lambda_{i+1}, Bq_{j+1}\right)\right]. \qquad \text{(F.1)}$$

The integral over the probability distribution $\Pi\left(\lambda_i, Bq_j\right)$ on the grid might deviate from one, depending on the specification of the distribution. Therefore, the scaling prefactor $\frac{1}{V}$ is included to normalise the result and thus reduce the error. The calculation of $\boldsymbol{M}$ goes equivalently, the formula was given in equation (7.3).

The fitting routine described in section 7.4.2 uses the non-linear optimisation method *least_squares* from SciPy. The fitting routine operates with the standard deviations and the correlation coefficient computed from the covariance matrix $\boldsymbol{M}$, not directly with the entries of $\boldsymbol{M}$.

Bibliography

[1] R. Skalak, N. Ozkaya and T. C. Skalak, 'Biofluid Mechanics', Annual Review of Fluid Mechanics **21**, 167–204 (1989) `10.1146/annurev.fl.21.010189.001123`.

[2] J. B. Freund, 'The flow of red blood cells through a narrow spleen-like slit', Physics of Fluids **25** (11), 110807 (2013) `10.1063/1.4819341`.

[3] H. H. Lipowsky, 'Microvascular Rheology and Hemodynamics', Microcirculation **12** (1), 5–15 (2005) `10.1080/10739680590894966`.

[4] L. Lanotte, J. Mauer, S. Mendez, D. A. Fedosov, J.-M. Fromental, V. Claveria, F. Nicoud, G. Gompper and M. Abkarian, 'Red cells' dynamic morphologies govern blood shear thinning under microcirculatory flow conditions', Proceedings of the National Academy of Sciences **113** (47), 13289–13294 (2016) `10.1073/pnas.1608074113`.

[5] N. Z. Piety, J. Stuntz, N. Yilmaz, H. Xia, T. Yoshida and S. S. Shevkoplyas, 'Microfluidic capillary networks are more sensitive than ektacytometry to the decline of red blood cell deformability induced by storage', Scientific Reports **11**, 604 (2021) `10.1038/s41598-020-79710-3`.

[6] A. K. Dasanna, J. Mauer, G. Gompper and D. A. Fedosov, 'Importance of Viscosity Contrast for the Motion of Erythrocytes in Microcapillaries', Frontiers in Physics **9**, 666913 (2021) `10.3389/fphy.2021.666913`.

[7] M. Diez-Silva, M. Dao, J. Han, C.-T. Lim and S. Suresh, 'Shape and Biomechanical Characteristics of Human Red Blood Cells in Health and Disease', MRS Bulletin **35** (5), 382–388 (2010) `10.1557/mrs2010.571`.

[8] O. Otto et al., 'Real-time deformability cytometry: on-the-fly cell mechanical phenotyping', Nature Methods **12** (3), 199–202 (2015) `10.1038/nmeth.3281`.

[9] E. Henry, S. H. Holm, Z. Zhang, J. P. Beech, J. O. Tegenfeldt, D. A. Fedosov and G. Gompper, 'Sorting cells by their dynamical properties', Scientific Reports **6** (1), 34375 (2016) `10.1038/srep34375`.

[10] C.-H. Wang and A. S. Popel, 'Effect of red blood cell shape on oxygen transport in capillaries', Mathematical Biosciences **116** (1), 89–110 (1993) `10.1016/0025-5564(93)90062-F`.

[11] M. Kubánková, B. Hohberger, J. Hoffmanns, J. Fürst, M. Herrmann, J. Guck and M. Kräter, 'Physical phenotype of blood cells is altered in COVID-19', Biophysical Journal **120** (14), 2838–2847 (2021) `10.1016/j.bpj.2021.05.025`.

[12] S. M. Recktenwald et al., 'Cross-talk between red blood cells and plasma influences blood flow and omics phenotypes in severe COVID-19', eLife **11**, e81316 (2022) `10.7554/eLife.81316`.

[13] P. Gaehtgens, C. Dührssen and K. Albrecht, 'Motion, Deformation, and Interaction of Blood Cells and Plasma During Flow Through Narrow Capillary Tubes', Blood Cells **6**, 799–812 (1980).

[14] G. Tomaiuolo, M. Simeone, V. Martinelli, B. Rotoli and S. Guido, 'Red blood cell deformation in microconfined flow', Soft Matter **5** (19), 3736 (2009) `10.1039/b904584h`.

[15] A. Farutin and C. Misbah, 'Symmetry breaking and cross-streamline migration of three-dimensional vesicles in an axial Poiseuille flow', Physical Review E **89** (4), 042709 (2014) `10.1103/PhysRevE.89.042709`.

[16] G. Prado, A. Farutin, C. Misbah and L. Bureau, 'Viscoelastic Transient of Confined Red Blood Cells', Biophysical Journal **108** (9), 2126–2136 (2015) `10.1016/j.bpj.2015.03.046`.

[17] A. Guckenberger, A. Kihm, T. John, C. Wagner and S. Gekle, 'Numerical-experimental observation of shape bistability of red blood cells flowing in a microchannel', Soft Matter **14** (11), 2032–2043 (2018) `10.1039/C7SM02272G`.

[18] B. Kaoui, G. Biros and C. Misbah, 'Why Do Red Blood Cells Have Asymmetric Shapes Even in a Symmetric Flow?', Physical Review Letters **103** (18), 188101 (2009) `10.1103/PhysRevLett.103.188101`.

[19] L. Shi, T.-W. Pan and R. Glowinski, 'Deformation of a single red blood cell in bounded Poiseuille flows', Physical Review E **85** (1), 016307 (2012) `10.1103/PhysRevE.85.016307`.

[20] B. Kaoui, T. Krüger and J. Harting, 'How does confinement affect the dynamics of viscous vesicles and red blood cells?', Soft Matter **8** (35), 9246 (2012) `10.1039/c2sm26289d`.

[21] N. Tahiri, T. Biben, H. Ez-Zahraouy, A. Benyoussef and C. Misbah, 'On the problem of slipper shapes of red blood cells in the microvasculature', Microvascular Research **85**, 40–45 (2013) `10.1016/j.mvr.2012.10.001`.

[22] D. S. Hariprasad and T. W. Secomb, 'Prediction of noninertial focusing of red blood cells in Poiseuille flow', Physical Review E **92** (3), 033008 (2015) `10.1103/PhysRevE.92.033008`.

[23]D. A. Fedosov, M. Peltomäki and G. Gompper, 'Deformation and dynamics of red blood cells in flow through cylindrical microchannels', Soft Matter **10** (24), 4258–4267 (2014) `10.1039/C4SM00248B`.

[24]F. Reichel, J. Mauer, A. A. Nawaz, G. Gompper, J. Guck and D. A. Fedosov, 'High-Throughput Microfluidic Characterization of Erythrocyte Shapes and Mechanical Variability', Biophysical Journal **117** (1), 14–24 (2019) `10.1016/j.bpj.2019.05.022`.

[25]F. Guglietta, M. Behr, L. Biferale, G. Falcucci and M. Sbragaglia, 'On the effects of membrane viscosity on transient red blood cell dynamics', 8th Apr. 2020, Available at `http://arxiv.org/abs/2004.04109`.

[26]P. Matteoli, F. Nicoud and S. Mendez, 'Impact of the membrane viscosity on the tank-treading behavior of red blood cells', Physical Review Fluids **6** (4), 043602 (2021) `10.1103/PhysRevFluids.6.043602`.

[27]Z. Wang, R. Lu, W. Wang, F. B. Tian, J. J. Feng and Y. Sui, 'A computational model for the transit of a cancer cell through a constricted microchannel', Biomechanics and Modeling in Mechanobiology **22**, 1129–1143 (2023) `10.1007/s10237-023-01705-6`.

[28]O. Aouane, A. Farutin, M. Thiébaud, A. Benyoussef, C. Wagner and C. Misbah, 'Hydrodynamic pairing of soft particles in a confined flow', Physical Review Fluids **2** (6), 063102 (2017) `10.1103/PhysRevFluids.2.063102`.

[29]A. Guckenberger, 'From models to applications: Simulation of blood flow with an extended boundary integral method', Doktorarbeit (Universität Bayreuth, Bayreuth, 2018).

[30]V. Bennett, 'The membrane skeleton of human erythrocytes and its implications for more complex cells', Annual Review of Biochemistry **54** (1), 273–304 (1985) `10.1146/annurev.bi.54.070185.001421`.

[31]J. B. Freund, 'Numerical Simulation of Flowing Blood Cells', Annual Review of Fluid Mechanics **46** (1), 67–95 (2014) `10.1146/annurev-fluid-010313-141349`.

[32]R. Skalak, A. Tozeren, R. Zarda and S. Chien, 'Strain Energy Function of Red Blood Cell Membranes', Biophysical Journal **13** (3), 245–264 (1973) `10.1016/S0006-3495(73)85983-1`.

[33]D. Barthès-Biesel, A. Diaz and E. Dhenin, 'Effect of constitutive laws for two-dimensional membranes on flow-induced capsule deformation', Journal of Fluid Mechanics **460**, 211–222 (2002) `10.1017/S0022112002008352`.

[34]D. Barthès-Biesel, 'Motion and Deformation of Elastic Capsules and Vesicles in Flow', Annual Review of Fluid Mechanics **48** (1), 25–52 (2016) `10.1146/annurev-fluid-122414-034345`.

[35] T. Krüger, *Computer simulation study of collective phenomena in dense suspensions of red blood cells under shear* (Springer Spektrum, Wiesbaden, 2012), 163 pp.

[36] P. Li and J. Zhang, 'A finite difference method with subsampling for immersed boundary simulations of the capsule dynamics with viscoelastic membranes', International Journal for Numerical Methods in Biomedical Engineering **35** (6), e3200 (2019) `10.1002/CNM.3200`.

[37] P. Canham, 'The minimum energy of bending as a possible explanation of the biconcave shape of the human red blood cell', Journal of Theoretical Biology **26** (1), 61–81 (1970) `10.1016/S0022-5193(70)80032-7`.

[38] W. Helfrich, 'Elastic Properties of Lipid Bilayers: Theory and Possible Experiments', Zeitschrift für Naturforschung C **28** (11-12), 693–703 (1973) `10.1515/znc-1973-11-1209`.

[39] A. Guckenberger, M. P. Schraml, P. G. Chen, M. Leonetti and S. Gekle, 'On the bending algorithms for soft objects in flows', Computer Physics Communications **207**, 1–23 (2016) `10.1016/j.cpc.2016.04.018`.

[40] A. Guckenberger and S. Gekle, 'Theory and algorithms to compute Helfrich bending forces: a review', Journal of Physics: Condensed Matter **29** (20), 203001 (2017) `10.1088/1361-648X/aa6313`.

[41] G. Xu, 'Discrete Laplace–Beltrami operators and their convergence', Computer Aided Geometric Design **21** (8), 767–784 (2004) `10.1016/j.cagd.2004.07.007`.

[42] T. M. Fischer, 'Shape Memory of Human Red Blood Cells', Biophysical Journal **86** (5), 3304–3313 (2004) `10.1016/S0006-3495(04)74378-7`.

[43] E. Evans and Y.-C. Fung, 'Improved measurements of the erythrocyte geometry', Microvascular Research **4** (4), 335–347 (1972) `10.1016/0026-2862(72)90069-6`.

[44] D. Cordasco and P. Bagchi, 'On the shape memory of red blood cells', Physics of Fluids **29** (4), 041901 (2017) `10.1063/1.4979271`.

[45] J. Evans, W. Gratzer, N. Mohandas, K. Parker and J. Sleep, 'Fluctuations of the Red Blood Cell Membrane: Relation to Mechanical Properties and Lack of ATP Dependence', Biophysical Journal **94** (10), 4134–4144 (2008) `10.1529/biophysj.107.117952`.

[46] G. Popescu, T. Ikeda, K. Goda, C. A. Best-Popescu, M. Laposata, S. Manley, R. R. Dasari, K. Badizadegan and M. S. Feld, 'Optical Measurement of Cell Membrane Tension', Physical Review Letters **97** (21), 218101 (2006) `10.1103/PhysRevLett.97.218101`.

[47] D. E. Discher, D. H. Boal and S. K. Boey, 'Simulations of the Erythrocyte Cytoskeleton at Large Deformation. II. Micropipette Aspiration', Biophysical Journal **75** (3), 1584–1597 (1998) `10.1016/S0006-3495(98)74076-7`.

[48] K.-i. Tsubota, S. Wada and H. Liu, ‘Elastic behavior of a red blood cell with the membrane’s nonuniform natural state: equilibrium shape, motion transition under shear flow, and elongation during tank-treading motion’, Biomechanics and Modeling in Mechanobiology **13** (4), 735–746 (2014) `10.1007/s10237-013-0530-z`.

[49] J. Li, G. Lykotrafitis, M. Dao and S. Suresh, ‘Cytoskeletal dynamics of human erythrocyte’, Proceedings of the National Academy of Sciences **104** (12), 4937–4942 (2007) `10.1073/pnas.0700257104`.

[50] A. Viallat and M. Abkarian, ‘Red blood cell: from its mechanics to its motion in shear flow’, International Journal of Laboratory Hematology **36** (3), 237–243 (2014) `10.1111/ijlh.12233`.

[51] K. Sinha and M. D. Graham, ‘Dynamics of a single red blood cell in simple shear flow’, Physical Review E **92** (4), 042710 (2015) `10.1103/PhysRevE.92.042710`.

[52] D. Cordasco, A. Yazdani and P. Bagchi, ‘Comparison of erythrocyte dynamics in shear flow under different stress-free configurations’, Physics of Fluids **26** (4), 041902 (2014) `10.1063/1.4871300`.

[53] Z. Peng, A. Mashayekh and Q. Zhu, ‘Erythrocyte responses in low-shear-rate flows: effects of non-biconcave stress-free state in the cytoskeleton’, Journal of Fluid Mechanics **742**, 96–118 (2014) `10.1017/jfm.2014.14`.

[54] M. Levant and V. Steinberg, ‘Intermediate regime and a phase diagram of red blood cell dynamics in a linear flow’, Physical Review E **94** (6), 062412 (2016) `10.1103/PhysRevE.94.062412`.

[55] J. P. Mills, L. Qie, M. Dao, C. T. Lim and S. Suresh, ‘Nonlinear Elastic and Viscoelastic Deformation of the Human Red Blood Cell with Optical Tweezers’, Mech Chem Biosyst **1** (3), 169–180 (2004).

[56] Y.-Z. Yoon, J. Kotar, G. Yoon and P. Cicuta, ‘The nonlinear mechanical response of the red blood cell’, Physical Biology **5** (3), 036007 (2008) `10.1088/1478-3975/5/3/036007`.

[57] E. Evans, ‘Bending elastic modulus of red blood cell membrane derived from buckling instability in micropipet aspiration tests’, Biophysical Journal **43** (1), 27–30 (1983) `10.1016/S0006-3495(83)84319-7`.

[58] E. Evans, N. Mohandas and A. Leung, ‘Static and dynamic rigidities of normal and sickle erythrocytes. Major influence of cell hemoglobin concentration.’, Journal of Clinical Investigation **73** (2), 477–488 (1984) `10.1172/JCI111234`.

[59] B. Kaoui and J. Harting, ‘Two-dimensional lattice Boltzmann simulations of vesicles with viscosity contrast’, Rheologica Acta **55** (6), 465–475 (2016) `10.1007/s00397-015-0867-6`.

[60] G. R. Cokelet and H. J. Meiselman, ‘Rheological Comparison of Hemoglobin Solutions and Erythrocyte Suspensions’, Science **162** (3850), 275–277 (1968) `10.1126/science.162.3850.275`.

[61] R. Wells and H. Schmid-Schönbein, ‘Red cell deformation and fluidity of concentrated cell suspensions.’, Journal of Applied Physiology **27** (2), 213–217 (1969) `10.1152/jappl.1969.27.2.213`.

[62] S. M. Recktenwald, K. Graessel, F. M. Maurer, T. John, S. Gekle and C. Wagner, ‘Red blood cell shape transitions and dynamics in time-dependent capillary flows’, Biophysical Journal **121** (1), 23–36 (2022) `10.1016/j.bpj.2021.12.009`.

[63] S. Chien, S. Usami, H. M. Taylor, J. L. Lundberg and M. I. Gregersen, ‘Effects of hematocrit and plasma proteins on human blood rheology at low shear rates’, Journal of Applied Physiology **21** (1), 81–87 (1966) `10.1152/jappl.1966.21.1.81`.

[64] C. Pozrikidis, *Boundary Integral and Singularity Methods for Linearized Viscous Flow* (Cambridge University Press, 1992).

[65] A. Guckenberger and S. Gekle, ‘A boundary integral method with volume-changing objects for ultrasound-triggered margination of microbubbles’, Journal of Fluid Mechanics **836**, 952–997 (2018) `10.1017/jfm.2017.836`.

[66] H. Zhao, A. H. Isfahani, L. N. Olson and J. B. Freund, ‘A spectral boundary integral method for flowing blood cells’, Journal of Computational Physics **229** (10), 3726–3744 (2010) `10.1016/j.jcp.2010.01.024`.

[67] C. Pozrikidis, ‘Interfacial Dynamics for Stokes Flow’, Journal of Computational Physics **169** (2), 250–301 (2001) `10.1006/jcph.2000.6582`.

[68] Bronzino, Joseph D. (Ed.), *Biomedical Engineering Fundamentals* (CRC Press, 2006).

[69] A. Guckenberger, ‘Simulation of red blood cells and microbubbles in infinite and periodic Stokes flow’, Masterarbeit (Universität Bayreuth, Bayreuth, 2015).

[70] A. Daddi-Moussa-Ider, A. Guckenberger and S. Gekle, ‘Long-lived anomalous thermal diffusion induced by elastic cell membranes on nearby particles’, Physical Review E **93** (1), 012612 (2016) `10.1103/PhysRevE.93.012612`.

[71] S. Quint, A. F. Christ, A. Guckenberger, S. Himbert, L. Kaestner, S. Gekle and C. Wagner, ‘3D tomography of cells in micro-channels’, Applied Physics Letters **111** (10), 103701 (2017) `10.1063/1.4986392`.

[72] J. B. Freund, ‘Leukocyte margination in a model microvessel’, Physics of Fluids **19** (2), 023301 (2007) `10.1063/1.2472479`.

[73] M. Meyer, M. Desbrun, P. Schröder and A. H. Barr, ‘Discrete Differential-Geometry Operators for Triangulated 2-Manifolds’, in Visualization and Mathematics III (2003), pp. 35–57, `10.1007/978-3-662-05105-4_2`.

[74] M. Deserno, ‘Fluid lipid membranes: From differential geometry to curvature stresses’, Chemistry and Physics of Lipids **185**, 11–45 (2015) `10.1016/j.chemphyslip.2014.05.001`.

[75] G. R. Cowper, ‘Gaussian quadrature formulas for triangles’, International Journal for Numerical Methods in Engineering **7** (3), 405–408 (1973) `10.1002/nme.1620070316`.

[76] C. Pozrikidis, ‘Finite deformation of liquid capsules enclosed by elastic membranes in simple shear flow’, Journal of Fluid Mechanics **297**, 123–152 (1995) `10.1017/S002211209500303X`.

[77] M. Loewenberg and E. J. Hinch, ‘Numerical simulation of a concentrated emulsion in shear flow’, Journal of Fluid Mechanics **321**, 395–419 (1996) `10.1017/S002211209600777X`.

[78] H. Hasimoto, ‘On the periodic fundamental solutions of the Stokes equations and their application to viscous flow past a cubic array of spheres’, Journal of Fluid Mechanics **5** (02), 317 (1959) `10.1017/S0022112059000222`.

[79] D. Saintillan, E. Darve and E. S. G. Shaqfeh, ‘A smooth particle-mesh Ewald algorithm for Stokes suspension simulations: The sedimentation of fibers’, Physics of Fluids **17** (3), 033301 (2005) `10.1063/1.1862262`.

[80] Y. Saad and M. H. Schultz, ‘GMRES: A Generalized Minimal Residual Algorithm for Solving Nonsymmetric Linear Systems’, SIAM Journal on Scientific and Statistical Computing **7** (3), 856–869 (1986) `10.1137/0907058`.

[81] P. Bogacki and L. Shampine, ‘A 3(2) pair of Runge - Kutta formulas’, Applied Mathematics Letters **2** (4), 321–325 (1989) `10.1016/0893-9659(89)90079-7`.

[82] A. Farutin, T. Biben and C. Misbah, ‘3D numerical simulations of vesicle and inextensible capsule dynamics’, Journal of Computational Physics **275**, 539–568 (2014) `10.1016/j.jcp.2014.07.008`.

[83] M. C. Sukop and D. T. Thorne, *Lattice Boltzmann Modeling - An introduction for Geoscientists and Engineers* (Springer Berlin Heidelberg, 2007).

[84] B. Dünweg and A. J. Ladd, ‘Lattice Boltzmann Simulations of Soft Matter Systems’, in *Advanced Computer Simulation Approaches for Soft Matter Sciences III. Advances in Polymer Science*, Vol. 221 (Springer Berlin Heidelberg), `10.1007/978-3-540-87706-6_2`.

[85] C. K. Aidun and J. R. Clausen, 'Lattice-Boltzmann Method for Complex Flows', Annual Review of Fluid Mechanics **42** (1), 439–472 (2010) `10.1146/annurev-fluid-121108-145519`.

[86] T. Krüger, H. Kusumaatmaja, A. Kuzmin, O. Shardt, G. Silva and E. M. Viggen, *The Lattice Boltzmann Method: Principles and Practice* (Springer International Publishing, Cham, 2017), `10.1007/978-3-319-44649-3`.

[87] J. Lu, H. Han, B. Shi and Z. Guo, 'Immersed boundary lattice Boltzmann model based on multiple relaxation times', Physical Review E **85** (1), 016711 (2012) `10.1103/PhysRevE.85.016711`.

[88] H. Limbach, A. Arnold, B. Mann and C. Holm, 'ESPResSo—an extensible simulation package for research on soft matter systems', Computer Physics Communications **174** (9), 704–727 (2006) `10.1016/j.cpc.2005.10.005`.

[89] A. Arnold, O. Lenz, S. Kesselheim, R. Weeber, F. Fahrenberger, D. Roehm, P. Kosovan and C. Holm, 'ESPResSo 3.1: Molecular Dynamics Software for Coarse-Grained Models', in Meshfree Methods for Partial Differential Equations VI, Vol. 89 (2013), pp. 1–23, `10.1007/978-3-642-32979-1`.

[90] F. Weik et al., 'ESPResSo 4.0 – an extensible software package for simulating soft matter systems', The European Physical Journal Special Topics **227** (14), 1789–1816 (2019) `10.1140/epjst/e2019-800186-9`.

[91] C. S. Peskin, 'The immersed boundary method', Acta Numerica **11**, 479–517 (2002) `10.1017/S0962492902000077`.

[92] R. Mittal and G. Iaccarino, 'IMMERSED BOUNDARY METHODS', Annual Review of Fluid Mechanics **37** (1), 239–261 (2005) `10.1146/annurev.fluid.37.061903.175743`.

[93] T. Krüger, F. Varnik and D. Raabe, 'Efficient and accurate simulations of deformable particles immersed in a fluid using a combined immersed boundary lattice Boltzmann finite element method', Computers & Mathematics with Applications **61** (12), 3485–3505 (2011) `10.1016/j.camwa.2010.03.057`.

[94] R. Blythman, T. Persoons, N. Jeffers, K. Nolan and D. Murray, 'Localised dynamics of laminar pulsatile flow in a rectangular channel', International Journal of Heat and Fluid Flow **66**, 8–17 (2017) `10.1016/j.ijheatfluidflow.2017.05.006`.

[95] S. M. Recktenwald, C. Wagner and T. John, 'Optimizing pressure-driven pulsatile flows in microfluidic devices', Lab on a Chip **21** (13), 2605–2613 (2021) `10.1039/D0LC01297A`.

[96] D. A. Fedosov, B. Caswell and G. E. Karniadakis, 'A Multiscale Red Blood Cell Model with Accurate Mechanics, Rheology, and Dynamics', Biophysical Journal **98** (10), 2215–2225 (2010) `10.1016/j.bpj.2010.02.002`.

[97] T. M. Fischer, ‘Tank-Tread Frequency of the Red Cell Membrane: Dependence on the Viscosity of the Suspending Medium’, Biophysical Journal **93** (7), 2553–2561 (2007) `10.1529/biophysj.107.104505`.

[98] M. Abkarian, M. Faivre and A. Viallat, ‘Swinging of Red Blood Cells under Shear Flow’, Physical Review Letters **98** (18), 188302 (2007) `10.1103/PhysRevLett.98.188302`.

[99] A. Z. K. Yazdani, R. M. Kalluri and P. Bagchi, ‘Tank-treading and tumbling frequencies of capsules and red blood cells’, Physical Review E **83** (4), 046305 (2011) `10.1103/PhysRevE.83.046305`.

[100] G. Danker, P. M. Vlahovska and C. Misbah, ‘Vesicles in Poiseuille Flow’, Physical Review Letters **102** (14), 148102 (2009) `10.1103/PhysRevLett.102.148102`.

[101] J. Mauer, S. Mendez, L. Lanotte, F. Nicoud, M. Abkarian, G. Gompper and D. A. Fedosov, ‘Flow-Induced Transitions of Red Blood Cell Shapes under Shear’, Physical Review Letters **121** (11), 118103 (2018) `10.1103/PhysRevLett.121.118103`.

[102] P. Li and J. Zhang, ‘Similar but Distinct Roles of Membrane and Interior Fluid Viscosities in Capsule Dynamics in Shear Flows’, Cardiovascular Engineering and Technology **12** (2), 232–249 (2021) `10.1007/s13239-020-00517-4`.

[103] M. Nouaman et al., ‘Effect of Cell Age and Membrane Rigidity on Red Blood Cell Shape in Capillary Flow’, Cells **12** (11), 1529 (2023) `10.3390/cells12111529`.

[104] T. M. Fischer and R. Korzeniewski, ‘Angle of Inclination of Tank-Treading Red Cells: Dependence on Shear Rate and Suspending Medium’, Biophysical Journal **108** (6), 1352–1360 (2015) `10.1016/j.bpj.2015.01.028`.

[105] A. Yazdani and P. Bagchi, ‘Influence of membrane viscosity on capsule dynamics in shear flow’, Journal of Fluid Mechanics **718**, 569–595 (2013) `10.1017/jfm.2012.637`.

[106] P. Li and J. Zhang, ‘Finite-difference and integral schemes for Maxwell viscous stress calculation in immersed boundary simulations of viscoelastic membranes’, Biomechanics and Modeling in Mechanobiology **19** (6), 2667–2681 (2020) `10.1007/s10237-020-01363-y`.

[107] J. M. Charrier, S. Shrivastava and R. Wu, ‘Free and constrained inflation of elastic membranes in relation to thermoforming — non-axisymmetric problems’, The Journal of Strain Analysis for Engineering Design **24** (2), 55–74 (1989) `10.1243/03093247V242055`.

[108] S. Shrivastava and J. Tang, ‘Large deformation finite element analysis of non-linear viscoelastic membranes with reference to thermoforming’, The Journal of Strain Analysis for Engineering Design **28** (1), 31–51 (1993) `10.1243/03093247V281031`.

[109] A. F. Bower, *Applied Mechanics of Solids* (CRC Press, 5th Oct. 2009), `10.1201/9781439802489`.

[110] F. Häusl, 'Soft Objects in Newtonian and Non-Newtonian Fluids - a Computational Study of Bubbles and Capsules in Flow', Masterarbeit (Universität Bayreuth, Bayreuth, 2021).

[111] E. Evans and R. Hochmuth, 'Membrane viscoelasticity', Biophysical Journal **16** (1), 1–11 (1976) `10.1016/S0006-3495(76)85658-5`.

[112] S. Chien, K. Sung, R. Skalak, S. Usami and A. Tözeren, 'Theoretical and experimental studies on viscoelastic properties of erythrocyte membrane', Biophysical Journal **24** (2), 463–487 (1978) `10.1016/S0006-3495(78)85395-8`.

[113] R. Hochmuth, P. Worthy and E. Evans, 'Red cell extensional recovery and the determination of membrane viscosity', Biophysical Journal **26** (1), 101–114 (1979) `10.1016/S0006-3495(79)85238-8`.

[114] R. Hochmuth, K. Buxbaum and E. Evans, 'Temperature dependence of the viscoelastic recovery of red cell membrane', Biophysical Journal **29** (1), 177–182 (1980) `10.1016/S0006-3495(80)85124-1`.

[115] O. Linderkamp and H. Meiselman, 'Geometric, osmotic, and membrane mechanical properties of density- separated human red cells', Blood **59** (6), 1121–1127 (1982) `10.1182/blood.V59.6.1121.1121`.

[116] R. Tran-Son-Tay, S. Sutera and P. Rao, 'Determination of red blood cell membrane viscosity from rheoscopic observations of tank-treading motion', Biophysical Journal **46** (1), 65–72 (1984) `10.1016/S0006-3495(84)83999-5`.

[117] R. Dimova, S. Aranda, N. Bezlyepkina, V. Nikolov, K. A. Riske and R. Lipowsky, 'A practical guide to giant vesicles. Probing the membrane nanoregime via optical microscopy', Journal of Physics: Condensed Matter **18** (28), S1151–S1176 (2006) `10.1088/0953-8984/18/28/S04`.

[118] R. Dimova, C. Dietrich, A. Hadjiisky, K. Danov and B. Pouligny, 'Falling ball viscosimetry of giant vesicle membranes: Finite-size effects', The European Physical Journal B **12** (4), 589–598 (1999) `10.1007/s100510051042`.

[119] W. den Otter and S. Shkulipa, 'Intermonolayer Friction and Surface Shear Viscosity of Lipid Bilayer Membranes', Biophysical Journal **93** (2), 423–433 (2007) `10.1529/biophysj.107.105395`.

[120] H. Noguchi and G. Gompper, 'Shape transitions of fluid vesicles and red blood cells in capillary flows', Proceedings of the National Academy of Sciences **102** (40), 14159–14164 (2005) `10.1073/pnas.0504243102`.

[121] R. M. Hochmuth and R. E. Waugh, 'Erythrocyte Membrane Elasticity and Viscosity', Annual Review of Physiology **49** (1), 209–219 (1987) `10.1146/annurev.ph.49.030187.001233`.

[122] G. Lim H.W., M. Wortis and R. Mukhopadhyay, 'Stomatocyte-discocyte-echinocyte sequence of the human red blood cell: Evidence for the bilayer-couple hypothesis from membrane mechanics', Proceedings of the National Academy of Sciences **99** (26), 16766–16769 (2002) `10.1073/pnas.202617299`.

[123] L. Miao, U. Seifert, M. Wortis and H.-G. Döbereiner, 'Budding transitions of fluid-bilayer vesicles: The effect of area-difference elasticity', Physical Review E **49** (6), 5389–5407 (1994) `10.1103/PhysRevE.49.5389`.

[124] A. Jay, 'Geometry of the human erythrocyte. I. Effect of albumin on cell geometry', Biophysical Journal **15** (3), 205–222 (1975) `10.1016/S0006-3495(75)85812-7`.

[125] S. Mendez, E. Gibaud and F. Nicoud, 'An unstructured solver for simulations of deformable particles in flows at arbitrary Reynolds numbers', Journal of Computational Physics **256**, 465–483 (2014) `10.1016/j.jcp.2013.08.061`.

[126] K. Müller, D. A. Fedosov and G. Gompper, 'Smoothed dissipative particle dynamics with angular momentum conservation', Journal of Computational Physics **281**, 301–315 (2015) `10.1016/j.jcp.2014.10.017`.

[127] C. Pozrikidis, 'Resting shape and spontaneous membrane curvature of red blood cells', Mathematical Medicine and Biology **22** (1), 34–52 (2005) `10.1093/imammb/dqh021`.

[128] J. Dupire, M. Abkarian and A. Viallat, 'A simple model to understand the effect of membrane shear elasticity and stress-free shape on the motion of red blood cells in shear flow', Soft Matter **11** (42), 8372–8382 (2015) `10.1039/C5SM01407G`.

[129] J. Dupire, M. Socol and A. Viallat, 'Full dynamics of a red blood cell in shear flow', Proceedings of the National Academy of Sciences **109** (51), 20808–20813 (2012) `10.1073/pnas.1210236109`.

[130] A. Z. K. Yazdani and P. Bagchi, 'Phase diagram and breathing dynamics of a single red blood cell and a biconcave capsule in dilute shear flow', Physical Review E **84** (2), 026314 (2011) `10.1103/PhysRevE.84.026314`.

[131] S. Mendez and M. Abkarian, 'In-plane elasticity controls the full dynamics of red blood cells in shear flow', Physical Review Fluids **3** (10), 101101 (2018) `10.1103/PhysRevFluids.3.101101`.

[132] F. Guglietta, M. Behr, L. Biferale, G. Falcucci and M. Sbragaglia, 'Lattice Boltzmann simulations on the tumbling to tank-treading transition: effects of membrane viscosity', Philosophical Transactions of the Royal Society A: Mathematical, Physical and Engineering Sciences **379** (2208), 20200395 (2021) `10.1098/rsta.2020.0395`.

[133] M. Dao, C. Lim and S. Suresh, ‘Mechanics of the human red blood cell deformed by optical tweezers’, Journal of the Mechanics and Physics of Solids **51** (11-12), 2259–2280 (2003) `10.1016/j.jmps.2003.09.019`.

[134] S. Suresh, J. Spatz, J. Mills, A. Micoulet, M. Dao, C. Lim, M. Beil and T. Seufferlein, ‘Connections between single-cell biomechanics and human disease states: gastrointestinal cancer and malaria’, Acta Biomaterialia **1** (1), 15–30 (2005) `10.1016/j.actbio.2004.09.001`.

[135] S. Hénon, G. Lenormand, A. Richert and F. Gallet, ‘A New Determination of the Shear Modulus of the Human Erythrocyte Membrane Using Optical Tweezers’, Biophysical Journal **76** (2), 1145–1151 (1999) `10.1016/S0006-3495(99)77279-6`.

[136] P. Bronkhorst, G. Streekstra, J. Grimbergen, E. Nijhof, J. Sixma and G. Brakenhoff, ‘A new method to study shape recovery of red blood cells using multiple optical trapping’, Biophysical Journal **69** (5), 1666–1673 (1995) `10.1016/S0006-3495(95)80084-6`.

[137] J. Li, M. Dao, C. Lim and S. Suresh, ‘Spectrin-Level Modeling of the Cytoskeleton and Optical Tweezers Stretching of the Erythrocyte’, Biophysical Journal **88** (5), 3707–3719 (2005) `10.1529/biophysj.104.047332`.

[138] I. V. Pivkin and G. E. Karniadakis, ‘Accurate Coarse-Grained Modeling of Red Blood Cells’, Physical Review Letters **101** (11), 118105 (2008) `10.1103/PhysRevLett.101.118105`.

[139] B. Walsh and F. J. Boyle, ‘In-Flow dynamics of an area-difference-energy spring-particle red blood cell model on non-uniform grids’, Computer Methods in Biomechanics and Biomedical Engineering **25** (1), 52–64 (2022) `10.1080/10255842.2021.1931845`.

[140] D. A. Fedosov, B. Caswell and G. E. Karniadakis, ‘Systematic coarse-graining of spectrin-level red blood cell models’, Computer Methods in Applied Mechanics and Engineering **199** (29-32), 1937–1948 (2010) `10.1016/j.cma.2010.02.001`.

[141] T. Krüger, D. Holmes and P. V. Coveney, ‘Deformability-based red blood cell separation in deterministic lateral displacement devices—A simulation study’, Biomicrofluidics **8** (5), 054114 (2014) `10.1063/1.4897913`.

[142] J. Sigüenza, S. Mendez and F. Nicoud, ‘How should the optical tweezers experiment be used to characterize the red blood cell membrane mechanics?’, Biomechanics and Modeling in Mechanobiology **16** (5), 1645–1657 (2017) `10.1007/s10237-017-0910-x`.

[143] D. Cordasco and P. Bagchi, ‘Dynamics of red blood cells in oscillating shear flow’, Journal of Fluid Mechanics **800**, 484–516 (2016) `10.1017/jfm.2016.409`.

[144] Y. Sui, Y. T. Chew, P. Roy, Y. P. Cheng and H. T. Low, 'Dynamic motion of red blood cells in simple shear flow', Physics of Fluids **20** (11), 112106 (2008) `10.1063/1.3026569`.

[145] W. R. Dodson and P. Dimitrakopoulos, 'Oscillatory tank-treading motion of erythrocytes in shear flows', Physical Review E **84** (1), 011913 (2011) `10.1103/PhysRevE.84.011913`.

[146] Z. Peng and Q. Zhu, 'Deformation of the erythrocyte cytoskeleton in tank treading motions', Soft Matter **9** (31), 7617 (2013) `10.1039/c3sm50895a`.

[147] T. Fischer, M. Stohr-Lissen and H. Schmid-Schonbein, 'The red cell as a fluid droplet: tank tread-like motion of the human erythrocyte membrane in shear flow', Science **202** (4370), 894–896 (1978) `10.1126/science.715448`.

[148] H. Basu, A. K. Dharmadhikari, J. A. Dharmadhikari, S. Sharma and D. Mathur, 'Tank Treading of Optically Trapped Red Blood Cells in Shear Flow', Biophysical Journal **101** (7), 1604–1612 (2011) `10.1016/j.bpj.2011.08.043`.

[149] A. Yazdani and P. Bagchi, 'Three-dimensional numerical simulation of vesicle dynamics using a front-tracking method', Physical Review E **85** (5), 056308 (2012) `10.1103/PhysRevE.85.056308`.

[150] C. Geuzaine and J.-F. Remacle, 'Gmsh: A 3-D finite element mesh generator with built-in pre- and post-processing facilities', International Journal for Numerical Methods in Engineering **79** (11), 1309–1331 (2009) `10.1002/nme.2579`.

[151] G. Chétrite and R. Cassoly, 'Affinity of hemoglobin for the cytoplasmic fragment of human erythrocyte membrane band 3', Journal of Molecular Biology **185** (3), 639–644 (1985) `10.1016/0022-2836(85)90076-2`.

[152] J. Eisinger, J. Flores and J. M. Salhany, 'Association of cytosol hemoglobin with the membrane in intact erythrocytes.', Proceedings of the National Academy of Sciences **79** (2), 408–412 (1982) `10.1073/pnas.79.2.408`.

[153] G. Nash and S. Wyard, 'Erythrocyte membrane elasticity during in vivo ageing', Biochimica et Biophysica Acta (BBA) - Biomembranes **643** (2), 269–275 (1981) `10.1016/0005-2736(81)90072-9`.

[154] G. Nash, C. Johnson and H. Meiselman, 'Mechanical properties of oxygenated red blood cells in sickle cell (HbSS) disease', Blood **63** (1), 73–82 (1984) `10.1182/blood.V63.1.73.73`.

[155] R. Waugh, 'Effects of 2,3-diphosphoglycerate on the mechanical properties of erythrocyte membrane', Blood **68** (1), 231–238 (1986) `10.1182/blood.V68.1.231.231`.

[156] N. Toepfner et al., 'Detection of human disease conditions by single-cell morpho-rheological phenotyping of blood', eLife **7**, e29213 (2018) `10.7554/eLife.29213`.

[157] A. Walther et al., 'Depressive disorders are associated with increased peripheral blood cell deformability: a cross-sectional case-control study (Mood-Morph)', Translational Psychiatry **12** (1), 150 (2022) `10.1038/s41398-022-01911-3`.

[158] P. Müller et al., *Shape-Out version 2.14.0: Graphical user interface for analysis and visualization of RT-DC data sets [Software]*, 2019, Available at `https://github.com/ZELLMECHANIK-DRESDEN/ShapeOut2`.

[159] P. Müller and C. Herold, *Shape-Out 2 Documentation Release 2.14.0*, 7th Nov. 2023, Available at `https://shapeout2.readthedocs.io/en/stable/`.

[160] N. Toepfner et al., 'Detection of human disease conditions by single-cell morpho-rheological phenotyping of blood [Video 1]', eLife [Creative Commons Attribution License, https://creativecommons.org/licenses/by/4.0/] **7**, e29213 (2018) `10.7554/eLife.29213.011`.

[161] B. Büyükurgancı, S. K. Basu, M. Neuner, J. Guck, A. Wierschem and F. Reichel, 'Shear rheology of methyl cellulose based solutions for cell mechanical measurements at high shear rates', Soft Matter **19** (9), 1739–1748 (2023) `10.1039/D2SM01515C`.

[162] F. Reichel and B. Büyükurgancı, 'Effective viscosity of methyl cellulose solutions in phosphate buffered saline in real-time deformability cytometry', arXiv, `10.48550/arXiv.2302.01664` (2023) `10.48550/arXiv.2302.01664`.

[163] R. Kellnberger, T. Jüngst and S. Gekle, 'Novel lattice Boltzmann method for simulation of strongly shear thinning viscoelastic fluids', International Journal for Numerical Methods in Fluids (under review) (2024).

[164] C. B. Barber, D. P. Dobkin and H. Huhdanpaa, 'The quickhull algorithm for convex hulls', ACM Transactions on Mathematical Software **22** (4), 469–483 (1996) `10.1145/235815.235821`.

[165] F. Reichel et al., 'Changes in Blood Cell Deformability in Chorea-Acanthocytosis and Effects of Treatment With Dasatinib or Lithium', Frontiers in Physiology **13**, 852946 (2022) `10.3389/fphys.2022.852946`.

[166] E. Jones, T. Oliphant, P. Peterson et al., *SciPy: open source scientific tools for Python*, 2001–, `http://www.scipy.org/`.

[167] R. Fåhraeus, 'The Suspension Stability of the Blood', Physiological Reviews **9** (2), 241–274 (1929) `10.1152/physrev.1929.9.2.241`.

[168] T. W. Secomb, 'Blood Flow in the Microcirculation', Annual Review of Fluid Mechanics **49**, 443–461 (2017).

[169] D. Bento, C. Fernandes, J. Miranda and R. Lima, 'In vitro blood flow visualizations and cell-free layer (CFL) measurements in a microchannel network', Experimental Thermal and Fluid Science **109**, 109847 (2019) `10.1016/j.expthermflusci.2019.109847`.

[170] Q. Zhou, J. Fidalgo, L. Calvi, M. O. Bernabeu, P. R. Hoskins, M. S. Oliveira and T. Krüger, 'Spatiotemporal Dynamics of Dilute Red Blood Cell Suspensions in Low-Inertia Microchannel Flow', Biophysical Journal **118** (10), 2561–2573 (2020) `10.1016/j.bpj.2020.03.019`.

[171] A. I. Rodríguez-Villarreal, M. Carmona-Flores and J. Colomer-Farrarons, 'Effect of Temperature and Flow Rate on the Cell-Free Area in the Microfluidic Channel', Membranes **11** (2), 109 (2021) `10.3390/membranes11020109`.

[172] R. Lima, T. Ishikawa, Y. Imai, M. Takeda, S. Wada and T. Yamaguchi, 'Radial dispersion of red blood cells in blood flowing through glass capillaries: The role of hematocrit and geometry', Journal of Biomechanics **41** (10), 2188–2196 (2008) `10.1016/j.jbiomech.2008.04.033`.

[173] P. Balogh and P. Bagchi, 'The cell-free layer in simulated microvascular networks', Journal of Fluid Mechanics **864**, 768–806 (2019) `10.1017/jfm.2019.45`.

[174] C. Bächer, A. Kihm, L. Schrack, L. Kaestner, M. W. Laschke, C. Wagner and S. Gekle, 'Antimargination of Microparticles and Platelets in the Vicinity of Branching Vessels', Biophysical Journal **115** (2), 411–425 (2018) `10.1016/j.bpj.2018.06.013`.

[175] C. Bächer, L. Schrack and S. Gekle, 'Clustering of microscopic particles in constricted blood flow', Physical Review Fluids **2** (1), 013102 (2017) `10.1103/PhysRevFluids.2.013102`.

[176] D. A. Fedosov, B. Caswell, A. S. Popel and G. E. Karniadakis, 'Blood Flow and Cell-Free Layer in Microvessels: Blood Flow and Cell-Free Layer in Microvessels', Microcirculation **17** (8), 615–628 (2010) `10.1111/j.1549-8719.2010.00056.x`.

[177] J. B. Freund and M. M. Orescanin, 'Cellular flow in a small blood vessel', Journal of Fluid Mechanics **671**, 466–490 (2011) `10.1017/S0022112010005835`.

[178] D. Katanov, G. Gompper and D. A. Fedosov, 'Microvascular blood flow resistance: Role of red blood cell migration and dispersion', Microvascular Research **99**, 57–66 (2015) `10.1016/j.mvr.2015.02.006`.

[179] K. Vahidkhah, P. Balogh and P. Bagchi, 'Flow of Red Blood Cells in Stenosed Microvessels', Scientific Reports **6** (1), 28194 (2016) `10.1038/srep28194`.

[180] W. Chien, G. Gompper and D. A. Fedosov, 'Effect of cytosol viscosity on the flow behavior of red blood cell suspensions in microvessels', Microcirculation **28** (2), `10.1111/micc.12668` (2021) `10.1111/micc.12668`.

[181] D. Oh, S. Ii and S. Takagi, ‘Numerical Study of Particle Margination in a Square Channel Flow with Red Blood Cells’, Fluids **7** (3), 96 (2022) `10.3390/fluids7030096`.

[182] M. Gracka, R. Lima, J. M. Miranda, S. Student, B. Melka and Z. Ostrowski, ‘Red blood cells tracking and cell-free layer formation in a microchannel with hyperbolic contraction: A CFD model validation’, Computer Methods and Programs in Biomedicine **226**, 107117 (2022) `10.1016/j.cmpb.2022.107117`.

[183] R. N. Pittman, ‘Oxygen Transport in the Microcirculation and Its Regulation’, Microcirculation **20** (2), 117–137 (2013) `10.1111/micc.12017`.

[184] A. Abay, S. M. Recktenwald, T. John, L. Kaestner and C. Wagner, ‘Cross-sectional focusing of red blood cells in a constricted microfluidic channel’, Soft Matter **16** (2), 534–543 (2020) `10.1039/C9SM01740B`.

[185] E. Sollier, M. Cubizolles, Y. Fouillet and J.-L. Achard, ‘Fast and continuous plasma extraction from whole human blood based on expanding cell-free layer devices’, Biomedical Microdevices **12** (3), 485–497 (2010) `10.1007/s10544-010-9405-6`.

[186] J. Marchalot, Y. Fouillet and J.-L. Achard, ‘Multi-step microfluidic system for blood plasma separation: architecture and separation efficiency’, Microfluidics and Nanofluidics **17** (1), 167–180 (2014) `10.1007/s10404-013-1296-4`.

[187] M. Kersaudy-Kerhoas, D. M. Kavanagh, R. S. Dhariwal, C. J. Campbell and M. P. Y. Desmulliez, ‘Validation of a blood plasma separation system by biomarker detection’, Lab on a Chip **10** (12), 1587 (2010) `10.1039/b926834k`.

[188] S. M. Recktenwald, K. Graessel, Y. Rashidi, J. N. Steuer, T. John, S. Gekle and C. Wagner, ‘Cell-free layer of red blood cells in a constricted microfluidic channel under steady and time-dependent flow conditions’, Physical Review Fluids **8** (7), 074202 (2023) `10.1103/PhysRevFluids.8.074202`.

[189] C. Loudon and A. Tordesillas, ‘The Use of the Dimensionless Womersley Number to Characterize the Unsteady Nature of Internal Flow’, Journal of Theoretical Biology **191** (1), 63–78 (1998) `10.1006/jtbi.1997.0564`.

List of publications

Publications directly related to this thesis

S. M. Recktenwald*, K. Graessel*, F. M. Maurer, T. John, S. Gekle and C. Wagner, Red blood cell shape transitions and dynamics in time-dependent capillary flows, *Biophysical Journal* 121 (1), 23–36 (2022)

S. M. Recktenwald, K. Graessel, Y. Rashidi, J. N. Steuer, T. John, S. Gekle and C. Wagner, Cell-free layer of red blood cells in a constricted microfluidic channel under steady and time-dependent flow conditions, *Physical Review Fluids* 8 (7), 074202 (2023)

Other publications

K. Graessel, C. Bächer and S. Gekle, Rayleigh–Plateau Instability of Anisotropic Interfaces. Part 1. An Analytical and Numerical Study of Fluid Interfaces, *Journal of Fluid Mechanics* 910, A46 (2021)

C. Bächer, K. Graessel and S. Gekle, Rayleigh–Plateau Instability of Anisotropic Interfaces. Part 2. Limited Instability of Elastic Interfaces, *Journal of Fluid Mechanics* 910, A47 (2021)

---

* These authors contributed equally.

Danksagung

Ich danke dem Betreuer meiner Arbeit Prof. Dr. Stephan Gekle für die Überlassung des Themas und die hervorragende Betreuung.

Dr. Christian Bächer, Dr. Steffen M. Recktenwald und Dr. Felix Reichel danke ich für die ergiebige und stets angenehme Zusammenarbeit. Der ganzen Arbeitsgruppe und im Besonderen meinen Bürokollegen Dr. Christian Bächer und Richard Kellnberger gebührt Dank für viele gewinnbringende fachliche Diskussionen und eine immer angenehme Arbeitsatmosphäre. Ich danke Claudia Brandt für jegliche administrative Unterstützung und Markus Hilt für seine Hilfestellung bei rechnertechnischen Problemen.

Der Studienstiftung des deutschen Volkes danke ich für die Finanzierung meines Projekts und der DFG für die Unterstützung im Rahmen der Research Unit FOR 2688 (Instabilities, Bifurcations and Migration in Pulsating Flow).

Meiner lieben Familie danke ich für allen Rückhalt und jede Unterstützung.

Eidesstattliche Versicherung

Hiermit versichere ich an Eides statt, dass ich die vorliegende Arbeit selbstständig verfasst und keine anderen als die von mir angegebenen Quellen und Hilfsmittel verwendet habe.

Weiterhin erkläre ich, dass ich die Hilfe von gewerblichen Promotionsberatern bzw. -vermittlern oder ähnlichen Dienstleistern weder bisher in Anspruch genommen habe, noch künftig in Anspruch nehmen werde.

Zusätzlich erkläre ich hiermit, dass ich keinerlei frühere Promotionsversuche unternommen habe.

Bayreuth, den